




Universitat Autònoma de Barcelona

**ADVERTIMENT.** L'accés als continguts d'aquesta tesi queda condicionat a l'acceptació de les condicions d'ús establertes per la següent llicència Creative Commons:  [http://cat.creativecommons.org/?page\\_id=184](http://cat.creativecommons.org/?page_id=184)

**ADVERTENCIA.** El acceso a los contenidos de esta tesis queda condicionado a la aceptación de las condiciones de uso establecidas por la siguiente licencia Creative Commons:  <http://es.creativecommons.org/blog/licencias/>

**WARNING.** The access to the contents of this doctoral thesis it is limited to the acceptance of the use conditions set by the following Creative Commons license:  <https://creativecommons.org/licenses/?lang=en>



**Universitat Autònoma  
de Barcelona**

**An Optofluidic Microwell Structure for the Rapid  
Determination of the Minimum Inhibitory  
Concentration (MIC) of Antibiotics**

**Jiri Dietvorst**

**Doctoral Thesis  
PhD in Biotechnology**

Supervised by:

**Dr. F. Xavier Muñoz Berbel**

**Prof. M. Pilar Marco Colás**

**Dr. M. Lluïsa Vilaplana Holgado**

Tutored by:

**Prof. Jordi Mas Gordi**

**Departament de Biotecnologia**

**Facultat de Ciències**

**2021**



The present thesis, entitled “**An Optofluidic Microwell Structure for the Rapid Determination of the Minimum Inhibitory Concentration (MIC) of Antibiotics**”, is submitted by Jiri Dietvorst as a partial fulfilment of the requirements for the Doctor of Philosophy degree in Biotechnology.

This thesis is a collaboration between the Institute of Microelectronics of Barcelona (IMB-CNM, CSIC), in the Grup de Transductors Químics (GTQ), under the supervision of Dr. Xavier Muñoz Berbel, and the Institut de Química Avançada de Catalunya (IQAC), in the Grup de Nanobiotecnologia pel Diagnòstic, under the supervision of Prof. M. Pilar Marco and Dr. Lluïsa Vilaplana.

This thesis was supported by the European Commission through the project ND4ID (H2020-MSCA-ITN-2015-675412) and the project LAB4CELL (RTI2018-100773-B-C31) from the Spanish Government.

Wit

Dr. F. Xavier Muñoz Berbel  
(Director)

Prof. Pilar Marco Colás  
(Director)

Dr. M. Lluïsa Vilaplana Holgado  
(Director)

Prof. Jordi Mas Gordi  
(Tutor)

Jiri Dietvorst  
(Author)





# Acknowledgements

The completion of this thesis would not have been possible without the help and support of a great number of people. To list and express the contribution of each and every one of them would take longer than the current work, which is why only a few people are mentioned. There are many others not appearing on the list below but that does not mean their contribution was not valid or appreciated. Besides, everyone knows I am bad with names and I might have just written a wrong one or two.

I will start expressing my thanks to people of ND4ID, the project that not only launched my PhD career, but also provided extensive trainings and professional help from all sides. In particular I would like to acknowledge Herman Goossens and Pieter Moons for the full organisation and bringing the project to a successful end. Among the students of ND4ID, I would emphasise a couple that, due to circumstances, provided just a little bit extra to my work than others. My friend Yang, for his amazing company in all of the ND4ID meetings, Weijin for the numerous collaborations we did, Sharath for his friendship and all the collaborations we performed, and finally Matilda, an amazing friend who was always there for me, both for small talk and for support.

The major execution of my thesis took place at the CNM, within the GTQ group. A few people stood out during my time there, though it would have been hard to have completed the work without those not mentioned. I would like to start with Juanma and Pablo, who were of great help and would support you any time you needed it. I want to make a special mention too to Miguel for the near weekly kebab trips.

Also within the CNM, including some I shared the office with for multiple years, there are a couple of people deserving extra attention. Sara, though she arrived towards the final year of my work, she provided great help with the chemistry and the related assays. Alex, not only for the special humour you provided, but also for the teamwork. Amparo, it goes without saying your help and contribution meant a lot to me. Your presence in the office made every day just that bit better. Xavi, do not worry, I will complain about you later.

Additionally, even though they left before my thesis came to its completion, I would like to thank Toby and Augusto, my predecessors, for the support you provided in the beginning, the help along the way and the experience and confidence you passed on.

I would like to make an extra dedication to Michele, for not just his friendship, but also his support through the years. His, often cynical, wisdom but also his big heart and companionship meant a lot to me.

There is also a small number of people that require mentioning from my time in Barcelona. Especially the group of Nb4D, in particular Pilar and Lluïsa, who were essential for the completion of the work. Though, due to circumstances, we collaborated less than I would have wanted, they provided a continuous source of support, and I hope they realize their help meant a lot. In addition, I would like to thank Gonzalo for his

infinite wisdom when it comes to chemistry, who helped us solve a multitude of issues. Finally, an extra thanks to Jordi for giving me the possibility to perform all the microbiological work in his laboratory. Within the group, an important mention to Núria, a great example of how to help and guide people, and always available for any required support.

Related to the secondment performed in Sweden, I would like to thank Wouter and Aman for the possibility to experience a 3-month stay there, providing insight in not only their research but also how research is performed differently at various locations. I would like to thank some students too, for helping me out during the secondment, but I will omit some of them to avoid their names appearing double and preventing their ego from growing even larger. However, a small mention is required for Linnea Gustafsson for her help with the silk fibroin.

To start closing up, I would like to thank my family for their endless love and support. Although they were far away, they never made me feel alone. To the family of my girlfriend, who took care of me when my family couldn't. Thank you for the love and patience and making me experience the Catalan culture.

A special thanks to my friends, in particular, Davy, Leonie, Frederik, Dries and Willem, to enable me to keep my sanity after the horrifying hours in the laboratories, and for the numerous laughs in all the activities we do together. Decisively, to Darragh, my best friend, for just being you. I would not have made this without you.

To Xavi, who was more than just a supervisor. He was a friend who became a role model to me over the years. Whenever someone asks me about my thesis, I can proudly say mine was amazing due to the best supervisor possible. I was sad to inform him I would not continue in academia, but I do hope our paths will meet plenty of times.

And finally, to Aina. Words cannot explain what you mean to me or how essential you were during the last 3 years. The value of your presence and support cannot be explained in a few words here, but I hope I will have a lifetime to show you.

# Contents

1. Motivation.....	1
2. Introduction.....	1
2.1. Infectious diseases: from plagues to COVID-19 .....	7
2.2. Bacterial infections: incidence, causes and treatment .....	7
2.2.1. Antibiotic resistance: types, mechanisms and prevention. ....	11
2.2.2. Diagnostic tools for MIC testing .....	14
2.3. Thesis starting point.....	30
2.4. Bibliography .....	32
3. Fundamentals.....	41
3.1. Bacteria: classification, proliferation and basic metabolic concepts.....	43
3.1.1. Bacterial classification .....	43
3.1.2. Bacterial proliferation .....	44
3.1.3. Bacterial metabolism .....	45
3.2. Optics Concepts: Absorbance and Reflectance.....	46
3.2.1. Light extinction mechanisms.....	47
3.2.2. Light refraction .....	49
3.3. Electrochemical concepts: Amperometry.....	50
3.4. Microfluidics.....	52
3.4.1. Laminar vs turbulent flow .....	52
3.4.2. Diffusion vs Convection.....	53
3.4.3. Surface tension vs gravity .....	54
3.4.4. Microfluidic components .....	56
3.5. Fabrication methods .....	58
3.5.1. Microfabrication technologies .....	58
3.5.2. Fast prototyping technologies.....	63
3.6. Bibliography .....	65
4. Objectives.....	67
5. Materials and methods .....	69
5.1. Design and Simulation Software .....	71
5.1.1. Design and optical simulations of the $\mu$ COR.....	71
5.1.2. Design and fluidic simulations of the gradient generator.....	73
5.2. Materials and Fabrication Methods.....	73
5.2.1. Manufacturing of $\mu$ COR by microfabrication technologies .....	74



5.2.2. Manufacturing the gradient generator through fast prototyping techniques .....	77
5.2.3. Optical shutter.....	80
5.3. Reagents and solutions .....	80
5.4. Electronic components.....	81
5.5. Bacterial cultures.....	81
5.5.1. Alginate hydrogels for bacterial-sensing and light routing .....	82
5.5.2. Bacterial-sensing alginate hydrogels.....	82
5.5.3. Electrodeposable alginate waveguides for light routing .....	83
5.6. Silk-based capillary substrates .....	84
5.6.1. Setup for freeze-drying silk substrates.....	85
5.6.2. Setup for the production of silk-based spiral components.....	85
5.6.3. Characterization of silk substrates .....	86
5.7. Iron-based metabolic indicators for bacterial detection and minimal inhibitory concentration determination.....	87
5.7.1. Composition of metabolic indicator precursor solutions .....	87
5.7.2. Determination of live bacterial concentration.....	87
5.7.3. MIC testing .....	88
5.8. Real samples.....	90
5.9. Data treatment and statistics.....	91
5.10. Bibliography .....	91
6. Bioassay.....	93
6.1. Bioelectrochromic hydrogel for fast antibiotic-susceptibility testing.....	97
6.1.1. Biomaterial electrodeposition and cell entrapment.....	97
6.1.2. Electrochromic response of the biomaterial.....	99
6.1.3. Electrochromic sensing of bacterial metabolism with the biomaterial .....	100
6.1.4. Antibiotic susceptibility testing with the electrochromic biomaterial.....	103
6.2. Ferricyanide in liquid cultures .....	106
6.2.1. Ferricyanide reaction mechanism .....	106
6.2.2. Ferricyanide reduction by bacterial metabolism .....	107
6.2.3. Minimal inhibitory concentration determination with the ferricyanide-based test .....	110
6.3. Prussian blue formation .....	113
6.3.1. Prussian blue reaction mechanism .....	113
6.3.2. Prussian blue formation by bacterial metabolism .....	114
6.3.3. Optimization of the Prussian blue protocol for bacterial detection .....	115
6.3.4. Metabolic formation of Prussian blue in the determination of MIC .....	117

6.4. Cyanotype-based protocol .....	120
6.4.1. Cyanotype-based bacterial detection reaction mechanism .....	120
6.4.2. Cyanotype-based reaction for bacterial detection .....	121
6.4.3. Optimization of the cyanotype-based protocol for bacterial detection.....	125
6.4.4. Cyanotype-based mechanism for the detection of very low bacterial concentrations characterization.....	130
6.4.5. Cyanotype-based protocol for susceptibility testing .....	140
6.4.6. Cyanotype-based bacterial detection in real samples .....	141
6.4.7. Cyanotype conclusions.....	144
6.5. Final remarks .....	145
6.6. Bibliography .....	147
7. Fluidics.....	149
7.1. State of the art .....	151
7.2. Generation 0: Prior work.....	153
7.2.1. Gen 0: Vacuum annealed silk fibroin .....	153
7.2.2. Gen 0: Freeze dried silk fibroin .....	154
7.3. Generation 1: Secondment in Stockholm .....	157
7.3.1. Gen 1: SF patterning through freeze-drying .....	157
7.3.2. Gen 1: Origami silk spring.....	159
7.4. Generation 2: gradient generator .....	162
7.4.1. Geometrical control valve design and simulations .....	163
7.4.2. Gradient generator Generation 1 .....	163
7.4.3. Gradient generator Generation 2 .....	168
7.4.4. Gradient generator Generation 3 .....	170
7.4.5. Gradient generator Generation 4 .....	177
7.5. Conclusions .....	184
7.6. Bibliography .....	185
8. Results Optics .....	189
8.1. Scheme of progress .....	192
8.2. Gen 1: Microfluidic-controlled optical router for lab on a chip .....	193
8.2.1. Micro-lens systems optimization .....	193
8.2.2. Design and performance of the $\mu$ COR .....	195
8.2.3. Characterization of PDMS-based $\mu$ COR .....	198
8.3. Gen 2: hydrogel waveguide formation by the electrodeposition of an alginate solution .....	203
8.3.1. Hydrogel optimization.....	204

8.3.2. Refractive index determination .....	205
8.3.3. Alginate as waveguide: characterization and proof of concept.....	206
8.3.4. Conclusions.....	208
8.4. Gen 3: optical shutter.....	209
8.4.1. Optimization.....	210
8.4.2. Characterization .....	212
8.4.3. Performance.....	215
8.4.4. Miniaturization and integration .....	216
8.4.5. Conclusions.....	217
8.5. Gen 4: frequency modulation .....	217
8.5.1. Design and principle.....	218
8.5.2. Conclusions.....	221
8.6. Final Remarks .....	222
8.7. Bibliography .....	224
9. Final device.....	229
9.1. Disposable part.....	231
9.2. Housing.....	232
9.3. Bibliography .....	235
10. Final conclusions .....	237
11. Supplementary .....	239
11.1. Supplementary: personal CV.....	239
11.1.1. List of publications .....	239
11.1.2. List of planned publications .....	239
11.1.3. List of conferences .....	239
11.1.4. List of students .....	240
11.2. Supplementary: Optimization cyanide-based assay .....	240
11.3. Supplementary: Ink aperture .....	245

# List of abbreviations

A.U.	Absorbance Units
ABTS	2,2'-azino-bis(3-ethylbenzothiazoline-6-sulfonic acid
AMR	Antimicrobial resistance
ASSURED	Affordable, sensitive, specific, user-friendly, rapid and robust, equipment-free and deliverable to end users
AST	Antimicrobial Susceptibility test
ATP	Adenosine triphosphate
BMD	Broth microdilution
CFU	Colony Forming Units
CGG	Concentration gradient generators
CLSI	Clinical and Laboratory Standards Institute
COVID-19	Severe acute respiratory syndrome coronavirus2 (SARS-CoV-2)
CV	Cyclic voltammetry
DLVM-AST	Deep learning video microscopy-based AST
DNA	Deoxyribonucleic acid
dRAST	Direct and rapid antimicrobial susceptibility test
EDTA	Ethylenediaminetetraacetic acid
EHT	Electron high tension
ETC	Electron transport chain
EUCAST	European Committee of Antimicrobial Susceptibility Testing
FeCN	Ferricyanide
FTIR	Fourier-transform infrared spectroscopy
HRP	Horseradish peroxidase
ICU	Intensive Care Units
ITO	Indium tin oxide
IUPAC	International Union of Pure and Applied Chemistry
Kmc	Kanamycin
LB	Lysogeny broth or Luria-Bertani broth

LoC	Lab on a Chip
MH	Mueller Hinton (broth)
MIC	Minimal inhibitory concentration
$\mu$ COR	Microfluidic-controlled optical router
NiOx	Nickel Oxide
PB	Prussian blue
PDMS	polydimethylsiloxane
PEB	Post exposure bake
PhLoC	photonic Lab on a Chip
PMMA	polymethylmetacrylate
POC	Point-of-care
PSA	pressure-sensitive adhesive
QC (EUCAST)	Quality Control (EUCAST)
Re	Reynolds number
RGB	red, green and blue
RI	Refractive Index
RS	Raman spectroscopy
SCE	saturated calomel electrode
SEM	scanning electron microscopy
SF	Silk fibroin
SHE	Standard Hydrogen electrode
TIR	total internal reflection
UTI	urinary tract infections
UV	Ultra violet
WE/RE/CE	Working, Reference and Counter Electrode
WHO	World Health Organization

# List of Tables and Figures

## List of tables

Table 2.1: Overview of the most common healthcare acquired bacterial infections worldwide.	8
Table 2.2: Overview of the most common bacterial infections and their corresponding morbidity and mortality.	9
Table 2.3: The various mechanisms of antibiotic action.	10
Table 2.4: Comparison of commercially available AST tests.	20
Table 2.5: Comparison of research and near future based technologies available AST tests.	26
Table 5.1: List of milling heads used in the fabrication of the fluidic designs.	78
Table 5.2: Parameters used in for laser cutting of various PMMA substrates.	78
Table 5.3: Summary of the variations of the performed assays	89
Table 6.1: MIC results of various strains when tested with gentamicin after 20 hours.	111
Table 6.2: Summary of various MIC tests performed using Prussian blue generation as indicator.	119
Table 6.3: Summary of various MIC tests performed using cyanotyping based bacterial sensing.	140
Table 6.4: Overview and comparison of the various generations of the bioassays.	146
Table 7.1: Overview of the various conditions used for the generation of the silk microsprints.	159
Table 7.2: Evolution and comparisson of the various generation of the geometrical valve design.	163
Table 7.3: COMSOL settings of generation 1 level set.	164
Table 7.4: Differences between level set method and the phase field method.	165
Table 7.5: COMSOL settings of generation 1 phase field.	166
Table 7.6: Parameter added to Table 7.5 in the COMSOL simulations of generation 1b.	171
Table 7.8: Observations of the performances of the fabricated generation 4 fluidics.	173
Table 7.8: Comparison between the Laser Cutter and the Milling machine,	174
Table 7.9: List of methods for bonding the fluidics to a top cover and the impact of the bonding.	175
Table 7.10: contact angle measurements of PMMA with various treatments.	178
Table 7.11: COMSOL settings of generation 4.	183
Table 8.1: Optimization of the concentrations of the reagents for the alginate hydrogel electrodeposition.	204
Table 8.2: Summary of the various methods employed in the optimization of the usage and deposition of an electrochromic molecule on an indium tin oxide (ITO) electrode.	211
Table 8.3: Analysis of the cyclic voltammogram of Figure 8.16.	214
Table 8.4: Description of transmittance peak belonging to the FTIR spectra of Figure 8.17.	215
Table 8.5: Overview and comparison of the various generations of the optical routers.	223

## List of figures

Figure 2.1: Graph showing the time between antibiotic development and the appearance of resistance processes. ....	12
Figure 2.2: Illustration depicting antibiotic action (A) and the corresponding resistance mechanisms (B). ....	13
Figure 2.3: Golden standard techniques require pure bacterial cultures.....	15
Figure 2.4: Minimum inhibitory concentration.....	16
Figure 2.5: Single cell versus culture based methods. ....	17
Figure 2.6: Overview of the different single cell based technologies. ....	27
Figure 3.1: Chemical composition of the cell wall of gram-negative and gram-positive bacteria. ....	44
Figure 3.2: Figure depicting the growth curve of bacteria.....	45
Figure 3.3: Figure illustrating the electron transport chain (ETC) over a bacterial membrane. .	46
Figure 3.4: Electromagnetic spectrum. ....	47
Figure 3.5: Beer-Lambert law visualized. ....	48
Figure 3.6: Refraction and total internal reflection. ....	49
Figure 3.7: Representation of a characteristic chronoamperometrical plot. ....	51
Figure 3.8: Illustration of a three-electrode cell and an example of a cyclic voltammogram. ...	52
Figure 3.9: Image illustration the principles of laminar and turbulent flow.....	53
Figure 3.10: Illustration of the contact angle of a liquid droplet on a solid substrate.....	55
Figure 3.11: Illustration of the various parameters required for determining the capillary rise height. ....	56
Figure 3.12: Image illustration the principle of a photoresist.....	60
Figure 3.13: The basic steps in photolithography. ....	60
Figure 3.14: Basic process of replica moulding. ....	63
Figure 5.1: Schematic overview of the optofluidic router and its working principle.....	71
Figure 5.2: Optimization of the light focusing lenses using Tracepro.....	72
Figure 5.3: COMSOL simulation of the generation 5 valve, using a symmetric valve and assymetric inlets.....	73
Figure 5.4: Characterization of the light focusing principle with different micro-chambers being filled with a solution of fluorescein.....	75
Figure 5.5: Overview of the optofluidic setup for the characterization of the $\mu$ COR.....	76
Figure 5.6: Optofluidic setup for the characterization of the gradient generator.....	79
Figure 5.7: Schematic showing the setup and working principle of the generation of silk microsprings. ....	86
Figure 6.1: Scheme of the continuity of the various generation of the bioassay under development. ....	96
Figure 6.2: Optimization of biomaterial electrodeposition. ....	98
Figure 6.3: Bacterial entrapment in the biomaterial. ....	99
Figure 6.4: Electrochromic response of the biomaterial.....	100
Figure 6.5: Metabolic sensing of the biomaterial. ....	102
Figure 6.6: Response of the biomaterial to metabolic stimulators and inhibitors. ....	103
Figure 6.7: Antibiotic susceptibility test with the biomaterial.....	104
Figure 6.8: Reaction mechanism of ferricyanide reduction by bacterial metabolism. ....	106
Figure 6.9: Bacterial ferricyanide reduction over time at various bacterial concentrations. ...	108
Figure 6.10: Optimization of the ferricyanide concentration using Escherichia coli as model organism.....	109

Figure 6.11: Gentamicin MIC using ferricyanide.....	112
Figure 6.12: Reaction mechanism of Prussian blue formation by bacterial metabolism. ....	114
Figure 6.13: Formation of Prussian blue by bacterial metabolism.. ....	114
Figure 6.14: Optimization of the Prussian blue assay. ....	116
Figure 6.15: Prussian blue precipitation experiments based on FeCN-FeCl <sub>3</sub> ratios in MH medium.. ....	117
Figure 6.16: MIC determination of E. coli against kanamycin using Prussian blue.....	118
Figure 6.17: Reaction mechanism of cyanotype based Prussian blue formation by bacterial metabolism.....	121
Figure 6.18: Cyanotype-based reaction proof of concept. ....	122
Figure 6.19: Images of the cyanotyping based protocol for Prussian blue formation by bacterial metabolism.....	124
Figure 6.20: Cyanotyping-based reaction optimization under dark conditions.....	125
Figure 6.21: Cyanotype-based reaction optimization under light conditions. ....	126
Figure 6.22: Picture of the cyanotype-based reaction optimization under light conditions... ..	128
Figure 6.23: Cyanotype-based protocol sensitivity in dark and light.....	129
Figure 6.24: Evaluation of performance and reaction between the various reagents of the cyanotype-based protocol performed in dark. ....	131
Figure 6.25: Evaluation of performance and reaction between the various reagents of the cyanotype-based protocol performed under continuous illumination. ....	132
Figure 6.26: Cyclic voltammograms of the various reagents of the cyanotype-based protocol performed in dark. ....	134
Figure 6.27: Cyclic voltammograms of the various reagents of the cyanotype-based protocol performed under continuous illumination. ....	135
Figure 6.28: Ccetylsalicylic acid experiments for the detection of free iron (III). ....	136
Figure 6.29: Cyanotype-based reaction and controls. ....	138
Figure 6.30: Sensitivity of the cyanotyping assay performed in spiked human serum.....	142
Figure 6.31: Sensitivity of the cyanotyping assay performed in spiked pig's blood. ....	143
Figure 7.1: Scheme of the continuity of the various generation of the fluidics under development. ....	152
Figure 7.2: Glucose biosensor using a silk fibroin matrix. ....	154
Figure 7.3: SF microstructure, surface area and porosity. ....	155
Figure 7.4: Capillary flow rate using SF thin film.....	156
Figure 7.5: SF thin film with honeycomb pattern. ....	158
Figure 7.6: Silk thread highlighted under microscope. ....	160
Figure 7.7: Scheme of the principle of a geometrical valve. ....	162
Figure 7.8: COMSOL simulation of the generation 1 valve using the level set method. ....	165
Figure 7.9: COMSOL simulation of the generation 1 valve using the phase field method. ....	167
Figure 7.10: COMSOL simulation of the generation 1 c valve, using assymmetric inlets. ....	168
Figure 7.11: COMSOL simulation of the generation 2 valve using an assymmetric valve and inelt design. ....	169
Figure 7.12: COMSOL simulation of the generation 3 valve, using a symmetric valve and assymmetric inlets.....	170
Figure 7.13: COMSOL simulation of the generation 3 valves, with each of the 4 variations....	171
Figure 7.14: CoreIDRAW design of the four fluidic structures .....	172
Figure 7.15: Depiction of the drawbacks of the laser cutter .....	175
Figure 7.16: Highlights of the function of the 3rd generation. ....	177
Figure 7.17: Depiction of the measurement of the contact angle.....	178



Figure 7.18: Influence of NaOH treatment and channel depth on flow behaviour.....	179
Figure 7.19: Simulation of flow valves. ....	181
Figure 7.20: COMSOL simulation of the generation 4 valves, using a symmetric valve and asymmetric inlets.....	182
Figure 10.1: Scheme of the continuity of the various generations of optical routers under development. ....	192
Figure 8.2: Optimization and analysis of the light focusing lenses. ....	194
Figure 8.3: The performance of the spline optimized lens systems .....	195
Figure 8.4: Schematic overview of the optofluidic router and its working principle.....	196
Figure 8.5: Architecture and working principle of phase-guides. ....	197
Figure 8.6: AutoCAD highlight of the positioning of the primer phase-guides and their influence on the flow propagation.. ....	198
Figure 8.7: Characterization of the light focusing principle. ....	198
Figure 8.8: Time dependence of the flow rate in terms of lapse-time and switching. ....	200
Figure 8.9: Cross-talk levels between the optical outputs.....	201
Figure 8.10: Design of the electrode layout for sequential cycling of the hydrogel formation.	204
Figure 8.11: Determination of the refractive index by observing changes in refraction upon passing through the alginate hydrogel.....	205
Figure 8.12: Image highlighting the positioning of the fibers relative to each other and the electrodes respectively. ....	206
Figure 8.13: Optical measurements of the formation and reversal of the alginate hydrogels.	207
Figure 8.14: Scheme of the working principle of the optical shutter .....	210
Figure 8.15: Reaction mechanism of the NiO oxidation reduction process in a water based environment.....	212
Figure 8.16: Cyclic voltammetry of a NiO film.....	213
Figure 8.17: Fourier-transform infrared spectroscopy of NiO redox states. ....	214
Figure 8.18: Imaging of the switching rate of the optical shutter at a constant rate between its two redox states.....	216
Figure 8.19: Image of a silicon wafer with a nickel oxide thin film formed through thermal oxidation.. ....	217
Figure 8.20: Conceptual block design of the coupling of various RGB LED lights .....	219
Figure 8.21: Electronic schematic the RGB spectrophotometer for one RGB channel.....	220
Figure 8.22: Protoboard setup of the RGB spectrophotometer using a single RBD LED light source.....	221
Figure 9.1: Optical funnel for the collection of parallel light rays to a single output. ....	233
Figure 9.2: Prototype of the final standalone device for rapid AST testing of antibiotics.....	235

# Abstract

Bacterial infections are a common occurrence, in most cases easily treated using antibiotics. However, even though treatments are available, they still account for the top five global mortality cases. The misuse and overuse of antibiotics results in a continuous increasing number of antibiotic resistant bacterial strains, able to overcome even the most powerful of treatments. The continuation of this trend will enable bacterial infections to overtake the number 1 mortality cause, possibly setting society back to the pre-antibiotic era.

Various methods can be employed to decelerate or even entirely prevent this future, with a new generation of fast antibiotic susceptibility testing (AST) being one of them. AST tests, such as broth microdilution (BMD), disk diffusion and the E-test, provide information about the resistance profile of the tested strain, identifying which antibiotic would prove optimal and at which concentration. However, they, and other marketed methods, require sample extraction and enrichment, resulting in long incubation times (2-7 days from test to result) that severely limit the decision-making process. There is a need for tests able to generate resistance profiles within 2-4 hours.

This thesis tackles this issue by the development of a new rapid diagnostic tool, built around a novel bioassay. The work itself was divided into three major parts: the bioassay, optics and fluidics, which were finally integrated into the new diagnostic strategy.

The **bioassay** was based on the use of bioelectrochromic molecules that change colour in response to bacterial metabolism (i.e. metabolic indicators), being able to selectively detect live bacteria. Four strategies were evaluated, namely: **(i) an electrodepositable iron-based alginate hydrogel** able to entrap bacteria and change colour in response to their metabolism; **(ii) ferricyanide alone**, being reduced to ferrocyanide by bacterial metabolism; **(iii) Prussian Blue formation** by the reaction between metabolically produced ferrocyanide and iron (III) chloride; and **(iv) the cyanotype-based reaction**, where the previous iron donor was substituted by the photo-sensitive ferric ammonium citrate. The best results were obtained with the photo-catalytic reaction that allowed the detection of 1 CFU/mL within 4 hours. The assay was further demonstrated as proof of concept as direct viability test in serum and blood.

Regarding to the **optical components**, the objective was to use optical routers to minimize the use of light sources and photo-detectors when multiple tests were running in parallel to perform the AST. Four light routing strategies were developed: **(i) a microfluidically-controlled optical router**, requiring external pumps to redirect the light into the optical detection channels; **(ii) electrodepositable alginate hydrogels**, acting as waveguides, to guide the light to the detection area; **(iii) electrically controlled optical shutters**, based on the use of nickel oxide that change from transparent to deep black to allow/avoid the light to cross; and **(iv) frequency-modulation system**, where each monochromatic light source is pulsed at a specific frequency and can be identified

subsequently even when using a single photo-detector. Though still in its infancy, the frequency modulation showed great promise as a highly flexible, adaptable and cheap system to measure near all biological assays.

**Microfluidics** were implemented in the system to manage the small sample and reagent volumes required. To avoid the use of external pumps, capillary-based systems were implemented and tested, including silk nanoporous layers or capillary based fluidic channels. Passive valve was designed and integrated in the microfluidic system with the objective of performing sample processing, i.e. dilution, automatically on chip, minimizing hands-on time. The geometric valves were designed as a logical AND-valve, where two separate liquids met at the valve and could only propagate past if both were present. By matching the breaching of the valve and controlling the pressures inside the system, a 1-1 dilution of both liquids would occur after the valve. Sequential valves provided a 2-fold dilution of one of the inlet solutions. The valves were simulated using COMSOL, optimized and validated experimentally after fabrication by fast prototyping techniques.

Finally, each of the three components were integrated into a single prototype. Composed of two parts, a reusable and a disposable part, the device would enable read-out of a single resistance profile within 4 hours, without any external equipment. The disposable part included the fluidics and the bioassay itself. Since neither required high precision of fabrication, they were solemnly composed of cheap materials. The reusable part incorporated the more precise optical components and the electronics responsible for powering and controlling the optics. Using an ARDUINO controller, the device was completely autonomous for fast antibiotic susceptibility testing.

# Resum

Les infeccions bacterianes són patologies comunes que, en la majoria dels casos, es tracten mitjançant antibiòtics. Malgrat aquesta accessibilitat a tractaments, les infeccions causades per bacteris són una de les cinc causes més comunes de mortalitat al món. L'ús excessiu i el mal ús en general dels antibiòtics és un dels motius d'aquesta elevada mortalitat, la qual s'associa a un increment en el nombre de soques bacterianes resistents als antibiòtics capaces, fins i tot, de superar els tractaments més agressius. Continuar amb un ús imprudent dels antibiòtics pot situar les malalties infeccioses bacterianes com a primera causa de mort, posicionant la societat en una situació similar a l'anterior al descobriment dels antibiòtics.

Actualment, s'han identificat varies estratègies per prevenir aquest desenllaç, essent el desenvolupament de mètodes ràpids per a la determinació de susceptibilitat a antibiòtics (AST de l'anglès *antibiotic susceptibility test*) una de les destacades. Els mètodes tradicionals per a la determinació de susceptibilitat a antibiòtics, com els basats en microdilució de cultius, difusió en discs o el E-test, proporcionen informació sobre el perfil de resistència a antibiòtics de les soques bacterianes testades, identificant l'antibiòtic òptim pel tractament, així com la dosi adequada. No obstant, tan aquests com altres mètodes comercialment accessibles requereixen la purificació i enriquiment de la mostra, el que prolonga l'assaig entre 2 i 7 dies (segons el tipus de bacteri), endarrerint la selecció del tractament. Per tant, hi ha la necessitat de desenvolupar tests que permetin avaluar la susceptibilitat/resistència de les soques en temps curts d'entre 2-4 hores.

Aquesta tesi aborda aquest problema proposant el desenvolupament d'un nou test de diagnòstic ràpid, desenvolupat en el marc d'un nou bioassaig. El treball es divideix en tres parts principals: el bioassaig, els components òptics i el components fluídics, tots ells finalment integrats en el nou sistema de diagnòstic ràpid.

El **bioassaig** es basa en l'ús de molècules bioelectrocròmiques que canvien de color en resposta al metabolisme bacterià (també coneguts com a indicadors metabòlics), essent així capaces de detectar la presència de bactèries vives. S'han avaluat quatre estratègies: **(i) un hidrogel d'alginat amb ions ferro com a agent entrellaçant** capaç d'atrapar bacteris i canviar de color en resposta al seu metabolisme; **(ii) ferricianur**, un complex de ferro que és reduït a ferrocianur pel metabolisme bacterià; **(iii) la formació de Blau de Prússia** com a resultat de la reacció entre el ferrocianur produït metabòlicament i el clorur de ferro (III); i **(iv) una reacció basada en la cionotípia**, on el clorur de ferro (III) emprat prèviament com a donador de ions ferro és substituït per citrat fèrric d'amoni, un compost foto-sensible on el ferro s'allibera per acció de la llum. Els millors resultats es van obtenir amb la reacció fotocatalítica que permetia la detecció de 1 bacteri viable per mL en 4 hores de reacció. El bioassaig va ser demostrat, com a prova de concepte, en la detecció directe de bacteris en mostres de sèrum i sang completa.

En relació amb els **components òptics**, l'objectiu consistia en desenvolupar elements de direccionament de la llum (*routers*) que permetessin reduir el nombre de fonts de llum i detectors en sistemes multiplexats com els requerits en AST, en els que varis tests tenen lloc a la vegada. Novament, es van desenvolupar i testar quatre estratègies de direccionament de la llum: **(i) un router òptic controlat microfluídicament**, que requeria bombes microfluídiques externes per controlar i direccionar el feix de llum a cada un dels canals òptics de detecció; **(ii) routers basats en hidrogels d'alginat electrodepositables**, en els quals el gel, un cop format, actuava com a guia d'ona i dirigia la llum cap al canal de detecció; **(iii) obturadors òptics controlats elèctricament**, basats en l'ús d'òxid de níquel, un material electrocròmic que canvia de transparent a negre permetent o evitant el pas de llum, segons la seva coloració; i **(iv) moduladors de polsos de freqüència**, sistemes electrònics que permeten generar patrons de freqüència diferents per cada font de llum monocromàtica emprada i així identificar-la, encara que es faci servir un únic fotodetector per a la mesura. Encara que en la seva infància, el modulador de polsos de freqüència ha mostrat un gran potencial en la mesura de processos biològics per ser molt flexible, adaptable i barat.

Els **components microfluídics** es van implementar en el sistema per gestionar els petits volums de mostra i reactius empleats en l'assaig. Per evitar l'ús de bombes fluídiques externes, es van implementar i avaluar components basats en forces capil·lars tals com capes nanoporoses de seda o microcanals fluídics. Es van dissenyar i integrar en el sistema vàlvules passives que permetien el processament de la mostra, concretament una dilució automàtica en el chip, minimitzant la manipulació de la mostra. Les vàlvules geomètriques van ser dissenyades com una vàlvula lògica, on dos líquids separats coincidien en un punt d'aquesta i només podien propagar si prèviament entraven en contacte físic. Controlant les pressions i la força de ruptura de la vàlvula en el sistema, era possible obtenir una dilució de la mostra de 1:1 en el flux sortint de la vàlvula. La incorporació de vàries vàlvules seqüencials permetia realitzar una dilució 1:2 de la mostra inicialment inoculada. Les vàlvules van ser simulades mitjançant COMSOL, optimitzades i validades experimentalment després de la seva fabricació per tècniques de prototipat ràpid.

Finalment, els tres components anteriors es van integrar en un únic prototip. El prototip, format per una part reutilitzable i una d'un sol ús, permetia la determinació de la resistència o susceptibilitat dels bacteris presents en un fluid biològic en 4 hores de forma autònoma i sense requerir cap instrument extern addicional. La component d'un sol ús incloïa els components fluídics i el bioassaig. Com que aquests components no requerien una gran precisió en la fabricació, es van manufacturar en materials de baix cost. La part reutilitzable incorporava els elements òptics més cars i precisos, així com els components electrònics responsables de controlar la mesura i processar els senyals. Fent servir el microcontrolador de la plataforma ARDUINO, el dispositiu era completament autònom en la determinació de la susceptibilitat a antibiòtics.

# Resumen

Las infecciones bacterianas son patologías comunes que, en la mayoría de los casos, se tratan con antibióticos. Esta accesibilidad a tratamientos, no obstante, no impide que las infecciones bacterianas sean aun una de las cinco causas más comunes de muerte en el mundo. El uso excesivo e incorrecto de antibióticos es una de las principales causas de esta elevada mortalidad, la cual, se asocia a un incremento en el número de cepas bacterianas resistentes a antibióticos capaces de resistir los tratamientos más agresivos. Continuar con este uso imprudente de los antibióticos podría situar las enfermedades infecciosas bacterianas como la primera causa de muerte, dirigiendo la sociedad a una situación similar a la anterior al descubrimiento de los antibióticos.

Actualmente se han identificado varias estrategias para prevenir este desenlace, siendo el desarrollo de métodos rápidos para la determinación de susceptibilidad a antibióticos (AST del inglés *antibiotic susceptibility test*) una de las más destacadas. Los métodos tradicionales para la determinación de la susceptibilidad a antibióticos, como los basados en microdilución de cultivos, difusión en discos o el E-test, proporcionan información sobre el perfil de resistencia a antibióticos de las cepas bacterianas testadas, identificando tanto el antibiótico óptimo para el tratamiento como la dosis requerida. No obstante, tanto estos como otros métodos comercialmente disponibles requieren la purificación y enriquecimiento de la muestra, lo que prolonga el ensayo entre 2 y 7 días (según el tipo de bacteria), retrasando la selección del tratamiento. Por lo tanto, hay la necesidad de desarrollar tests que permitan evaluar la susceptibilidad/resistencia de las cepas en tiempos cortos de entre 2-4 horas.

Esta tesis aborda este problema desarrollando un nuevo test de diagnóstico rápido basado en un innovador bioensayo. El trabajo presentado se divide en tres partes principales: el bioensayo, los componentes ópticos y los componentes fluídicos, todos ellos integrados finalmente en el nuevo sistema de diagnóstico rápido.

El **bioensayo** se basa en el uso de moléculas bioelectrocrómicas que cambian de color en respuesta al metabolismo bacteriano (conocidas como indicadores metabólicos), siendo capaces de detectar la presencia de bacterias vivas. Se han evaluado cuatro estrategias: **(i) un hidrogel de alginato con iones de hierro como agente entrelazante** capaz de atrapar bacterias y cambiar de color en respuesta a su metabolismo; **(ii) ferricianuro**, un complejo de hierro que es reducido a ferrocianuro por parte del metabolismo bacteriano; **(iii) la formación de Azul de Prusia** como resultado de la reacción entre ferrocianuro producido metabólicamente y cloruro de hierro (III); y **(iv) una reacción basada en la cianotipia**, usando como donador de iones hierro citrato férrico de amonio, un compuesto fotosensible en el que el hierro se libera por la acción de la luz, en lugar de cloruro de hierro (III). Los mejores resultados se obtuvieron con la reacción fotocatalítica que permitía la detección de 1 bacteria viable por mL en 4 horas de reacción. El bioensayo se demostró, como prueba de concepto, en la detección directa de bacterias en muestras de suero y sangre completa.

En relación con los **componentes ópticos**, el objetivo consistía en desarrollar elementos de direccionamiento de la luz (*routers*) que permitiesen reducir el número de fuentes de luz y detectores en sistemas multiplexados como los empleados en AST, en los que varios ensayos tienen lugar a la vez. Nuevamente, se desarrollaron y evaluaron cuatro tecnologías de direccionamiento de la luz: **(i) un router óptico controlado microfluídicamente**, que requería bombas microfluídicas externas para controlar y direccionar el haz de luz a cada uno de los canales ópticos de detección; **(ii) routers basados en hidrogeles de alginato electrodepositables**, en los cuales el gel, una vez formado, actuaba como una guía de luz dirigiendo la luz al canal de detección; **(iii) obturadores ópticos controlados eléctricamente**, basados en el uso de óxido de níquel, un material electrocrómico que cambia de transparente a negro permitiendo o evitando así el paso de luz, según su coloración; y **(iv) moduladores de pulsos de frecuencia**, sistemas electrónicos que permiten generar patrones de frecuencia diferentes para cada fuente de luz monocromática empleada y así identificarla, incluso con un único fotodetector. Aunque aún en un estado de desarrollo muy inicial, el modulador de pulsos de frecuencia ha mostrado un gran potencial en la medida de procesos biológicos por ser muy flexible, adaptable y barato.

Los **componentes microfluídicos** fueron implementados al sistema para gestionar los pequeños volúmenes de muestra y reactivos empleados en el ensayo. Para evitar el uso de bombas externas, se implementaron y evaluaron componentes basados en fuerzas capilares como capas nanoporosas de seda o microcanales fluídicos. Se diseñaron e integraron en el sistema fluídico válvulas pasivas que permitían el procesamiento de la muestra, concretamente la dilución automática en el chip, minimizando la manipulación de la muestra. Las válvulas geométricas se diseñaron como una válvula lógica en la que dos líquidos separados coincidían en un punto de la misma y solo podían propagar al entrar en contacto físico. Controlando las presiones y la fuerza de ruptura de la válvula en el sistema era posible obtener una dilución de la muestra de 1:1 en el flujo de salida de la válvula. La incorporación de varias válvulas secuenciales permitía realizar una dilución 1:2 de la muestra inicialmente inoculada. Las válvulas se simularon y optimizaron mediante COMSOL, y fueron validadas experimentalmente una vez fabricadas por técnicas de prototipado rápido.

Finalmente, los tres componentes anteriores se integraron en un único prototipo. El prototipo, formado por una parte reutilizable y una de un solo uso, permitía la determinación de la susceptibilidad/resistencia a antibióticos en fluidos biológicos en 4 horas, de forma autónoma y sin requerir ningún instrumento externo adicional. La componente de un solo uso incluía los componentes fluídicos y el bioensayo. Como estos componentes no requerían una gran precisión en la fabricación, se fabricaron en materiales de bajo coste. La parte reutilizable incorporaba los elementos ópticos más caros y precisos, así como los componentes electrónicos responsables de controlar la medida y procesar las señales. Usando el microcontrolador de la plataforma ARDUINO, el dispositivo era completamente autónomo en la determinación de la susceptibilidad a antibióticos.

# **1. Motivation**



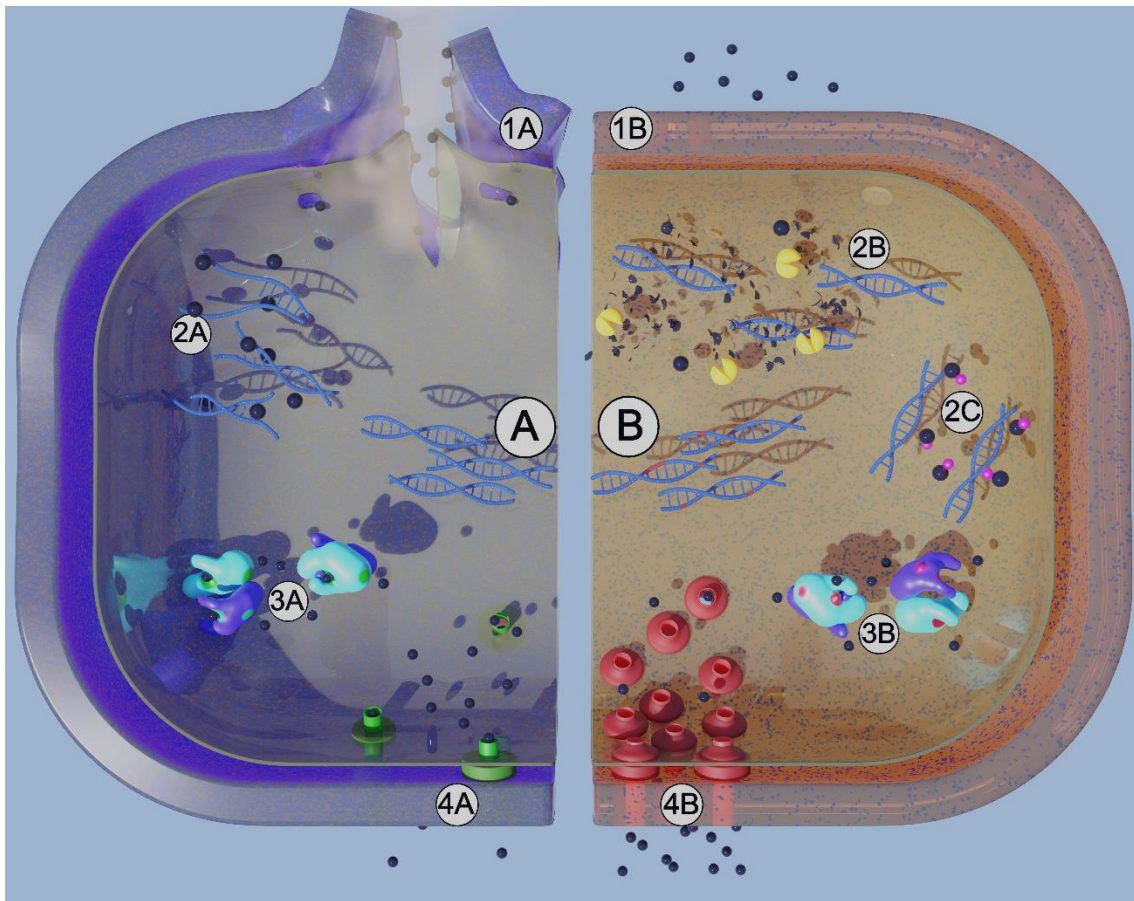


In the current globalised world, infectious diseases are a general problem affecting any society and economy without exception. The socio-economic impact of such pathologies is deep and persistent around the world. Just checking the statistics from official organizations [8], infectious diseases have positioned three pathologies, i.e. lower respiratory infections, diarrheal diseases and tuberculosis, in the top ten causes of death worldwide. Even in the EU, infectious diseases are the third most common cause of death [9], just after circulatory diseases and cancer. Worryingly, rather than alleviated, this situation is being aggravated by the emergence of three new societal factors: (1) the aging/longevity of human population, with a higher susceptibility of elderly people to infection [10]; (2) human migrations/mobility; and (3) climate change. Considering the two last ones, human migration and climate change are foreseen to alter traditional epidemiological patterns by producing changes in the local hosts, pathogens and transmission mechanisms [11]. This is affecting the incidence and distribution of human infectious diseases. Apart from that, the emergence and proliferation of antimicrobial resistances (AMRs) is also affecting the global management of infectious diseases. Antimicrobial drugs, traditionally used in the treatment of infectious diseases (e.g. antibiotics to treat bacterial infections), are now losing activity by the proliferation of AMR strains. The impact of such resistances on treatment of infectious disease is wide considering both personal and economical costs [12]. As an example, and although a strict evaluation should consider population surveillance networks [13], it has been estimated that drug resistant strains kill 33.000 persons every year in the EU (700.000 worldwide [14]) with a total estimated cost of €1.5 billion to the European healthcare systems and society [15]. Moreover, these numbers are expected to increase in the near future for the selective pressure imposed to them, and mostly associated to antibiotic overuse [1]. It is reported by the pharmaceutical industry that the global antibiotics consumption has increased by 35% from 2000 and 2010 worldwide, with countries such as Brazil, Russia and India reaching a dramatic increase of 76% [2]. This difference in antibiotic consumption is also stated in the comprehensive directory of antibiotic use in EU reported by Goosens et al. [3], which reveals that southern and eastern Europe countries present a higher consumption of antibiotics, which may also be related to a higher AMR incidence.

**This thesis is thus motivated by the increasing incidence of antibiotic resistance, aiming to provide tools for a faster and more precise diagnostic and treatment of patients suffering from bacterial infections leading to a more rational use of antibiotics.**



## 2. Introduction





## 2.1. Infectious diseases: from plagues to COVID-19

An infection is defined by the Medical Dictionary as “*the invasion of an organism's body tissues by pathogens, their multiplication, and the reaction of host tissues to the infectious agents and the toxins they produce*”, where the definition of pathogen corresponds to “*any disease-producing agents, especially a bacterium, virus or other micro-organisms.*”

From the first epidemic plague reported, the Plague of Justinian, firstly reported in 541 and extending up to 760, infectious diseases have been striking all humans societies and civilizations throughout the history ([4]). Probably the Plague or the Black Death is one of the most famous ones, being the deadliest pandemic reported in human history up to now ([5]). This epidemic, caused by the bacterium *Yersinia pestis*, spread along Europe from 1336 to 1343 costing the lives of nearly one third of the European population. Another well-known epidemic was the Spanish flu, caused by the H1N1 influenza A virus, further known as the 1918 flu pandemic, which was responsible of the death of between 17 and 50 million people worldwide ([6]). Recently, the COVID-19, caused by severe acute respiratory syndrome coronavirus2 (SARS-CoV-2), which started its spread in 2019, led to at least 30 million cases with close to a 1 million deaths worldwide at the time of writing. Even with the death toll lower compared to infectious diseases like tuberculosis (10 million cases with 1.5 million deaths in 2018), the pandemic had a major impact on the global economy ([7]).

Although, less showy and with less presence in the media, other infections are affecting our society year-by-year with an important accumulating number of infected people and deaths. This is the case for influenza, tuberculosis, malaria, lower respiratory tract infections caused by bacteria like *Pseudomonas aeruginosa* or *Staphylococcus aureus*, urinary tract infections caused by *Escherichia coli*, or human immunodeficiency virus (HIV), among others. It is worth noting that there are inherent and important physiological differences between viral, bacterial and fungal infections, and hence on their socio-economic impact and needs. **This thesis will exclusively focus on bacterial infections** and thus, these infections, their cause, diagnostic and treatment will be analysed in detail in the following sections.

## 2.2. Bacterial infections: incidence, causes and treatment

Bacteria are small unicellular organisms (i.e. microorganisms) belonging to the prokaryotic empire. With a size between 0.5 and 5 micrometres, bacteria can be found almost everywhere in the Earth including air, soil and water, either alone or grouped in bacterial aggregates or biofilms ([8]). Surprisingly, bacterial strains have been found in very remote locations even with extreme conditions, such as aquatic volcanoes ([9]), salt pans ([10]) or waters highly contaminated by metal ions ([11]), where they survive thanks to their capacity to adapt to almost any type of harsh environment ([12]). This ubiquity and adaptability makes bacteria a common partner for humans' life. The interaction between human beings and bacteria is constant and, although mostly innocuous, sometimes bacteria can cause an infection, leading to healthcare complication and even death ([13]). For example, *Staphylococcus aureus* is carried by

20-30 % of the human population in the nostrils, but can cause severe healthcare issues when they spread to other regions. Some of the most popular bacterial infections are **strep throat** (caused by a group A *Streptococcus* bacteria); **bacterial urinary tract infections** (UTIs; often caused by coliform bacteria); **bacterial food poisoning** (often caused by *E. coli*, *Salmonella* or *Shigella*), **gonorrhoea** (caused by the bacterium *Neisseria gonorrhoeae*), **chlamydia** (caused by the bacterium *Chlamydia pneumoniae*), **sypphilis** (caused by the bacterium *Treponema pallidum*), **tuberculosis** (caused by the bacterium *Mycobacterium tuberculosis*), **cholera** (caused by the bacterium *Vibrio cholerae*), **botulism** (caused by the bacterium *Clostridium botulinum*) or **tetanus** (caused by the bacterium *Clostridium tetani*), among others.

Due to the personal and environmental hygienic conditions and the effective treatments in the developed countries, in these regions bacteria are mostly opportunistic pathogens, taking benefit of stress, illness or any situation when the immune response of the host is reduced to infect and cause the pathology. This is particularly common in hospitals and healthcare centres and receives the name of hospital acquired or nosocomial infections. **Table 2.1** highlights in alphabetical order the most common healthcare acquired bacterial infections, those contracted after receiving health care for another condition, the acquisition channel and the rate of infection.

**Table 2.1: Overview of the most common healthcare acquired bacterial infections worldwide**, with the type of disease they cause and how they are acquired. GTI = gastrointestinal tract infection, UTI = urinary tract infection, \* all percentages are taken from the European Centre for Disease prevention and Control (ECDC) annual epidemiological report for 2017. All percentages relate to Intensive Care Units (ICU) acquired infections in European countries.

Strain	Disease	Acquisition	Rate of infection
<i>Acinetobacter baumannii</i>	Pneumonia, sepsis, UTI	ICU burn units and mechanical ventilator	0.39/1000 patients [14] 4.5 % pneumonia, 2.3 % sepsis, 1.4 % UTI*
<i>Enterococcus faecalis</i>	Endocarditis, GTI, UTI, sepsis,	Person to person	5 - 15% of infectious endocarditis [15] 15 % sepsis, 20.6 % UTI*
<i>Escherichia coli</i>	GTI, Pneumonia, UTI	Person to person, oral-faecal	14 % pneumonia, 9.2 % sepsis, 32 % UTI*
<i>Klebsiella pneumonia</i>	Pneumonia, sepsis, UTI	Medical devices, catheters, ventilators	15 % pneumonia, 12.4 % sepsis, 15.5 % UTI*
<i>Pseudomonas aeruginosa</i>	Pneumonia, sepsis, UTI	Moist surfaces, medical devices	20 % pneumonia, 9.5 % sepsis, 14.3% UTI*
<i>Staphylococcus aureus</i>	Pneumonia, sepsis	Person to person, contaminated object	18.5 % pneumonia, 12 % sepsis*

The aforementioned table shows the type of bacterial infections most people will encounter in first world countries. However, they are not the most prevalent types, nor the most deadly ones. **Table 2.2** highlights the most commonly found bacterial infections in humans, especially in third world countries.

**Table 2.2: Overview of the most common bacterial infections and their corresponding morbidity and mortality.** Further highlighted are the pathogens responsible and how spread usually occurs. Data related to the World Health Organization (WHO) are obtained in 2018.

<b>Infectious disease</b>	<b># new cases/year</b>	<b># deaths/year</b>	<b>Bacterial strain</b>	<b>Spread</b>
<b>Cholera</b>	2 – 4 million (WHO)	> 100.000	<i>Vibrio cholerae</i>	Infected food or water
<b>Gonorrhoea</b>	> 80 million [16]	> 10.000	<i>Neisseria gonorrhoeae</i>	Sexually transmitted
<b>Group A Streptococcal Infections (GAS)</b>	> 600 million GAS pharyngitis [17]	> 500.000	<i>Streptococcus pyogenes</i>	Body fluids
<b>Malaria</b>	> 220 million (WHO)	> 400.000	<i>Plasmodium vivax/knowlesi</i>	Mosquito bite
<b>Tuberculosis</b>	> 10 million (WHO)	1.6 million	<i>Mycobacterium tuberculosis</i>	Person to person through air

Regarding the treatment, bacterial infections are normally treated with wide spectrum antibiotics, without previous identification of the bacterial species responsible of the pathology. According to the IUPAC, antibiotics are “*substances produced by, and obtained from, certain living cells (especially bacteria, yeasts and moulds), or an equivalent synthetic substance, which is biostatic or biocidal at low concentrations to some other form of life, especially pathogenic or noxious organisms*”. (IUPAC 2003) Biostatic and biocidal refers to antibiotic activity. Thus, antibiotics are bacteriostatic when they prevent multiplication of the bacteria, but do not inherently kill them. In this case, bacterial death is usually dependent on the host defence system and removal of the bacteriostatic agent might lead to bacterial recovery and growth. Conversely, bactericidal antibiotics directly kill the bacteria. It is worth mentioning here that this differentiation is based on antibiotic behaviour in the lab, and plenty of antibiotics are not easily classified as either one or the other.

From a historical point of view, the first antibiotic, i.e. penicillin, was discovered in 1928 by the Scottish physician and microbiologist Prof. Alexander Fleming, who identified it in bacterial cultures contaminated by fungus. From that moment, the discovery of chemicals with antibacterial properties was progressing rapidly up to middle sixties, with what is known as the antibiotic golden era. During this golden era, most of antibiotic families were identified and classified according to their chemical structure, way of action and function as shown in **Table 2.3**. Some antibiotics do not belong to a specific class and are referred to as “others”.



**Table 2.3: The various mechanisms of antibiotic action.** Included are how they generally function, with which class belongs to each mechanisms. Finally, several examples of each antibiotic class are given. BS = bacteriostatic

Group	Function	Classes	Examples
<b>Nucleic acid inhibitors</b>	Target different stages and pathways of nucleic acid synthesis (DNA, RNA,...), preventing replication of genetic material and thus the bacteria themselves (Figure 2.2: 2A)	(fluoro-) quinolones	Ciprofloxacin, Levofloxacin and Moxifloxacin
		Others	Metronidazole
<b>Protein synthesis inhibitors</b>	Targets the bacterial ribosome. The ribosome is responsible for synthesising proteins. The classes interfere in different stages of the protein synthesis. Bacterial death occurs, because it cannot make more essential proteins (Figure 2.2: 3A)	Aminoglycosides	Gentamicin, kanamycin, Streptomycin
		Lincosamides (BS)	Clindamycin, lincomycin
		Macrolides (BS)	Azithromycin, Erythromycin
		Oxazolidinones (BS)	Linezolid, Posizolid
		Tetracycline (BS)	Doxycycline, metacycline, Tetracycline
		Others	Chloramphenicol, Mupirocin, Thiamphenicol
<b>Cell wall inhibitors</b>	Targets and prevent synthesis of the cell membrane whilst the bacteria is growing or dividing, weakening the rest of the wall, eventually leading to lysis. Several groups also target intact membranes, creating holes or weaknesses, causing lysis even when not dividing (Figure 2.2: 1A)	Carbapenem ( $\beta$ )	Imipenem/cilastatin Meropenem
		Cephalosporins (1 <sup>st</sup> – 5 <sup>th</sup> generation) ( $\beta$ )	Cefazolin (I), cefaclor (II), ceftriaxone (III), Cefepime (IV), Ceftobiprole (V)
		Glycopeptides	Vancomycin
		Lipopeptide	Daptomycin
		Monobactam ( $\beta$ )	Aztreonam
		Penicillin ( $\beta$ )	Amoxicillin, Ampicillin, Oxacillin, Piperacillin
		Polypeptides	Bacitracin, Colisitin, Polymyxin B
		Others	Fosfomycin
<b>Folic acid synthesis inhibitors</b>	Targets the folic pathway synthesis in bacteria, preventing formation of folate, disabling nucleic acid synthesis and thus DNA.	Sulfonamides	Prontosil
		Others	Dapsone

From that moment, only a limited number of antibiotics have been discovered or developed, which reduces the therapeutic possibilities of bacterial infections. In fact, in the last ten years only two new classes of antibiotics have been marketed, namely Daptomycin ([18]) and Oxazolidinones. The reason for this slow development is on the small attractiveness for the pharma industry to invest money and time in the search and development of new antibiotics, independently on their application spectrum of effectivity. The development of a new antibiotic is very expensive with the risk that healthcare organization such as WHO may advise to keep it as a final line of defence against resistant bacteria, reducing its use and minimizing the potential profit. Thus, the profit on antibiotics development is very small. Part of this problem is, therefore, due to the emergence and prevalence of antibiotic resistant strains.

### 2.2.1. Antibiotic resistance: types, mechanisms and prevention.

Antibiotics are, in general, effective substances to fight against bacterial infections. Unfortunately, from time to time, bacteria adapt to the action of a specific antibiotic, inhibiting or fully resisting its effect. In this situation, it is said that the microorganism develops resistance against this antibiotic, which is no longer effective in the treatment of this specific bacterial strain.

Antibiotic resistance is a natural process occurring spontaneously in nature and, in fact, it was reported before the first antibiotic was commercialized [19]. By the late 1960s, less than 30 years after the introduction of the first antibiotic in the market, resistance to penicillin was observed in more than 80% of both community and hospital isolates from *Staphylococcus aureus*. However, antibiotic resistance is not exclusive of penicillin, but observed to happen in any antibiotics discovered or produced some time after their application to the treatment of bacterial infections. This fact is represented in **Figure 2.1**, which illustrates the lapse time from the first introduction of the antibiotic to bacterial infections treatment until the detection of the first resistant strain.

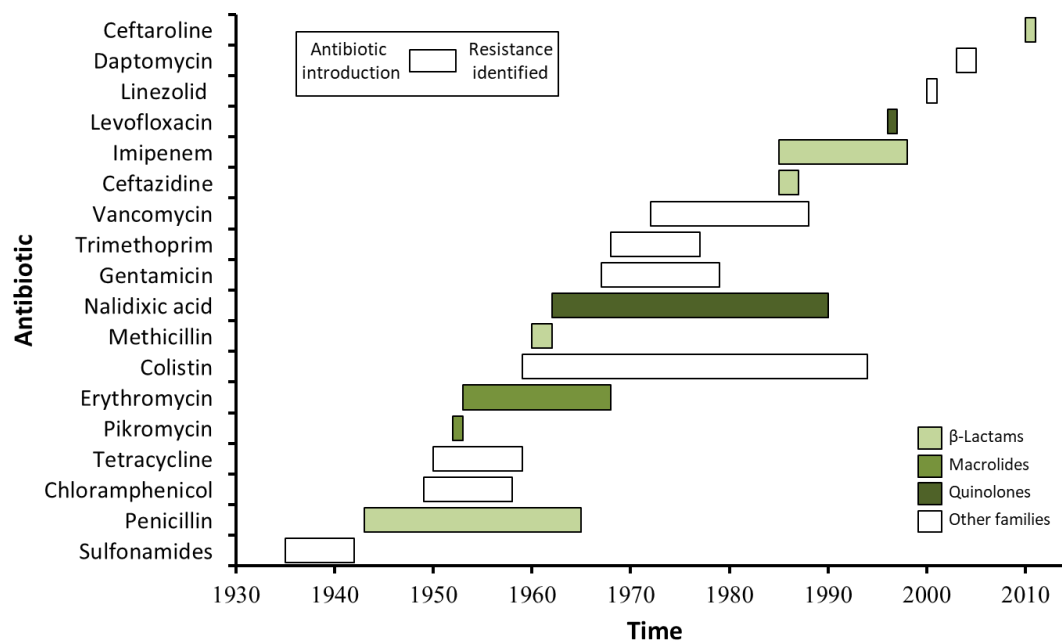


**Figure 2.1: Graph showing the time between antibiotic development and the appearance of resistance processes.** Highlighted in colour are various classes of antibiotics.

As shown, the lapse time for resistance appearance was larger or shorter depending on the antibiotic, but resistant strains have been identified for each and every antibiotic developed. The mechanisms bacteria utilize to acquire antibiotic resistance can be divided into three [20]:

- **Prevention of antibiotic from accessing the target.** Two main mechanisms have been observed based on this principle: (i) the reduction of antibiotic permeability/transport through the cell membrane by downregulating or increasing the specificity of the main entries to the cell, i.e. porins; and (ii) the overexpression of efflux pumps responsible for ejection of toxic substances, such as antibiotics, outside the cell. Efflux pumps can be selective to one antibiotic or to a group of compounds with similar chemical structure. (Figure 2.2: 4B)
- **Change or modification of the target.** Antibiotic activity involves the selective recognition of a specific target in the bacterium. Any changes occurring to the antibiotic target site will confer resistance to the microorganisms since, even if reaching the target, the antibiotic will not be able to interact with it. Most common mechanisms of target side modification include (i) random mutations, down to a single point mutation, in the genes expressing the target site (Figure 2.2: B); (ii) transformation, known as the uptake of DNA from the environment; (iii) methylation (Figure 2.2: 3B); (iv) the expression of affinity proteins competing with the antibiotic for the target side; or (v) the mutation of genes expressing lipid A that lead to a change in the full lipopolysaccharide structure, (Figure 2.2: 1B), among others.

- **Direct modification or inactivation of the antibiotic.** This mechanisms include: (i) the acquisition of enzymatic activity, e.g.  $\beta$ -lactamase, from plasmids (**Figure 2.2: 2B**); or (ii) the transference of chemical groups, e.g. acyl and phosphate groups, to the antibiotic to prevent its interaction with the target site, e.g. by steric hindrance. (**Figure 2.2: 2C**)

A schematic summary of antibiotic targets and the corresponding antibiotic resistances are illustrated in **Figure 2.2**.

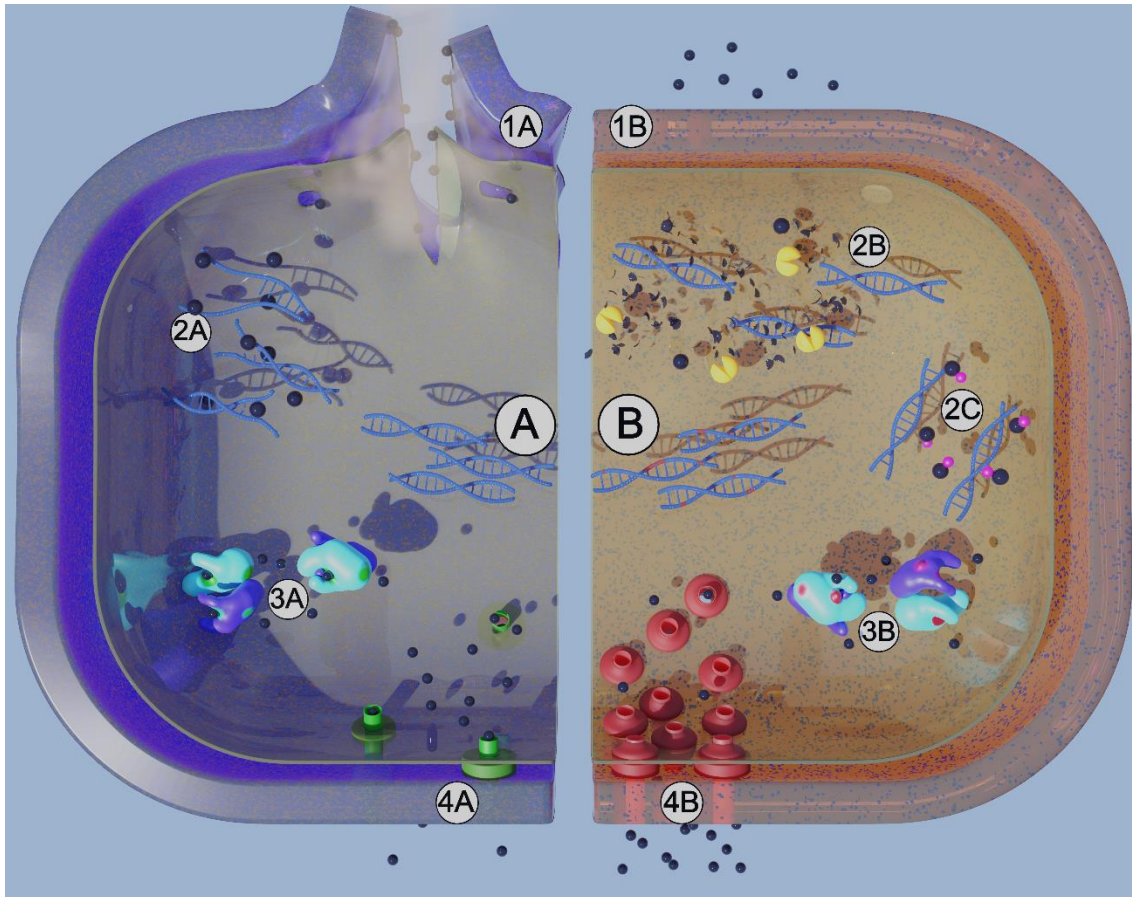


**Figure 2.2: Illustration depicting antibiotic action (A) and the corresponding resistance mechanisms (B).** 1A Antibiotics targeting and breaking the cell wall, 1B change in composition of the cell wall renders resistance. 2A antibiotics breaking down DNA, 2B production of  $\beta$  lactamases (yellow) to break down antibiotics or modifying antibiotics rendering them useless (blue attachments). 3A antibiotics targeting different sites of the ribosome, 3B prevention of antibiotic binding through modification of the target or steric hindrance. 4A antibiotic influx through porins, 4B antibiotic efflux through efflux pumps. (Made in Blender)

Although naturally occurring, the incidence of resistant bacteria has dramatically increased last years due to human activity, concretely to the misuse and overuse of antibiotics. For example, sectors such as agriculture and farming are using antibiotics preventively to minimize infection and production problems [21]. On the other hand, medical doctors are normally prescribing antibiotics based on an “empirical” diagnosis rather than a definitive experimental data, i.e. susceptibility testing and resistant bacteria identification. To deal with the “antibiotic crisis” resulting from the increasing

number of resistant strains and the lack of suitable treatments for bacterial infections, governments, healthcare entities and organizations have established a plan involving actions at four different levels:

- **Rational use of antibiotics** in the most critical sectors, i.e. food and beverage industry, farming, agriculture, clinical settings, etc.
- **Development of new antibiotics**, something costly and difficult that not many pharmaceutical companies are interested in doing. The quinolones discovered in the 1960s were the last broad-spectrum class of antibacterial agents to enter the clinic [22] and only two new classes of antibiotics were marketed in the past 10 years. In addition, antibiotic development is highly expensive and not nearly as profitable as other targets since discovered. Furthermore, healthcare organizations such as WHO would advise to keep it as a final line of defence against multiresistant strains, reducing its use and minimizing the potential profit.
- **Combination of therapies**, e.g. using two antibiotics together. This combined therapies increases the antibacterial spectrum of the therapy and take benefit of any synergistic effects of the two antibiotics, such as the case of beta-lactams and aminoglycoside combinations [23]. However, more research is needed to determine which antibiotics can be used together, both to serve as treatment and without being detrimental for the patient.
- **Improvement in diagnostic tools**, concretely by developing tests capable of rapidly determining whether the patient infection is caused by bacteria or not, and specifying the susceptibility of the infectious strain against a range of antibiotics will not only provide improved treatments, but also reduce the misuse of antibiotics. Being able to determine the correct antibiotic type reduces the chances of generating new resistances.

**The present thesis precisely aims to develop a fast susceptibility test device for improving patient's treatment.** For this reason, the current and near future technologies for susceptibility testing and resistant bacteria detection are discussed below.

### 2.2.2. Diagnostic tools for MIC testing

As previously stated, antibiotics are normally prescribed by medical doctors without any empirical analysis and only in those cases where the patient has allergies or the symptoms are not remitting with the treatment, a complete analysis of the infectious agent is performed. The infectious agent analysis includes (i) **the collection of the biological fluid**, e.g. urine, blood, sputum, saliva or faeces; (ii) **the transport to the clinical laboratory** under proper storage conditions; (iii) **the isolation and/or enrichment of the infectious agent**, normally by culturing in suitable culture media; and (iv) **bacterial identification and/or susceptibility testing** through phenotypic (e.g. cell culture in agar plates) or genotypic technics (e.g. polymerase chain reaction, PCR). Genotypic techniques are faster than phenotypic and allow the simultaneous bacterial identification and susceptibility testing, the latter through the detection of resistance

genes either in the genome or plasmids of the microorganism. However, the presence of the sequence of the resistance gene does not directly involve its expression, and these techniques are susceptible to error. Based on that, phenotypic techniques are still preferred, which are widely discussed below.

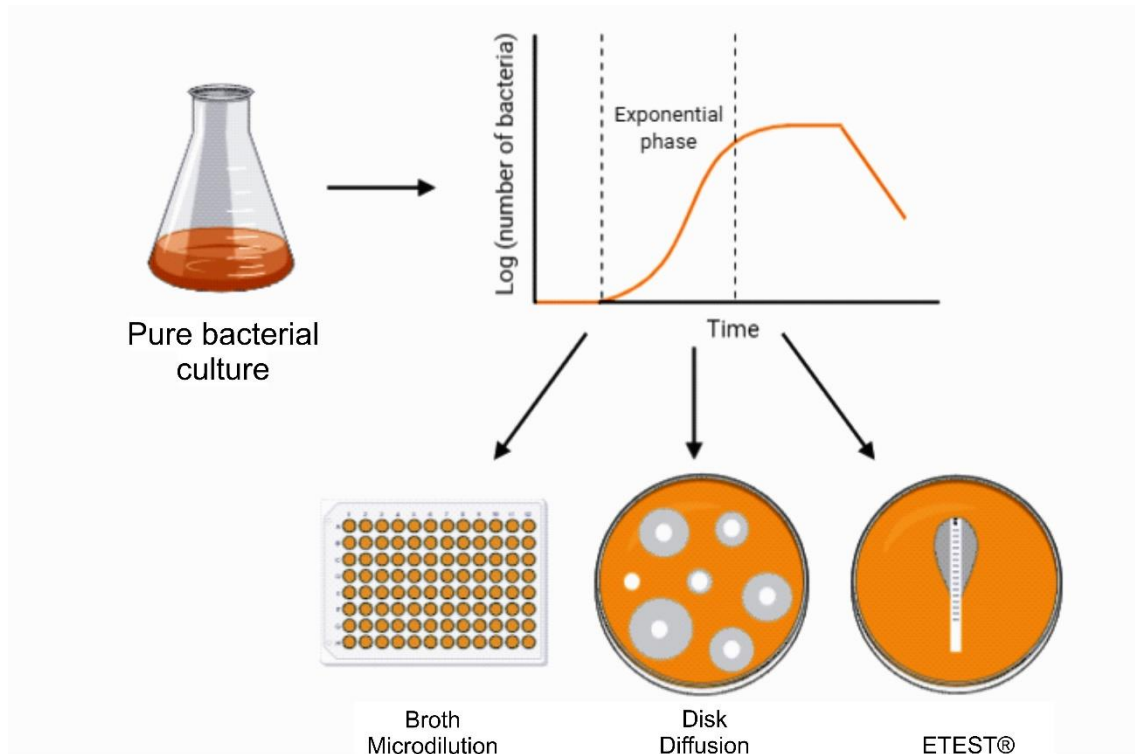


**Figure 2.3: Golden standard techniques require pure bacterial cultures**, which should be incubated until the majority of microorganisms are actively growing in the exponential phase. All of them rely on measuring bacterial growth in presence of antibiotics. The most common ones are Broth microdilution, Disk diffusion and E-test.

Current golden standard methods on phenotypic analysis are disk diffusion, broth microdilution and antibiotic strips (E-test). The operation principle of these methods is presented in **Figure 2.3**. In the **disk diffusion**, nitrocellulose disks containing different concentrations of the antibiotic are prepared and incorporated in an agar plate cultured with the bacterial strain under test. After 16-20 hours inhibition halos resulting from the dead of bacteria are formed around the antibiotic discs, with the diameter directly related to the sensitivity of the tested strain versus the antibiotic. Halo diameters are interpreted and categorized as susceptible, intermediate or resistant according to the European Committee of Antimicrobial Susceptibility Testing (EUCAST) clinical breakpoint tables. The amount of disks per plate is dependent on the tested strain and antibiotic, to ensure enough space is kept between each disk, with an advised maximum of six disks on a 90-mm plate.

**The E-test** is a variation of the disk diffusion method, where the disks have been replaced by a plastic strip containing an antibiotic gradient. Upon transferring the strip

to the agar, the antibiotic gradient is transferred. Bacterial growth is controlled after 16-20 hours, where the inhibition halos will take a symmetrical ellipse around the strip. The MIC value can be read from the strip where the inhibition zone intersects.

The final method, **broth microdilution**, is a liquid based method. A sterile plastic tray containing a two-fold concentration gradient of one or more antibiotics is inoculated with the bacterial strain. After 16-20 hours the results should be analysed visually, checking for each concentration and each antibiotic where growth is inhibited. The lowest concentration of the antibiotic that prevents visible growth (**Figure 2.4**) is known as the minimal inhibitory concentration (**MIC**). These numbers can be compared with tables provided by the EUCAST (Europe) or the Clinical and Laboratory Standards Institute (CLSI, USA) to check if the tested strain is seen as susceptible or resistant versus the tested antibiotic.

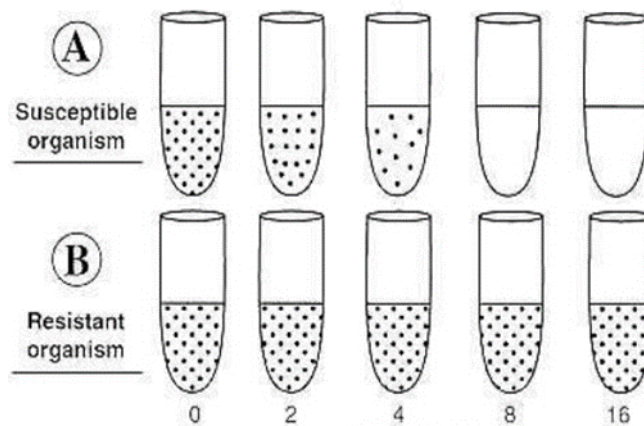


**Figure 2.4: Minimum inhibitory concentration.** The image shows an identical antibiotic with one strain susceptible A and one strain resistant B to the antibiotic. The MIC value for strain A corresponds to 8, whereas for strain B it is bigger than 16.

These approaches are sensitive and accurate but rely on tedious pre-analytical processing, narrow organism spectrum and long measurement times, which expands the time to result from 18 to more than 48 h [24]. Even when some of them have been automated, i.e. Vitek 2 (bioMérieux) or Microscan WalkAway (Siemens), they still require bacterial enrichment of at least 24h. Hence, new technologies should surmount challenges on different aspects such as sensitivity (avoiding tedious bacterial cultures and contamination chances), accuracy, reproducibility, fastness, simplicity, cost-effectiveness, multiplexing capabilities and portability, among others. Given the limitations and drawbacks of the automated golden standards, various groups and companies are developing the next generation of antibiotic susceptibility tests (**AST**), some of them already available in the market. For simplification, these technologies have been classified in the three following categories, illustrated in **Figure 2.5**:

- **Culture-based technologies**, comprising those technologies where the resulting signal is the average response of a group of bacteria (i.e. the culture).
- **Culture-based technologies with single-cell sensitivity**, where the cells are analysed individually but the final result is again provided as an average of the full culture, thus the individual variability of a single cell is lost.
- **Single cell technologies**, where the same cell is monitored over time at multiple data points. The effect of an antibiotic is related to the individual response, where the individual differences are evidenced.

In next section the new technologies will be compared considering currently marketed and near-future technologies.

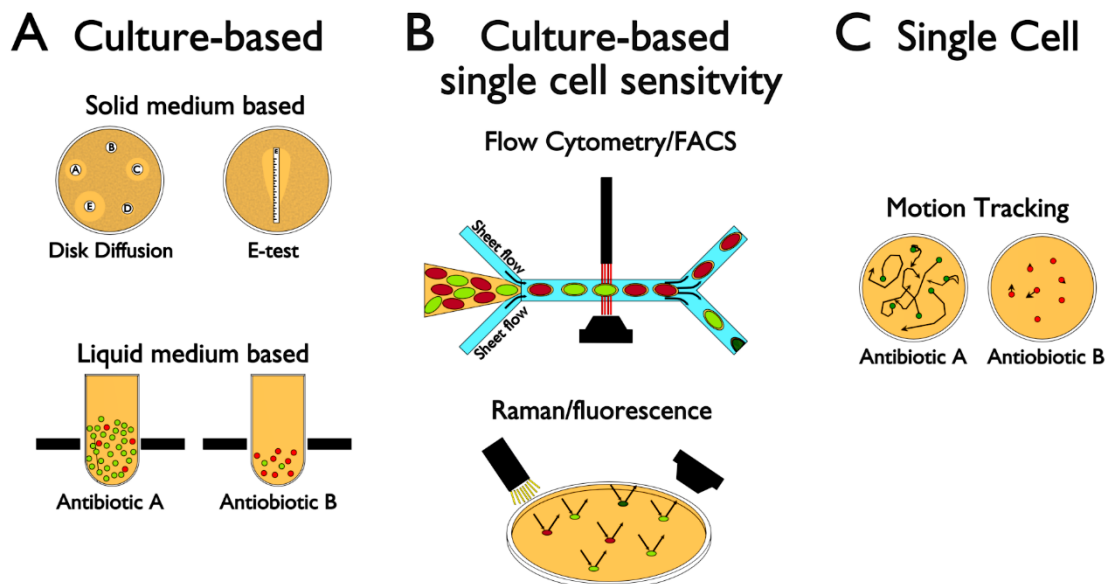


**Figure 2.5: Single cell versus culture based methods.** A shows standard methods based on culture growth using plating or liquid media. The Antimicrobial Susceptibility Test (AST) relies on the overall result of the culture behaviour. B represents possible single cell sensitivity methods, but rely on the full culture for analysis. Final AST depends on the combined result of the possible individually measured cells. C is a representation of a true single cell method where each cell is tracked or analysed continuously. AST can be determined for each cell individually. Cells in green indicate life cells. Cells in red represent dead or dying cells. Each depicted technology will be clarified later. (Made in Blender)

### 2.2.2.1. Currently marketed technologies for AST

**The technologies currently marketed for susceptibility testing** [25,26] are summarized in **Table 2.4**, where they are compared to golden standards regarding key operation, fabrication and performance indicators.



### 2.2.2.1.1. Culture-based technologies

Considering **culture-based**, two main technologies are now available on the market, namely **fluorescence-based test kits** and **mass-sensitive technologies**, which are briefly discussed below.

- **Fluorescence based-tests:** In classical fluorescence-based tests, dead and live cells are selectively labelled with a fluorescent tag that enables their differentiation, such as the SYBR Green/PI test [27]. The differentiation is possible by the use of two DNA cross-linkers, one capable to cross intact cell membranes to stain DNA and another only capable to cross-link DNA when the membranes are broken or damaged, corresponding to non-viable cells. The susceptibility test with these reagents is performed as follows. Bacteria are incubated with the antibiotic and then stained with the fluorescent reagent mixture. After staining, the detection of live or dead cells evidences the susceptibility or resistance of the bacterial strain to the tested antibiotic.

Apart from these classical end-point fluorescence-based assays, alternatives based on **metabolic indicators**, i.e. resazurin and derived complexes like **Alamar blue** and **PrestoBlue**, are also available. Metabolic indicators are redox molecules susceptible to bacterial metabolism, where they interact with the proteins involved in the electron transport chain, being reduced by them. In this case, bacterial metabolism (mitochondrial reductase activity) reduces resazurin to resorufin, with the latter being fluorescent and can be detected optically. The signal intensity is thus reflecting the metabolic activity, which correlates with the amount of live bacteria after incubation with the antibiotic [28–30].

Fluorescence based tests often have sensitivity, down to (nearly) single cell level, though they often suffer from high levels of background noise. Furthermore, special illumination sources and a fluorescent microscope are required, which are highly costly, bulky and require trained personnel. Additionally, end-point based assays suffer from the limitation of the time of detection. If the end-point assay is performed too soon, important data gets lost and the assay needs repeating for a longer time. Waiting for too long, will not skew the experiment, but reduce its potential as fast susceptibility test. Finally, the data relies only what happened at the moment the assay was performed, without giving information of any prior occurrences. On the other hand, metabolic assays have the advantage of allowing continuous measurement, thus ensuring that important information is not lost along the experiment. However, metabolic assays are very dependent on the concentration and metabolic activity of the bacterial strain, only being interesting for these ones with fast metabolisms, and when present in high concentrations. Generally, long incubation times, between 18-20 hours, are necessary to get the results, especially for low bacterial concentrations.

- **Mass-sensitive technologies:** These technologies are based on the use of cantilevers for susceptibility testing. A cantilever is a beam anchored at a support material on one end, while the other end is free (free-moving end) to move or deflect. Depending on its mass and length, cantilevers resonate at a specific frequency, i.e. its resonant frequency. The attachment of molecules on the cantilever produces a change

in its mass, and consequently in its resonant frequency. When applied to susceptibility testing, bacterial deposition on the beam is responsible for the resonant frequency changes. In the presence of antibiotics, susceptible bacteria do not proliferate producing a lower change in the resonant frequency than resistant strains, which proliferate faster increasing the bacterial mass attached to the cantilever. These differences can be detected with precision and in real time with the current instruments. Two systems are now available for mass-sensitive susceptibility testing: **LifeScale**<sup>®</sup>, trademarked by Affinity Biosensors, and **Resistell**<sup>™</sup> commercialized by Resistell.

In **LifeScale**<sup>®</sup>, the cantilever's beam is implemented in a microfluidic channel where the liquid containing bacteria and antibiotics are flowing through, and the changes produced to the culture by the presence of antibiotic are recorded under physiological conditions with the cantilever. The beam is suspended in vacuum to maximize the response, reaching almost single-cell sensitivity, and being able to identify morphological changes associated to antibiotics activity, e.g. cell lysis. The technology is versatile and high throughput, and it can be implemented in 96 well plates, making it directly compatible to broth microdilution [31].

**Resistell**<sup>™</sup> uses the same principle of the cantilevers but instead of leaving them flowing through the system, bacteria are covalently bonded to the cantilever's surface with glutaraldehyde. The detection principle is also different since it is based on bacterial motility. Even in the absence of flagella or pili, live bacteria possess a high intrinsic movement (Brownian motion), resulting in detectable vibrations. This enables them to differentiate live cells (moving) from dead ones (static). In susceptibility testing, the cantilever is immersed directly into the antibiotic solution and the vibrational change is recorded over time and analysed.

Compared to the previous one, this technology is still in its infancy and requires high manual steps to be operative. Additionally, since bacteria are immobilized, each sensor can only test a single condition and thus they are not prepared for high throughput analysis. One big advantage, however, is that it can provide results significantly faster than the previous one, which is especially relevant in the case of bacteria with long duplication times such as *Bordetella pertussis* [32].

**Table 2.4: Comparison of commercially available AST tests.** Pink colour indicates a bad parameter, orange intermediate, green implies positive parameter. ABs = antibiotics, PC = purified culture, BC = blood culture, UR = urine sample. L = low cost, I = intermediate cost, H = high cost, NK = not known. \*Fastest blood culture tools, \*\*selected panel only

Assay Type	Name/publication	Pre-treatment (h)	Test Time (h)	Sample type	Multiplex (ABs)	Portable	Cost	Automation	Identification	Real time
<b>Golden Standards</b>										
Antibiotic disk	Disk diffusion	20	16 – 24	PC	Yes	No	L	No	No	No
Antibiotic strip	E-test	20	16 – 24	PC	No	No	L	No	No	No
Microdilution	Broth microdilution	20	16 – 24	PC	Yes	No	L	No	No	No
<b>Commercial test based on culture growth</b>										
Automated broth microdilution	BD Phoenix™ [34]	20	5 – 18	PC	Yes**	No	H	Yes	Yes**	Yes
	Microscan Walkaway [35]	20	9 – 16	PC	Yes**	No	H	Yes	Yes**	Yes
	Sensititre™ [36]	20	6 – 16	PC	Yes**	No	H	Yes	Yes**	Yes
	Vitek®-2 (compact) [37]	20	18 – 24	PC	Yes**	No	H	Yes	Yes**	Yes
Fluorescence-based test kits	SYBR green/PI [27]	20	3 – 4	PC	No	No	L	No	No	No
	Resazurin [28–30]									
Mass-sensitive technology	LifeScale® [31]	>8*	3 – 4	(PC)/BC	Yes**	No	NK	Yes	No	No, but possible
	Resistell™ [32]	20/ >8*	1 – 4	PC/BC	No	Semi	NK	No	No	Yes
<b>Commercial test based on single cell analysis</b>										
Forward light scattering	BacterioScan [38,39]	20/ >8*	3 – 10	PC/UR/BC	Yes	No	I/H	Yes	No	Yes
Live cell imaging	Astrego® Technology [40]	>8* / 30 min	1 – x	BC/UR	Yes	No	NK	Yes	No	Yes
	oCelloScope [41,42]	20/ >8*/2	2 – 6	PC/BC/UR	Possible	Semi	L/I	Yes	No	Yes
Real time microscopy	Accelerate diagnostics™ [33,43,44]	>8*	4 – 9	BC	No	No	I/H	Yes	Yes**	Yes

#### 2.2.2.1.2. Single-cell technologies

A number of technologies based on **single cell analysis** are now commercially available, which are classified according to the transduction mechanism in **forward light scattering**, **live cell imaging** and **real time microscopy**, as detailed below.

- **Laser light scattering:** In laser light scattering, the laser beam irradiates a liquid sample where both optical density and low-angle forward scattering in the direction that passes near the laser beam are measured simultaneously and captured by a 2D-camera sensor. The technique measures the angular variation in the intensity of the light, this variation being proportional to the number, size and shape of the particles. The second measurement allows the correction of the optical density, increasing the sensitivity two orders of magnitude. The flagship of laser light scattering systems is BacterioScan™. It allows the simultaneous measurement of 16 samples, which are automatically measured every 3 minutes to determine bacterial growth. Thanks to its high sensitivity, it provides results regarding “Likely Positive (resistant)” or “Likely Negative (susceptible)” in 3 hours. Furthermore, the device allows measurements in standard culture medium, urine and positive blood samples, given the right preparation steps [38]. Since the technique analyses particles in suspension, it is nearly impossible to distinguish live from dead bacteria if they are not lysed, and additionally strong analytical methods and mathematical modelling are required to eliminate background noise [39].

- **Live-cell imaging:** There are two systems on the market based on live-cell imaging, i.e. the Astrego Captiver and the oCelloscope. The **Astrego Captiver** is a microfluidic system combining single cell entrapment in fluidic channels and imaging by microscopy. This technology integrates 2000 single bacteria-sized channels with a constriction at the back preventing cells from passing through, but enabling the medium to flow. Furthermore, the entrapment of a cell increases the fluidic resistance in the trap, reducing the odds of loading another cell in the same channel. This guarantees that only one bacterium is entrapped per channel. With this system, bacterial trapping after inoculation of the sample is monitored over time, and the load time gives an estimation of the bacterial density (concentration) in the sample. By the geometry and dimensions of the channels, cells inside the trap can only grow longitudinal, where the length of the individual cells (used to evaluate their division from a very early stage) and the length of the colony per trap are monitored. In susceptibility testing, the trapped bacterium is subjected to the treatment with the antibiotic and bacterial length is determined over time as a measurement of the number of bacteria dead (not changing of size) or alive (changing of size due to division) in very short times. Thanks to its configuration, different traps can be subjected to different antibiotics or different antibiotic concentrations, thus enabling high throughput analysis. However, the system only provides qualitative results, indicating either susceptibility to the antibiotic/dose tested or resistance. Using time lapse phase contrast microscopy the average growth is calculated real time, enabling susceptibility testing within an hour, though longer measure times can be performed if necessary [40].

The **oCelloscope**, on the other hand, is an advanced imaging technology providing high-resolute 3D images at single-cell level. The technology involves a 6.25°-tilted camera along the horizontal plane and combines phase contrast, bright field and confocal-like microscopy with advanced image processing algorithms implemented in the FluidScope™ software. The system acquires multiple Z-layers simultaneously, enabling fast scanning. The reconstruction of the Z-stack provides highly detailed 3D information of individual cells. With the reconstruction, it is possible to distinguish bacteria from potential interfering elements in the sample, e.g. condensation, debris, crystals formation or inhomogeneity, thus enabling to monitor single bacteria proliferation in real samples with little to no pre-treatment, staining or addition of reagents [41,42]. The use of this technology for susceptibility testing is similar to the previous one and considers the size changes experienced by live bacteria prone to proliferate, in contrast to dead cells which do not duplicate. As an advantage, this technology is compatible with most standard microtiter plates, from 6-wells to 96-well plates, and allows direct testing in real samples without pre-treatment, e.g. blood, urine, milk or water. As main disadvantages, (i) the device has no thermal control and requires to be placed in an incubator, (ii) it is barely portable, sitting at 9.6 kg, (iii) can only measure a single plate at a time, which limits high-throughput analysis and (iv) only the measurement is automatic, requiring manual preparation of the sample and plate filling.

- **Real time microscopy:** Accelerate Diagnostics has developed the **Accelerate Pheno**, a system based on real time microscopy for fully automated antimicrobial susceptibility test (AST) based on single cell analysis. It implements sample pre-treatment, concentration, real time susceptibility testing (by microscopy analysis) and bacterial identification through fluorescence in-situ hybridization. Incorporating advanced enrichment/concentration elements, this technology can work with a positive blood culture, saving significant pre-treatment time. The samples are automatically enriched using in house technologies, further followed by a concentration step. A dark-field microscope is used to image the cells every 10 minutes to follow either cell proliferation or cell lysis over time. The time lap images are automatically processed, with AST results obtained within 7 hours. One of the main limitations of this technology is that only a single cartridge can be used per machine, limiting the high-throughput required in big central laboratories [33,43,44].

#### 2.2.2.2. Research, near-future technologies

The discrepancy between what it is needed to solve the antibiotic crisis and what it is currently available on the market is promoting the development of new methodologies for AST [45]. Promising alternatives to previous commercial technologies are discussed here, with potential mid-short term market possibilities, comparing their advantages, disadvantages and commercialization potential (**Table 2.5**). The technologies included in this section have demonstrated a high readiness level, close to commercialization. Various publications exist with similar or better performance parameters than the ones included, although they have not been considered since they were only demonstrated in laboratory settings and/or not fully validated (only demonstrated in one publication).

#### 2.2.2.2.1. Culture-based technologies

Culture-based tests published between 2016 and 2020 are classified based on the assay type and detection method in calorimetric [46,47], colorimetric [48–50], and electrical [51,52], and compared in **Table 2.5**. Each technology is discussed below.

- **Colorimetry:** Colorimetric measurements rely on the capacity of bacteria to produce changes on target reagents used as indicators of bacterial metabolism. Most common indicators are target reagents reduced by bacterial metabolism, whereupon the reduction is accompanied by a change of colour (i.e. electrochromic molecules). Also, pH indicators are used to determine live bacterial due to the acidification of the medium resulting from bacterial metabolism [53]. When incubated with a bacterial sample, the rate of colour change or the absolute colour at a fixed time indicates the amount of viable bacteria present. Though multiple products are available, the most commonly used are resazurin and its derivatives Alamar Blue and Presto Blue [49]. Even though both reagents have been described before as fluorescence probes, their metabolically mediated reduction is accompanied by a visible colour change too. Colorimetry has the high advantage of being easily compatible with standard broth microdilution technology, requiring only the addition of the corresponding reagents and being able to monitor the change of colour with spectroscopic instrumentation already implemented. Furthermore, these reagents can often be immobilized and dried before the assay, further reducing manual work. The main limitation of colorimetry is the fact that colorimetric products are prone to cross reaction with other compounds, either antibiotics or media components, and sensitive to other processes due to their low specificity [49,50].

- **Electrical:** AST testing based on electrical properties, like measuring current, voltage/charge, medium conductance, etc., is promising due to its rapid, robust and label free testing. Instruments for electrical analysis are usually cheap, miniaturized and portable, which allows in situ testing and reduces the cost per assay. These tests are often based on biosensors and thus dependant on specific biological interactions to capture the bacteria, to elicit changes in the measured property. Most often used are antibodies (i.e. immunosensors) though various cases exist where strain-specific aptamers are used (also called aptasensors). One of the big advantages of the high specificity of these bio-macromolecules is the reduced background due to contaminants, making measurements with different matrices such as blood and urine possible. Furthermore, using a strain-specific capture molecule intrinsically provides identification of the infection as well, with the added cost requiring one recognition molecule for any bacterial strain of interest [51,52]. Several technologies have been based on electrical biosensors, but highlighted here are two examples of the most promising ones, namely **capacitance based** and **current amplification**.

Regarding the former, Song et al (2019) developed a vertical capacitance aptasensor for AST testing in blood. In capacitance-based biosensors, bacteria act as dielectric particles that produce a dielectric layer onto the electrode surface after selective recognition by the biorecognition molecule. This layer can be directly

determined through impedimetric measurement, even in blood samples and without requiring pre-treatment and with good sensitivity, down to  $10^0$ - $10^3$  CFU/mL, after 12 hours of analysis [51].

Similarly, Shi et al (2018) recognized specific bacterial strains after 84 min analysis using selective antibodies, being able to perform complete AST in less than 2 hours. The detection platform is based on field effect enzymatic detection (FEED), a method employing an immune-assay platform, for direct bacteria detection without culture enrichment. The FEED technique incorporates a gating voltage, which induces an electric field at the solution-enzyme-electrode interface. This interface reduces the tunnel barrier for electrons, the resulting signal current, due to the tunnel between electrode and enzyme is amplified by the gating voltage. This allows ultrasensitive, quantitative detection of bacteria without sample processing. The big drawback is the requirement for highly sensitive and selective antibodies to detect different types of strains [52].

- **Calorimetry:** Isothermal microcalorimetry is a non-destructive method to detect heat changes associated to bacterial metabolic activity with high sensitivity in the microwatt range. The measurement principle is based on the fact that bacterial metabolism generates heat, which reduces when the culture is exposed to susceptible antibiotics. Matrix components do not affect this technology and real samples can be used without pre-treatment, as long as they allow heat transfer and maintaining optimal growing/testing conditions. Moreover, calorimetry provides additional information not attainable with other technologies, such as: (i) able to determine AST in raw mixed cultures, which has been found to strongly differ from the MICs of the isolated and enriched bacterial strains [46]; (ii) to monitor persister cells and determine when they revert to a normal growth; or (iii) to determine AST in biofilms [47]. Current limitations of this technology are, first, the acquisition of such systems. Commercial calorimetry systems are now available, but they usually need some adaption for AST. Besides, the resulting data is often hard to interpret, and the success of the test is heavily dependent on the calibration of the system [46,47].

#### 2.2.2.2.2. Culture-based technologies with single-cell sensitivity

As previously stated, there are a number of technologies that, even when presenting high sensitivities at single cell level, do not monitor the same cell over time but the results are the combination of multiple single-cell analysis (averaged or population based). These technologies are here disclosed considering the transduction mechanism and discussed in terms of advantages and limitations.

- **Flow cytometry:** In flow cytometry, a fluid containing particles (e.g. cells) is injected through a fluidic micro-channel where they are focused in a way that only one passes through the laser beam, and is analysed, at a time. Single-cell scattering is recorded over time, providing characteristic information of the cell and its components, i.e. cell size and complexity, which considers morphology, structure and optical properties such as refractive index of each component, and additional properties coming from labelling with specific fluorescent dyes. In susceptibility testing, the process of averaging the growth rate from several hundred of individual bacteria makes it

possible to detect changes in growth as fast as the biological responses to the antibiotic [40]. Since physiological changes occur faster than growth inhibition, flow cytometry allows faster processing than conventional methods requiring cell proliferation. However, in practice, it is very limited due to (i) problems with bio-variability, staining inefficiency of the dyes, auto-fluorescence of certain bacteria, noisy fluorescence background or variability in bacteria-antibiotic interaction; (ii) the need for high resolution cameras and sophisticated instruments for signal amplification, which are subjected to day-to-day fluctuations resulting in false-positives; and (iii) the requirement of robust statistical metrics to enable quantification of the differences between antibiotic treated or untreated samples and obtaining consistent results among different replicates or with different instruments [54–56].

- **Raman spectroscopy:** Raman spectroscopy (RS) is a non-invasive optical technique that measures molecular vibrational modes, providing a chemical fingerprint of the acquired bacteria on the substrate resulting from the analysis of the inelastic scattering spectra of the cells. Since this fingerprint is strain specific, it can directly serve as an identification method, although no libraries are readily available right now. Although the tool is highly sensitive, biological samples provide weak responses and signal amplification/treatment is necessary. Amplification strategies include the use of (i) deuterated glucose as carbon source, which is incorporated in live and metabolically active bacteria [57], and (ii) heavy water labelling ( $D_2O$ ), where the isotope is randomly incorporated in newly synthesized biomolecules, e.g. lipids or proteins, of live bacteria, but not in dead ones [58]. Single cell RS has been combined with data treatment, i.e. unsupervised classification based on principal component analysis or machine learning, enabling automated differentiation of live and dead cells [59]. The technique is sensitive down to single cell level, also with real urine samples, and MIC results are usually acquired within 2.5 hours, but can go down to 30 minutes. Main drawbacks are on their labour intensive protocols, requiring many manual steps for preparation and measuring, and the impossibility to evaluate bacteriostatic antibiotics.



**Table 2.5: Comparison of research and near future based technologies available AST tests.** Pink colour indicates bad parameter, orange intermediate, green implies positive parameter. ABs = antibiotics, PC = purified culture, BC = blood culture, UR = urine sample. L = low cost, I = intermediate cost, H = high cost, \*Fastest blood culture tools, \*\*selected panel only

Assay Type	Name/publication	Pre-treatment (h)	Test Time (h)	Sample type	Multiple x (ABs)	Portable	Cost	Automation	Identification	Real time
<b>Golden Standards</b>										
Antibiotic disk	Disk diffusion	20	16 – 24	PC	Yes	No	L	No	No	No
Antibiotic strip	E-test	20	16 – 24	PC	No	No	L	No	No	No
Microdilution	Broth microdilution	20	16 – 24	PC	Yes	No	L	No	No	No
<b>Research, near-future technologies based on culture growth</b>										
Colorimetry	Resazurin, Prussian Blue [49,50]	20 / 8 – 10	4 – 6	PC/UR	Yes	Possible	L	Possible	No	Yes
Electrical	Current amplification [52]	>8*	3	BC	No	Possible	L	No	Yes**	No
	Vertical capacitance [51]	>8*	12	BC	Yes	Yes	L	Yes	No	Yes
Isothermal microcalorimetry	Isothermal microcalorimetry [46,47]	20	24 – 48	PC/Milk	Yes	No	I/H	Yes	No	Yes
<b>Research, near-future technologies based on culture growth with single-cell sensitivity</b>										
Flow cytometry	Flow Cytometry [54–56]	20 / >8*	1 – 3	PC/BC	No	No	H	No	No	No
Raman spectroscopy	Raman [57–59]	20 / 0.5	0.5 – 2	PC/UR	No	No	H	No	Yes	No
<b>Research, near-future technologies based on single cell analysis</b>										
Laser Tweezers	Raman based [60]	20	2 – 4	PC	No	No	H	No	No	Yes
Microfluidic technologies	dRAST [61]	>8*	6	BC	No	No	H	No	Yes**	No
	Dropfast, Resazurin [62]	20	1	PC	No	No	H	Yes	No	Yes
	Droplet, bead based [63]	20	0.5 – 2	PC/UR	No	No	I/H	No	No	Yes
	Droplet, Fluorescence: alamarBLUE [64]	20	4	PC	No	No	H	No	No	No
	Trapping, polymicrobial samples, Hoechst 33342 [65]	>8*	0.5-2.5	BC/UR	No	No	I/H	No	Yes**	Yes
Motion Tracking	DLVM-AST [66,67]	20 / 1	0.5 – 2	PC/UR	No	No	I/H	No	No	Yes
	Inverted optical microscope Submicron [68]	20	2	UR	No	No	I/H	No	No	Yes

### 2.2.2.2.3. Single cell-based technologies

To overcome the limitation of traditional phenotypic ASTs based on bacterial cultures, which involve long detection times of 1-2 days, new assays have been developed in recent years where the detection of changes on growth or/and cell morphology at early stages is possible through single-cell analysis. These technologies are illustrated in **Figure 2.6** and described below on the basis of the detection mechanism.

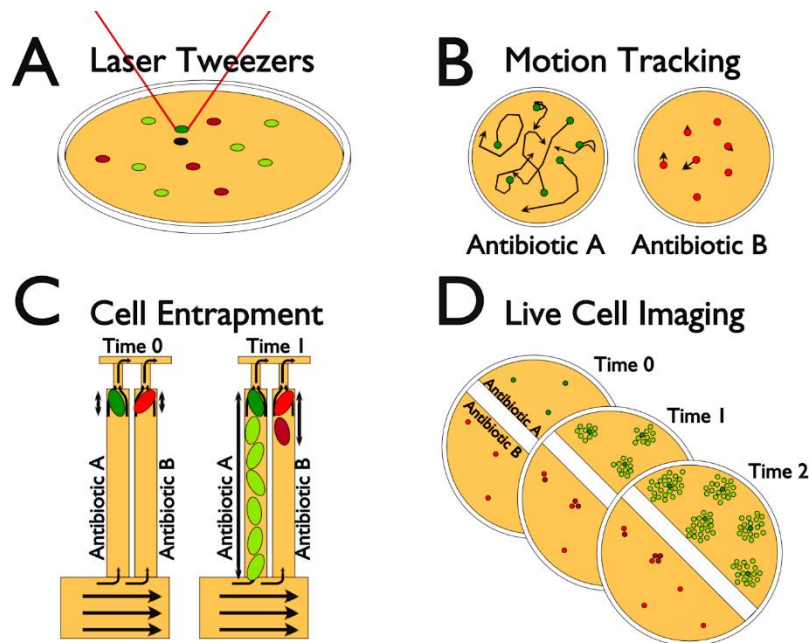


**Figure 2.6: Overview of the different single cell based technologies.** A represents the usage of laser tweezers, where a single cell is collected for analysis. B shows the motion tracking principle, where the position of each cell is monitored over time, corresponding to its viability. C uses microfluidics for cell entrapment. Using choke points, a single cell is trapped in each chamber, after which they can only growth longitudinally. D uses highly specific cameras and software to follow cells over time (shown in darker colour). Cells in green indicate life cells. Cells in red represent dead or dying cells. (Made in Blender)

- **Laser Tweezers:** Previous RS has been combined with optical tweezers, giving rise to the so-called laser tweezer Raman spectroscopy, where single bacteria are trapped by the tweezer and transported to the incubation micro-chambers where they are individually analysed by time-lapse imaging and RS. The laser trap retains bacteria, preventing their movement even when antibiotics are flushed through the system for AST, which avoids interferences during image acquisition or RS recordings. Furthermore, bacteria are immobilized in the laser's focus, thus maximizing Raman signal [60].

- **Motion tracking:** Optical tracking of moving cells is employed by these technologies to study antibiotics activity through changes in the cell size, morphology of the cell wall or nucleoid, lysing frequency and cell division anomalies, among others [40]. Since growth and morphology changes depend on the bacterial strain, the combination of imaging with suitable machine learning algorithms allows bacterial identification, early prediction of susceptibility/resistance and to minimize errors [61]. As an example, deep learning video microscopy-based AST (DLVM-AST)[66] carries out the AST in less than 30 minutes in urine samples, after filtration of large particles from the sample. Other technologies combine single-cell motion recording with long or short-term

memory neural networks to learn if a bacterium is active or inactive after incubation [67]. In addition, more sensitive version of motion tracking-based technologies have been developed, where bacteria are bound to antibodies or chemicals, enabling fast AST analysis in 2 hours with an inverted optical microscope and suitable motion-tracking algorithms [68]. The main limitation of such technologies is the size and cost of the required equipment, the need for highly experienced and trained personnel and the complexity of the data treatment algorithms, which will require intensive refinement to minimize false positive and negative before commercialization.

- **Microfluidic technologies:** Microfluidics has revolutionized the diagnostic and detection fields by providing technological solutions based on mass-production protocols, low cost polymeric materials and miniaturized architectures with highly integrated components. The resulting devices are thus low cost, require small sample (and reagents) volumes, present shortened analysis times for the reduction of the diffusion distances and enable high-throughput analysis by the miniaturization and high degree of integration. In AST, microfluidic-based technologies present the added value of being able to produce microfluidic elements with the dimension of a single cell, enabling selective confinement, manipulation and analysis of individual bacteria which are entrapped in microchannels, microchambers or droplets, among others. Single bacteria are then analysed in situ through spectroscopic techniques or imaging after incubation with the antibiotic, reducing AST to a few hours while improving the analytical performance of the assay thanks to an important reduction of the background noise [40]. Each microfluidic structure presents advantages and disadvantages. Microfluidic chambers confine bacteria in a micrometric cavity, which are simple to operate. The main limitation is on the time-lapse image recording, since bacteria in the cavity still move and float. Droplet-based structures are advantageous in this sense. Droplet microfluidics manipulate discrete cells in a medium drop generated by immiscible multiphase flows inside microchannels [69], which are formed either by continuous flow of the emulsion or by electrowetting [26]. In the droplet, bacteria are trapped and immobile facilitating the recordings and the large amount of droplets generated and their monodispersity enables quantitative comparison, and high-throughput analysis [69]. Examples of droplet-based systems for AST are: (i) the integrated droplet-based platform dropFAST [62] that enables single-cell encapsulation, incubation and AST by fluorescent detection of bacterial growth using resazurin in only 1 hour; (ii) a platform allowing identification of resistant bacteria sub-populations in cultures in less than 4 hours by co-encapsulation of bacterial cells and viability probes, such as Alamar Blue [64]; or (iii) the droplet-based approach where bacterial cells are captured with antibody-conjugated beads and AST is determined in 2 hours by analysing cell division and morphology by microscopy after staining with Hoechst. Unfortunately, droplet-based systems require cultured isolates, only one condition can be measured per microfluidic chip and have been optimized in a small panel of pathogens, thereby limiting their general applicability for infectious disease diagnostics [63]. Only two microfluidic platforms have demonstrated capacity to perform AST directly in real samples: (i) the direct and rapid antimicrobial susceptibility test (dRAST) developed by

Choi et al (2017)[61], where sample is mixed with agarose (to trap bacteria) and deposited in 96-well plate with antibiotics for AST under a microscope, which performs the test from a positive blood culture bottle in 6 hours; and (ii) the microfluidic platform developed by Li et al [65] that traps and classifies major classes of pathogen according to their shape and size by applying different pressures and perform single-cell AST in clinical urine or blood samples in less than 1 hour.

#### 2.2.2.3. What is next?

The weaknesses detected in golden standard and current commercially available AST technologies together with the urgent need for improving the performance of these assays have positioned this subject as a hot topic in the field, as reflected on the number of publications and contributions in AST. In this sense, some reviews have been published focusing on specific new generations of AST such as molecular techniques [70], photonics [71] or nanotechnology [72]. Beyond this, the integration of several technologies to benefit from the advantages of each one for improving AST seems promising, e.g. the coupling of nanotechnology with microfluidics. This partnership emerges as a very interesting alternative. Nanotechnology, on the one hand, provides improved sensing strategies, with high sensitivity (at the single-cell level) and selectivity, thanks to a many fold enhancement of the signal-to-noise ration. Microfluidics, on the other hand, allows the reduction of the size and cost of the technology, important aspects for the future commercialization of the systems. At the same time, it ensures low sample volumes, fast reaction kinetics, compartmentalization, multiplexing and integration of many stages of sample pre-treatment in a single miniaturized, portable and automated structure requiring minimal user intervention.

In the same direction, the development of lateral flow-based technologies, employing paper or other material with capillary pumping capacity, would contribute to simplify the structure of the final instrument (e.g. in a pumpless configuration) while providing highly functional and cost-effective devices. The use of such simple, cheap, miniaturized and portable technologies may boost the development of wearable point-of-care (POC) devices enabling real time monitoring of patients, reducing antibiotic doses and broad spectrum antibiotic administration.

**Since the focus of the current thesis is on the development of simple POC structure for susceptibility testing on healthcare setting with limited analytical capacities,** a brief overview of the criteria for POC testing for AST testing is analysed in the following section.

#### 2.2.2.4. Point of care tests for AST

The optimal POC AST device should follow the ASSURED criteria, described by the WHO. ASSURED stands for: affordable, sensitive, specific, user-friendly, rapid and robust, equipment-free and deliverable to end users. All described technologies are targeting the rapid, sensitive and specific criteria, but all miss multiple of the others ones. Especially the deliverable to end-users and equipment-free are the big hurdles, due to the difficulties involved in reaching the rapid parameter itself. However, continuous

improvements are being made, which is clearly reflected in the strengths of the near-future based systems compared to the commercial ones.

Several types of assay are inherently limiting for POC assays, due to the size and/or cost of the required equipment, like Raman spectroscopy. Because of that, most POC AST tests aim for low cost detection methods like electrochemical [73] or optical [74,75]. However, plenty publications claim POC, like those mentioned here, but they still rely on external equipment like a potentiostat or fluorescence microscope for the actual measurement. On the other hand, technologies like a PDMS based fluidic AST device from Xu et al. or the Teflon based dipstick from Reis et al. require only a simple camera for detection, however, they still require 15 hours to result [76,77]. These examples highlight how challenging developing an AST PoC test adhering to all ASSURED criteria is. Nonetheless, Michael et al. developed a fidget spinner for UTI testing, able to detect AST within 2 hours. Though the device has been validated using fluorescence microscopy, they claim visual read-out is possible [78]. Even though the examples of successful POC AST tests are few, the technology and knowledge are here to finally achieve it.

### **2.3. Thesis starting point**

The present thesis takes as starting point the work by Dr. Ferran Pujol Vila on general toxicity assessment. Dr. Pujol used ferricyanide as a colorimetric metabolic indicator. That is, in the presence of live and metabolically-active bacteria, the yellowish ferricyanide was reduced to colourless ferrocyanide by bacterial metabolism. The kinetic of the reaction was dependant on the number of living bacteria in the sample and thus, after incubation with water samples, the ferricyanide-reduction kinetics was proportional to the toxicity of the sample. It was probed by real water samples from different origin, in microfluidic devices [79] and even in solid substrates such as cellulose paper [80].

Based on the same principle (i.e. metabolic reduction of ferricyanide), an alginate-based hydrogel with bioelectrochromic capacity and sensitivity to bacterial metabolism was developed in collaboration with Dr. Pujol and applied for the very first time to differentiate between susceptible and resistant bacterial strains [81]. In this case, ferricyanide is not directly measured but the ferricyanide reduction is coupled to the formation of Prussian blue molecules, another iron-based complex with an intense blue colour that increased 50 times the sensitivity of the method. Apart from an increased sensitivity, the use of hydrogels provided reproducibility to the method, since hydrogels could be electrodeposited in a very repetitive manner, and high miniaturization potential. However, the protocol relied on the low stability of alginate hydrogels, with high storage constrains associated to the high tendency of hydrogels to dehydrate over time.

The current thesis takes these results as starting point in the development of a POC system for fast AST in limited-resources settings. The thesis is organized in the following chapters:

1. **Introduction**, where, after a brief overview of the motivation of the work, infectious diseases, and particularly bacterial infectious diseases, are extensively discussed, as well as the treatments, antibiotic resistances and the current and near future AST strategies, with especial emphasis on those based on POC systems.
2. **Fundamentals**, describing all these concepts in microbiology, optics, electrochemistry and microfluidics necessary for a complete understanding of the thesis.
3. **Objectives**, as the main motivational subjects of the thesis.
4. **Material and Methods**, including all these fabrication technologies, reagents, protocols and methodologies employed along the thesis.
5. **Results and Discussion**, exposing as part of an evolutionary tree, the different generations of bioassays, microfluidic and optic components developed and their integration in the final POC system.
6. **Conclusions**, as the main outcomes of the thesis.

Part of this introduction has been published as a **review paper in Track Trends in Analytical Chemistry** ([82]).

## 2.4. Bibliography

- [1] N. Taneja, S. Sethi, A. Kumar Tahlan, Y. Kumar, Introductory Chapter: Stepping into the Post-Antibiotic Era— Challenges and Solutions, in: *Antimicrob. Resist. - A Glob. Threat*, IntechOpen, 2019. <https://doi.org/10.5772/intechopen.84486>.
- [2] T.P. Van Boeckel, S. Gandra, A. Ashok, Q. Caudron, B.T. Grenfell, S.A. Levin, R. Laxminarayan, Global antibiotic consumption 2000 to 2010 : an analysis of national pharmaceutical sales data, *14* (2017). [https://doi.org/10.1016/S1473-3099\(14\)70780-7](https://doi.org/10.1016/S1473-3099(14)70780-7).
- [3] H. Goossens, M. Ferech, R. Vander Stichele, M. Elseviers, Outpatient antibiotic use in Europe and association with resistance: a cross-national database study, *Lancet*. *365* (2005) 579–587. [https://doi.org/10.1016/s0140-6736\(05\)17907-0](https://doi.org/10.1016/s0140-6736(05)17907-0).
- [4] S. Scott, C.J. Duncan, *Biology of plagues: evidence from historical populations*, Cambridge Univ. Press. *39* (2001) 39-0349-39-0349. <https://doi.org/10.5860/choice.39-0349>.
- [5] S. Haensch, R. Bianucci, M. Signoli, M. Rajerison, M. Schultz, Distinct Clones of *Yersinia pestis* Caused the Black Death, *PLoS Pathog.* *6* (2010) 1001134. <https://doi.org/10.1371/journal.ppat.1001134>.
- [6] K. Kuszewski, L. Brydak, The epidemiology and history of influenza, *Biomed. Pharmacother.* *54* (2000) 188–195. [https://doi.org/10.1016/S0753-3322\(00\)89025-3](https://doi.org/10.1016/S0753-3322(00)89025-3).
- [7] M. Nicola, Z. Alsafi, C. Sohrabi, A. Kerwan, A. Al-Jabir, C. Iosifidis, M. Agha, R. Agha, The socio-economic implications of the coronavirus pandemic (COVID-19): A review, *Int. J. Surg.* *78* (2020) 185–193. <https://doi.org/10.1016/j.ijisu.2020.04.018>.
- [8] K.N. Kragh, J.B. Hutchison, G. Melaugh, C. Rodesney, A.E.L. Roberts, Y. Irie, P. Jensen, S.P. Diggle, R.J. Allen, V. Gordon, T. Bjarnsholt, Role of multicellular aggregates in biofilm formation, *MBio.* *7* (2016). <https://doi.org/10.1128/mBio.00237-16>.
- [9] A. Poli, G. Anzelmo, B. Nicolaus, Bacterial exopolysaccharides from extreme marine habitats: Production, characterization and biological activities, *Mar. Drugs.* *8* (2010) 1779–1802. <https://doi.org/10.3390/md8061779>.
- [10] T. Kamat, S. Kerkar, Bacteria from Salt Pans: A Potential Resource of Antibacterial Metabolites, *Recent Res. Sci. Technol.* *3* (2011) 46–52. [www.scholarjournals.org/Awww.recent-science.com](http://www.scholarjournals.org/Awww.recent-science.com).
- [11] R.E. Sherburn, P.J. Large, Amine borate catabolism by bacteria isolated from contaminated metal- working fluids, *J. Appl. Microbiol.* *87* (1999) 668–675. <https://doi.org/10.1046/j.1365-2672.1999.00906.x>.
- [12] J. Seckbach, *Journey to Diverse Microbial Worlds*, Springer Netherlands, Dordrecht, 2000. <https://doi.org/10.1007/978-94-011-4269-4>.
- [13] J. Mitchell, *Streptococcus mitis: Walking the line between commensalism and*

- pathogenesis, *Mol. Oral Microbiol.* 26 (2011) 89–98. <https://doi.org/10.1111/j.2041-1014.2010.00601.x>.
- [14] P.E. Fournier, H. Richet, The Epidemiology and Control of *Acinetobacter baumannii* in Health Care Facilities, 2006. [www.bacterio.cict.fr/a/acinetobacter.html](http://www.bacterio.cict.fr/a/acinetobacter.html).
- [15] N.I. Agudelo Higueta, M.M. Huycke, Enterococcal Disease, Epidemiology, and Implications for Treatment, n.d.
- [16] R.D. Kirkcaldy, E. Weston, A.C. Segurado, G. Hughes, Epidemiology of gonorrhoea: A global perspective, *Sex. Health.* 16 (2019) 401–411. <https://doi.org/10.1071/SH19061>.
- [17] M.W. Jonathan R Carapetis, Andrew C Steer, E Kim Mulholland, The global burden of group A streptococcal diseases, *Lancet Infect Dis.* 5 (2005) 685–694. [https://doi.org/10.1016/S1473-3099\(05\)70267-X](https://doi.org/10.1016/S1473-3099(05)70267-X).
- [18] P.I. Hair, S.J. Keam, Daptomycin, *Drugs.* 67 (2007) 1483–1512. <https://doi.org/10.37667/pk.2009.700>.
- [19] E.P. Abraham, E. Chain, An enzyme from Bacteria able to Destroy Penicillin, *Clin. Infect. Dis.* 146 (1940). <https://doi.org/10.1093/clinids/10.4.677>.
- [20] J.M. A Blair, M.A. Webber, A.J. Baylay, D.O. Ogbolu, L.J. V Piddock, Molecular mechanisms of antibiotic resistance, (2015). <https://doi.org/10.1038/nrmicro3380>.
- [21] V. Economou, P. Gousia, Agriculture and food animals as a source of antimicrobial-resistant bacteria, *Infect. Drug Resist.* 8 (2015) 49–61. <https://doi.org/10.2147/IDR.S55778>.
- [22] A.R. Coates, G. Halls, Y. Hu, Novel classes of antibiotics or more of the same?, *Br. J. Pharmacol.* 163 (2011) 184–194. <https://doi.org/10.1111/j.1476-5381.2011.01250.x>.
- [23] A. Ahmed, A. Azim, M. Gurjar, A.K. Baronia, Current concepts in combination antibiotic therapy for critically ill patients, *Indian J. Crit. Care Med.* 18 (2014) 310–314. <https://doi.org/10.4103/0972-5229.132495>.
- [24] A. Van Belkum, W.M. Dunne, Next-generation antimicrobial susceptibility testing, *J. Clin. Microbiol.* 51 (2013) 2018–2024. <https://doi.org/10.1128/JCM.00313-13>.
- [25] E. Matuschek, J. Åhman, C. Webster, G. Kahlmeter, Antimicrobial susceptibility testing of colistin – evaluation of seven commercial MIC products against standard broth microdilution for *Escherichia coli*, *Klebsiella pneumoniae*, *Pseudomonas aeruginosa*, and *Acinetobacter* spp., *Clin. Microbiol. Infect.* 24 (2018) 865–870. <https://doi.org/10.1016/j.cmi.2017.11.020>.
- [26] B. Behera, G.K. Anil Vishnu, S. Chatterjee, V.S.N. Sitaramgupta V, N. Sreekumar, A. Nagabhushan, N. Rajendran, B.H. Prathik, H.J. Pandya, Emerging technologies for antibiotic susceptibility testing, *Biosens. Bioelectron.* 142 (2019) 111552. <https://doi.org/10.1016/j.bios.2019.111552>.



- [27] J. Feng, R. Yee, S. Zhang, L. Tian, W. Shi, W.H. Zhang, Y. Zhang, A rapid growth-independent antibiotic resistance detection test by SYBR Green/Propidium Iodide viability assay, *Front. Med.* 5 (2018). <https://doi.org/10.3389/fmed.2018.00127>.
- [28] K. Hsieh, H.C. Zec, L. Chen, A.M. Kaushik, K.E. MacH, J.C. Liao, T.H. Wang, Simple and Precise Counting of Viable Bacteria by Resazurin-Amplified Picoarray Detection, *Anal. Chem.* 90 (2018) 9449–9456. <https://doi.org/10.1021/acs.analchem.8b02096>.
- [29] M. Ghatole, V. Kashetty, A. Ghule, Resazurin assay for rapid drug susceptibility testing of *Mycobacterium tuberculosis*, *Indian J. Microbiol. Res.* 5 (2018) 138–142. <https://doi.org/10.18231/2394-5478.2018.0028>.
- [30] H. Jia, R. Fang, J. Lin, X. Tian, Y. Zhao, L. Chen, J. Cao, T. Zhou, Evaluation of resazurin-based assay for rapid detection of polymyxin-resistant gram-negative bacteria, *BMC Microbiol.* 20 (2020). <https://doi.org/10.1186/s12866-019-1692-3>.
- [31] T.P. Burg, M. Godin, S.M. Knudsen, W. Shen, G. Carlson, J.S. Foster, K. Babcock, S.R. Manalis, Weighing of biomolecules, single cells and single nanoparticles in fluid, *Nature.* 446 (2007) 1066–1069. <https://doi.org/10.1038/nature05741>.
- [32] M.I. Villalba, P. Stupar, W. Chomicki, M. Bertacchi, G. Dietler, L. Arnal, M.E. Vela, O. Yantorno, S. Kasas, Nanomotion Detection Method for Testing Antibiotic Resistance and Susceptibility of Slow-Growing Bacteria, *Small.* 14 (2018) 1–6. <https://doi.org/10.1002/smll.201702671>.
- [33] Y. Bordiya, Z. Yi, Nam Ji-Chul, B. April, H.W. Choi, Lee Bum-Kyu, K. Jonghwan, D.F. Klessig, H.-G. Kang, Z. Fei, EVALUATION OF AUTOMATIC CLASS III DESIGNATION FOR Accelerate PhenoTest BC Kit, 2015. <https://doi.org/10.3835/plantgenome2015.04.0023>.
- [34] J.W. Snyder, G.K. Munier, C.L. Johnson, Direct comparison of the BD phoenix system with the MicroScan WalkAway system for identification and antimicrobial susceptibility testing of Enterobacteriaceae and nonfermentative gram-negative organisms, *J. Clin. Microbiol.* 46 (2008) 2327–2333. <https://doi.org/10.1128/JCM.00075-08>.
- [35] M. R, S. L, P. O, S. Moodley A, The Efficacy of the MicroScan®Walkaway System in Reporting Carbapenemase-Producing Enterobacteriaceae in Patients with Bacteremia, South Africa, *J. Antimicrob. Agents.* 03 (2017). <https://doi.org/10.4172/2472-1212.1000153>.
- [36] M. Aguilar-Santelises, J. Castillo-Vera, R. Gonzalez-Molina, A. Garcia del Valle, M. Cruz Millan, L. Aguilar-Santelises, Clinical isolates of *Escherichia coli* are resistant both to antibiotics and organotin compounds, *Folia Microbiol. (Praha).* (2019). <https://doi.org/10.1007/s12223-019-00707-1>.
- [37] A.M. Bobenchik, E. Deak, J.A. Hindler, C.L. Charlton, R.M. Humphries, Performance of Vitek 2 for antimicrobial susceptibility testing of Enterobacteriaceae with Vitek 2 (2009 FDA) and 2014 CLSI breakpoints, *J. Clin. Microbiol.* 53 (2015) 816–823. <https://doi.org/10.1128/JCM.02697-14>.

- [38] A.L. Roberts, U. Joneja, T. Villatoro, E. Andris, J.A. Boyle, J. Bondi, Evaluation of the BacterioScan 216Dx for standalone preculture screen of preserved urine specimens in a clinical setting, *Lab Med.* 49 (2018) 35–40. <https://doi.org/10.1093/labmed/lmx052>.
- [39] E.A. Idelevich, M. Hoy, D. Knaack, D. Görlich, G. Peters, M. Borowski, K. Becker, Direct determination of carbapenem-resistant Enterobacteriaceae and *Pseudomonas aeruginosa* from positive blood cultures using laser scattering technology, *Int. J. Antimicrob. Agents.* 51 (2018) 221–226. <https://doi.org/10.1016/j.ijantimicag.2017.10.009>.
- [40] Ö. Baltekin, A. Boucharin, E. Tano, D.I. Andersson, J. Elf, Antibiotic susceptibility testing in less than 30 min using direct single-cell imaging, *Proc. Natl. Acad. Sci.* (2017) 201708558. <https://doi.org/10.1073/pnas.1708558114>.
- [41] M. Fredborg, K.R. Andersen, E. Jørgensen, A. Droce, T. Olesen, B.B. Jensen, F.S. Rosenvinge, T.E. Sondergaard, Real-time optical antimicrobial susceptibility testing, *J. Clin. Microbiol.* 51 (2013) 2047–2053. <https://doi.org/10.1128/JCM.00440-13>.
- [42] H.P. McLaughlin, D. Sue, Rapid antimicrobial susceptibility testing and  $\beta$ -lactam-induced cell morphology changes of Gram-negative biological threat pathogens by optical screening, *BMC Microbiol.* 18 (2018) 1–15. <https://doi.org/10.1186/s12866-018-1347-9>.
- [43] K. Ehren, A. Meißner, N. Jazmati, J. Wille, N. Jung, J.J. Vehreschild, M. Hellmich, H. Seifert, Clinical Impact of Rapid Species Identification From Positive Blood Cultures With Same-day Phenotypic Antimicrobial Susceptibility Testing on the Management and Outcome of Bloodstream Infections, *Clin. Infect. Dis.* (2019) 1–9. <https://doi.org/10.1093/cid/ciz406>.
- [44] J.G. Schneider, J.B. Wood, B.H. Schmitt, C.L. Emery, T.E. Davis, N.W. Smith, S. Blevins, J. Hiles, A. Desai, J. Wrin, B. Bocian, J.J. Manaloor, Susceptibility Provision Enhances Effective De-escalation (SPEED): Utilizing rapid phenotypic susceptibility testing in Gram-negative bloodstream infections and its potential clinical impact, *J. Antimicrob. Chemother.* 74 (2019) 116–123. <https://doi.org/10.1093/jac/dky531>.
- [45] S.C. Ersoy, D.M. Heithoff, L. Barnes, G.K. Tripp, J.K. House, J.D. Marth, J.W. Smith, M.J. Mahan, Correcting a Fundamental Flaw in the Paradigm for Antimicrobial Susceptibility Testing, *EBioMedicine.* 20 (2017) 173–181. <https://doi.org/10.1016/j.ebiom.2017.05.026>.
- [46] U. von Ah, N. Shani, M. Chollet, A. Solokhina, O. Braissant, Measuring antibiotic resistance in mixed cultures: Isothermal microcalorimetry as a novel analytical tool, *Int. Dairy J.* 77 (2018) 73–79. <https://doi.org/10.1016/j.idairyj.2017.09.007>.
- [47] M.E. Butini, G. Abbandonato, C. Di Rienzo, A. Trampuz, M. Di Luca, Isothermal microcalorimetry detects the presence of persister cells in a *Staphylococcus aureus* biofilm after vancomycin treatment, *Front. Microbiol.* 10 (2019) 1–13. <https://doi.org/10.3389/fmicb.2019.00332>.

- [48] B.S. Mahmoud, S.A. ElMasry, N.A.E.M.M. Fahim, M.A. Abd ElSattar, O.A. Shaker, Detection of antibiotic susceptibility by colorimetric minimum inhibitory concentration in staphylococcal isolates, *J. Appl. Microbiol.* 3 (2019) 693–700. <https://doi.org/10.1111/jam.14347>.
- [49] M. Lescat, L. Poirel, C. Tinguely, P. Nordmann, A Resazurin Reduction-Based Assay for Rapid Detection of Polymyxin Resistance in *Acinetobacter baumannii* and *Pseudomonas aeruginosa*, *J. Clin. Microbiol.* 57 (2019) 1–6. <https://doi.org/10.1128/JCM.01563-18>.
- [50] F. Pujol-Vila, J. Dietvorst, L. Gall-Mas, M. Díaz-González, N. Vigués, J. Mas, X. Muñoz-Berbel, Bioelectrochromic hydrogel for fast antibiotic-susceptibility testing, *J. Colloid Interface Sci.* (2017). <https://doi.org/10.1016/j.jcis.2017.09.004>.
- [51] J.H. Song, S.M. Lee, I.H. Park, D. Yong, K.S. Lee, J.S. Shin, K.H. Yoo, Vertical capacitance aptasensors for real-time monitoring of bacterial growth and antibiotic susceptibility in blood, *Biosens. Bioelectron.* 143 (2019) 111623. <https://doi.org/10.1016/j.bios.2019.111623>.
- [52] X. Shi, U. Kadiyala, J.S. Vanepps, S.T. Yau, Culture-free bacterial detection and identification from blood with rapid, phenotypic, antibiotic susceptibility testing, *Sci. Rep.* 8 (2018) 1–11. <https://doi.org/10.1038/s41598-018-21520-9>.
- [53] X. Xu, Y. Yuan, G. Hu, X. Wang, P. Qi, Z. Wang, Q. Wang, X. Wang, Y. Fu, Y. Li, H. Yang, Exploiting pH-Regulated Dimer-Tetramer Transformation of Concanavalin A to Develop Colorimetric Biosensing of Bacteria, *Sci. Rep.* 7 (2017) 1–8. <https://doi.org/10.1038/s41598-017-01371-6>.
- [54] T.H. Huang, Y.L. Tzeng, R.M. Dickson, FAST: Rapid determinations of antibiotic susceptibility phenotypes using label-free cytometry, *Cytom. Part A.* 93 (2018) 639–648. <https://doi.org/10.1002/cyto.a.23370>.
- [55] K.T. Mulroney, J.M. Hall, X. Huang, E. Turnbull, N.M. Bzdyl, A. Chakera, U. Naseer, E.M. Corea, M.J. Ellington, K.L. Hopkins, A.L. Wester, O. Ekelund, N. Woodford, T.J.J. Inglis, Rapid susceptibility profiling of carbapenem-resistant *Klebsiella pneumoniae*, *Sci. Rep.* 7 (2017) 1–13. <https://doi.org/10.1038/s41598-017-02009-3>.
- [56] D. Fonseca e Silva, A. Silva-Dias, R. Gomes, I. Martins-Oliveira, M.H. Ramos, A.G. Rodrigues, R. Cantón, C. Pina-Vaz, Evaluation of rapid colistin susceptibility directly from positive blood cultures using a flow cytometry assay, *Int. J. Antimicrob. Agents.* 54 (2019) 820–823. <https://doi.org/10.1016/j.ijantimicag.2019.08.016>.
- [57] W. Hong, C.W. Karanja, N.S. Abutaleb, W. Younis, X. Zhang, M.N. Seleem, J.X. Cheng, Antibiotic Susceptibility Determination within One Cell Cycle at Single-Bacterium Level by Stimulated Raman Metabolic Imaging, *Anal. Chem.* 90 (2018) 3737–3743. <https://doi.org/10.1021/acs.analchem.7b03382>.
- [58] K. Yang, H.Z. Li, X. Zhu, J.Q. Su, B. Ren, Y.G. Zhu, L. Cui, Rapid Antibiotic Susceptibility Testing of Pathogenic Bacteria Using Heavy-Water-Labeled Single-

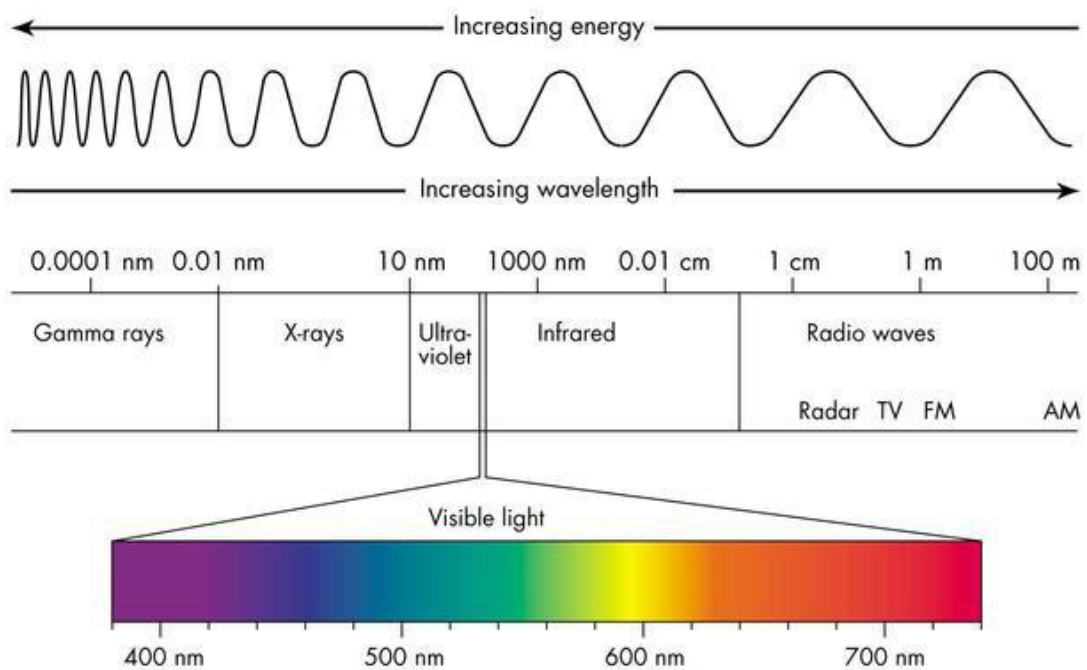
- Cell Raman Spectroscopy in Clinical Samples, *Anal. Chem.* 91 (2019) 6296–6303. <https://doi.org/10.1021/acs.analchem.9b01064>.
- [59] A. Novelli-Rousseau, I. Espagnon, D. Filiputti, O. Gal, A. Douet, F. Mallard, Q. Josso, Culture-free Antibiotic-susceptibility Determination from Single-bacterium Raman Spectra, *Sci. Rep.* 8 (2018). <https://doi.org/10.1038/s41598-018-22392-9>.
- [60] Z. Pilát, S. Bernatová, J. Ježek, J. Kirchhoff, A. Tannert, U. Neugebauer, O. Samek, P. Zemánek, Microfluidic Cultivation and Laser Tweezers Raman Spectroscopy of *E. coli* under Antibiotic Stress, *Sensors.* 18 (2018) 1623. <https://doi.org/10.3390/s18051623>.
- [61] J. Choi, H.Y. Jeong, G.Y. Lee, S. Han, S. Han, B. Jin, T. Lim, S. Kim, D.Y. Kim, H.C. Kim, E.C. Kim, S.H. Song, T.S. Kim, S. Kwon, Direct, rapid antimicrobial susceptibility test from positive blood cultures based on microscopic imaging analysis, *Sci. Rep.* 7 (2017). <https://doi.org/10.1038/s41598-017-01278-2>.
- [62] A.M. Kaushik, K. Hsieh, L. Chen, D.J. Shin, J.C. Liao, T.H. Wang, Accelerating bacterial growth detection and antimicrobial susceptibility assessment in integrated picoliter droplet platform, *Biosens. Bioelectron.* 97 (2017) 260–266. <https://doi.org/10.1016/j.bios.2017.06.006>.
- [63] P. Sabhachandani, S. Sarkar, P.C. Zucchi, B.A. Whitfield, J.E. Kirby, E.B. Hirsch, T. Konry, Integrated microfluidic platform for rapid antimicrobial susceptibility testing and bacterial growth analysis using bead-based biosensor via fluorescence imaging, *Microchim. Acta.* 184 (2017) 4619–4628. <https://doi.org/10.1007/s00604-017-2492-9>.
- [64] F. Lyu, M. Pan, S. Patil, J.H. Wang, A.C. Matin, J.R. Andrews, S.K.Y. Tang, Phenotyping antibiotic resistance with single-cell resolution for the detection of heteroresistance, *Sensors Actuators, B Chem.* 270 (2018) 396–404. <https://doi.org/10.1016/j.snb.2018.05.047>.
- [65] H. Li, P. Torab, K.E. Mach, C. Surette, M.R. England, D.W. Craft, N.J. Thomas, J.C. Liao, C. Puleo, P.K. Wong, Adaptable microfluidic system for single-cell pathogen classification and antimicrobial susceptibility testing, *Proc. Natl. Acad. Sci.* (2019) 201819569. <https://doi.org/10.1073/pnas.1819569116>.
- [66] H. Yu, W. Jing, R. Iriya, Y. Yang, K. Syal, M. Mo, T.E. Gryns, S.E. Haydel, S. Wang, N. Tao, Phenotypic Antimicrobial Susceptibility Testing with Deep Learning Video Microscopy, *Anal. Chem.* 90 (2018) 6314–6322. <https://doi.org/10.1021/acs.analchem.8b01128>.
- [67] R. Iriya, W. Jing, K. Syal, M. Mo, C. Chen, H. Yu, S.E. Haydel, S. Wang, N. Tao, Rapid antibiotic susceptibility testing based on bacterial motion patterns with long short-term memory neural networks, *IEEE Sens. J.* 1748 (2020) 1–1. <https://doi.org/10.1109/jsen.2020.2967058>.
- [68] K. Syal, S. Shen, Y. Yang, S. Wang, S.E. Haydel, N. Tao, Rapid Antibiotic Susceptibility Testing of Uropathogenic *E. coli* by Tracking Submicron Scale Motion of Single Bacterial Cells, *ACS Sensors.* 2 (2017) 1231–1239. <https://doi.org/10.1021/acssensors.7b00392>.

- [69] L. Shang, Y. Cheng, Y. Zhao, Emerging Droplet Microfluidics, *Chem. Rev.* 117 (2017) 7964–8040. <https://doi.org/10.1021/acs.chemrev.6b00848>.
- [70] M.F. Anjum, E. Zankari, H. Hasman, Molecular Methods for Detection of Antimicrobial Resistance, *Antimicrob. Resist. Bact. from Livest. Companion Anim.* (2017) 33–50. <https://doi.org/10.1128/microbiolspec.arba-0011-2017>.
- [71] A. Tannert, R. Grohs, J. Popp, U. Neugebauer, Phenotypic antibiotic susceptibility testing of pathogenic bacteria using photonic readout methods: recent achievements and impact, *Appl. Microbiol. Biotechnol.* 103 (2019) 549–566. <https://doi.org/10.1007/s00253-018-9505-4>.
- [72] Y. Li, X. Yang, W. Zhao, Emerging Microtechnologies and Automated Systems for Rapid Bacterial Identification and Antibiotic Susceptibility Testing, *SLAS Technol.* 22 (2017) 585–608. <https://doi.org/10.1177/2472630317727519>.
- [73] P. Mishra, D. Singh, K.P. Mishra, G. Kaur, N. Dhull, M. Tomar, V. Gupta, B. Kumar, L. Ganju, Rapid antibiotic susceptibility testing by resazurin using thin film platinum as a bio-electrode, *J. Microbiol. Methods.* 162 (2019) 69–76. <https://doi.org/10.1016/j.mimet.2019.05.009>.
- [74] Y.T. Kao, T.S. Kaminski, W. Postek, J. Guzowski, K. Makuch, A. Ruszczak, F. Von Stetten, R. Zengerle, P. Garstecki, Gravity-driven microfluidic assay for digital enumeration of bacteria and for antibiotic susceptibility testing, *Lab Chip.* 20 (2020) 54–63. <https://doi.org/10.1039/c9lc00684b>.
- [75] M. Azizi, M. Zaferani, B. Dogan, S. Zhang, K.W. Simpson, A. Abbaspourrad, Nanoliter-Sized Microchamber/Microarray Microfluidic Platform for Antibiotic Susceptibility Testing, *Anal. Chem.* 90 (2018) 14137–14144. <https://doi.org/10.1021/acs.analchem.8b03817>.
- [76] B. Xu, Y. Du, J. Lin, M. Qi, B. Shu, X. Wen, G. Liang, B. Chen, D. Liu, Simultaneous identification and antimicrobial susceptibility testing of multiple uropathogens on a microfluidic chip with paper-supported cell culture arrays, *Anal. Chem.* 88 (2016) 11593–11600. <https://doi.org/10.1021/acs.analchem.6b03052>.
- [77] N.M. Reis, J. Pivetal, A.L. Loo-Zazueta, J.M.S. Barros, A.D. Edwards, Lab on a stick: Multi-analyte cellular assays in a microfluidic dipstick, *Lab Chip.* 16 (2016) 2891–2899. <https://doi.org/10.1039/c6lc00332j>.
- [78] I. Michael, D. Kim, O. Gulenko, S. Kumar, S. Kumar, J. Clara, D.Y. Ki, J. Park, H.Y. Jeong, T.S. Kim, S. Kwon, Y.K. Cho, A fidget spinner for the point-of-care diagnosis of urinary tract infection, *Nat. Biomed. Eng.* 4 (2020) 591–600. <https://doi.org/10.1038/s41551-020-0557-2>.
- [79] F. Pujol-Vila, P. Giménez-Gómez, N. Santamaria, B. Antúnez, N. Vigués, M. Díaz-González, C. Jiménez-Jorquera, J. Mas, J. Sacristán, X. Muñoz-Berbel, Portable and miniaturized optofluidic analysis system with ambient light correction for fast in situ determination of environmental pollution, *Sensors Actuators, B Chem.* 222 (2016) 55–62. <https://doi.org/10.1016/j.snb.2015.07.095>.
- [80] F. Pujol-Vila, N. Vigués, A. Guerrero-Navarro, S. Jiménez, D. Gómez, M. Fernández,

- J. Bori, B. Vallès, M.C. Riva, X. Muñoz-Berbel, J. Mas, Paper-based chromatic toxicity bioassay by analysis of bacterial ferricyanide reduction, *Anal. Chim. Acta.* 910 (2016) 60–67. <https://doi.org/10.1016/j.aca.2016.01.006>.
- [81] F. Pujol-Vila, J. Dietvorst, L. Gall-Mas, M. Díaz-González, N. Vigués, J. Mas, X. Muñoz-Berbel, Bioelectrochromic hydrogel for fast antibiotic-susceptibility testing, *J. Colloid Interface Sci.* 511 (2018). <https://doi.org/10.1016/j.jcis.2017.09.004>.
- [82] J. Dietvorst, L. Vilaplana, N. Uria, M.P. Marco, X. Muñoz-Berbel, Current and near-future technologies for antibiotic susceptibility testing and resistant bacteria detection, *TrAC - Trends Anal. Chem.* 127 (2020) 1–13. <https://doi.org/10.1016/j.trac.2020.115891>.



# 3. Fundamentals







Due to its multidisciplinary nature, the following chapter is devoted to define and describe relevant concepts appearing along the thesis, as well as physical, chemical and biological principles and theories necessary for a complete understanding of the work.

### 3.1. Bacteria: classification, proliferation and basic metabolic concepts

**Bacteria are unicellular** biological entities belonging to the **prokaryotic empire**, which are smaller (i.e. between 0.5 – 5, micrometres) and simpler (e.g. lack a nucleus) than eukaryotic cells, such as plant, animal and fungal cells. Bacteria in the natural environment exist in communities of millions and can be found in nearly every habitat.

#### 3.1.1. Bacterial classification

Bacteria cover an enormous taxonomy, and several methods exist to **classify** them. Two of them are of interest by the current thesis and presented below:

- **Morphology:** it includes spherical (cocci) and the rod-shaped (bacilli), which are the most common, as well as slightly curved rods (vibrio), spiral-shaped (spirilla) or tightly coiled (spirochaetes).
- **Gram staining:** the gram staining is the most popular method of classification of bacteria and enables to distinguish them according to the chemical composition and the structure of their outer cell wall. It consists of staining bacteria with crystal violet and safranin, which results in two groups of bacteria, namely **gram-positive**, which appear purple after staining with the crystal violet, and **gram-negative**, which appear pink/red after the decolouration of the crystal violet with ethanol and counterstaining with safranin. The structural differences between these two groups are illustrated in **Figure 3.1**. Gram-positive bacteria have a cytoplasmic membrane, a small periplasmic space and a thick peptidoglycan layer (20 – 80 nm). Conversely, gram-negative bacteria have a cytoplasmic membrane, a thin peptidoglycan layer of 2 – 3 nm and an outer membrane, containing lipopolysaccharides in its outer leaflet and phospholipids in its inner leaflet. Between the cytoplasmic and outer membrane there is a big periplasmic space. The outer membrane can contain porins for the transport of specific molecules.

## GRAM-NEGATIVE

## GRAM-POSITIVE

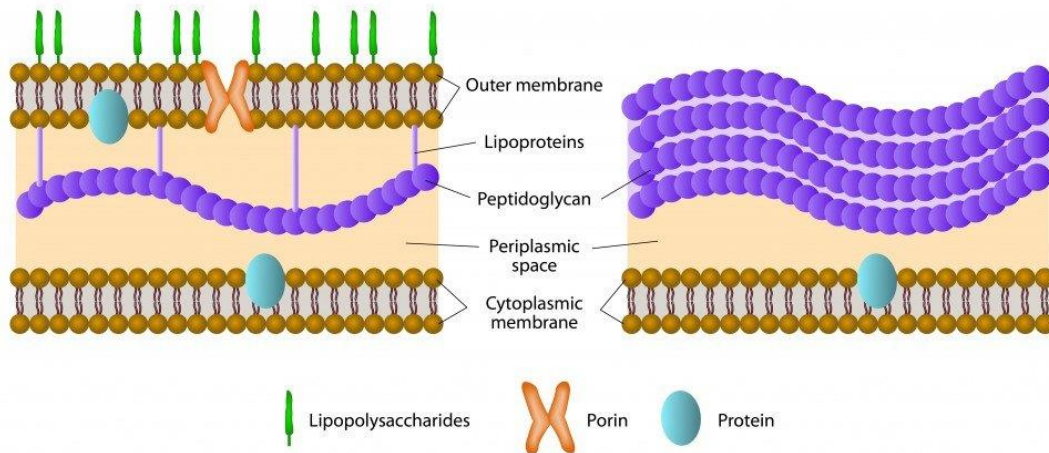


**Figure 3.1: Chemical composition of the cell wall of gram-negative and gram-positive bacteria.** Notice the difference in thickness in the peptidoglycan layer and the extra outer membrane in the case of gram-negative bacteria. Image reproduced with permission from istockphoto .

**In this thesis, both gram-positive and gram-negative bacteria of clinical relevance are analysed to validate the protocol and the final system.**

### 3.1.2. Bacterial proliferation

**Bacterial reproduction** is asexual, through binary fission, where the bacterium grows to a specific size before dividing into two identical daughter cells, clones of the parent. The **duplication time** depends on the bacterial strain and environmental conditions (e.g. temperature, access to nutrients, environmental conditions, etc.) and some bacteria are able to replicate every 10 minutes while other need hours. Bacterial growth follows the four phases illustrated in **Figure 3.2:**

- The **lag phase**, initial phase where bacteria adapt to the environmental conditions before proliferating. They synthesise RNA, enzymes and other molecules necessary for cell division and it can last for 1 hour up to several days.
- The **log phase**, also called exponential growth phase, where bacteria start cell division and proliferation. This growth is usually plotted as the natural logarithm of the cell number against time. If no growth restrictions occur (e.g. lack of nutrients, oxygenation, etc.), this representation results in a straight line and the slope of this line is the specific growth rate of the organism in the given environment, i.e. the duplication time. A variation in environment can affect the doubling frequency and survivability of the daughter cells.
- Growth-limiting factors such as nutrient depletion and waste build up lead to the third phase, the **stationary phase**, where the number of bacterial divisions is matching with the number of dead cells, resulting in a constant size of bacterial population and a smooth flat line in the growing plot.

- The **death phase** starts when, due to very unfavourable conditions such as a high concentration of toxic molecules, the dying velocity surpasses bacterial proliferation and the total number of live bacteria is reduced over time.

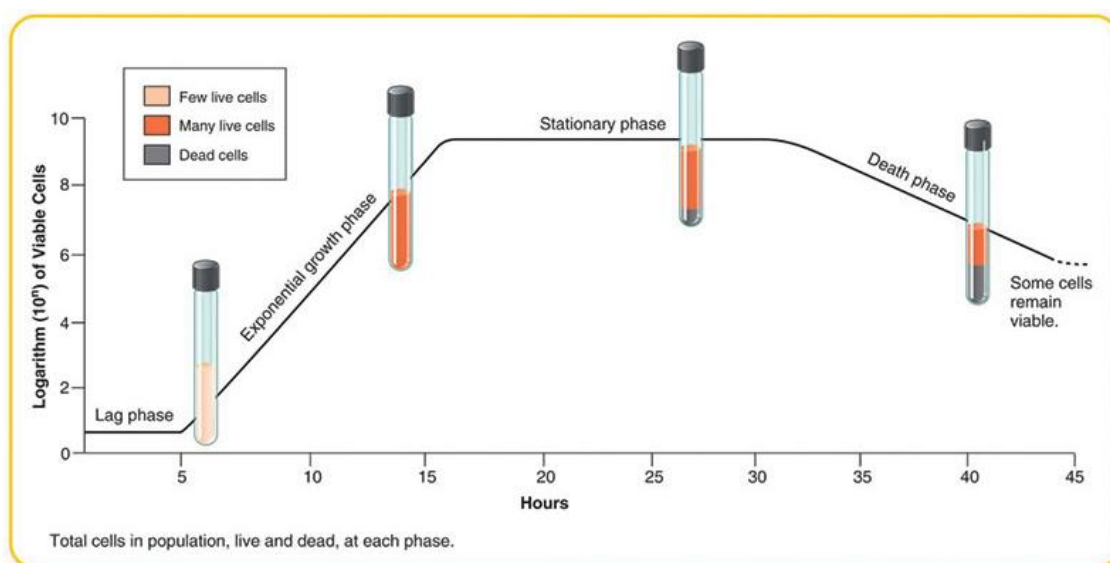


**Figure 3.2:** Figure depicting the growth curve of bacteria expressed as the logarithm of viable cells per hour. Reproduced with permission from the Microbe Notes website.

### 3.1.3. Bacterial metabolism

Bacterial survival and reproduction rely on their capacity to obtain energy from nutrients, i.e. **bacterial metabolism**. Bacteria are very versatile microorganisms with a wide variety of metabolic strategies, including **phototropism** (when obtaining energy from the light) and **chemotropism** (when obtaining energy from chemical compounds). Regardless of the strategy, bacterial metabolism results in the production of adenosine triphosphate (ATP) molecules, the energy molecule in nature, through a reducing process, which exemplified by the case of *Escherichia coli* in **Figure 3.3**. In this process, electrons are generated and transferred through sequential redox reactions between proteins (or protein complexes) in the cell membrane (i.e. **the electron transport chain, ETC**) to the **final electron acceptor**, this being oxygen in the case of **aerobic metabolism** (or respiration), inorganic compound like nitrate or sulphate in **anaerobic metabolism** and organic molecules in **fermentation**. The electron flow produces a proton gradient across the membrane, which in turn is used for ATP synthesis.

**The electron flow through the ETC is used in this thesis to detect live and metabolically-active bacteria and to determine the MIC after incubation with antibiotics. To this end, molecules with a redox potential suitable to react with one or various components of the ETC upon which they change of colour, bioelectrochromic molecules, are selected and used as metabolic indicators for live bacteria determination.**

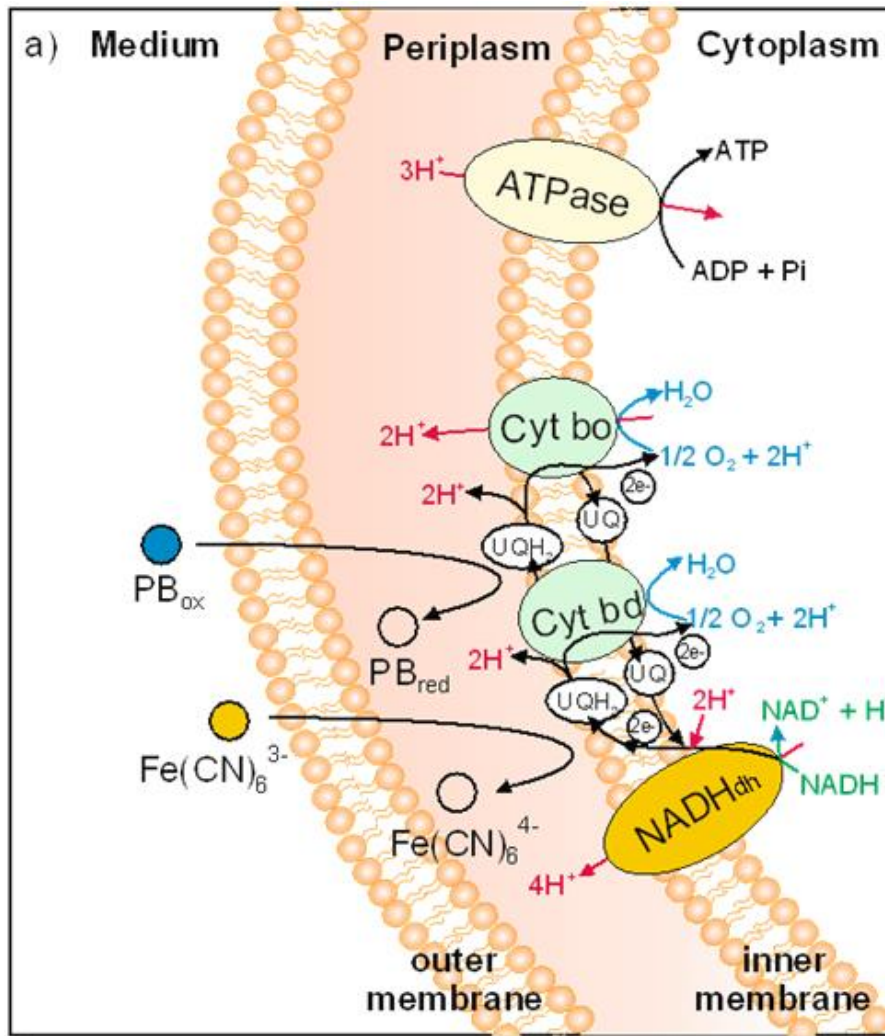


**Figure 3.3:** Figure illustrating the electron transport chain (ETC) over a bacterial membrane. The ETC mainly takes place over the inner membrane, where a series of oxidation-reduction reactions, using various proteins, results in the transfer of protons to the periplasm. These are sequentially used to generate energy in the form of ATP. The final electron acceptor in this ETC is oxygen in the case of aerobic bacteria.

### 3.2. Optics Concepts: Absorbance and Reflectance

In physics, **optics** is devoted to study the properties and behaviour of light. Inside optics, **spectroscopy** investigates the interaction between matter and electromagnetic radiation. The electromagnetic spectrum is divided in a number of regions (i.e. gamma-rays, X-rays, ultraviolet, visible, infrared and radio waves) that depend on the frequency, wavelengths and/or energy of the radiation (**Figure 3.4**). The Planck's equation relates the previous parameters: the shorter the wavelength, the higher the frequency and the energy.

The visible region includes the radiation that can be perceived by the human eye and ranges from 380 to 800 nm approximately. The interaction of visible light with matter results in a number of processes, being **light extinction** and **reflection** the most relevant for the present thesis.

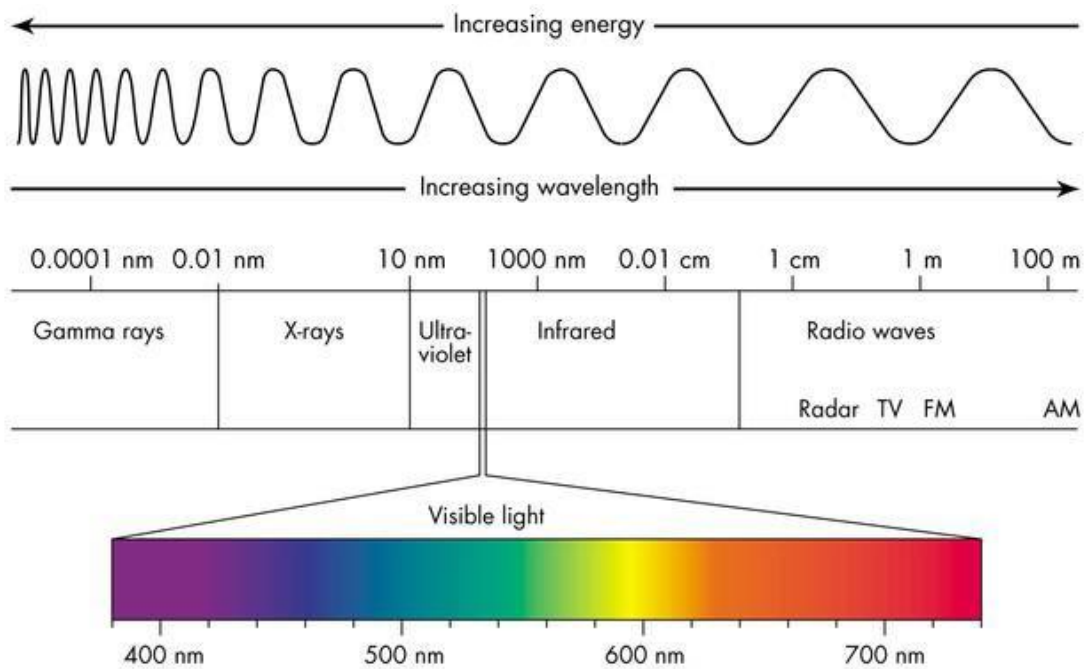


**Figure 3.4: Electromagnetic spectrum.** The top graph shows the inverse relation between energy and wavelength. The bottom 2 graphs show the different regions of the electromagnetic spectrum, highlighting the visible light region.

### 3.2.1. Light extinction mechanisms

**Light extinction** refers to a loss of light due to the interaction of this radiation with matter. This light attenuation (weakening) depends on the material and the radiation wavelength through the extinction coefficient ( $\epsilon$ ): high extinction coefficients imply high energy losses. There are two main mechanisms involved in light extinction, namely **absorption** and **scattering**.

**In absorption**, the energy from the electromagnetic field is taken up by electrons of the material and converted into another form of energy, usually dissipated as heat. Interestingly, absorption has an accumulative effect and light intensity is gradually reduced when it propagates through the material. This is expressed in the Beer-Lambert law (**Figure 3.5**), which relates the quantity of incident light absorbed by an object, understood as a single attenuating species of uniform concentration  $c$  (in M), with the length of the optical path  $L$  (in cm) and the intrinsic molar extinction coefficient (or attenuation coefficient or molar absorptivity) of the species  $\epsilon$  (in  $M^{-1} cm^{-1}$ ), as follows:

$$A = \epsilon lc$$

In spectroscopy, the transmission ( $T$ ) or amount of transmitted light is measured as the ratio between the intensities of the incident radiation ( $I_0$ ) and the measured emerged beam after the sample ( $I$ ). From this quantity, the absorbance ( $A$ ) can be computed as detailed below:

$$T = \frac{I}{I_0}$$

$$A = -\log T$$

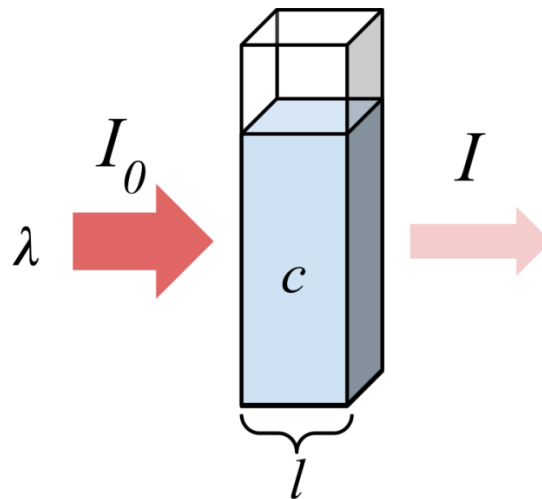


**Figure 3.5: Beer-Lambert law visualized.** Light, visualized as  $\lambda$  comes in at an intensity  $I_0$ , passes through a liquid containing a concentration  $c$  of the measured species over an optical path of length  $L$ , and comes out at intensity  $I$ .

Combining the two expressions, it is very simple to determine the concentration of coloured species when knowing the optical path and the extinction coefficient by a simple transmission measurement, or after a previous calibration with known concentrations of the analyte of interest and using the same optical setup. Additionally, since absorption is a wavelength-specific (inelastic) process, it allows the identification and even simultaneous quantification of several species present in the same medium/material by determining the absorbance of each species at its specific wavelengths.

**In this thesis, absorption is employed to quantify the colorimetric metabolic indicators used to determine bacterial concentration.**

**Scattering** is a physical process where light interacting with matter is absorbed by the object and re-emitted in all directions but with different light intensities. Main scattering processes involving visible light, i.e. Rayleigh and Mie-scattering, are elastic and involve negligible energy transfer (energy is conserved in the interaction).

**Rayleigh scattering** refers to the elastic scattering of light by particles of a size much smaller than the wavelength of the radiation. This effect is due to the polarizability of the particles, where the oscillating electric field of the incident light waves can act on the charges of the particles causing them to move at the same frequency. After this, the particle becomes a small dipole that radiates, which is defined as scattered light.

**Mie scattering**, on the other hand, is produced by elastic scattering of light by particles of similar size to the wavelength of the radiation, even though Mie scattering theory has no upper size limitation.

**In this thesis, the scattering produced by bacterial cells is used to quantify them and evaluate their proliferation over time.**

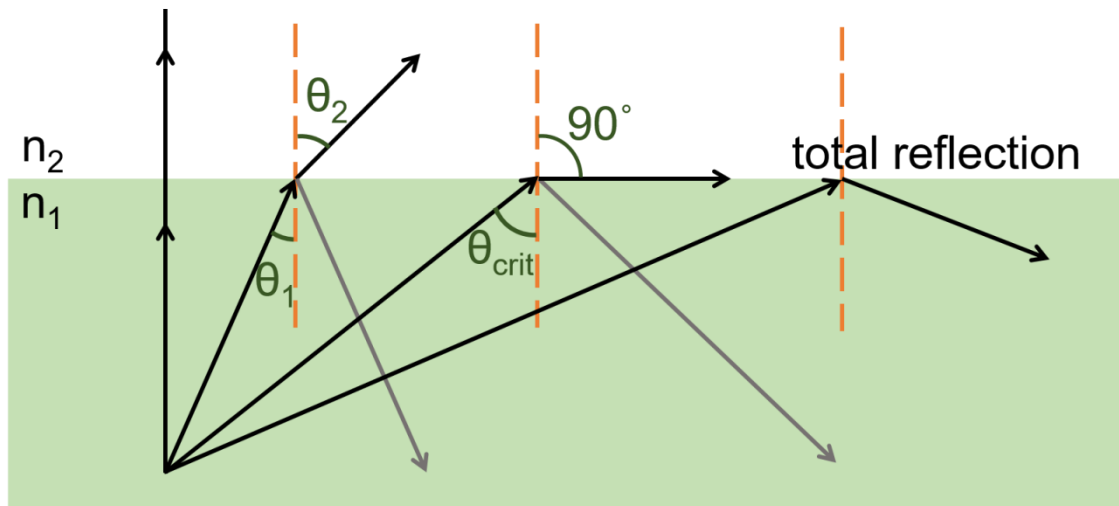


**Figure 3.6: Refraction and total internal reflection.** The image shows the possible refracted angles when light travels from a medium with a high refractive index  $n_1$ , to one with a low refractive index  $n_2$ . As the incident light enters at an angle  $\theta_1$ , light refracts out at a bigger angle  $\theta_2$ . When reaching the critical angle  $\theta_{crit}$ , light refracts at  $90^\circ$ , travelling along the interface. Any incident angle bigger than  $\theta_{crit}$  will cause light to reflect back inside medium 1, also known as total internal reflection.

### 3.2.2. Light refraction

**Light refraction** refers to a change of direction of the light when passing through a smooth and plane boundary between two different media. The Snell's law, also known as the law of refraction, predicts the behaviour of the light in the boundary according to the refractive indexes (RIs) of the two materials and the incidence angle of the light ( $\theta$ ). Since the RI is indicative of the velocity of the light travelling through the material (which is determined by the expression  $n_1 = c/v_1$ , where  $c$  is the speed of light in vacuum), Snell's law can be either expressed as the relation of the sinus of the angles of the incident light in both media with their phase velocities ( $v$ ) or RI (which represented by  $n$  in the equation):

$$\text{Snell's Law: } \frac{\sin(\theta_2)}{\sin(\theta_1)} = \frac{v_2}{v_1} = \frac{n_1}{n_2}$$

where parameters labelled as 1 correspond to the medium 1 and the ones labelled as 2 correspond to the medium 2.

When light travels from a medium with a high refractive index towards a medium with a lower one, depending on the incidence angle with the perpendicular to the interface (**Figure 3.6**), the following behaviours can occur for the refracted light:

- **Light is refracted at an angle  $\theta_2$** , when  $\theta_1 < \theta_{crit}$  and  $\theta_2 > \theta_1$ .
- **Light is refracted at an angle of  $90^\circ$** , when  $\theta_1 = \theta_{crit}$ .
- **Light is totally reflected**, when  $\theta_1 > \theta_{crit}$  (i.e. total internal reflection, TIR).

The critical angle depends on the RI of both media and can be calculated by the following expression:



$$\theta_{crit} = \arcsin\left(\frac{n_2}{n_1}\right)$$

In this thesis, light refraction and reflection is used to design the micro-optical components of the system, particularly the light coupling and routing components.

### 3.3. Electrochemical concepts: Amperometry

In electrochemistry, when a voltage is applied between two electrodes in contact with an electroactive analyte susceptible to be oxidized in the anode (releasing electrons) or reduced in the cathode (accepting electrons), **the changes of the measured electrical current are monitored, typically as a function of time or electrode potential.**

Usually, the magnitude of the measured current over time can be related to the concentration of the analyte that has been reduced or oxidized by means of the **Cottrell's equation** as follows:

$$i = \frac{nFAc_j^0\sqrt{D_j}}{\sqrt{\pi t}}$$

where  $i$  is the current magnitude (A),  $n$  is the number of exchange electrons,  $F$  is the Faraday constant (96485 C/mol),  $A$  is the area of the electrode ( $\text{cm}^2$ ),  $c_j^0$  is the initial concentration of the analyte  $j$  ( $\text{mol}/\text{cm}^3$ ),  $D_j$  is the diffusion coefficient for specie  $j$  ( $\text{cm}^2/\text{s}$ ) and  $t$  is the time (s).

Even when a minimum of two electrodes is required, electrochemical measurements are generally performed with a **three-electrode configuration**, including:

- **The working electrode:** where the cell reaction takes place.
- **The reference electrode:** with a stable and well-known potential, the reference electrode is used to set the electrical potential of the working electrode with precision along the experiment. Typical reference electrodes are:
  - Standard Hydrogen Electrode (SHE), which is declared to be 0V at any temperature to form a basis of comparison.
  - Saturated Calomel Electrode (SCE) with a potential of 0.241 V at 25 ° vs. SHE.
  - Ag/AgCl with a potential of 0.197 V at 25°C vs. SHE.
- **The counter electrode:** used to close the electrical circuit, and to collect or generate the electrons either produced or consumed in the working electrode.

A number of electrochemical techniques exist which differ in the way the potential or current is applied/recorded over time. The most relevant for the thesis are **amperometry** and **voltammetry**, which are discussed below.

- In **amperometry** (also known as chronoamperometry), a constant reducing or oxidizing potential is applied to the working electrode while the resulting current is measured over time (**Figure 3.7**).

**In this thesis, amperometry is used in the electrodeposition of alginate hydrogels.**

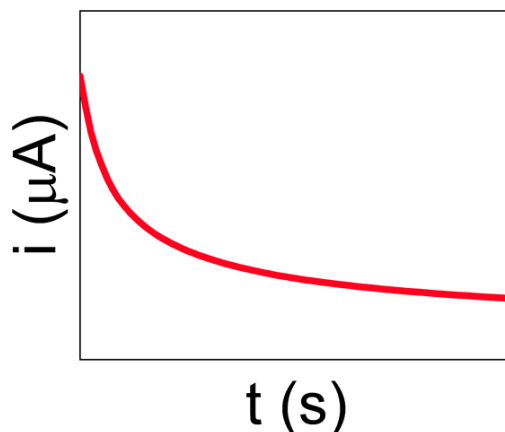


**Figure 3.7: Representation of a characteristic chronoamperometrical plot.** When a constant potential is applied, the current  $i$  ( $\mu\text{A}$ ) changes over time  $t$ (s).

- In **voltammetry**, the electrochemical current of the cell is monitored whilst actively manipulating the cell's potential by applying a constant or varying potential. One specific type of voltammetry is **cyclic voltammetry (CV)**, where the working electrode potential is ramped linearly over time and then reversed in the opposite direction to reach back the initial potential value. The characteristic plots show the current intensity at the working electrode versus the potential applied. The CV curve results in a double wave, one corresponding to the oxidation processes and another to the reduction one. Each electron exchange in the reaction under study results, therefore, in two peaks of certain intensity ( $i_p$ ), one for the reduction process ( $i_{p,c}$ ) and another for the oxidation ( $i_{p,a}$ ) at a certain potential ( $E_{p,c}$  and  $E_{p,a}$ , respectively). In the simplest case, i.e. the analyte under study is fully reversible, both peaks are completely symmetric and proportional to the concentration of analyte. Nonetheless, most redox processes are quasi-reversible or non-reversible and do not present symmetric peaks in the plot[1].

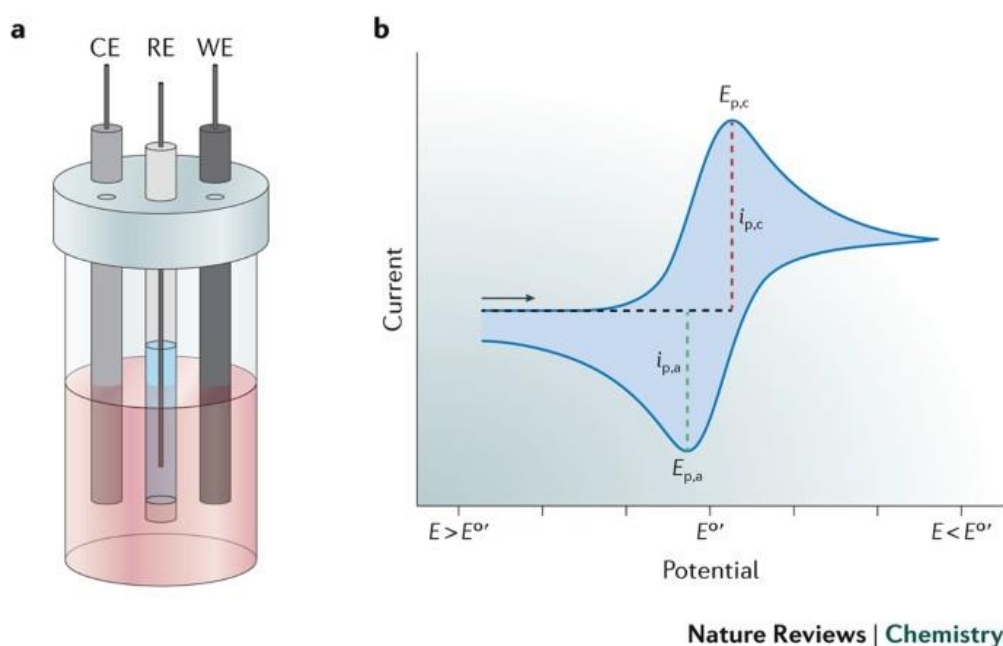


**Figure 3.8: Illustration of a three-electrode cell and an example of a cyclic voltammogram.** a) Shows a typical cyclic voltammetry setup, which involves the analyte solution contacting three electrodes: working electrode (WE), counter electrode (CE) and reference electrode (RE). b) Depicts a cyclic voltammogram for a species undergoing reversible one-electron reduction. As the potential is scanned in the negative direction, the reduction of the analyte results in a cathodic current, with a maximum magnitude  $i_{p,c}$  at a potential  $E_{p,c}$ . Reversing the scan will lead to oxidation, giving rise to an anodic current, which reaches a maximum magnitude  $i_{p,a}$  at potential  $E_{p,a}$ . Reproduced with permission from Lee et al. [2]

This method has a lot of applications, ranging from characterization of electrodes and electrochemical systems to the study of reduction potential of a certain analyte and its electrochemical reactivity.

**In this thesis, CV has been used to study the mechanism of the cyanotyping-based protocol.**

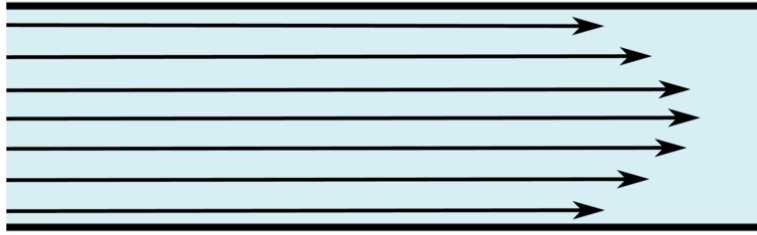
### 3.4. Microfluidics

Microfluidics deal with the behaviour, precise control and manipulation of small fluid volumes (nL to fL) that are geometrically constrained to a small, typically sub-millimetre, scale. At this scale, fluid flow is mostly governed by a laminar flow and capillary forces, and mass transport only depends on diffusion, while migration and convection are mostly negligible. To understand the differences between micro- and macro-fluidics, several phenomena need to be explained, which are detailed in the following sections.

#### 3.4.1. Laminar vs turbulent flow

The first major difference between microfluidic and macrofluidic devices is the presence of **laminar flow** in the former, whereas the latter is dominated by **turbulent flows**. In the laminar flow, the fluid particles are following through smooth paths that flow in parallel along each other with little to no mixing. Conversely, the turbulent flow is characterized by chaotic changes in pressure and flow velocity that produce a constant and random movement of the fluid particles, which are continuously colliding and mixing (**Figure 3.9**).

## laminar flow



## turbulent flow

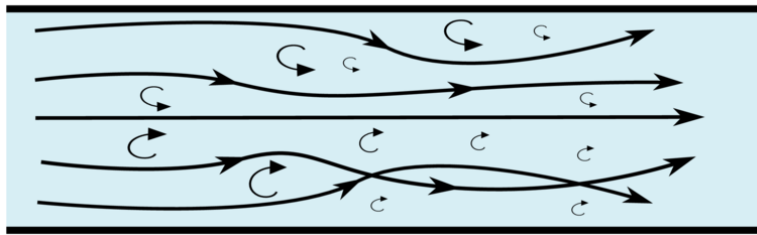


**Figure 3.9: Image illustration the principles of laminar and turbulent flow.** In laminar flow all fluid particles follow smooth paths parallel to each other. Turbulent flow is characterized by chaotic movements and mixing of fluid particles.

The flow behaviour of a system can be predicted using a dimensionless number, called **the Reynolds number**,  $Re$ , which can be calculated as follows:

$$Re = \frac{\rho u L}{\mu} = \frac{u L}{\nu}$$

With  $L$  the characteristic linear dimension (m),  $u$  is the flow speed (m/s),  $\rho$  the density of the liquid ( $\text{kg/m}^3$ ),  $\mu$  the dynamic viscosity of the fluid ( $\text{kg/(m.s)}$ ), and  $\nu$  the kinetic viscosity of the liquid ( $\text{m}^2/\text{s}$ ).

At low Reynolds numbers ( $<2000$ ) the flow behaves laminar, implying the viscous forces dominate the inertial forces ( $\mu > u$ ). With microfluidic systems having a very small characteristic linear dimension ( $<\text{mm}$ ), they are all laminar in behaviour. At high Reynolds number ( $>4000$ ) the inertial forces dominate the viscous forces, also known as turbulent flow ( $\mu \ll u$ ).

### 3.4.2. Diffusion vs Convection

One of the main consequences of working at the microscale in a laminar flow is that mass transport is exclusively dominated by **diffusion**, in contrast to the macroscale where other phenomena, such as **convection or migration**, are also relevant. By definition, diffusion is the net movement of analyte from a region of higher concentration to another of a lower one. The **Fick's laws** describe how diffusion occurs. **The Fick's first law** relates the diffusive flux to the gradient of the concentration. The flux goes from high to low concentration, with a magnitude proportional to the concentration gradient and is written as:

$$J = -D \frac{d\phi}{dx}$$

With J the diffusion flux (mol/m<sup>2</sup>s), the amount of substance flowing through a unit area during a time interval, D the diffusion coefficient (m<sup>2</sup>/s),  $\phi$  the concentration (mol/m<sup>3</sup>) and x the position (m).

This expression can be used to obtain the **diffusion coefficient D**, which is a proportional constant between the molar flux due to molecular diffusion and the gradient of the species (the driving force of the diffusion).

**The Fick's second law** predicts how the diffusion causes the concentration to change over time.

$$\frac{\delta\phi}{\delta t} = D \frac{\delta^2\phi}{\delta x^2}$$

It is important to note that the diffusion coefficient D is a constant for a given system, resulting in diffusion occurring at a constant velocity. Thus, microfluidic systems, which are nearly always laminar of nature, highly depend on diffusion for the mixing of species. This may be a disadvantage when compared to macrofluidic systems where mass transport and thus mixing is dominated for faster processes such as convection. However, due to the small distances of microfluidic systems, diffusion processes take place fast and various mixing strategies have been already developed to minimize this limitation, mainly in the form of microfluidic mixers [3].

### 3.4.3. Surface tension vs gravity

Two main forces are governing liquid movement in fluidic systems, i.e. **surface tension** and **gravity**. Surface tension measures the tendency of a liquid to shrink to the minimum surface areas possible. It results from attractive forces that pull neighbouring molecules from every direction to each other, which can be either **cohesive forces** (when between molecules of the same type) or **adhesive forces** (when between molecules of different type). One particular case is molecules in the border, since they do not have the same amount and type of molecules on all directions. The balance between cohesive and adhesive forces in this situation determines the degree of wetting of a specific liquid with a specific surface. This wetting gives rise to an intrinsic contact angle and the shape of the liquid's meniscus:

- When the cohesive forces dominate the adhesive ones, the liquid tends to draw into itself. The surface on which this occurs is called **hydrophobic**, due to the low wettability.
- When the adhesive forces dominate, the liquid tends to spread out as much as possible. The surface is called **hydrophilic**, due to the high wettability.

The contact angle can be determined through **the Young equation**, based on the thermodynamic equilibrium between the three phases.

$$\gamma_{sg} = \gamma_{sl} + \gamma_{lg} \cos \theta_c$$

Where it relates the surface tension between the three phases,  $\gamma_{sg}$  (N/m) is the interfacial energy between the solid and gas state,  $\gamma_{sl}$  (N/m) between the solid and liquid state, and  $\gamma_{lg}$  (N/m) between the gas and liquid state. The angle  $\theta_c$  is thus known as the contact angle between the liquid and solid. The interaction between the various energies and states is shown below.

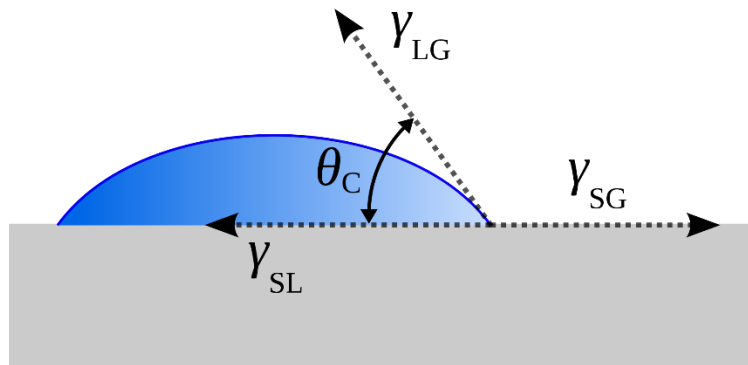


**Figure 3.10: Illustration of the contact angle of a liquid droplet on a solid substrate**, with the corresponding interfacial energies between the various states.  $\gamma_{sg}$  is the energy between the solid and gas state,  $\gamma_{sl}$  between the solid and liquid state, and  $\gamma_{lg}$  between the gas and liquid state. The angle  $\theta_c$  is the resulting contact angel. Image taken from Wikipedia: contact angle.

The value of the contact angle can again be linked to the hydrophobic/hydrophilic nature of the surface:

- If the angle is smaller than  $90^\circ$ , the surface is called hydrophilic, because the liquid tends to spread out.
- When the angle is bigger than  $90^\circ$  is hydrophobic.

In microfluidic systems, the surface tension of a liquid can lead to the physical phenomenon called **capillary action**. **Capillarity refers to the ability of a liquid to flow in narrow spaces without the assistance of external forces, or even in opposition to those forces, like gravity**. This occurs due to combination of the surface tension and the adhesive forces between the liquid and the surface.

In fluid statics, the capillary pressure is the pressure between two immiscible media in a thin tube. This occurs when the force pulling the liquid up is equal to the force pulling the liquid down and is expressed by the **Young-Laplace equation**, which, inside a cylinder is expressed as:

$$\Delta P = \frac{2\gamma_{lg}}{R_c} \cos \theta_c$$

With the  $\gamma_{lg}$  surface tension (N/m), the  $R_c$  effective radius (m) of the interface and  $\theta_c$  the wetting angle. The capillary pressure is balanced by a change in height,  $h$  (m), which can be positive or negative depending on the wetting angle.

This allows the determination of the final height that a liquid can reach in static conditions, as:

$$h = \frac{2\gamma \cos \theta}{\rho g a}$$

With the  $\gamma$  surface tension (N/m),  $g$  the gravitational acceleration ( $\text{m/s}^2$ ),  $a$  the radius of the tube (m),  $\rho$  the density of the liquid ( $\text{kg/m}^3$ ), and  $\theta$  the wetting angle.

A visualization of the capillary rise is shown in **Figure 3.11** below.

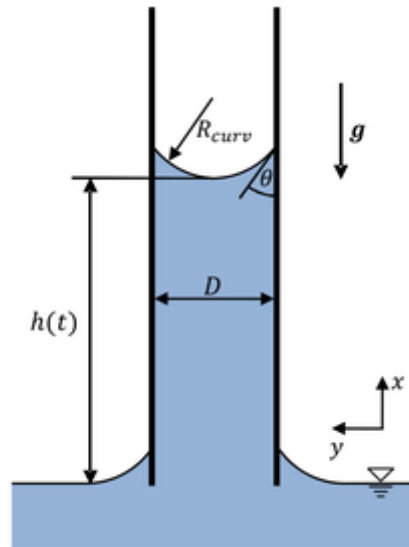


**Figure 3.11: Illustration of the various parameters required for determining the capillary rise height.**  $h(t)$  is the final height of the capillary rise,  $D$  the diameter of the tube,  $R_{curv}$  the effective radius of the interface,  $\theta$  the wetting angle and  $g$  the gravitational acceleration.

The same phenomenon is happening in fluidic structures at the microscale but in horizontal, when the small dimensions of the channels or porous substrates (e.g. cellulose papers) increase surface tension above gravity, resulting in systems where the fluid is pushed without the need for external pumps.

**One of the main challenges of this thesis is precisely to produce a system based on capillary flow that can manage fluids without the need of external components.**

#### 3.4.4. Microfluidic components

For fluid management, microfluidic devices integrate microfluidic components that, depending on the operation principle, may be divided into **active** and **passive**:

- In **passive components**, all fluid flow is physically controlled by the properties and structures of the used materials.
- **Active components** require external forces, like pumps, to drive or manipulate the liquid.

In general, active components allow for a better and more precise management of fluids but rely on bulky and complex setups, difficult to be implemented out of the laboratory. Although interesting approaches have been performed to reduce the size, cost and complexity of these microfluidic active components (mostly pumps and valves), most of the microfluidic systems already commercial or close to the market for point-of-care

analysis are based on simple passive structures, e.g. cellulose-paper with capillary pumping capacity. One of the main limitations of such systems is not on fluid pumping but on liquid management, for instance sample dilution or mixing of reagents. In this sense, important efforts have been performed in the development of **passive valves** enabling a complete control of the fluid without requiring external actuation.

Passive valves are usually divided into two groups, namely mechanical and non-mechanical valves. Mechanical valves consist of structures that allow flow in one direction, but not the other through a mechanical component, like flaps or a membrane. The non-mechanical valves are usually capillary based, structures or modifications of the surface resulting in a change of flow. One such possibility is modifying a piece of channel by making it more hydrophobic. This will cause the liquid to (temporarily) stop, since the capillary driving force is lost. Geometrical valves alter the fluid flow by sudden changes in geometrical parameter. A small channel entering a wider one will result in sudden pressure drop, causing the liquid to stop. Another example is the use of very sharp angles in or between channels, where the angle is larger than the contact angle of the liquid-material in question, causing a momentary stop. Depending on the design, these valves result in a temporary stop or will need external actuation to overcome the barrier.

**In this thesis, passive valves are developed in microcapillary structures for a complete fluid management.**



## 3.5. Fabrication methods

The current thesis deals with a number of microfabrication technologies and technological processes, which will be briefly described here for completeness and favour understanding.

### 3.5.1. Microfabrication technologies

Microfabrication technologies are a group of processes and protocols derived from the integrated circuits industry. These technologies aim to produce components, devices and systems with patterns in the micro and sub-micrometric scale. Due to the small pattern size, these technologies are normally conducted inside facilities with controlled environment where the number of particles is minimized to reduce the interference of the dust and other particles in the fabrication process (note that these particles are of the same size of the patterns and may interfere the fabrication process). These facilities are known as **Clean Rooms** and implement mechanisms for reducing the number of particles in the air as an important filtration system, laminar flow (in the regions with less particles), overpressure or a strict access system involving clean cloths, air showers, etc.

The fabrication workflow can generally be divided into main approaches, namely **top-down** or **bottom-up**:

- With a **top down** approach, also called planar technology, the device fabrication is done by patterning all the parts in place, so the final structure is built in and there is no need for assembly of the pieces with bulk production (i.e. monolithic integration).
- The **bottom-up** methodologies are those where the components are assembled after separated fabrication, achieving less compositional defects but with lower throughput and more difficulty to integrate in the final device.

Various fabrication methods exist for both technologies and they are often used together in the creation of a final device. Although describing all different methods is out of the scope of this thesis, the most relevant ones will be discussed in more detail considering both **additive techniques** (where a material is deposited on the substrate) and **subtractive techniques** (which remove partially or totally materials from the substrate).

#### 3.5.1.1. Additive techniques

Additive techniques, also referred to as layering, consist of the addition of thin layers to the wafer surface. It can be done by epitaxial growth (growing over the crystalline structure of the silicon), by oxidation (generating a layer of silicon oxide,  $\text{SiO}_2$ ) or by deposition (typically Chemical Vapour Deposition, and Physical Vapour Deposition).

- **Chemical vapour deposition** is a vacuum deposition technique where the substrate is exposed to volatile precursors that react or decompose and deposit on top of the substrate leading to high quality solid layers.

- **Physical vapour deposition** is a vacuum deposition technique to produce thin films and coatings onto a substrate where the source material goes from a condensed form, to a vapour phase and ends up in a thin film condensed phase. Under the physical vapour deposition there exist various processes, with the two most common:
  - **Sputtering:** deposition of thin films by eroding material of a target source onto a substrate.
  - **Evaporation:** the source material is evaporated in a vacuum, allowing the vapour particles to travel to the target where they will be condensed back to a solid state.

### 3.5.1.2. Subtractive techniques

- **Etching** is a fabrication method where layers are removed chemically during manufacturing. During etching part of the substrate is protected with the etchant through a 'mask'. A masking material is a material which resists etching. Precise control over the mask and the etchant allows highly precise etching. Variations of etching exist, depending on the type of etchant used:
  - In **wet etching** a liquid phase is used, for example buffered hydrofluoric acid to etch silicon dioxide over a silicon substrate. Wet etching is usually isotropic, meaning it etches in all directions equally. This can lead to under-etching, where material is also etched out under the protected mask.
  - **Dry etching** uses a bombardment of ions (such as plasma or reactive gases) to dislodge portions of the exposed material. Dry etching is usually anisotropic, allowing higher control over the etched surface. **Examples of dry etching are: (i) Reactive-ion etching (RIE)** is a form of dry etching using chemically reactive plasma. This plasma is generated in a vacuum by an electromagnetic field. The high energy ions from the plasma attack and react with the substrate surface; **(ii) Deep reactive-ion etching (DRIE)** is a variation of the RIE used when requiring a highly anisotropic etching. This is achieved by alternating repeatedly between a standard plasma etch, for a vertical attack, and a deposition of a chemical inert passivation layer, to protect the walls against etching.
- **Lithography** is a fabrication method consisting of transferring a pattern from a mask or mould to the substrate of interest. Various methods of lithography exist for the fabrication of integrated circuits; the most relevant for the thesis are listed below.
  - **Optical lithography or photolithography:** Photolithography uses light to transfer geometrical patterns from a photo-mask (or optical mask) into a substrate, e.g. a silicon wafer, which is covered with a light-sensitive chemical resist. To do so, a wafer is placed on a spinner and the resist is drop-casted on top of it, creating a uniform layer covering the wafer, a process known as spin coating. There are two main categories of optical resists: the **positive photoresist** and the **negative photoresist**. With a

positive photoresist, the exposed areas to the UV light become soluble, whereas with a negative photoresist the unexposed areas are the ones that remain soluble and thus removed after development. In the development stage, the developer, a chemical substance or solvent that can dissolve the non-cured/non-polymerized parts of the resist, is used to drag away it and reveal the transferred patterns. A representation of both processes (with positive and negative resists) can be found in **Figure 3.12**. A typical positive photoresist is DNQ-Novolac photoresist, a mixture of diazonaphthoquinone (DNQ) and novolac resin (phenol formaldehyde-based resin). A relevant example of negative example is SU-8, an epoxy-based polymer, used in this thesis.

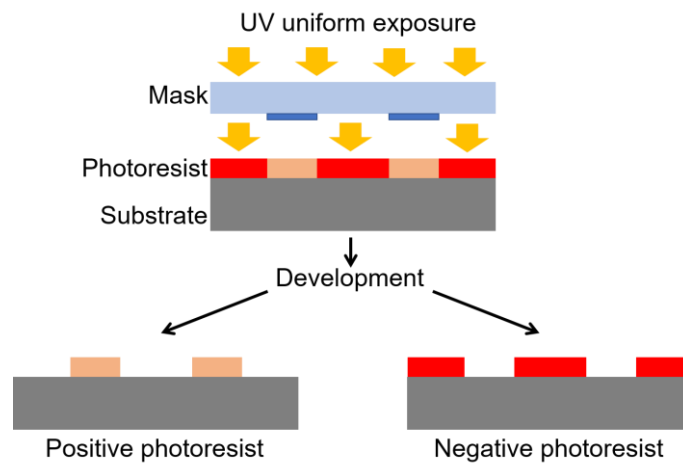


**Figure 3.12: Image illustration the principle of a photoresist.** With a positive photoresist the remaining pattern is coincident with the mask after exposure and development. With a negative photoresist, all areas coinciding with the mask will be washed away and the negative of the mask will stay.

On CMOS technology the substrate usually needs to undergo a photolithographic cycle several times (up to 50) due the highly complex structure of the final device. Each cycle can be composed by several steps, generally highlighted in **Figure 3.13** below:

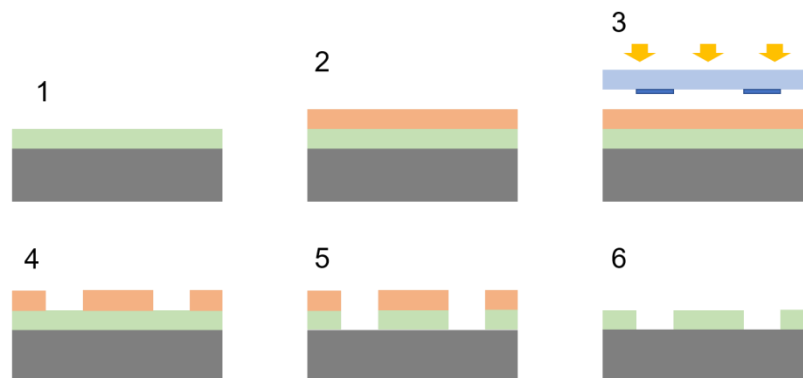


**Figure 3.13: The basic steps in photolithography.** 1) Layering (green) over the substrate (grey). 2) Spin-coating of the photoresist (orange). 3) UV exposure with the use of an optical mask (blue). 4) Developed image on the resist. 5) Material etching. 6) Photoresist removal.

Other steps that can be included in the photolithographic cycle are **doping procedures** (addition of specific amounts of doping atoms near the wafer surface in order to modulate the electronic properties of the targeted area), **heating treatments** (the wafers are heated to achieve dopant diffusion, defect annealing, dielectric reflow or metal annealing) and **cleaning procedures** (to remove particles and chemical residues with deionized water, ammonium-peroxide mixture or sulphuric-peroxide mixture as a few examples of chemical cleaning agents).

Of key relevance in the optical photolithography is the fabrication and alignment of the master mask. A photomask is typically a transparent fused silica substrate (borosilicate or sometimes quartz), covered by a highly absorbing chrome metal layer which contains the patterns of interest. The patterns of the mask are generally produced by electron beam lithography (see below), which makes mask fabrication a slow and expensive procedure. After fabrication, and just before the transference of the pattern, the mask is aligned to the substrates to ensure that the patterns are transferred to the regions of interest. For this, an aligner is used, which holds the photomask over the entire substrate to align them properly, in a very precise and reproducible way at the same spot as the chip undergoes several lithographic steps. In the current technology, a projection aligner is used where the mask is separated from the substrate instead of being in direct physical contact. In other cases, a stepper can be used to align a smaller mask or sections of a mask to a single chip on the substrate instead of the whole substrate.

The resolution of photolithography is limited by the diffraction effects on the optical components which limits the minimum size of the pattern to half of the irradiation wavelength. For this reason, smaller patterns require light sources with smaller wavelengths, resulting in the development of techniques such as deep-UV lithography (193 nm and 248 nm) or extreme UV (14 nm) lithography. Another strategy to reduce the pattern size is the use of phase shift masks that contain an additional layer on the silica-chrome mask that shifts the phase of the electrical field, preventing the intensity overlap on the wafer surface, thus allowing better differentiation of features very close to each other. In this case, the geometry of the mask features is changed on the design to compensate the proximity effects. With these two methods the feature size scales down to 30 nm. Another possibility is by working in a liquid environment, known as Immersion Lithography, for which the theoretical resolution can already be down to 35 nm. Finally, there has been also a new approach by using extreme ultra-violet light or X-rays, what is known as Next Generation Lithography. These last approaches reduce the feature size down to 15 nm, even 13.5nm for using extreme ultra-violet light.

- **Electron beam lithography:** scans a focused beam of electrons on a surface covered with an electron-sensitive film or resist to write and design the desired shapes. Contrary to photolithography, it is a maskless lithography technique with high resolution but low throughput, typically used for mask fabrication. This technique has a resolution of <10 nm. The low throughput is due to the writing time: e.g. an exposure area of 1 cm<sup>2</sup>, with a dose of 10<sup>-3</sup> C/cm<sup>2</sup> and a beam current of 10<sup>-9</sup> A, the resulting writing time would take around 12 days, excluding the time needed for the stage to move and the beam adjustments and corrections. Additionally, the equipment used is highly expensive: a full electron beam lithography system can cost up to \$1M.
- **Nanoimprint lithography:** is a pattern replication technology at the nanoscale, where imprint resists are mechanically deformed once applied on top of a master mould. These resists are typically a monomer or polymer that is afterwards cured by heat or UV light. It is a very simple technique, compared to the other alternatives, with high throughput, but expensive by the cost of production of masters with nano-scale resolution.
- **Soft lithography:** Although the microfabrication patterning is mostly done by photolithography (absolutely dominating the field), that technique shows several disadvantages. The optical diffraction limits the size of the features, which in turn limits the resolution and the miniaturization of the devices. Additionally, the use of highly energetic light sources demands dedicated and specialized facilities and technologies thus the process is extremely expensive. Besides, it is very difficult to adapt the processes to nonplanar surfaces and few materials can be used. In order to solve these problems, or at least address some of them, soft lithography techniques were developed. Soft lithography is a family of techniques for the fabrication or also the replication of structures using stamps, masks or photomasks. It is called soft because it uses elastomeric material (viscoelastic polymers), typically polydimethylsiloxane (PDMS). It allows to construct features of sizes down to the micrometre and nanometer scale without the need for a clean room facility. Compared to photolithography, it is very useful for production of devices at low cost, it is suitable for other materials expanding the electronics field to plastic electronics and for large nonplanar surfaces and the pattern-transferring methods can be widely varied due to more possibilities in the use of the ink. Since it does not depend on a radiation source, a photo-reactive surface is not used anymore and the resolution is not limited by this radiation. As a disadvantage, soft-lithography still relies on manual steps and cannot be implemented as a mass-production technology.

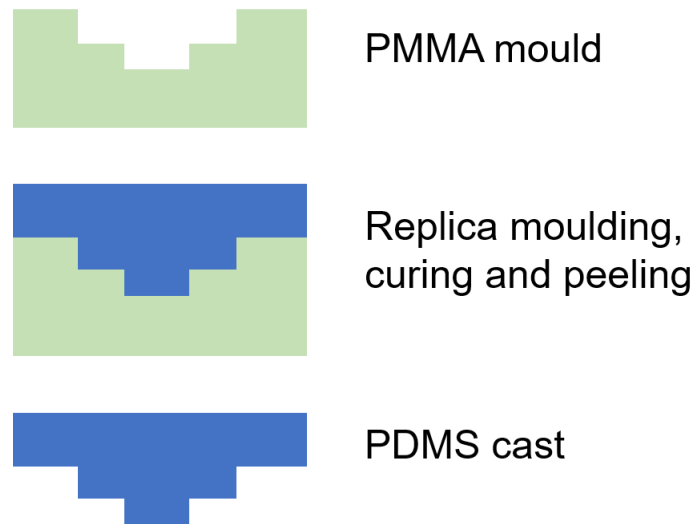


**Figure 3.14: Basic process of replica moulding.** A master mould is created in PMMA using a specified design. PDMS is poured over the mould, cured and peeled off. The removed PDMS obtains the mirrored design of the mould.

A typical fabrication by soft lithography in PDMS is described as follows, which known as **replica moulding**, shown in **Figure 3.14**. A master is fabricated, e.g. by conventional photo-lithography on silicon wafers using SU-8 as resist. Then PDMS replicas are obtained by a simple drop casting process, depositing the PDMS in the liquid form and curing for polymerization (e.g. 20 min at 80°C). After that, PMDS with the corresponding patterns is decasted and bonded on a substrate, e.g a soda-lime glass wafer. This is a very conventional protocol for the production of microfluidic structures, lab-on-a-chip devices and micro-total-analysis systems for its simplicity and low-requirements.

**In this thesis, soft-lithography is used for the fabrication of the  $\mu$ COR device.**

### 3.5.2. Fast prototyping technologies

All the aforementioned methods require a clean room in at least one of their processing steps, significantly adding to the cost and duration of the manufacturing. Fast prototyping refers to techniques that sacrifice precision for a significant increase of speed. These methods are often used to generate prototypes rapidly for basic testing, further enabling the possibility to make quick changes to any of the designs. **Various fast prototyping methods exist, but in this section only the two employed in the thesis are explained.**

**Laser ablation**, also known as photo-ablation, is a process where some material is removed from the surface of a solid (sometimes it can even be a liquid) by irradiating with a laser beam. The material is removed due to the absorption of the energy of the laser beam, resulting in either evaporation or sublimation (when a low laser flux is used) or it is converted to plasma (at high laser fluxes). Lasers of deep UV light are mostly used, usually with a wavelength of 200nm. Typically, laser pulses are used with a duration ranging from milliseconds to femtoseconds, a feature that can be precisely controlled, for a more precise patterning through sublimation (the melting of the material results in less resolute structures). The amount of material removed and the depth of the

incidence of the laser beam (that can lead up to a full cut) depends both on the optical properties of the materials and on the wavelength of the incoming beam, which can also be precisely tuned. Therefore, laser ablation is very useful for research and industrial applications.

**Milling** is a procedure that uses rotatory cutters to mechanically remove material from a solid. It is highly tuneable in several axes directions (x-y plane for horizontal features and z direction for height featuring), with some devices allowing rotation (fourth dimension). The cut features can be controlled by the cutter head turning speed and the applied pressure. Automation in this process allows easy pattern transferring from an original design to the substrate. Milling is sometimes producing some roughness that makes this strategy less convenient in the production of optical components.

**In this thesis, fast prototyping technologies have been used in the fabrication of the gradient generator and opto-fluidic components for the absorbance measurements.**

### 3.6. Bibliography

- [1] A.J. Bard, L.R. Faulkner, *Electrochemical Methods: Fundamentals and Applications*, 2001. <https://doi.org/10.1108/acmm.2003.12850eae.001>.
- [2] K.J. Lee, N. Elgrishi, B. Kandemir, J.L. Dempsey, Electrochemical and spectroscopic methods for evaluating molecular electrocatalysts, *Nat. Rev. Chem.* 1 (2017). <https://doi.org/10.1038/s41570-017-0039>.
- [3] M. Bayareh, M.N. Ashani, A. Usefian, Active and passive micromixers: A comprehensive review, *Chem. Eng. Process. - Process Intensif.* 147 (2020). <https://doi.org/10.1016/j.cep.2019.107771>.





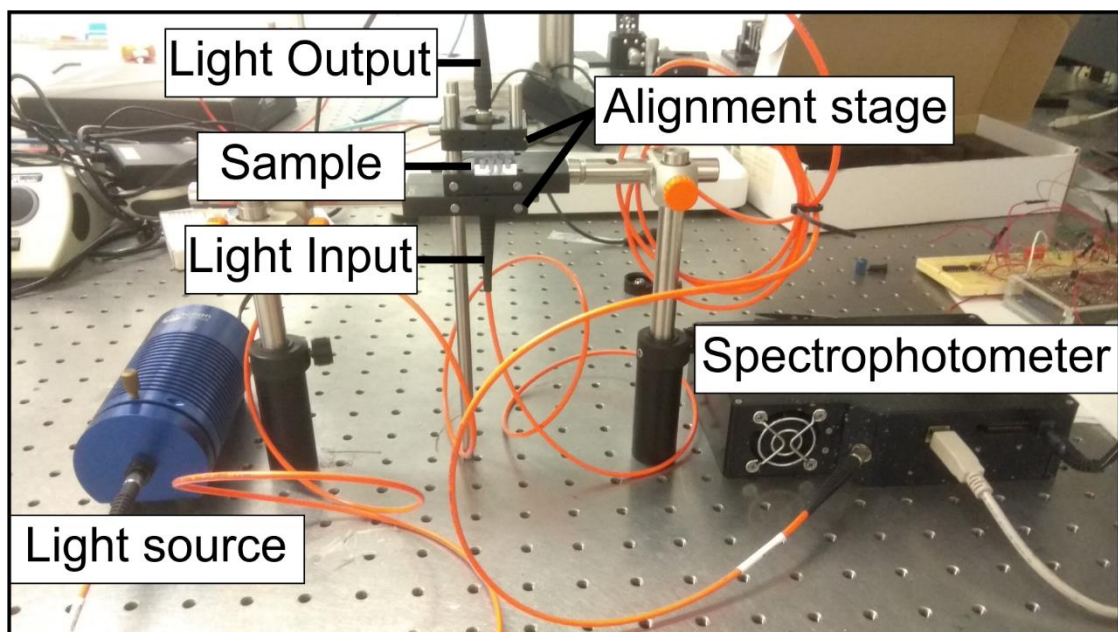
# 4. Objectives

The main objective of this thesis is the development of a novel diagnostic opto-fluidic system for the rapid determination of the minimum inhibitory concentration of antibiotics, an autonomous and standalone device able to provide results within 5 hours. Due to the complexity of the challenge and its multidisciplinary nature, the main objective was divided into three specific objectives as follows:

1. The development of a bioelectrochromic bioassay for rapid antibiotic susceptibility testing (AST), using purified, single strain cultures, with the following characteristics:
  - Being low-cost and providing phenotypic information in real-time of the viability status of the tested strains.
  - Reporting bacterial viability as a simple colour change, enabling detection through optical components.
  - Providing a resistance profile of a purified culture within 5 hours.
2. The production of a fluidic design to enable a standalone device, driven using capillary pumping without the need for external equipment, able to perform the AST test on chip. The capillary driven microfluidic device should be able to manage fluid and to perform sample preparations automatically on chip to minimize biological risk, and with minimal sample and reagents consumption.
3. The development of photonic structures and designs to enable the analysis of multiple optical detection channels, either sequentially or simultaneously, minimizing the instrumental needs of the system, i.e. number of light sources and photo-detectors.



## 5. Materials and methods





## 5.1. Design and Simulation Software

All model designs for the optics and fluidics were made using AutoCAD (Autodesk, California, US). All data related figures were processed using CorelDRAW X7 64bit (Corel Corporation, Canada). Various figures within this thesis were made by the author using the free 3D modelling software Blender (Blender Foundation, Amsterdam, Netherlands). To ensure no copy-right infringement all figures made in blender will have the Blender tag in their title.

### 5.1.1. Design and optical simulations of the $\mu$ COR

AutoCAD (Autodesk, California, US) was used in the design of the microfluidic-controlled optical router, further labelled as  $\mu$ COR. A schematic of the design with each of the components is shown in **Figure 5.1**. It consisted of a single layer integrating all micro-optical and microfluidic elements for in-coupling, guidance and in-coupling/out-coupling of light to four independent optical outputs. Micro-optical elements comprised self-alignment elements for fiber-optics positioning and alignment, pinholes based on liquid to minimize cross-talk between channels, and micro-lens systems for optimal in-coming light confinement and out-coming light collection. Microfluidic components included a fluidic inlet and outlet, micro-chamber, primer phase-guides for fluid management inside the micro-chamber and interconnecting meander-like micro-channels connecting the micro-chambers for a time delay and more robust and repetitive filling of the micro-chambers.

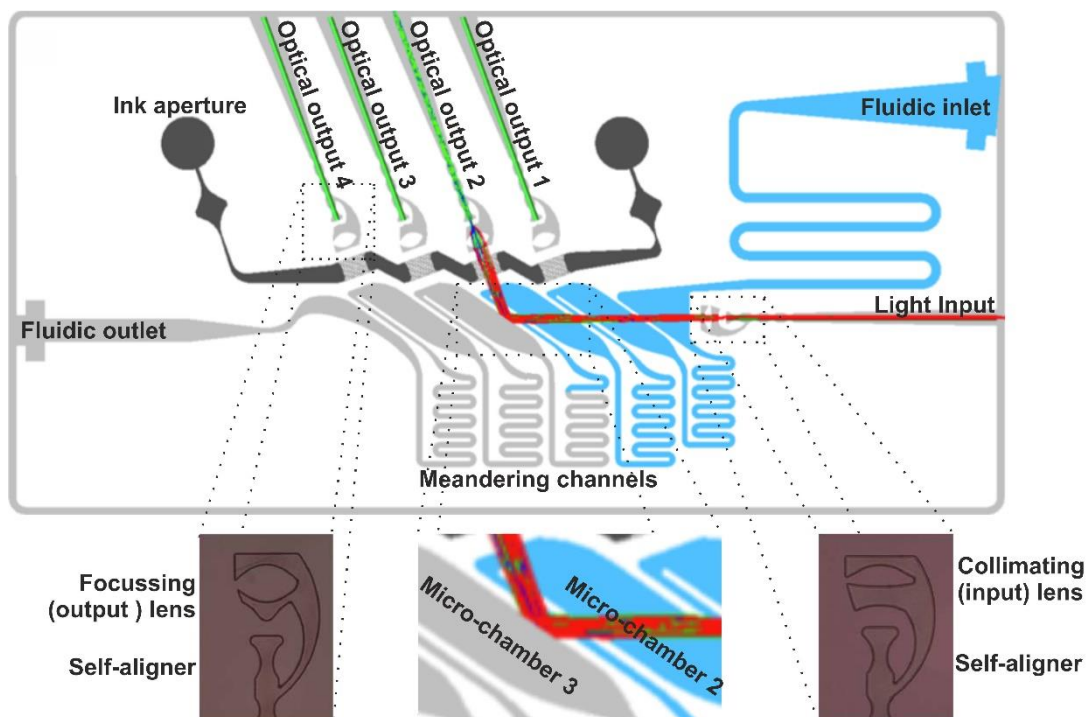


**Figure 5.1: Schematic overview of the optofluidic router and its working principle.** Highlighted in blue is the liquid flow through the device. Shown in red is the light beam coming from the light input until reaching optical output 2. The fibers inserted in the optical outputs are highlighted in green. Shown in black is the ink aperture. The bottom images show the optimized lenses for light focusing (highlighted both sides) and the TIR working principle conditions (center).

To obtain maximum light collection, the input light had to be focused using a collimating input lens. Additionally, light reaching the optical outputs had to be focused again, to ensure a maximum collection at the fiber, by the use of focussing lenses. To optimize the shape of the lenses, a 3D model of the designs of the individual components and the final device were analysed with the TracePro simulation software (Release 7.8, Lambda Research, Littleton, MA, USA). The 3D optimization tool is based on the Downhill-simplex method, which is a commonly applied nonlinear optimization method to find extrema in a multidimensional space. The optimization function was chosen to maximize light collection at typical distances (0-2 cm) considered in the  $\mu$ COR design.

The optical properties of each element in the 3D model were set according to the bibliography, i.e. refractive index and absorption coefficients of PDMS [1,2], water and air [3], corresponding to 1.41, 1.33 and 1 respectively. For consistency with experimental data, ray tracing simulations were performed considering the light source and detector connected to 0.5 m long optical fibers (cladding diameter 125  $\mu$ m; core diameter 105  $\mu$ m; numerical aperture 0.22). The optical power at the end facet of the output fiber is determined, given the same 0.22 NA. Fresnel reflection losses at the various interfaces along the system were considered in the simulation by enabling them at the material and surface properties. Total irradiance values were acquired at 635 nm, to match the laser being used for the characterization, as explained in **Chapter 5.2.1.1**. A total number of rays between 10.000 and 100.000 were analysed in each simulation, which were being emitted from the light source. An example of the simulation of the lenses with 100.000 rays is highlighted in **Figure 5.2**. The colour of each ray corresponded to its intensity, being red the highest, blue intermediate and green the lowest intensity. This figure is included for the reader to understand the method of the ray tracing in the optimization of the lenses. A full discussion of the highlighted image and results can be found in **Chapter 8.2.1**.

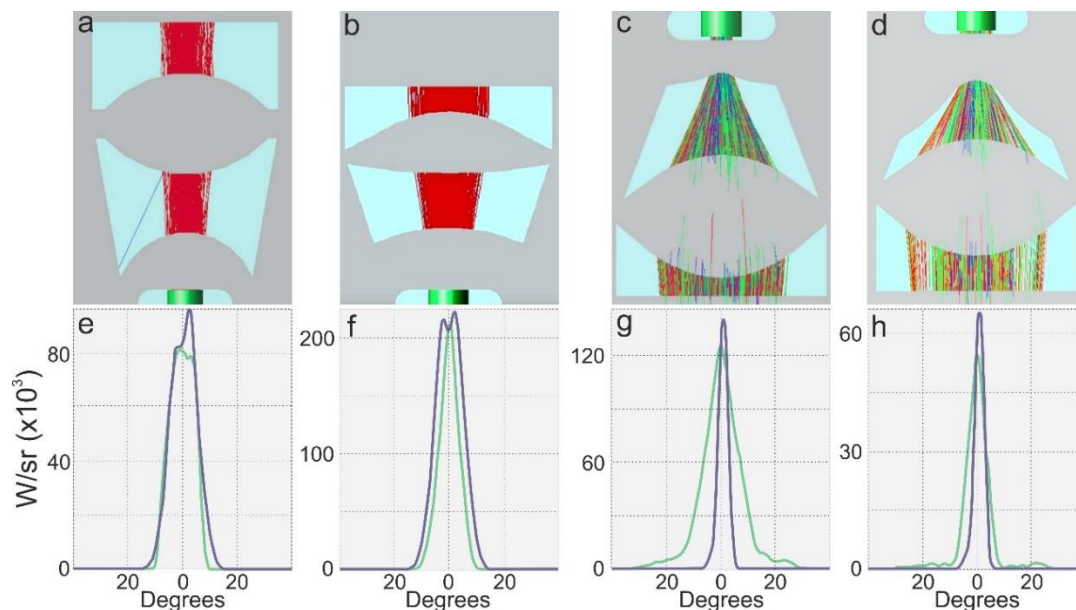


**Figure 5.2: Optimization of the light focusing lenses using Tracepro.** The top row shows the design in tracepro, along with the rays being considered and how they behave through the material. The lower row shows the corresponding candela plots

### 5.1.2. Design and fluidic simulations of the gradient generator

AutoCAD (Autodesk, California, US) was used for the designs of the fluidic channels and the valves of the gradient generator. These designs were utilized in the simulations of the systems using COMSOL (COMSOL Multiphysics® v. 5.4., Stockholm, Sweden). Utilizing the model builder and the “Fluid Flow & Heat Transfer” module. This module included the two-phase flow level set and the two-phase flow phase field methods used in the simulations of the flow behaviour. Each individual parameter utilized and modified in the simulations is highlighted in the corresponding experiment.

Various fluidic components were included in the designs as shown in **Figure 5.3**, with a full description in **Chapter 7.4.5**. Straight and curved channels serving as the capillary flow, serpentine channels for improved mixing of merging liquids, side structures for balancing pressure between channels and preventing backflow, and geometrical valves. Most optimizations were dedicated to the latter, which were designed as a logical AND-valve, where two separate liquids met at the valve and could only propagate past if both are present. COMSOL enabled analysing the fluidic pressure and flow rates, optimizing the designs to enable a 1-1 dilution of both liquids would occur after the valve. Sequential valves would provide a 2-fold dilution of one of the inlet solutions.

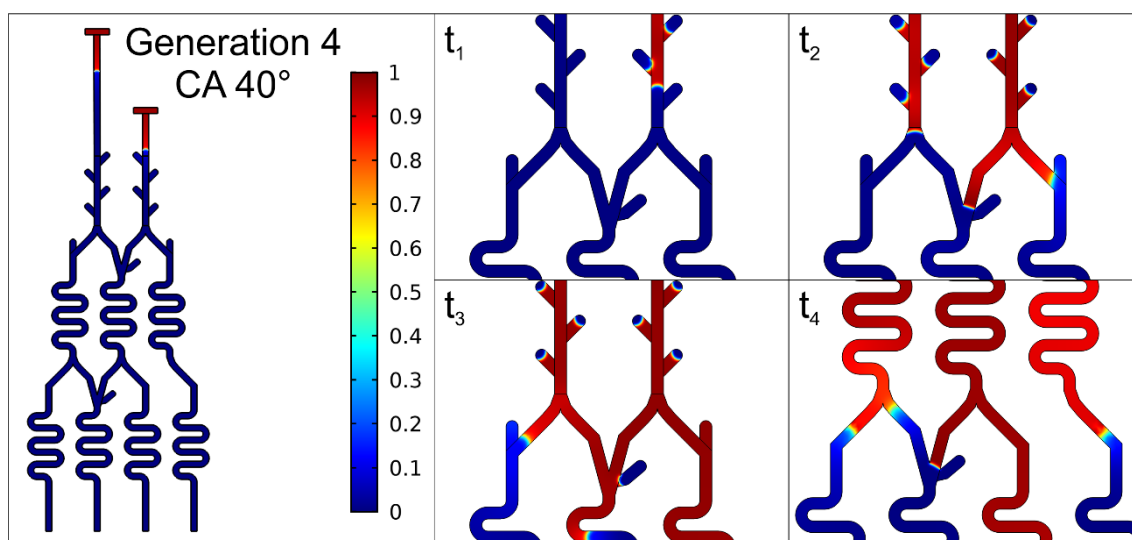


**Figure 5.3: COMSOL simulation of the generation 5 valve, using a symmetric valve and asymmetric inlets.** Highlighted in colour is the liquid-air ratio (red/1 = 100 % liquid, blue/0 100 % air). Images were taken at different times to highlight the collapse at both valves. Included in the figure are the side structures below the inlet to balance the pressure inside, and the serpentine channel to optimize mixing of the liquids.

## 5.2. Materials and Fabrication Methods

Three main materials were employed in the fabrication of the optical, fluidic and optofluidic components of the final system developed in this thesis: (i) polydimethylsiloxane (PDMS); (ii) polymethylmetacrylate (PMMA); and (iii) pressure-sensitive adhesive (PSA).

- **PDMS** was purchased from Sylgard. PDMS preparation was performed following the instructions of the supplier, mixed in a 1:10 proportion (inducer:elastomer) and cured at 80 °C for 20 minutes after air bubbles elimination in the vacuum.



- **PMMA foils** of different thicknesses (i.e. 0.175, 3 and 5 mm) were purchased from Goodfellow.
- The **PSA** adhesive is MA-93 acrylic medical grade. Clear polyester double-sided adhesive tape was purchased from ARcare.

### 5.2.1. Manufacturing of $\mu$ COR by microfabrication technologies

Microfabrication technologies derived from the integrated circuits industry were employed in the fabrication of this micro-system. In the fabrication of the  $\mu$ COR, a soft-lithography protocol in PDMS [4] previously developed in our group [5] was selected for providing the required smoothness in the fabrication of the lenses and channel walls to ensure suitable light coupling and minimal optical losses. The soft-lithographic process was performed in the Clean Room Facilities at IMB-CNM (CSIC). The fabrication protocol involved three main steps: the fabrication of the master, replica moulding and sealing of the system.

A two-level master was fabricated over a 4 inch 100 oriented silicon wafer using the following protocol:

1. Deposition of a seed layer of 5  $\mu$ m of SU8-2005:
  - Plasma treatment for 18 s at 500 W for cleaning the surface
  - Spin SU8-2005 over the wafer for 30 s using the spin coater (Delta 80) at 2400 rpm, without a lid
  - Planarize the spun solution for 5 min, using a glass lid
  - Soft Bake 65 °C to 95 °C in a 10 min ramp-up period, followed by cooling down for 30 min
  - Using a Karl-Suss MA6 mask aligner, expose the bake for 10 s without a mask
  - Post exposure bake (PEB) at 65 °C – 95 °C in a 10 min ramp-up period, followed by cooling down for 30 min
2. Plasma treatment at 500 Watt for 18 s
3. Fabrication of the fluidics using a thickness of 10  $\mu$ m SU8-2005:
  - Spin the SU8-2005 at 2400 rpm for 30 s without a Lid
  - Planarize the spun solution for 10 min, using a glass lid
  - Soft Bake at 65 °C to 95 °C in a 10 min ramp-up period, followed by cooling down for 30 min
  - Using a Karl-Suss MA6 mask aligner, expose the bake for 11 s, using soft contact
  - PEB at 65 °C – 95 °C in a 12 min ramp-up period and cool down for 30 min, followed by 1h of resting
4. Developed in Dev-r 600
5. Hard Bake at 65 °C – 120 °C in a 60 min ramp-up period
6. A planarization layer of 5  $\mu$ m SU8 2005 was added, resting at last 15 hours with cover lid and a little bit of developer to counteract swelling of the SU-8
7. Fabrication of the optical components using 115  $\mu$ m SU8-2050:
  - Spinning of SU8-2050 at 1250 rpm for 30 s, without a lid

- Planarize the spun solution for 25 min, using a glass lid
  - Soft Bake at 65 °C – 95 °C in a 90 min ramp-up period, followed by cooling down for 30 min
  - Using a Karl-Suss MA6 mask aligner, expose the bake for 24 s, using soft contact
  - PEB at 65 °C – 95 °C in a 20 min ramp-up period and cool down for 30 min
8. Fabrication of the Phase-Mirrors using 5  $\mu\text{m}$  SU8-2005:
- Spinning of SU8-2005 at 2500 rpm 30 s, without a lid
  - Planarize the spun solution for 10 min, using a glass lid
  - Soft Bake at 65 °C – 95 °C in a 25 min ramp-up period, followed by cooling down for 30 min
  - Using a Karl-Suss MA6 mask aligner, expose the bake for 24 s, using soft contact
  - PEB at 65 °C – 95 °C in a 20 min ramp-up period and cool down for 30 min
9. Fabrication of the Phase-Primer using 25  $\mu\text{m}$  SU8-2025:
- Spinning of SU8-2025 at 3000 rpm 30 s, without a lid
  - Planarize the spun solution for 20 min, using a glass lid
  - Soft Bake at 65 °C – 95 °C in a 60 min ramp-up period, followed by cooling down for 30 min
  - Using a Karl-Suss MA6 mask aligner, expose the bake for 17 s, using soft contact
  - PEB at 65 °C – 95 °C in a 15 min ramp-up period and cool down for 30 min, followed by 24 h of resting
10. Developed in Dev-r 600
11. Hard Bake at 65 °C – 120 °C in a 90 min ramp-up period

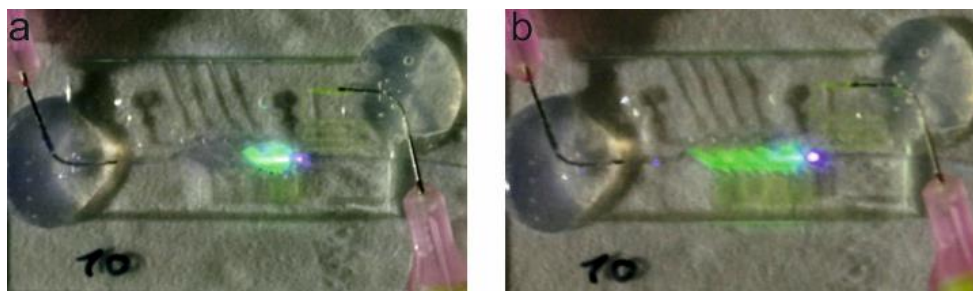


**Figure 5.4: Characterization of the light focusing principle with different micro-chambers being filled with a solution of fluorescein.** Shown in (a) is the reflection of the light towards optical output 2, due to the filling of micro-chambers 1 and 2. Shown in (b) is light being sent through the device, due to the filling of all micro-chambers. Most notable is that the light stops abruptly in (a) due to the TIR at the air interface, whereas full illumination of all micro-chambers is achieved when they are filled with water (b).

PDMS replicas were obtained from the previously prepared master after preparation of the PDMS solution (as indicated by the supplier), deposition on top of the master, planarization for 5 min, introduction into the vacuum chamber to remove air bubbles (15 min) and curing for 20 min at 80 °C. The PDMS replica was decasted from the silicon master and irreversibly bond to a soda-lime glass wafer after solvent-assisted bonding involving: (i) oxygen plasma treatment (500W, 18s); (ii) solvent-assisted alignment of

structures (96% ethanol); and (iii) solvent evaporation and permanent bonding by incubation at 60 °C for 20 min. Finally, the bent metallic needles (lavender Optimum® steel tips, Nordson EFD, Westlake, OH, USA) were assembled in the lateral microfluidic inlet and outlet and sealed with biocompatible silicone rubber glue (RS Components 692-542, Germany). An image of the final system is included in **Figure 5.4**.

#### 5.2.1.1. Optofluidic setup for characterization of the $\mu$ COR

The optical setup used for the characterization of the  $\mu$ COR device is illustrated in **Figure 5.5**. Optical fibers with 125  $\mu$ m cladding and 105  $\mu$ m core (AFS105/125Y, Thorlabs, Dachau, Germany) were stripped, cleaved and inserted into the self-alignment elements using ethanol as a lubricant. A 635 nm-laser source (S1FC635, Thorlabs, Dachau, Germany) was connected to the inlet optical fiber. Outlet fibers were connected to a power-meter (Newport 1931-C, Newport Corporation, Irvine, CA, USA) and spectrometers (QEPro, Flame, Maya; Ocean Optics, Largo, FL, USA) for simultaneous light detection. A NeMESYS syringe-pump was used as the fluidic driver (Cetoni GmbH, Germany). PEEK tubing (Upchurch Scientific) was used to connect to the optical router with a 2.5 mL gas-sealed glass syringe (Hamilton, Switzerland) implemented in the syringe pump and with the waste.

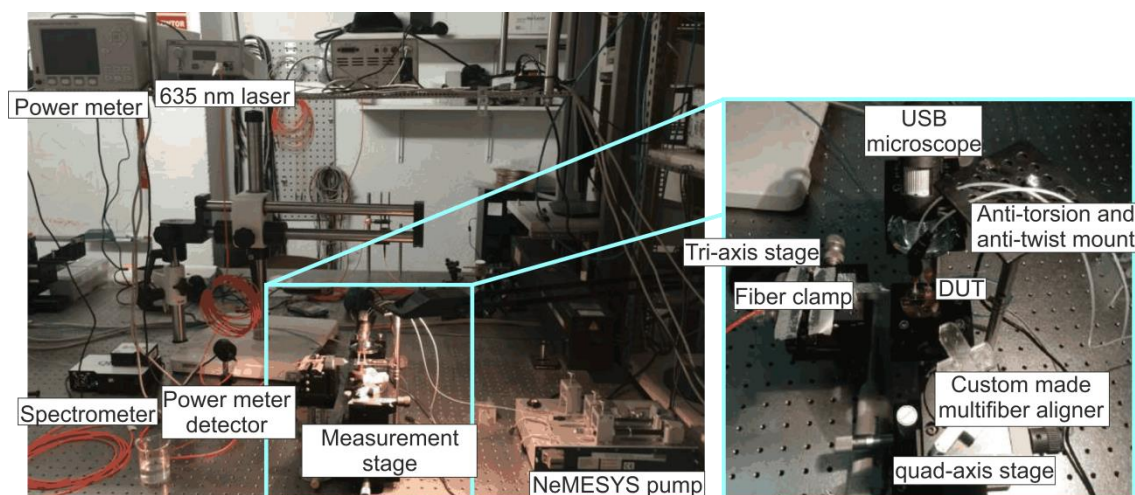


**Figure 5.5: Overview of the optofluidic setup for the characterization of the  $\mu$ COR:** The image left shows the various devices for the control and detection of the measurements. The image on the right is a highlight of the measurement stage with each of the individual connections.

A LabView Virtual Interface (VI) application (National Instruments, for the Austin, TX, EUA) was developed for simultaneous acquisition from multiple light detectors and synchronization of optical recordings with fluidic pumping. The LabView programs were developed by a former master thesis student of the research group, Jeroen Goyvaerts.

- Two programs were developed for the **Newport power meter**: the first program reads out and averages the data on request, and was used for the calibration measurements. The second was a high temporal resolution measurement where the data is first stored internally in the spectrometer before being transmitted towards the computer. For this last program, up to 250k data points can be stored in the power meter, at a maximal resolution of 0.1 ms, resulting in a 25s

long measurement. Though, this was quite intensive, and to compensate either the resolution or the duration (amount of samples) were lowered, depending on the experiment.

- Another was developed for the **spectrometer** family, which was more complicated, as it had to incorporate up to five spectrometers, which all have a maximal time resolution of 8ms. However, due to the speed of the Labview program, this is not attainable in absolute numbers, as all devices have to be called individually, but within the same measurement iteration. Besides the fact that a single wavelength is only compared over time, the entire spectrum is also outputted in every iteration for visual purposes. The devices can be corrected for non-linearity and electronic dark current detection.
- Another Labview program combined the detector with the **neMESYS pump** to calibrate the fluidic flow in the channels to start a measurement. The program was written to fix the problem of the high fluidic volume in the tubes and syringes versus the microfluidic channels in the device. The actual flow-rate in the device is ideally much lower to obtain sufficient large output durations for absorbance measurements. Thus, the program drove the liquid at high speed through the tubes, until the detector, which was coupled to the first channel, measures a light output above a user-chosen threshold. In this way, measurements could quickly start, with the appropriate fluid flow given the desired application.

### 5.2.2. Manufacturing the gradient generator through fast prototyping techniques

Fast prototyping techniques are conceived to manufacture components in a simple and fast manner, thus enabling the optimization of the components with minimal delays during optimization steps.

For the fabrication of the microfluidic components in the gradient generator, a milling machine CNC Roland MDX-40 (Roland, California, USA) was used. AutoCAD designs were loaded directly into the VCarve Pro 9.510 software of the instrument, which enabled a precise control of all milling parameters, including and not limited to: step size, spin rate, feed rate, on or next to the lines of the design, etc. The Roland Vpanel software enabled to override the VCarve software to enable user control of the machine after setting up the parameters. Various double flute end mills were used in the fabrication (details in **Table 5.1**). The larger double flute mills were used for the etching of the surface and the calibration of the PMMA to the milling machine platform. The smaller double flute mills were used for all the millings related to the fluidic chip. All end mills were obtained from DATRON (DATRON Dynamics, California, USA) and their corresponding parameters for the software are detailed below.

**Table 5.1: List of milling heads used in the fabrication of the fluidic designs.** The dimensions are corresponding to the diameter and length of the head of the double flute end mill.

Milling head	Dimensions (mm)	Spin rate (rpm)	Feed rate (mm/min)	Step size (mm)
DATRON 0068605	0.5 x 3.0	4500	60	0.25
DATRON 0068005	0.5 x 2.5	4500	60	0.25
DATRON 0068030A	3.0 x 10	15.000	10	0.10

To individualize each microfluidic chip, they were cut out of the PMMA layer using a laser cutter Epilog Mini 24 – 30 W (EpilogLaser, Colorado, USA). Additionally, the fluidic cover with inlets was also laser ablated using the Epilog laser cutter. All laser-ablated systems were first designed in CorelDRAW X7, which compatible with the Epilog Engraver WinX64 software of the instrument. The optimal conditions for laser ablation depended on the thickness of the PMMA layer and were adjusted accordingly. Optimal conditions are presented in the following table.

**Table 5.2: Parameters used in for laser cutting of various PMMA substrates.** Three variations in thickness were employed in this thesis. The velocity and power percentages are in function of the Epilog Engraver WinX64 software.

Thickness of the PMMA layer	Velocity	Power	Frequency
PMMA 5 mm	5 %	100 %	5000
PMMA 3 mm	5 %	95 %	5000
PMMA 0.175 mm	20 %	15 %	5000

The bonding of both PMMA pieces was performed using various strategies:

- **Semi-reversible bond with double sided PSA:** One side of the PSA cover was removed to adhere it to the PMMA substrate before the milling. This was done to ensure the PSA was following the layout of the fluidic channels. After the milling, the fluidic device was cut out as mentioned above. Finally, the second protective cover was removed, to enable bonding with the fluidic cover.
- **Fully reversible bond with magnets:** After the milling of the fluidic device, the fluidic device was cut out using the Epilog laser cutter, with the addition of six holes placed around the fluidic channels. The cover plate mirrored the position and the size of the holes, in addition to its standard inlets. These holes were designed to hold magnets of 2 mm diameter (S-02-02-N, Supermagnete) in place. To avoid the usage of glue, the holes were cut at an optimized diameter of 1.82 mm. The usage of the magnets enabled a full reversible bond between both plates.
- **Irreversible covalent bonding with methacrylic acid:** The methacrylic acid solution ( $\geq 98.0\%$ , Fluka, Sigma Alrich) was spread over one plate, after which

both were put together into a thermal press, (P.O. Weber, Germany) at 7.5 kN at 70 °C for 30 min.

- **Irreversible bonding with UV curing glue:** The UV curing glue (NOA68, Norland Products, USA) was spread between both plates, held together and exposed to UV (CS2010 UV Curing LED system, 365 nm, Thorlabs) for 30 seconds each site, resulting in a permanent bond.

#### 5.2.2.1. Optofluidic setup for characterization of the gradient generator

For the optical detection of the performance of the gradient generator a custom build setup was used (**Figure 5.6**). Optical fibers with 125  $\mu\text{m}$  cladding and 105  $\mu\text{m}$  core (AFS105/125Y, Thorlabs, Dachau, Germany) were used and positioned facing each other in a vertical alignment. Fibers were kept in place using optical mounts (Thorlabs). The distance between both fibers was set at 1 cm. The fluidic platform was placed on a multi-axis stage (3-axis stage, Thorlabs), to allow precise positioning of the gradient generator. The fluidic platform was kept in place between the multi-axis stage and a flat metal piece using screws, with the fluidic outlets hanging over the edge to enable optical measurements through each of the outlets directly. One optical fiber was coupled to the light source, i.e. a halogen lamp (HL-2000 FHSA, Ocean Optics), and the optical response was registered with the second fiber connected to a QE65000 Spectrometer (Ocean Optics), controlled by the SpectraSuit software (Ocean Optics). Light intensity data was registered in a wavelength range between **400** and **1000** nm, with a boxcar width of **1**, scans to average was set to **3** and an integration time of **100** ms.

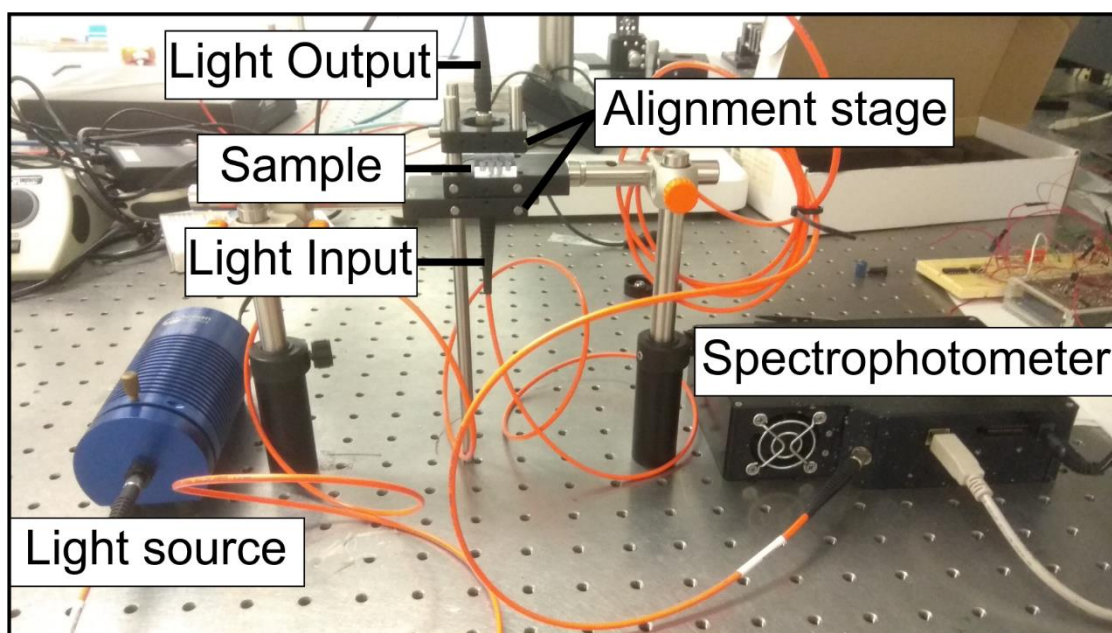


**Figure 5.6: Optofluidic setup for the characterization of the gradient generator.** From left to right, the light source provides the illumination, connected to the system by the light input. The sample, the gradient generator device, is squeezed and aligned using the alignment stage, between the input and output. The inlets were kept outside the cover, to enable filling of the device. The measured light is send to the spectrophotometer for detection.

### 5.2.3. Optical shutter

All electrodepositions and electrochemical characterisations of the NiCl<sub>2</sub> on the ITO for the development of the optical shutter were performed using the Autolab PGSTAT (12/30, Metrohm Autolab, Netherlands). The parameters of the assays were controlled using the NOVA 2.1.4 software (Metrohm Autolab, Netherlands). A typical three-electrode electrochemical cell was used, composed by the ITO electrode as working electrode (WE), a Pt wire as counter electrode (CE) and a Ag/AgCl electrode (SCE) as the reference (RE). The measurements were performed by cyclic voltammetry (CV) in the potential range between 0.2 V and 0.8 V and a scan rate of 50 mV/s. Electrodes were rinsed with distilled water after every measurement. When cleaning of the ITO electrodes was performed, an Ultrasonic bath was used (Branson, Emerson, USA)

FTIR experiments were performed using the Bruker 27 IR spectrophotometer (Bruker, USA), with a wavenumber from 4000 cm<sup>-1</sup> to 600 cm<sup>-1</sup>, to analyse the deposition of the nickel and its corresponding composition. Oxidized and reduced layers were analysed, which were obtained after constant application of the suitable oxidation or reduction potential for 1 minute, using the setup described above.

## 5.3. Reagents and solutions

All chemicals used in this thesis were used as received without additional purification protocols. Solutions were prepared in distilled water (2 MΩ/cm).

Ammonium iron(III) citrate, barium chloride, (99.9 %), Ciprofloxacin (≥98.0 %), D-(+)-Glucose (≥99.5 %), Fluorescein, Fosfomycin disodium salt, Gentamicin Sulfate salt (≥590 µg/mg Potency), methacrylic acid (≥98.0 %), Mueller Hinton Broth 2 (MH) cation adjusted, polypyrrole, Potassium chloride (KCl, ≥99 %), Potassium ferrocyanide (K<sub>4</sub>[Fe(CN)<sub>6</sub>], ≥98.5 %), Sodium Alginate, Sodium chloride (NaCl, ≥99 %), SDS, and sulphuric acid were obtained from Sigma Aldrich.

Ascorbic acid, Calcium carbonate (CaCO<sub>3</sub>, ≥98.5 %), Hydrochloric acid (HCl, 37 %), Iron (II) Chloride, Iron (III) Chloride 6-Hydrate, EDTA, Iron (II) Sulphate, Kanamycin and Potassium hexacyanoferrate (K<sub>3</sub>[Fe(CN)<sub>6</sub>], ≥99 %) were obtained from Panreac, Spain.

Other reagents and product include: Norland Optical Adhesive 68, UV curing glue (NOA68, Norland Products, USA), Prestoblue cell viability reagent (Invitrogen), Propylene glycol methyl ether acetate solution (PGMEA, MicroChem Corp., Newton, MA, USA), Silicone rubber glue (RS Components 692-542, Germany) and SU-8 polymer (MicroChem, Corp., Newton, MA, USA)

The following buffers, solutions and or reagents were prepared as stated below:

**Luria-Bertani (LB)** broth and agar were prepared by mixing 5 g of tryptone, 2.5 g of yeast extract and 5 g of NaCl in 500 mL of miliQ water. For the LB agar, 7.5 g of agar was added.

**Mueller Hinton (MH)** broth was prepared following the instruction of the supplier by mixing 200 g of the mixed reagent in 1000 mL of distilled water. The pH of the medium was lowered to 6.6, using HCl, before autoclaving.

**Alginate 2% w/v** was prepared by mixing 0.5 g of alginate in 25 mL of distilled water. The solution was put on a hot plate at 70 °C for 30 min with stirring, to acquire a homogenous solution.

**0.5 McFarland standard** was prepared by mixing 0.05 mL of 1.0 % barium chloride and 9.95 mL of 1.0 % sulphuric acid. Both solutions were prepared using distilled water.

## 5.4. Electronic components

The following electronic components were used in the fabrication and assembly of the frequency modulator for wavelength selection:

Standard Multicolour LED (3.2 x 2.8 mm 0.06 W SMD type, Multicomp), a Precision, High-Speed Transimpedance Amplifier (OPA380, Burr-Brown Products from Texas Instruments), an ambient light sensor (TEMD6200FX01, Vishay Intertechnology), and a multi CHIPLED® (LRTBR48G, OSRAM Opto semiconductors GmbH).

## 5.5. Bacterial cultures

Bacterial cultures were prepared and manipulated in the Environmental Microbiology laboratory at the Universitat Autònoma de Barcelona (UAB).

*E. coli* (ATCC 25922), *S. aureus* (ATCC 29213), *P. aeruginosa* (ATCC 27853) were donated by the University of Antwerp, from the group of Prof. Herman Goossens. *E. coli* K12 (CGSC 5073) and *Staphylococcus aureus* (ATCC 6538) were provided by the laboratory of Environmental Microbiology, from the group of Prof. Jordi Mas.

The bacterial cultures were prepared in two distinct ways, resulting in either a liquid or solid based overnight cultivation.

*E. coli* K12 (CGSC 5073) and *Staphylococcus aureus* (ATCC 6538) cultures were kept in storage on an LB agar plate at 4 °C. Cultures were grown aerobically for 18 h at 37 °C in LB broth the day before the experiment, by transferring bacteria from the storage plate to the liquid medium using an inoculation loop. The cultivated liquid was centrifuged at 10100 g for 15 min and re-suspended in 0.9% (w/v) sodium chloride. Cell concentration was determined by absorbance measurement at 600 nm and set at 10<sup>9</sup> CFU/mL, which corresponded to an optical density of 1.5 A.U.

*E. coli* (ATCC 25922), *S. aureus* (ATCC 29213), *P. aeruginosa* (ATCC 27853) were grown overnight on an LB agar plate at 37 °C, plated using the standard streaking method. These streaks were taken from plated cultures, stored at 4 °C in the fridge for a maximum of 2 weeks. Upon use, several colonies of bacteria were inoculated into a sterile saline solution (0.85 % NaCl w/v in water) using a cotton swab to obtain an optical density of a McFarland 0.5 standard. The optical density of the 0.5 McFarland standard was determined using a spectrophotometer (Smartspec™ Plus spectro-photometer, Bio-rad, California, US). The bacterial culture was prepared to match the same optical density, 0.160 for this device, which corresponds approximately to 10<sup>8</sup> CFU/mL of bacteria.



After every experiment, a bacterial count was performed to assess the starting concentration. The 0.5 McFarland solution was diluted twice 10 fold, to  $10^7$  CFU/mL and  $10^6$  CFU/mL sequentially in MH. From the  $10^6$  CFU/mL 5  $\mu$ L was put into 5 mL of MH, corresponding to approximately  $10^3$  CFU/mL. 100  $\mu$ L from this final solution was deposited in the middle of an LB agar plate. Using an L-shaped cell spreader (Biologix), the solution was homogeneously spread over the agar surface. The cultured plate was kept for 20 h at 37 °C inside the incubator. After the cultivation the number of colonies was counted manually, supported by a colony counter (Bioblock scientific colony counter 50971, Fisher Scientific).

### 5.5.1. Alginate hydrogels for bacterial-sensing and light routing

Alginate is a biomaterial from natural origin obtained from the brown algae, with *Macrocystis pyrifera* used as alginate source in this work. It is an anionic copolymer composed of homopolymeric blocks of (1-4)-linked  $\beta$ -D-mannuronate (M) and  $\alpha$ -L-guluronate (G) residues. These G-blocks can participate in the intermolecular cross-linking by the presence of divalent/trivalent cations, such as  $\text{Ca}^{2+}$  [6] or  $\text{Fe}^{3+}$  [7], resulting in the formation of a hydrogel. This hydrogel formation can easily be done by mixing alginate with, for example, a calcium-salt solution or iron salt (e.g.  $\text{CaCl}_2$ ,  $\text{FeCl}_3$ ).

Alginate has several important characteristics which make it popular for the use in different biomedical applications, like drug delivery or tissue generation. Its biocompatibility, low toxicity, relatively low-cost and gelation in soft conditions (room temperature, aqueous solution, and physiological pH) enable a versatile utilization ([8]).

In this thesis, alginate-based components have been employed in (i) the production of a **bacterial-sensitive material** for resistant bacteria detection and (ii) the production of **electro-depositable waveguides for light routing**.

### 5.5.2. Bacterial-sensing alginate hydrogels

In the production of bacterial-sensing alginate hydrogels, two strategies were used:

- **Direct gelation:** this process involved the addition of 0.5 mL of 60 M iron (III) chloride solutions to 0.5 ml of 1% sodium alginate samples at room temperature to induce the hydrogel formation. Alginate and iron (III) final concentrations in the hydrogel were 0.5% (w/v) and 30 mM, respectively. For bacterial hydrogel fabrication, 0.2 mL of bacterial suspension ( $10^9$  CFU/mL) in 0.9% (w/v) sodium chloride was mixed with 0.8 mL of 1.25 % alginate solution and gelation was carried out as before. After gelation, the excess liquid was removed and hydrogels were washed 3 times with 0.9% (w/v) sodium chloride to remove non-gelled alginate, residual iron (III) and non-entrapped bacteria (if present).
- **Electrodeposition:** A volume of 0.1 mL of an aqueous solution composed of 0.5 % sodium alginate and 20 mM iron (II) sulphate was dropped on screen-printed carbon electrodes (Dropsens, Oviedo, Spain). The gelling kinetics of iron (II) was much slower than iron (III) and thus hydrogels were not formed in the short time after addition of the sample. To induce gelation, iron (II) ions were oxidized to iron (III) electrochemically, which produced the electron-mediated deposition of

the gel on the electrode surface. This electrodeposition of the hydrogel was achieved by potentiostatic oxidation of iron (II) ions to iron (III) at 1.2 V (vs Ag/AgCl) with a multichannel potentiostat driven by Dropview software (Dropsens, Oviedo, Spain). For bacterial hydrogel electrodeposition, 0.25 mL of a bacterial suspension ( $10^9$  CFU/mL) in 0.9% (w/v) sodium chloride was mixed with alginate and iron (II) sulphate solution, and electrodeposited as before. Prior to hydrogel analysis, excess liquid was removed and hydrogels were washed 3 times with 0.9% (w/v) sodium chloride to remove iron, alginate and bacterial residues.

#### 5.5.2.1. Optical setup for bacterial-sensing analysis

Bacterial-sensing analysis of alginate hydrogels was carried out in an optical setup already reported [9]. The setup consisted of a PMMA cuvette with a 120  $\mu$ L reservoir for alginate hydrogel formation and two 230  $\mu$ m multimode optical fibers (Thorlabs, Dachau, Germany). Optical fibers were located and aligned on both sides of the PMMA structure at a distance of 1.6 cm (which corresponding to the optical path) and respectively connected to the light source, i.e. a halogen/deuterium lamp (DH-2000 UV–VIS–NIR Light Source, Ocean Optics, Florida, US), and to the detector (USB2000 + XR microspectrometer, Ocean Optics, Florida, US). SpectraSuite software (Ocean Optics, USA) was used for data acquisition. Hydrogels were fabricated in situ in the cuvette reservoir by the previous protocol.

#### 5.5.2.2. Protocol for resistant bacteria detection

A kanamycin stock concentration was prepared of 5 g/L in water, of which several dilutions were made to reach a final concentration of 128, 32 and 1 mg/L in each well. Bacterial cultures were cultivated in a liquid medium for an overnight as explained in **Chapter 5.5** for *E. coli* K12. The bacteria were diluted to a concentration of  $10^9$  CFU/mL in a 0.9% (w/v) sodium chloride solution. 0.2 mL of the bacterial solution was mixed with 0.8 mL 1.25 % alginate solution. For the antibiotic testing, 0.5 mL of the antibiotic was mixed with 0.5 mL of the bacteria-alginate solution in each of the wells. After 30 minutes, a 25  $\mu$ L of a 1 mM ferricyanide and 25  $\mu$ L of a 4 mM iron (III) chloride were added to each well to start the hydrogel formation. Results were read out after 20 minutes of hydrogel formation using a microplate reader (Thermo-Fisher) in the range between 400 nm to 800 nm (step size of 10 nm).

#### 5.5.3. Electrodepositable alginate waveguides for light routing

Alginate was selected in this case for: (i) presenting a high transmittance in the visible range (above 90%); (ii) being possible to selective electrodeposit it with precision and spatial resolution; and (iii) presenting a higher refractive index in the hydrogel form than when in solution. Thus, the electrodeposition of the alginate directly produced a polymeric optical component capable to bend or even confine and guide the light (i.e. a waveguide, where the alginate hydrogel is the core and the alginate solution the cladding).

To demonstrate the light routing principle with alginate waveguides, a Dropsens  $\mu$ STAT8000 potentiostat controlled with Dropview 8400 software was used. Both

screen-printed gold (Dropsens, 220BT) and screen-printed carbon electrodes (Dropsens, DRP-11L) were used, with a gold or carbon working and counter electrode and silver as pseudo-reference electrode. Two strategies were employed for the electrodeposition of alginate gels:

- **Irreversible electrodeposition with calcium carbonate:** 0.5 mL of a 2% alginate solutions were mixed with 0.5 mL of a 0.5 % (w/v) calcium carbonate solution to a final concentration of 1 % alginate and 0.25 % (w/v) calcium carbonate. A continuous potential of +1.4 V (vs. Ag/AgCl) was applied for 90 s to generate a hydrogel localized over the working electrode surface due to water splitting and calcium release [10].
- **Reversible electrodeposition with iron chloride:** 0.5 mL of a 2 % alginate solutions were mixed with 0.5 mL of a 50 mM iron (II) chloride to a final concentration of 1 % alginate and 25 mM iron chloride. A potential of 1 V was applied for 5 min to generate a hydrogel localized over the working electrode surface due to iron (II) oxidation to iron (III). Subsequent hydrogel disaggregation was achieved by reducing iron(III) ions by applying -1 V for 20 min.

#### 5.5.3.1. Optical setup for evaluation of light routing with alginate waveguides

Light routing with alginate hydrogels was studied with the custom-made optical setup. It consisted of two optical fibers with 230  $\mu\text{m}$  cladding and 200  $\mu\text{m}$  core (AFS200/230Y, Thorlabs, Dachau, Germany), which positioned aligned on top of working electrode and held in place by custom-made fiber alignment tools, at the location where the alginate hydrogel will be formed. Optical fibers were mounted on multi-axis stages (3-axis stage, Thorlabs), which allowed precise control and maintenance of the relative heights and angles of the two fibers. The input fiber was connected to a red laser light source (Fiber coupled laser source, S1FC635, 635 nm, 2.5 MW, Thorlabs), with the output fiber connected to the detector (USB2000 + XR microspectrometer, Ocean Optics, Florida, US). SpectraSuite software (Ocean Optics, USA) was used for data acquisition.

## 5.6. Silk-based capillary substrates

Silk fibroin (SF) was supplied by the group of Prof. Jose Luis Cenis at the Instituto Murciano de Investigación y Desarrollo Agrario y Alimentario (IMIDA, Murcia, Spain). They obtained silk from the cocoons of *Bombyx mori* silkworms. The silk was obtained by boiling pieces of the cocoon of around 5 g in 0.02 M  $\text{Na}_2\text{CO}_3$  for 30 min. With this process, sericine was solubilized and separated from fibroin, which remained insoluble. Fibroin was then dissolved in 9.3 M LiBr for 3 h at 60 °C to generate an aqueous fibroin solutions containing between 7-8% w/v fibroin. To concentrate the fibroin solution, two strategies were used:

- **Dialysis:** Silk-fibroin solutions were dialyzed against distilled water for 3 days (Snakeskin Dialysis Tubing 3.5 kDa MWCO, Thermo Scientific, USA) resulting in a 20% w/v fibroin solution. Distilled water was exchanged twice every day.

- **Evaporation:** The previously purchased purified 7-8 % w/v SF solution was concentrated to 10% w/v by water evaporation, maintaining the solution in a 3.5 kDa dialysis tube within a dry atmosphere and controlling the weight loss.

#### 5.6.1. Setup for freeze-drying silk substrates

Freeze-drying silk was performed using a custom-made setup consisting of a vacuum pump, vacuum chamber and freezer. In short, concentrated silk 8 % w/v was poured in a petri dish and put inside a vacuum chamber, attached to a vacuum pump (Electric vacuum pump, single stage, Arbor Scientific, US). For the patterning, the liquid silk solution was poured over the PDMS structure. The vacuum chamber was placed inside a freezer at -20 °C for the duration of the experiment, usually 12 – 20 hours, with the vacuum pump allowing pressures down to 5 Pa. After the freeze-drying, the silk was peeled off the PDMS using tweezers.

#### 5.6.2. Setup for the production of silk-based spiral components

Silk fibroins were tried to test the potential of self-assembly into micro-springs, based on an experiment using bevel-tip needles for the generation of hydrogel microsprings [11]. Using 0.4 mm inner diameter and 30° angled bevelled needles (22 gauge, Metal Hub needle, point style 4, Hamilton), the pumping of silk will lead to an anisotropic dehydration when exposed to a hygroscopic solution. This anisotropic exposure will lead to the one side of the silk gelating at a faster rate than the other side, resulting in the self-assembly into spring-like structures. Silk spiral experiments were performed by concentrating the silk up to 7.2 % w/v using dialysis. A bath of hygroscopic liquid was prepared in three variations: 80 % methanol with water, 80 % methanol with 20 % glycerol in water and 100 % methanol. Concentrated silk 7.2% w/v was collected into a syringe (20 mL, Hamilton) and placed inside an infusion syringe pump (NE-300 Micrux technologies). The syringe was connected to a Teflon tube equipped with a bevelled metal needle (0.4mm, Hamilton) either with or without Teflon coating or using PTFE tube tips (inner diameter of 300 µm). The fluidic tip was inserted inside the hygroscopic liquid with a flow rate between 20 µl/min and 500 µl/min (20, 50, 100, 200 and 500 µl/min) to find the optimal flow rate for each condition. A schematic setup is highlighted in **Figure 5.7** below.

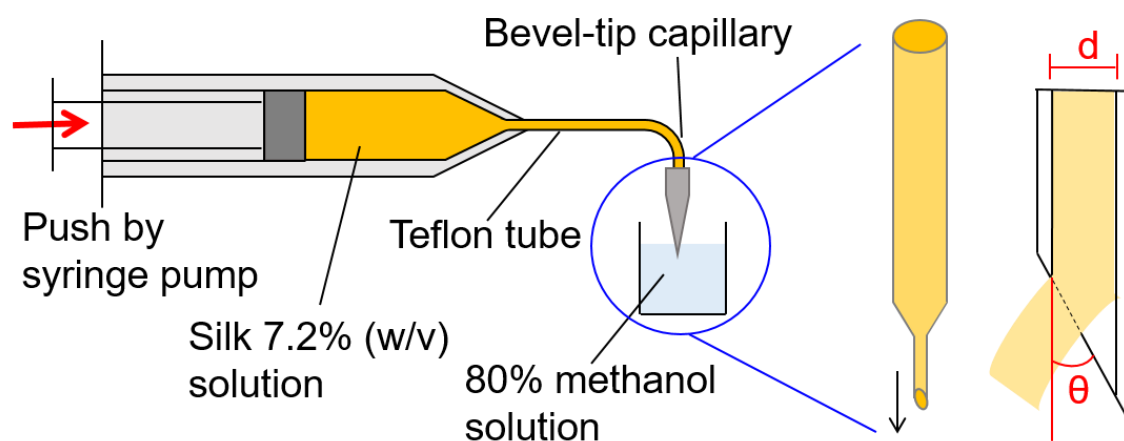


**Figure 5.7: Schematic showing the setup and working principle of the generation of silk microspheres.** A silk solution is continually pushed inside the methanol solution by means of a syringe pump. A bevel tipped capillary with a diameter  $d$  and bevel angle  $\theta$  are used to automatically generate the sphere when the silk comes in contact with the methanol due to anisotropic dehydration. Design is based on the figure from the work of Yoshida and Onoe [11].

### 5.6.3. Characterization of silk substrates

In the characterization of silk substrates three imaging techniques were used: (i) **optical microscopy** for the determination of the flow rate of the films; (ii) **fluorescence microscopy**; and (iii) **scanning electron microscopy (SEM)** for characterization of the structure and morphology of the substrates.

For the determination of the flow rate, silk was doped with various enzymes. Aqueous 20 % (w/v) silk solution was mixed with 25  $\mu\text{g}/\text{mL}$  glucose oxidase, 60  $\mu\text{g}/\text{mL}$  horseradish peroxidase and 90  $\mu\text{g}/\text{mL}$  ABTS. The mixed solution was then crystallized after drying and vacuum annealing, resulting in crystalline silk fibroin films of about 10  $\mu\text{m}$  thick. Crystalline film was placed inside a petri dish (90 mm, Fisher scientific), with a camera (Digimicro 2.0 Scale, Conrad) positioned above. A drop (200  $\mu\text{L}$ ) of 10 mM glucose solution was positioned near one edge of the silk film. Upon contact, the droplet will be pulled inside the silk film through capillary force, and the rate of transport of the silk was measured. Furthermore, the usage of glucose further allowed analysis of the rate of the reaction of the present enzymes through the colorimetric reaction.

The fluorescence microscopy experiments were used to analyse the freeze-drying and patterning experiments. The setup consisted of a Nikon microphot-FXA fluorescence microscope (Nikon, Japan), powered by a mercury lamp. The microscope was equipped with various filters for analysing the sample:

- G-1B, DM580:
  - excitation filter wavelengths: 541-551 nm (bandpass, 546 CWL)
  - Dichromatic Mirror Cut-on Wavelength: 580 nm (longpass, LP)
  - Barrier Filter Wavelengths (emission): 590 nm cut-on (longpass, LP)
- FITC:
  - excitation 465-495 nm
  - mirror cut-on 506 nm

- emission 515-555 nm
- DAPI:
  - excitation 340-380 nm
  - mirror cut-on 409 nm
  - emission 435-485 nm

For the SEM imaging, a Gemini Ultra 55 (Zeiss, Germany) was used, with an EHT of 1.00 kV, working distance between 2.7 and 6.7 mm, and a magnification between 104 x and 1170 x, depending on the image, which was highlighted in each image.

## 5.7. Iron-based metabolic indicators for bacterial detection and minimal inhibitory concentration determination

Three different strategies for bacterial detection and minimal inhibitory concentration (MIC) determination were evaluated, all of them based on the use of iron-based metabolic indicators: (i) **direct ferricyanide reduction**, (ii) **metabolic production of Prussian Blue (PB)** and (iii) **metabolically-mediated cyanotyping process**. The composition of the bacterial sensing solutions and the protocols for bacterial detection and MIC determination are detailed below.

### 5.7.1. Composition of metabolic indicator precursor solutions

The precursor solution composition depended on the bacterial sensing strategy (after optimization):

- **Direct ferricyanide reduction:** In this case, the precursor solution only contained 4 mM ferricyanide in Mueller Hinton cation adjusted broth 2 (MH), the conventional medium for MIC testing.
- **Metabolic production of PB:** The Prussian blue precursor solution contained 16 mM ferricyanide and 4 mM iron (III) chloride, which were suspended in MH broth.
- **Metabolically-mediated cyanotyping process:** The cyanotyping precursor solution contained ferricyanide and ferric ammonium citrate in MH broth. The composition of the precursor solution was optimized in the thesis analysing ferricyanide concentrations in the range between 0.625 and 2.5 mM and ferric ammonium citrate concentrations between 2.5 and 10 mM. Optimal composition was finally set at 0.625 mM ferricyanide and 2.5 mM ferric ammonium citrate.

### 5.7.2. Determination of live bacterial concentration

The viability assays were performed in 96-well plates (Cellculture microplate 96 well, PS, U-bottom, Cellstar), with the optical measurements carried out using a microplate reader (Thermo-Fisher) in the range between 400 nm to 800 nm (step size of 10 nm) and with measurements being performed every hour. The microtiter plate was kept at 37 °C inside an incubator. The process was a variation of the standard broth microdilution protocol [12], as defined by EUCAST and varied a little depending on the assay.

In the case of ferricyanide and PB formation, the 0.5 McFarland bacterial concentration was sequentially diluted 10-fold twice in MH, resulting in a concentration of  $10^6$  CFU/mL. The bacterial culture and precursor solutions were then transferred to the 96-well plate, for a total of 100  $\mu$ L, in a 2-1 ratio (bacteria-precursor) resulting in a final bacterial concentration of  $5 \times 10^5$  CFU/mL, and a 1/4 dilution of the precursor solution.

Conversely, for cyanotyping-based assays, the bacterial culture and reagents were transferred to the 96-well plate, for a total of 200  $\mu$ L, composed of 100  $\mu$ L bacteria, 50  $\mu$ L MH, and 25  $\mu$ L of each precursor, resulting in a final concentration of 0.625 mM and 1.25 mM respectively for ferricyanide and ferric ammonium citrate. The microtiter plate was kept at 37 °C inside an incubator, which contained a white LED lamp (Matel 6400 K, 15 W 1500 lumen) to enable homogeneous and constant illumination to the sample from above. The sample was kept inside the illumination chamber in between measurements. The total illumination time was 5 hours, after which the plate was kept inside the heated microplate reader for the sequential 19 hours with automatic measurements every hour.

### 5.7.3. MIC testing

Minimum inhibitory concentration testing was based on the standardized broth microdilution (BMD). First, a stock solution of the antibiotic of at least 1000  $\mu$ g/mL (or 10 times the highest concentration to be tested) was prepared in distilled water. The stock solution was then diluted into vials to produce a two-fold dilution series with concentrations twice as high as those of the final test. These solutions could be either stored for future use (at -20 °C) or inoculated in the microtiter plate.

The second solution was bacterial suspension. Bacteria were prepared as explained before, matching the 0.5 McFarland standard (**Chapter 5.5**). Bacterial suspension was diluted twice 10-fold and transferred to the microtiter plate within 15 minutes of preparation to avoid changes associated to bacterial proliferation. The bacterial concentration in the well after mixing with the antibiotics was  $5 \times 10^5$  CFU/mL. Plates were finally incubated at 37 °C for 16 to 20 hours and examined visually.

MIC tests with iron-based metabolic indicators, i.e. ferricyanide, PB and cyanotyping, follow the standard BMD test with the following variations:

- The final volume inside the wells was increased to 200  $\mu$ L.
- The final bacterial concentration was further halved to enable addition of the precursor solutions.
- During the first 5 hours of incubation the microtiter was measured every hour. In the case of cyanotyping, the microtiter plate was continuously illuminated to benefit photo-catalysis.
- After these 5 hours, the plate was kept inside the incubator at 37 °C for the rest of the overnight.
- The final MIC value was determined visually after 24 hours, to match the EUCAST standards and ensure reliability of the results.

All variation of the various assays compared to the standard BMD are summarized below.

**Table 5.3: Summary of the variations of the performed assays** compared to the standard broth microdilution MIC test (BMD MIC), with the BMD, Prussian blue and cyanotyping using MH as matrix. FeCN = potassium ferricyanide, citrate = ferric ammonium citrate, blood = cyanotyping assay performed in blood matrix.

Assay type	Final volume ( $\mu\text{L}$ )	Starting bacterial concentration (CFU/mL)	Illumination	Colorimetric precursors
<b>BMD MIC test</b>	100	$5 \times 10^5$	No	None
<b>Prussian blue</b>	200	$2.5 \times 10^5$	No	25 $\mu\text{L}$ of FeCN 25 $\mu\text{L}$ of iron (III) chloride
<b>Cyanotyping</b>	200	$2.5 \times 10^5$	5 h	25 $\mu\text{L}$ of FeCN 25 $\mu\text{L}$ of citrate
<b>Blood</b>	200	$2.5 \times 10^5$	5 h	25 $\mu\text{L}$ of FeCN 25 $\mu\text{L}$ of citrate

#### 5.7.3.1. Spectro-electrochemical analysis of cyanotyping-based protocol.

To elucidate the chemical mechanism behind the cyanotyping-based protocol, spectro-electrochemical analysis of cyanotyping samples was performed where electrochemical and optical properties of the samples were recorded simultaneously.

For optical measurements, a UV-Vis-NIR Deuterium-Halogen Lamp (DH-2000-BAL, Mikropack) was used as light source and the optical response was registered with a QE65000 Spectrometer (Ocean Optics), controlled by the software of the same brand. Spectrochemical measurements were performed in an optically transparent quartz cuvette with an optical path length of 3 mm. Light intensity data was registered in a wavelength range between 460 and 910 nm, with a boxcar width of 1, scans to average was set to 3 and an integration time of 4s. The intensity recorded for the distilled water was used as reference to obtain absorbance values.

Electrochemical analysis was performed with a  $\mu\text{AUTOLAB}$  (Type III)/FRA2 potentiostat (Metrohm Autolab B.V, Netherlands). A typical three-electrode electrochemical cell was used, composed by 1 mm Platinum (Pt) electrode as working electrode (WE), a Pt wire as counter electrode (CE) and a saturated calomel electrode (SCE) as the reference (RE). The measurements were performed by cyclic voltammetry (CV) in the potential range between 0.2 V and 0.6 V and a scan rate of 50 mV/s. Electrodes were rinsed with distilled water after every measurement.

In spectro-electrochemical analysis, samples containing  $10^8$  CFU/mL, 0.625 mM ferricyanide and 2.5 mM ferric ammonium citrate were prepared in MH broth. The bacterial detection protocol resembled that reported in **Chapter 5.7.2** but with 2 differences:



- Samples were prepared in MH and LB broth for comparing the two most common culture media.
- The volumes were adjusted to 40 mL for the need of high volumes for the analysis.

The protocol employed in the spectro-electrochemical analysis was the following. The samples were prepared and introduced in an incubator at 37 °C, where maintained for the duration of the experiment. Inside the incubator, samples were continuously irradiated with a white LED lamp to start photo-catalysis, although twin controls were run simultaneously without light irradiation. Every hour, 2 mL were taken for optical measurements, and 5 mL for cyclic voltammetry. The tested liquids were discarded after use. Measurements continued for a total of 5 hours, after which the samples were kept in dark inside the incubator. The following samples were also analysed as controls, either irradiated or in the dark:

- Medium alone (MH and LB).
- Medium with ferricyanide (0.625 mM).
- Medium with ferric ammonium citrate (2.5 mM).
- Medium with ferricyanide (0.625 mM) and ferric ammonium citrate (2.5 mM).
- Medium with bacteria ( $10^8$  CFU/mL *E. coli*).
- Medium with ferricyanide (0.625 mM) and bacteria ( $10^8$  CFU/mL *E. coli*).
- Medium with ferric ammonium citrate (2.5 mM) and bacteria ( $10^8$  CFU/mL *E. coli*).
- Medium with ferricyanide (0.625 mM) ferric ammonium citrate (2.5 mM) and bacteria ( $10^8$  CFU/mL *E. coli*).

## 5.8. Real samples

The cyanotype-based reaction was analysed using two different matrices, blood (Pig's blood, donated by Department of Basic Science at Universitat Internacional de Catalunya) and serum (Human serum, heat inactivated, Sigma Aldrich), serving as the stepping-stone towards clinical samples. Experiments performed were identical to those described in **Chapter 5.7.2**. Bacteria were prepared in MH to a 0.5 McFarland concentration, corresponding to  $10^8$  CFU/mL, followed by a 10-fold dilution in MH to  $10^7$  CFU/mL. The latter was diluted 10-fold using the corresponding matrix, serum or blood, to a final concentration of  $10^6$  CFU/mL. Further dilutions were performed using the same matrix. The cyanotype precursors were prepared using blood as the matrix, replacing the MH as described in **Chapter 5.7.1**. The final volumes and duration of illumination are highlighted in **Table 5.3**.

The pH of the serum was measured and adjusted using HCl before each experiment, providing final values of 6.6, 6.1 and 5.5 respectively. The pH of each of the experiments was analysed after each experiment too.

## 5.9. Data treatment and statistics

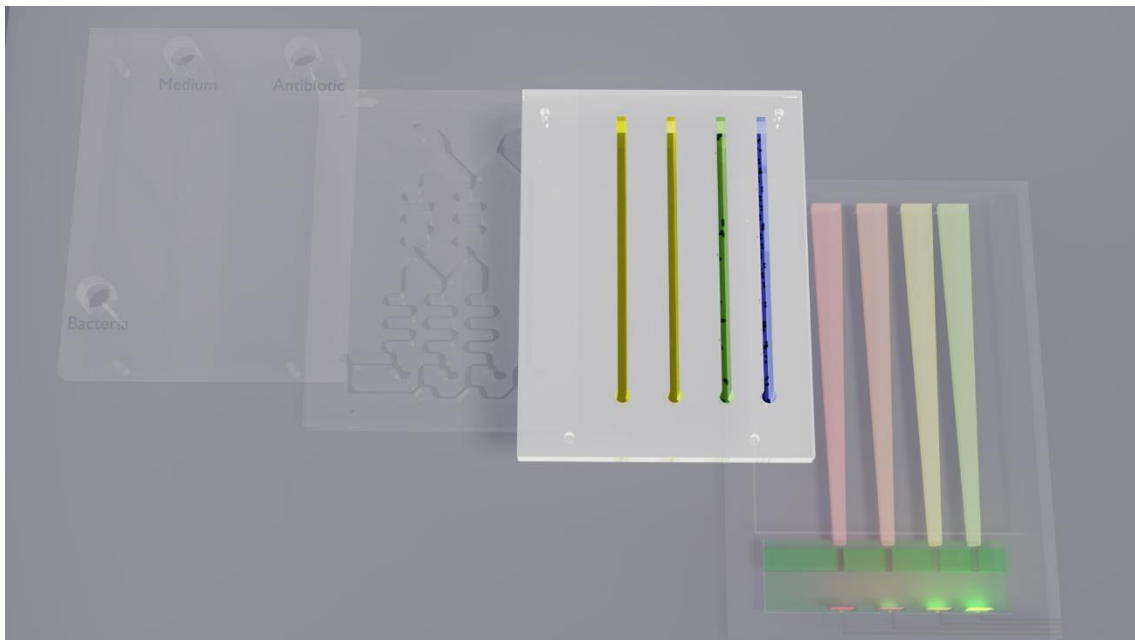
All data were plotted using Origin 2019 64 bit (OriginLab, Massachusetts, USA). Statistical analysis was performed through the GraphPad Prism (GraphPad Software, California, USA) which has the t-tests and two-way ANOVA modules implemented.

## 5.10. Bibliography

- [1] T. Roychowdhury, C. V. Cushman, R.A. Synowicki, M.R. Linford, Polydimethylsiloxane: Optical properties from 191 to 1688 nm (0.735–6.491 eV) of the liquid material by spectroscopic ellipsometry, *Surf. Sci. Spectra*. 25 (2018) 026001. <https://doi.org/10.1116/1.5046735>.
- [2] M.C. Bélanger, Y. Marois, Hemocompatibility, biocompatibility, inflammatory and in vivo studies of primary reference materials low-density polyethylene and polydimethylsiloxane: A review, *J. Biomed. Mater. Res.* 58 (2001) 467–477. <https://doi.org/10.1002/jbm.1043>.
- [3] A. Llobera, V.J. Cadarso, K. Zinoviev, C. Domínguez, S. Büttgenbach, J. Vila, J.A. Plaza, Poly(Dimethylsiloxane) waveguide cantilevers for optomechanical sensing, *IEEE Photonics Technol. Lett.* 21 (2009) 79–81. <https://doi.org/10.1109/LPT.2008.2008659>.
- [4] Y.N. Xia, G.M. Whitesides, Soft lithography, *Annu. Rev. Mater. Sci.* 37 (1998) 551–575. <https://doi.org/10.1146/annurev.matsci.28.1.153>.
- [5] X. Muñoz-Berbel, R. Rodríguez-Rodríguez, N. Vigués, S. Demming, J. Mas, S. Büttgenbach, E. Verpoorte, P. Ortiz, A. Llobera, Monolithically integrated biophotonic lab-on-a-chip for cell culture and simultaneous pH monitoring., *Lab Chip*. 13 (2013) 4239–47. <https://doi.org/10.1039/c3lc50746g>.
- [6] M. Bruchet, A. Melman, Fabrication of patterned calcium cross-linked alginate hydrogel films and coatings through reductive cation exchange, *Carbohydr. Polym.* 131 (2015) 57–64. <https://doi.org/10.1016/j.carbpol.2015.05.021>.
- [7] G.E. Giammanco, C.T. Sosnofsky, A.D. Ostrowski, Light-responsive Iron(III)-polysaccharide coordination hydrogels for controlled delivery, *ACS Appl. Mater. Interfaces*. 7 (2015) 3068–3076. <https://doi.org/10.1021/am506772x>.
- [8] A.D. Augst, H.J. Kong, D.J. Mooney, Alginate Hydrogels as Biomaterials, (n.d.). <https://doi.org/10.1002/mabi.200600069>.
- [9] D. Sanahuja, P. Giménez-Gómez, N. Vigués, T.N. Ackermann, A.E. Guerrero-Navarro, F. Pujol-Vila, J. Sacristán, N. Santamaria, M. Sánchez-Contreras, M. Díaz-González, J. Mas, X. Muñoz-Berbel, Microbial trench-based optofluidic system for reagentless determination of phenolic compounds, *Lab Chip*. 15 (2015) 1717–1726. <https://doi.org/10.1039/c4lc01446d>.
- [10] A. Márquez, J. Aymerich, M. Dei, R. Rodríguez-Rodríguez, M. Vázquez-Carrera, J. Pizarro-Delgado, P. Giménez-Gómez, Á. Merlos, L. Terés, F. Serra-Graells, C. Jiménez-Jorquera, C. Domínguez, X. Muñoz-Berbel, Reconfigurable multiplexed point of Care System for monitoring type 1 diabetes patients, *Biosens. Bioelectron.* 136 (2019) 38–46. <https://doi.org/10.1016/j.bios.2019.04.015>.

- [11] K. Yoshida, H. Onoe, Functionalized core-shell hydrogel microspheres by anisotropic gelation with bevel-tip capillary, *Sci. Rep.* 7 (2017) 1–9. <https://doi.org/10.1038/srep45987>.
- [12] CLSI, M24-A2 Susceptibility Testing of Mycobacteria, Nocardiae, and Other Aerobic Actinomycetes; Approved Standard-Second Edition A standard for global application developed through the Clinical and Laboratory Standards Institute consensus process, 2011. [www.clsi.org](http://www.clsi.org). (accessed November 4, 2020).

# 6. Bioassay





Colorimetric assays for bacterial detection and susceptibility testing rely on the capacity of bacterial metabolism to reduce the target electrochromic reagents, whereupon the reduction is accompanied by a change of colour. When incubated with a bacterial sample, the rate of colour change or the absolute colour at a fixed time indicates the amount of viable bacteria present. Even though the exact reaction is under debate, it is most likely related to the oxidation-reduction reactions occurring over the proteins present in the inner cell membrane responsible of the bacterial metabolism. The most commonly used colorimetric products are resazurin and its derivatives Alamar Blue and Presto Blue [47]. They were commercialized for fluorescence measurements originally, but can double as colorimetric reagents as well. Colorimetry has the high advantage of being easily compatible with standard broth microdilution technology, requiring only the addition of the corresponding reagents, and being able to monitor the change of colour with spectroscopic instrumentation already implemented in most of microbiology laboratories. Furthermore, these reagents can often be immobilized and dried before the assay, further reducing manual work and enabling automation. The main limitation of colorimetric products is on their low specificity, leading to potential cross reaction with other redox compounds, like antibiotics or media components.

**In this thesis, colorimetric assays for antibiotic susceptibility testing were developed using various iron-based reagents.** The progress scheme for the development of these bioelectrochromic assays is illustrated below.

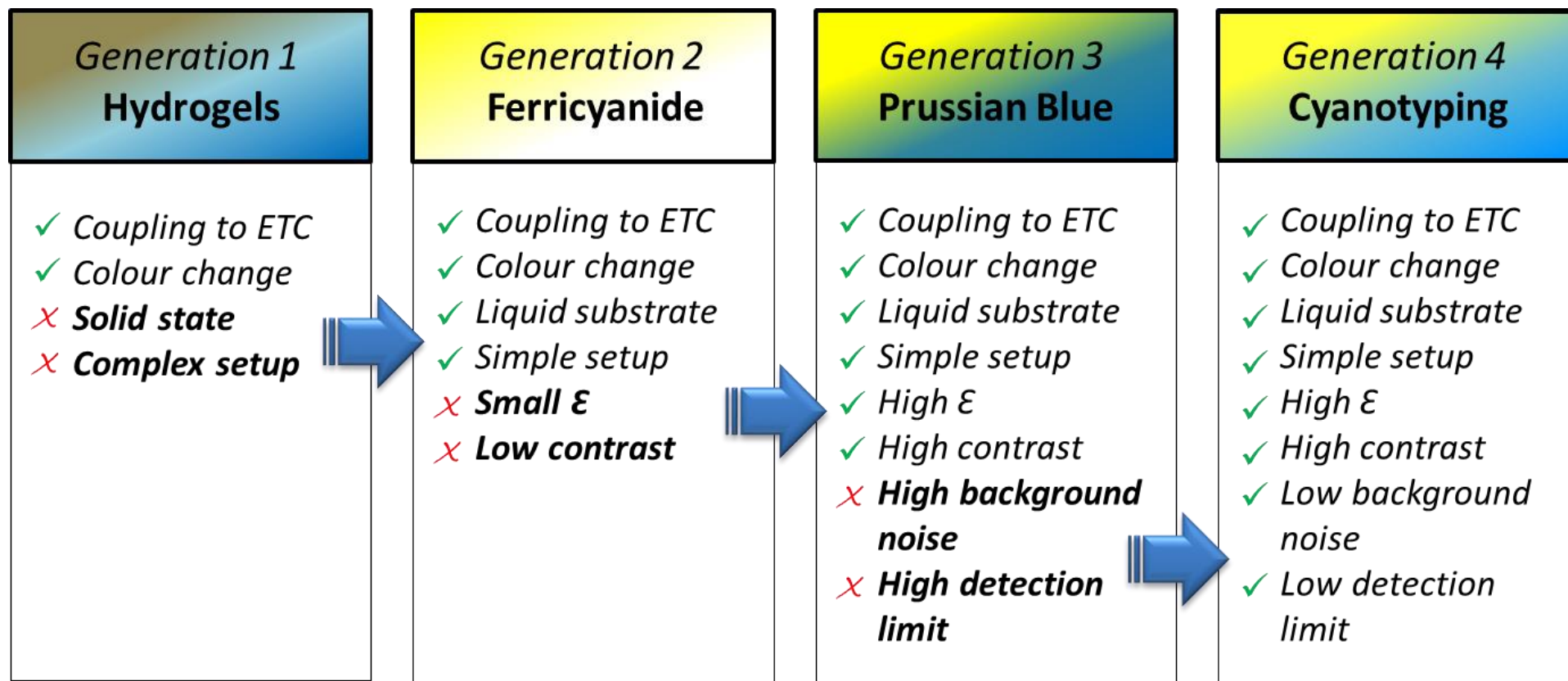


**Figure 6.1: Scheme of the continuity of the various generation of the bioassay under development.** Each generation is a continuation of the previous one, overcoming one or more of each's drawbacks. The description, experiments and corresponding results are disclosed in a separate dedicated chapter below. ETC = electron transfer chain,  $\epsilon$  = extinction coefficient.

## 6.1. Bioelectrochromic hydrogel for fast antibiotic-susceptibility testing

This section, relying on the production of electrochromic hydrogels sensitive to bacterial metabolism, was performed in collaboration with Prof. Jordi Mas and Dr. Ferran Pujol from the Universitat Autònoma de Barcelona.

Materials science offers new perspectives in the clinical analysis of antimicrobial sensitivity. However, a biomaterial with the capacity to respond to living bacteria was never reported before. In this first chapter an electrochromic iron(III)-complexed alginate hydrogel was developed, sensitive to bacterial metabolism, further applied to fast antibiotic-susceptibility testing. Entrapping bacteria inside the hydrogels upon formation, through the oxidation of iron (II) to iron (III), was possible in soft conditions (i.e. room temperature, pH 7, aqueous solution). Ferricyanide introduced to the hydrogels was reduced by bacterial metabolism, reducing it to ferrocyanide, which reacts with the iron (III) ions in the hydrogel to produce Prussian blue molecules. Additionally, since ferricyanide reduction required live bacteria, adding antibiotics resulted in hydrogels with and without live bacteria, reporting on the presence and absence of Prussian blue respectively.

### 6.1.1. Biomaterial electrodeposition and cell entrapment

Electrodeposition is very valuable for enabling: (i) control of the deposition process, (ii) control of hydrogel properties (i.e. porosity, thickness, density and the deposition area, among others), (iii) homogeneity and (iv) repeatability. Iron(III)/alginate hydrogels were prepared following the protocol detailed in [1]. Iron (II) ions were mixed with the alginate solution and *in situ* oxidized for local formation of the iron(III)/alginate hydrogels at very soft experimental conditions (i.e. room temperature, pH 7, aqueous solution). Thick hydrogel films were potentiostatically electrodeposited on the working electrode of screen-printed carbon electrodes (**Figure 6.2 a**). A potential of 1.2 V (vs Ag) was chosen from iron (II) sulphate cyclic voltammetry data (**Figure 6.2 a, inset**), as the lowest potential allowing iron (II) oxidation and hydrogel formation. As shown in **Figure 6.2 b**, electrodeposition enabled the control of the deposition area with high precision, generating hydrogels with very vertical walls. Optimal iron (II) sulphate concentration and electrodeposition times were selected from according to hydrogel thickness (from profilometry) and chronoamperometry data. Thicker hydrogels were obtained when increasing either the iron (II) concentration in the sample (**Figure 6.2 c**) or the electrodeposition time (**Figure 6.2 d**) up to stabilization at values around 60 mM iron (II) and 450–500 s, respectively. The thickness of the hydrogel, however, also affected permeability to ferricyanide. Chronoamperometry data shows important current limitation by hydrogels containing more than 20 mM iron (**Figure 6.2 e**), which corresponded to thicknesses above 100  $\mu\text{m}$ . Hydrogel permeability was, however, less affected by the electrodeposition time (**Figure 6.2 f**) since the influence of this parameter to the hydrogel thickness was lower. Electrodeposition at 1.2 V (vs Ag) of 20 mM iron (II) samples for 500 s, providing hydrogels of around 100  $\mu\text{m}$  was selected for further experiments. High bacterial densities were entrapped in the 3 D matrix of the



alginate hydrogel biomaterial, without compromising cell integrity or activity. It is clear in the live/dead stained hydrogel shown in **Figure 6.3 a**, where most entrapped cells present a green fluorescence indicative of the integrity of their plasmatic membrane and their viability (in opposition to red microorganisms which are non-viable).

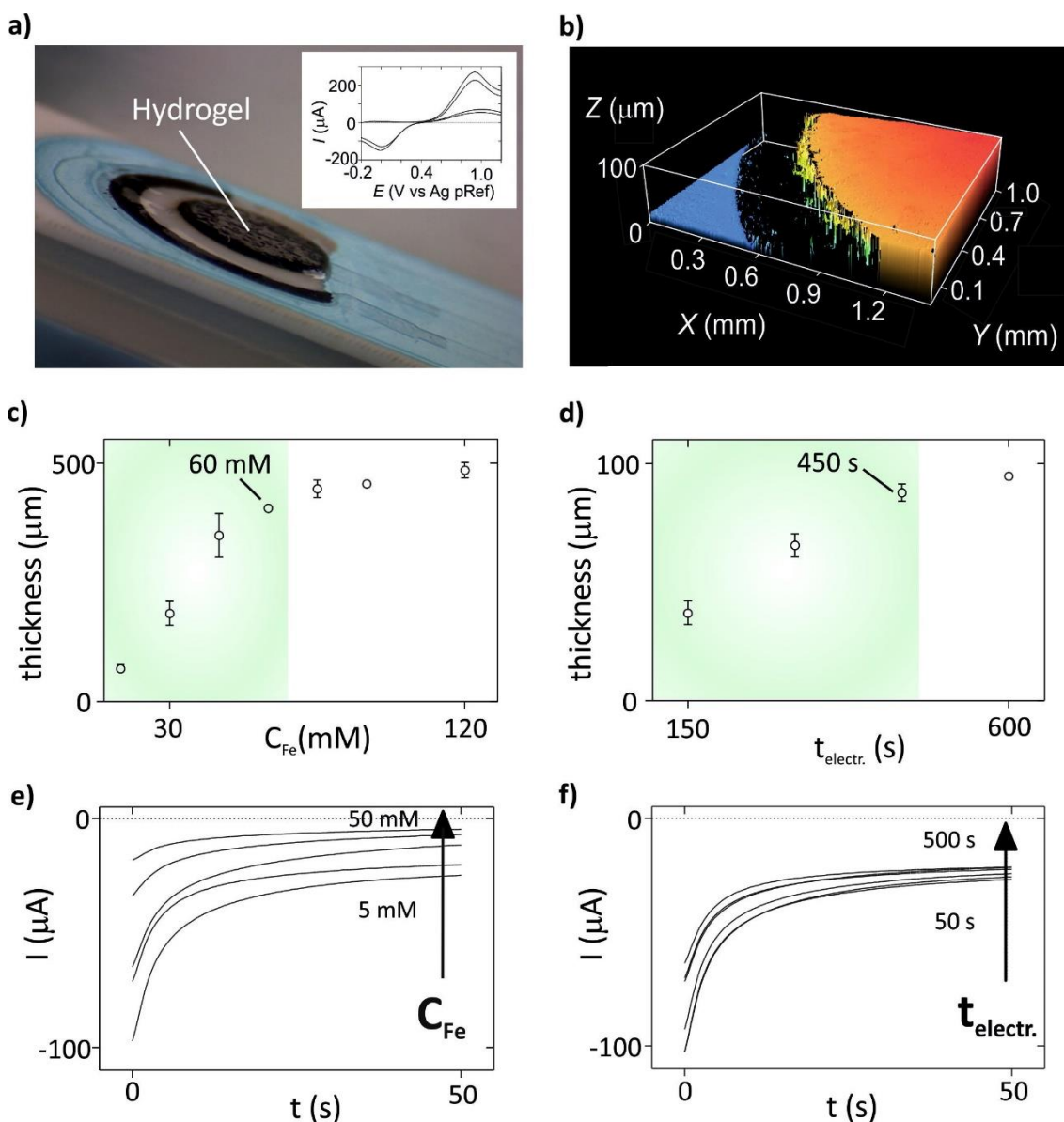


**Figure 6.2: Optimization of biomaterial electrodeposition.** (a) Image and (b) profile plot of iron (III)/alginate hydrogel electrodeposited on the working electrode of a screenprinted carbon electrodes. Inset (a) cyclic voltammetry of 30 mM iron (II) sulphate solutions. Electrodeposited hydrogel thickness (from optical profilometry) as a function of (c) the iron (II) sulphate concentration (from 15 to 120 mM) and (d) electrodeposition time (from 150 to 600 s). Green area indicates dynamic ranges until thickness stabilization. Chronoamperograms of ferricyanide (0.4 V vs Ag) illustrating the diffusion of this molecule through iron (III)/alginate hydrogels electrodeposited at different (e) iron (II) sulphate concentrations (from 5 to 50 mM) and (f) electrodeposition times (from 50 to 500 s).

However, bacterial concentrations above  $2.5 \times 10^8$  colony forming units per mL (CFU/mL) limited current flow and hydrogel formation (**Figure 6.3 b**). Thus, this concentration was considered the highest bacterial concentration able to be electrodeposited. Ferricyanide concentration for the bioassay was adjusted to the

number of immobilized bacteria. Based on previous works [2–4], ferricyanide concentration was set at 1 mM (for a hydrogel containing  $2.5 \times 10^8$  CFU/mL) with the objective to ensure a sensitive response of the biomaterial in less than one hour.

### 6.1.2. Electrochromic response of the biomaterial

The presence of iron (III) ions in the hydrogel conferred the biomaterial with redox activity and reactivity. This reactivity was exploited in the development of a biomaterial with sensitivity to bacterial metabolism, reporting on bacterial susceptibility to antibiotics and antibiotic resistance. The sensing principle of the biomaterial took benefit from the selective reactivity of iron (III)/alginate hydrogels to hexacyanoferrate molecules, which is illustrated in **Figure 6.4 a**. As shown, the biomaterial was not sensitive to the presence of ferricyanide, while it reacted with ferrocyanide producing an intense blue colour as a result of PB nanoparticles formation. This selective reactivity is clearly demonstrated by spectrometric analysis of the hydrogels. After addition of ferricyanide, an intense absorbance band at 420 nm appears in the hydrogel by the presence of ferricyanide molecules (**Figure 6.4 b**). The absorbance band of ferricyanide, however, remained stable over time, which confirmed the low reactivity of this reagent with the biomaterial. Ferrocyanide, on the other hand, reacted with the biomaterial, producing PB nanoparticles with an intense absorbance band at 680 nm (**Figure 6.4 c**). The increase in the absorbance magnitude at 680 nm (Abs680) over time reported on the PB formation kinetics.

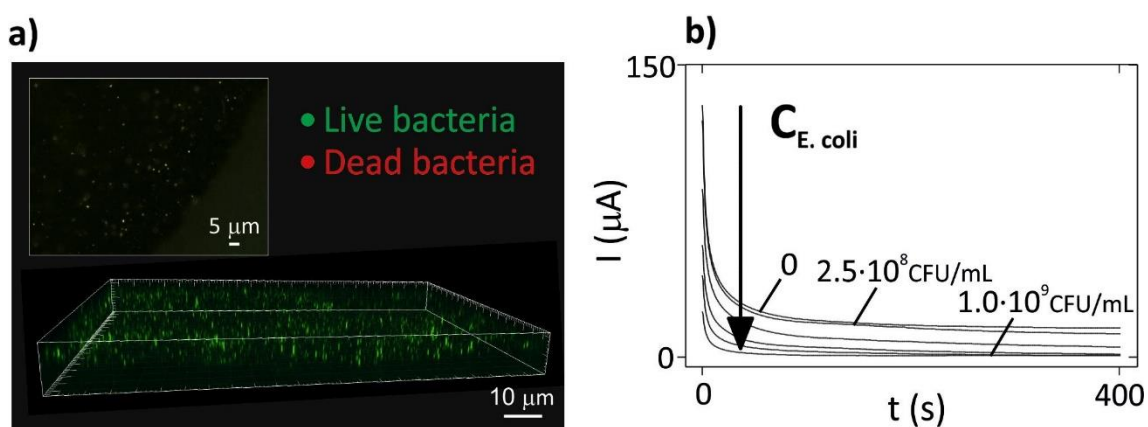


**Figure 6.3: Bacterial entrapment in the biomaterial.** (a) Confocal and epifluorescence images of electrodeposited bacterial hydrogels stained with Live/Dead Invitrogen Kit Bac Light from Invitrogen (live bacteria appear green and dead bacteria appear red). (b) Potentiostatic electrodeposition (1.2 V vs Ag) of bacterial hydrogels at different bacterial concentrations (from  $2.5 \times 10^8$  to  $10^9$  CFU/mL). Black arrow indicates an increasing concentration of bacteria in the initial suspension.

After 30 min, Abs680 reached a maximum indicating the end of the reaction under these experimental conditions. The formation of PB molecules depended on the initial concentration of ferrocyanide, being either directly added to the biomaterial (**Figure 6.4 d**) or *in situ* generated by reduction of ferricyanide with ascorbic acid (**Figure 6.4 e**). Biomaterial reactivity after direct addition and *in situ* formation of ferrocyanide was compared. To allow comparison, the stoichiometry of the reduction reaction, where one molecule of ascorbic acid reduced two molecules of ferricyanide, was considered. In

both cases, similar results were obtained after 30 min of reaction with the biomaterial (**Figure 6.4 f**). Minor differences were observed in the saturation region, mostly due to kinetic limitations of the reduction reaction [5]. Therefore, the biomaterial was also sensitive to processes involving the reduction of ferricyanide.

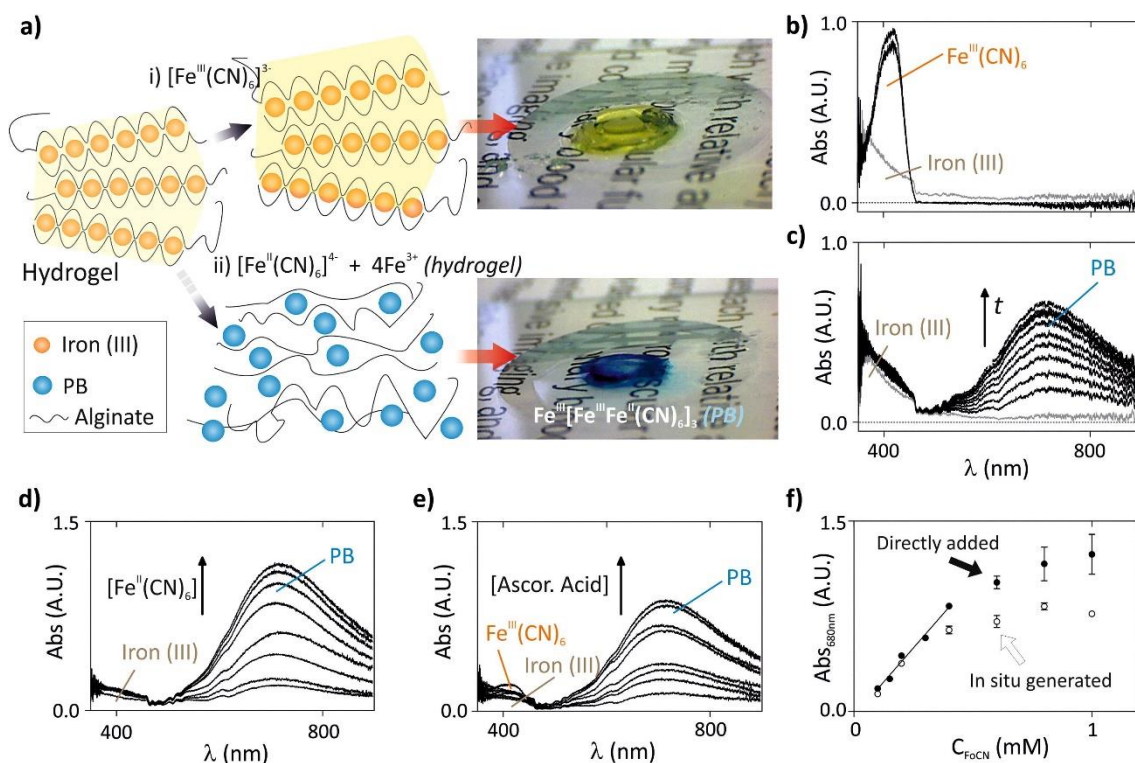


**Figure 6.4: Electrochromic response of the biomaterial.** (a) Scheme and (b) representative pictures illustrating the chromatic response mechanism of iron (III)/alginate hydrogels after reaction with (i) ferricyanide and (ii) ferrocyanide. Absorbance kinetic spectra of hydrogels after addition of (c) ferricyanide and (d) ferrocyanide (black lines). Black arrow indicates the time flow. Grey spectrum corresponds to the initial hydrogel (before reagents addition). Absorbance spectra of iron(III)/alginate hydrogels after (e) direct reaction with ferrocyanide (concentrations range = 0.1 mM to 1 mM) and (f) in situ generation of ferrocyanide by reduction of 1 mM ferricyanide with ascorbic acid (concentrations range = 0.05 – 1 mM. (g) Comparison of PB formation (absorbance at 680 nm) in iron (III)-alginate hydrogels after reaction with directly added or in situ generated ferrocyanide concentrations ranging from 0.1 mM to 1 mM. Error bars represent standard deviation (n = 3, confidence interval of 95%).

**6.1.3. Electrochromic sensing of bacterial metabolism with the biomaterial**

Ferricyanide, and other electrochromic molecules, present high redox potentials and can report on bacterial metabolism by the mechanisms summarized below [2]. Bacteria oxidize nutrients to obtain energy. In this process, they generate an electron flow in the cell membrane through a number of proteins, known as the electron transfer chain (see **Chapter 3.1.3**). This chain of proteins transfers the electrons to a final electron acceptor, i.e. oxygen in the case of aerobic metabolism. However, due to its redox potential, oxygen may be replaced by a suitable electrochromic molecule such as ferricyanide, which is metabolically reduced to ferrocyanide. Since the reduction is directly linked to bacterial metabolism, only living bacteria (and not dead ones) can produce ferricyanide reduction. The metabolic reduction of ferricyanide is here employed in the development of a biomaterial for fast antibiotic susceptibility testing. First, pre-cultured bacteria were

entrapped in the alginate matrix by electrodeposition with the previous protocol. Due to the iron complexation in the matrix, entrapped bacteria could not reduce iron (III) ions directly, ensuring the integrity and stability of the biomaterial. **Figure 6.5 a** schematizes the sensing mechanism of the biomaterial, where only living bacteria reduce ferricyanide to ferrocyanide inducing PB formation and the consequent change of colour. The response of the biomaterial containing  $2.5 \times 10^8$  CFU/mL of *Escherichia coli* (*E. coli* K12 (CGSC 5073), used as model bacterium) to the addition of 1 mM ferricyanide solution is illustrated in **Figure 6.5 b**. The presence of bacteria in the hydrogel increased absorbance due to cell scattering. Apart from scattering, absorbance bands corresponding to ferricyanide (420 nm) and PB (680 nm) were clearly identified. Spectrometric changes in the sensing biomaterial were mostly due to the formation of blue-coloured PB molecules, while ferricyanide reduction was difficult to appreciate due to its high excess in the solution. The increase in Abs<sub>680</sub> was fast and only required 30 – 35 min to reach a maximum in the absorbance magnitude. However, the sensitivity (slope in the curve) was smaller than that obtained by direct addition of ferrocyanide due to kinetic limitations of bacterial metabolism (**Figure 6.5 c**). Even though, the biomaterial was able to provide quantitative data after short time periods of minutes. Due to the metabolic nature of the electrochromic reaction in the biomaterial, the response of the hydrogel was subjected to the influence of environmental factors affecting bacterial activity such as metabolic stimulators (e.g. nutrients) or inhibitors (e.g. toxic agents). This modulation of metabolic activity was evaluated using glucose as stimulator and ethanol as inhibitor. **Figure 6.6 a** shows the absorbance spectra of hydrogels incubated with samples containing different glucose concentrations. After 30 min of incubation, PB formation, measured as Abs at 680 nm, presented a high dependence on the concentration of glucose in the sample up to saturation around 0.05% (w/v), while no significant changes were observed in the absorbance band corresponding to ferricyanide, i.e. Abs at 420 nm (**Figure 6.6 b and c**). The presence of ethanol influenced the absorbance spectrum of the biomaterial (**Figure 6.6 d**). In this case, ethanol reduced the metabolic activity and viability of cells, and consequently the PB formation. As before, most of the chromatic change recorded was associated to PB (**Figure 6.6 e**), demonstrating the enhancement of sensitivity when coupling ferricyanide reduction to PB formation. There was a clear relationship between metabolic activity inhibition and the concentration of ethanol in the sample, reaching 100% inhibition by values around 10% (v/v) of ethanol (**Figure 6.6 f**). These results validated the use of this biomaterial for fast and sensitive determination of bacterial activity and viability, as well as bacterial susceptibility to toxic agents such as ethanol.

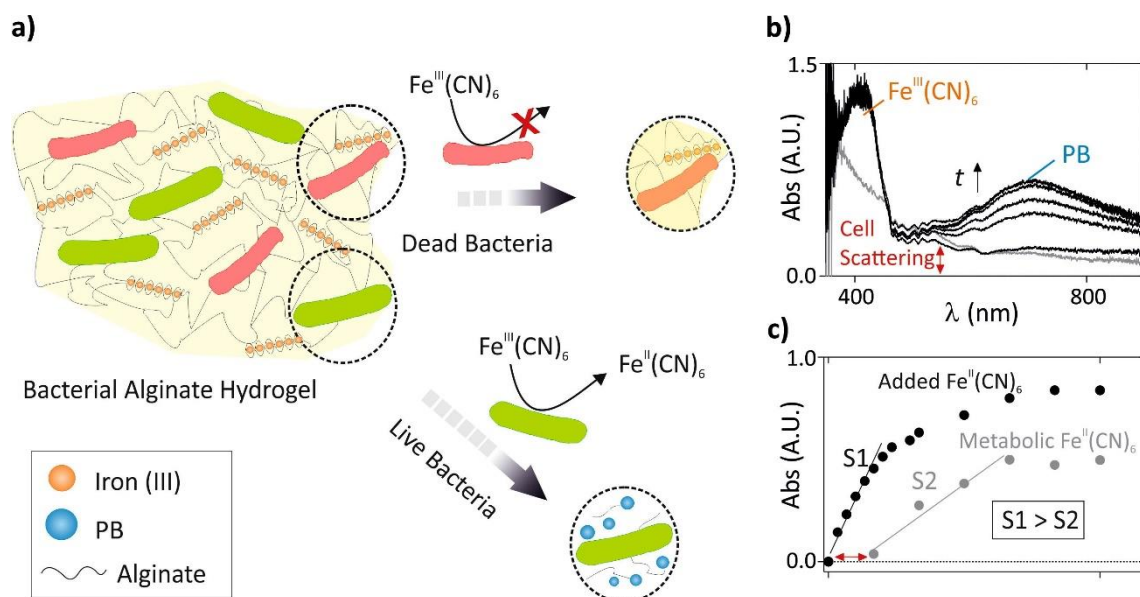


**Figure 6.5: Metabolic sensing of the biomaterial.** (a) Schematic illustration of the metabolic response mechanism of the hydrogel/bacteria hybrid biomaterial for live and dead bacteria. (b) Absorbance kinetic spectra of bacterial hydrogel before (grey curve) and after (black curve) addition of 1 mM ferricyanide. Black arrow indicates the time flow. (c) Comparison of the variation of PB formation kinetics (absorbance at 680 nm over time) after reaction of the hydrogel with ferrocyanide directly added (1 mM; black dots) or metabolically generated in situ from 1 mM ferricyanide (grey dots). S1 and S2 correspond to the slope (or kinetics) of PB formation from directly added and metabolically generated ferrocyanide, respectively.

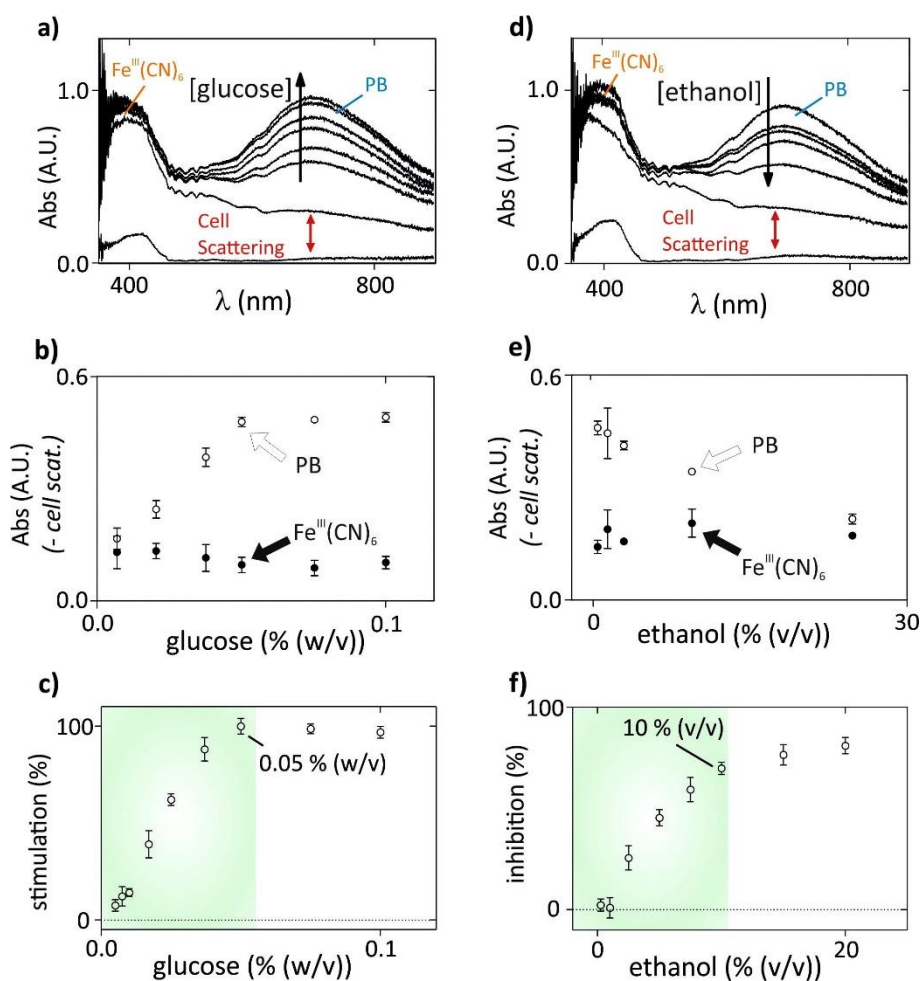


**Figure 6.6: Response of the biomaterial to metabolic stimulators and inhibitors.** Absorbance spectra of bacterial hydrogels after addition of samples containing different concentrations of (a) glucose (from 0.01 to 0.1% w/v), used as metabolic stimulator, and (d) ethanol (from 0.25 to 25% v/v), used as metabolic inhibitor. Black arrows indicate increasing glucose and ethanol concentrations, respectively. Absorbance spectra corresponding to hydrogels without bacteria are also included in both plots to illustrate bacterial scattering. Variation of the absorbance magnitude (after bacterial cell scattering subtraction) of ferricyanide (black dots; absorbance at 420 nm) and PB (white dots; absorbance at 680 nm) with the concentration of (b) glucose and (e) ethanol. Concentration-response curves for bacterial hydrogels after (c) metabolic stimulation with glucose and (f) metabolic inhibition with ethanol. The chromatic response of the bacterial hydrogel to incubation in Luria Bertani (LB) medium, corresponding to standard growing conditions, was used as reference. Error bars represent standard deviation. ( $n = 3$ , confidence interval of 95%).

#### 6.1.4. Antibiotic susceptibility testing with the electrochromic biomaterial

As a step forward, the biomaterial was finally applied to fast and simple antibiotic susceptibility testing. To this end, kanamycin (Kmc) was chosen as antimicrobial agent. High bacterial concentrations (i.e.  $2.5 \times 10^8$  CFU/mL) of the strains under study (in this case *E. coli* K12 (CGSC 5073) sensitive and *S. aureus* (ATCC 6538) resistant to Kmc antibiotic) were entrapped in the hydrogel matrix by direct gelation in 96-well plates. The susceptibility of these two strains to Kmc was previously characterized showing sensitivity in *E. coli* and resistance in *S. aureus* for the tested antibiotic concentrations (from 1 to 128 mg/mL). The biomaterial was then incubated with Kmc concentrations between 1 and 128 mg/L for 30 min, rinsed with distilled water and incubated with 1

mM ferricyanide for inducing the electrochromic response. The images of the biomaterials with resistant (RS) and non-resistant strains (NRS) at different incubation times are shown in **Figure 6.7 a**. From the images it is clear that there was a big difference between biomaterials containing NRS, which remained yellow for the presence of ferricyanide, and RS, which started developing blue colour (due to PB formation) even after only 5 min of incubation. With time, these differences between RS and NRS were accentuating since the colour intensity in the RS increased. At this antibiotic dose range, RS were completely resistant and no significant differences were observed. NRS, on the other hand, presented a dose-dependence on the antibiotic concentration range under study. Images in **Figure 6.7 a** show how there was a delay in colour development even in the sample that did not contain antibiotic (labelled as 0).

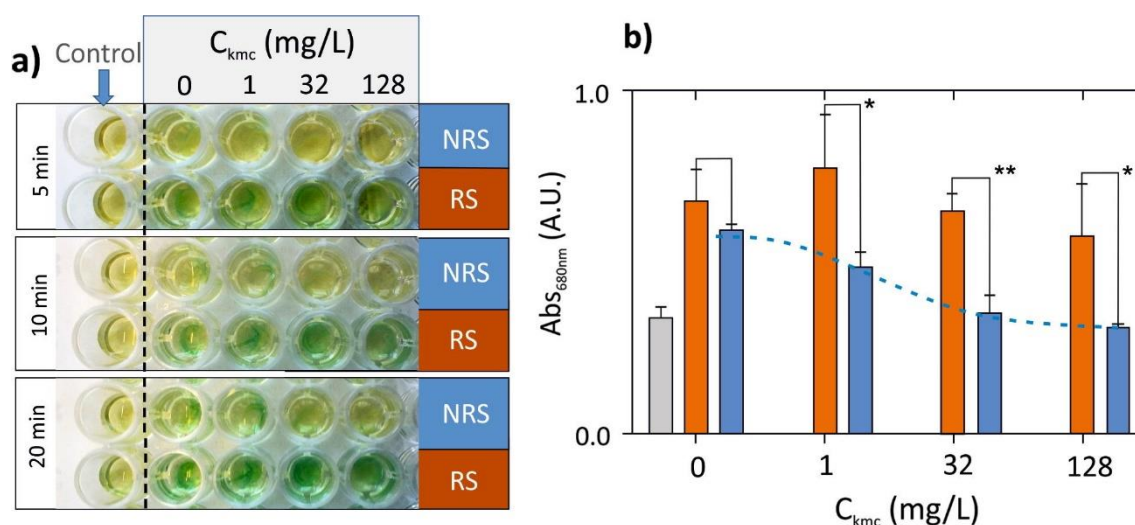


**Figure 6.7: Antibiotic susceptibility test with the biomaterial.** (a) Images of iron (III)/alginate hydrogel biomaterial in independent wells after 5, 10 and 20 min of incubation with ferricyanide. In the image, hydrogels containing resistant (RS) and non-resistant bacterial strains (NRS) are labelled accordingly. In both cases, biomaterials were previously incubated for 30 min with Kmc samples with a concentration ranging from 1 to 128 mg/L. Control samples correspond to the biomaterial without bacteria. The blue colour is the result of the formation of PB. (b) Absorbance spectra corresponding to hydrogels with RS (orange), NRS (blue) or without bacteria (in grey) for samples of biomaterial after 20 min of incubation with ferricyanide. The biomaterial was previously incubated with Kmc samples of 1, 32 and 128 mg/L. Error bars represent standard deviation. (n = 3, confidence interval of 95%). For statistics, a Kruskal-Wallis one-way analysis of variance was performed.

This may be due to differences in the metabolic state during growth phase or concentration of both strains. However, sample 0 and 1, which corresponded to a concentration of 1 mg/L of Kmc, presented a similar kinetic of blue colour development whereas samples containing 32 and 128 mg/L remained yellow. The same result was obtained when comparing the absorbance magnitude at 680 nm after 20 min of incubation with ferricyanide (**Figure 6.7 b**), which confirmed that the half maximal inhibitory concentration (IC50) of this antibiotic for this bacterial strain should be between 1 and 32 mg/L. Control samples corresponded to the biomaterial without bacteria. According to these results, the electrodepositable iron(III)/alginate hydrogel here presented was ideal for fast and sensitive testing of antibacterial susceptibility and for the identification of bacterial resistance by a simple change of colour, which could

be even perceptible with the bare eye (without the need of external instrumentation). The simplicity and versatility of the biomaterial and the sensing mechanism made this metabolic stimuli-sensitive material very interesting in a broad spectrum of applications, such as toxicity assessment, food quality control and clinical diagnosis.

**In conclusion, the electrochromic alginate hydrogels provided a new mechanism and substrate for fast antibiotic susceptibility testing. The generation and state of the hydrogel provided a biocompatible environment for bacterial growth under soft conditions. However, the technology was limited due to the need for external equipment and the amount of manual handling. Finally, due to their nature, hydrogels needed fresh preparations prior to testing to avoid contamination.**

**This work has been published in the Journal of Colloid and Interface Science (DOI: 10.1016/j.jcis.2017.09.004).**



## 6.2. Ferricyanide in liquid cultures

Bacterial sensing in hydrogels has great potential, but would see limited use in various applications, like susceptibility testing or sepsis diagnostics due to constraints resulting from the use of solid-state materials and the complexity of the setup needed for sample preparation and measurements. Hydrogels are formed either through electrodeposition, using equipment not readily available in any lab, or formed manually, leading to large variations in the hydrogels due to human errors, making it less reliable for high throughput experiments. Furthermore, the hydrogels themselves need to be prepared fresh for each culturing, since they are prone to dehydration and contamination. However, the experiments emphasised the potential to use ferricyanide as bacterial viability assay. This section will describe the usage of ferricyanide as electrochromic bacterial-sensing indicator (i.e. metabolic indicator) by proving its function, the optimization and the final application in antibiotic susceptibility testing.

### 6.2.1. Ferricyanide reaction mechanism

As already commented, bioelectrochromic molecules, such as ferricyanide, are susceptible to reduction by bacterial metabolism (**Chapter 3.1.3**), resulting in a detectable and quantifiable change of colour. The reaction mechanism of the ferricyanide as metabolic indicator is shown in **Figure 6.8**. Dead bacteria (red) cannot reduce ferricyanide molecules (yellow), which remain unchanged. Live bacteria (green), on the other hand, use ferricyanide as an alternative electron acceptor, reducing it to the colourless ferrocyanide molecules (transparent).

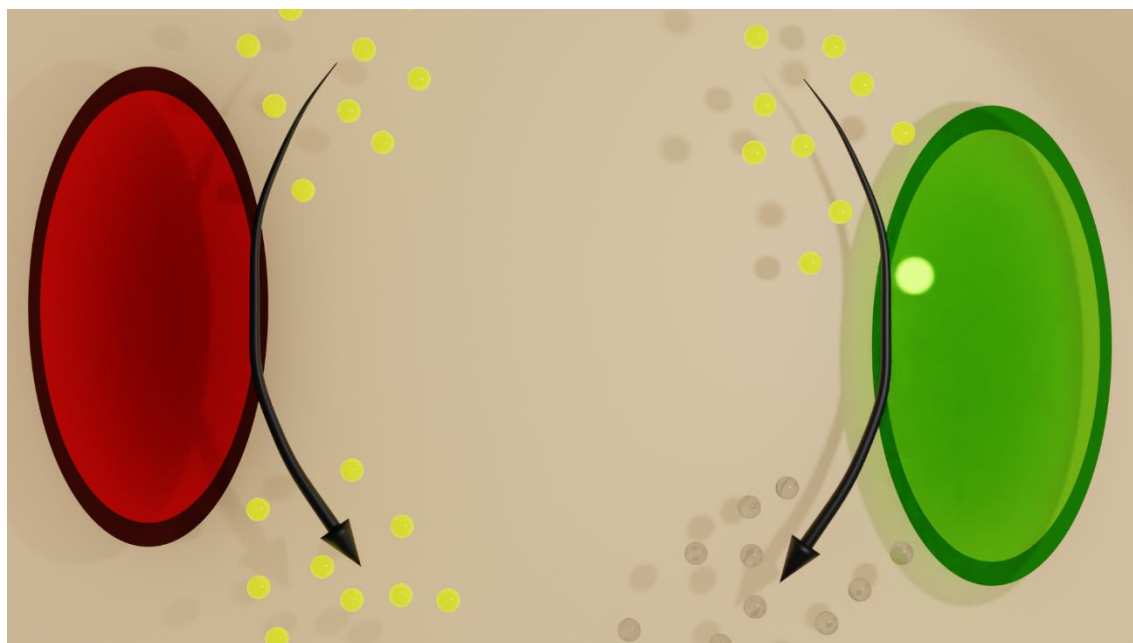


**Figure 6.8: Reaction mechanism of ferricyanide reduction by bacterial metabolism.** Ferricyanide (yellow) is brought into contact with dead (red) and live (green) bacteria. Only live bacteria reduce the ferricyanide to ferrocyanide (colourless). (Made in Blender)

### 6.2.2. Ferricyanide reduction by bacterial metabolism

The main aim of the research was to develop a test for rapid antibiotic susceptibility testing. Even though various methods and variations already exist, as explained in **Chapter 2.2.2**, the goal was to make the assay fast and simple, and as compatible as possible with the standardized MIC testing methods, as described by EUCAST. Since the broth microdilution method relies on culturing in Mueller Hinton (MH) broth, the following experiments were performed using the same medium for comparison and simple transference. To verify the use of ferricyanide as a general indicator, a total of three strains of the most common bacteria present in clinical settings were evaluated, including two gram-negative, *Escherichia coli* and *Pseudomonas aeruginosa*, and one gram-positive, *Staphylococcus aureus*. The bacterial-sensing mechanism was the following. Bacteria, through the metabolic electron flow produced in the ETC, reduced yellow ferricyanide molecules (with an absorbance peak at 420 nm) to colourless ferrocyanide. Therefore, by a simple absorbance measurement at a wavelength of 420 nm, the FeCN reduction could be followed over time, as a direct indication of bacterial metabolism. The results corresponding to the changes in ferricyanide absorbance over time (initial ferricyanide concentration: 2 mM; assay time: 5 hours) by the three bacterial strains under study and at different bacterial concentrations are summarized in **Figure 6.9**. Results are grouped together per concentration of bacteria, with blank referring to the negative control without bacteria, used to see the potential interaction between the metabolic indicator and the medium. Each group is subdivided into colours, with each colour corresponding to a different measurement time.

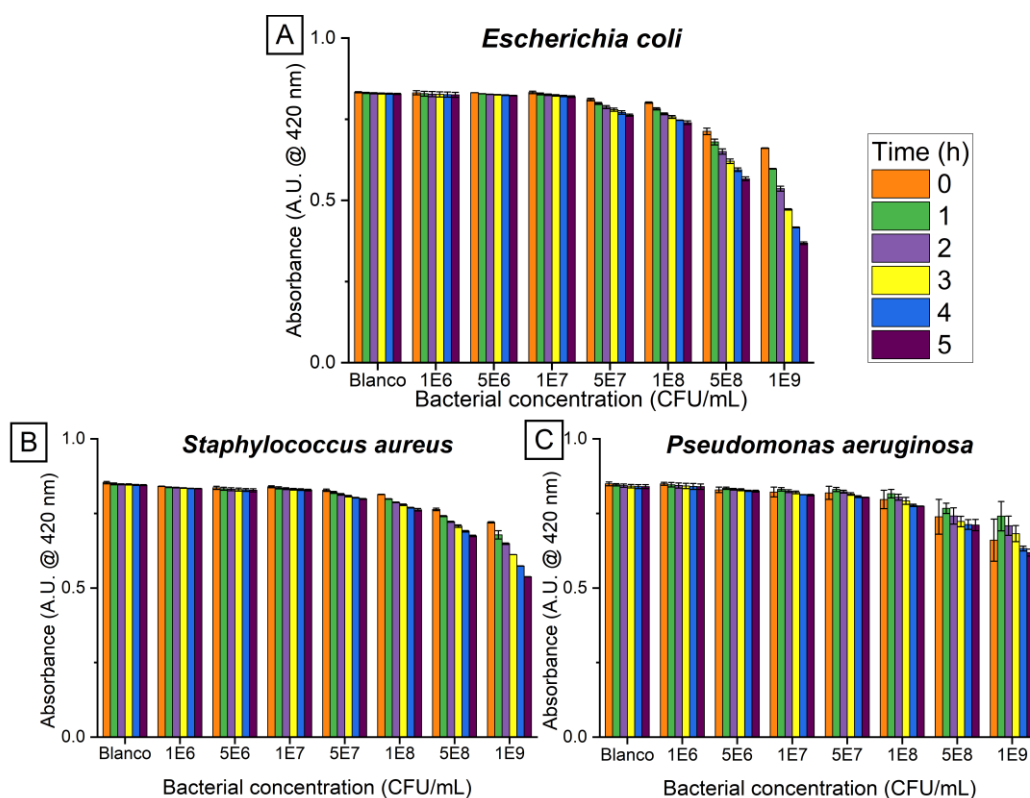


**Figure 6.9: Bacterial ferricyanide reduction over time at various bacterial concentrations.** The data shows the absorbance values taken at 420 nm, for each bacterial concentration, at every hour for a total of 5 hours. Three bacterial strains were tested, *Escherichia coli*, *Staphylococcus aureus* and *Pseudomonas aeruginosa*, corresponding to graphs a, b and c respectively. In each experiment a blank was included, a condition with no bacteria present. Ferricyanide concentration = 2 mM. (n=3)

The results confirmed that the three bacterial strains were capable to reduce ferricyanide to its colourless reduced form. The process was time and bacterial concentration dependent. Higher initial bacterial concentrations required lower times to produce a deeper colour change due to the larger amount of metabolically active organisms present. Additionally, the rate of reduction was dependent on the bacterial type. This was in accordance with the metabolic activity of these strains: *E. coli*, the one presenting the highest reduction rate for ferricyanide, was also the microorganisms with the highest metabolic activity from those under evaluation. It should be noted that larger errors bars were found in the case of *P. aeruginosa*. It was associated to a longer lag phase of this microorganism when compared to the other two, which resulted in large variations after short time periods.

The experiment demonstrated that metabolic reduction kinetics of ferricyanide, which could be detected spectrometrically, was proportional to bacterial concentration and may be used to determine the number of live bacteria remaining after, for example, incubation with antibiotics. **The potential function of ferricyanide as metabolic indicator for susceptibility testing is studied in the following sections.**

### 6.2.2.1. Optimization of ferricyanide-based susceptibility test

In the previous study, the conditions of the assay (i.e. assay time, ferricyanide and bacteria concentration, etc.) were established based on previous publications where this format was used to detect pollutants in water samples with a microbial biosensor [6]. Since susceptibility testing is a completely different approach, the assay was adjusted to this particular format. MH culture medium was used instead of LB. Bacterial concentration was set between  $10^8$  and  $10^9$  CFU/mL, as reported in most of susceptibility tests, and measurements were performed in an incubator at a controlled temperature (37°C). To fit with the standards of fast susceptibility testing, ferricyanide concentration was here optimized with the aim to provide information of bacterial concentration in less than 5 hours. Six ferricyanide concentrations were tested in the range from 0 to 8 mM, using *E. coli* as model organism, and monitoring the absorbance peak of ferricyanide at a wavelength of 420 nm over time.

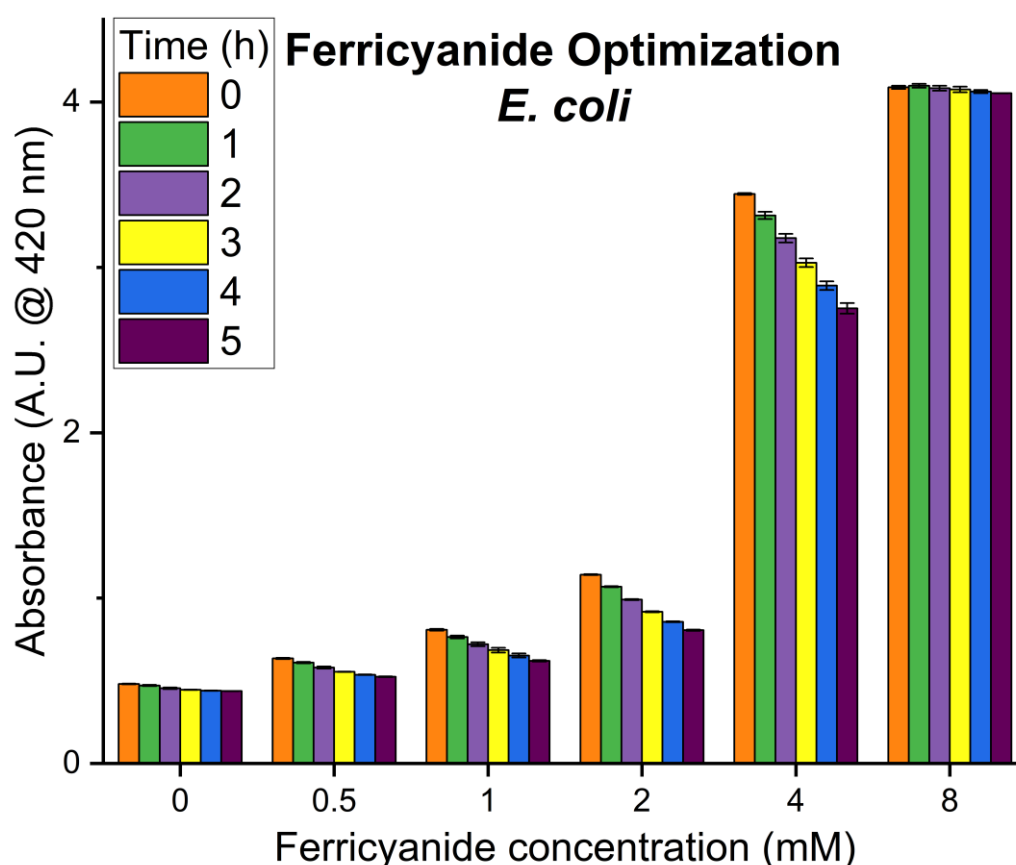


**Figure 6.10: Optimization of the ferricyanide concentration using *Escherichia coli* as model organism.** Absorbance values are taken every hour for each ferricyanide concentration at a wavelength of 420 nm. The bacterial concentration of *E. coli* was set to  $10^8$  CFU/mL. (n=2)

As shown in **Figure 6.10**, a decrease in absorbance magnitude was recorded over time for ferricyanide concentrations below 4 mM. The reduction rate (i.e. kinetic change of absorbance magnitude over time) depended on the initial concentration of the ferricyanide, being 4 mM ferricyanide the one providing the largest absorbance drop and thus, the highest sensitivity of the assay. Unfortunately, the reliability of the

absorbance values obtained for the 4 mM was low, since it corresponded to an initial absorbance magnitude of 3 A.U. Note that an absorbance magnitude of 3 results from an absorption of 99.9 % of the light initially introduced to the system, while only 0.01 % reached the detector and was measured. This conferred the method a high level of uncertainty and this condition was discarded (the calculation and indication of absorbance values has been explained in the fundamentals **Chapter 3.2.1**). Reliable optical systems should provide initial absorbance magnitudes not higher than 1 A.U., which corresponded to a concentration of 2 mM, the one selected as optimal and used in further experiments.

### 6.2.3. Minimal inhibitory concentration determination with the ferricyanide-based test

The experiments included in this section were performed in a 2-week secondment at the University of Antwerp, in the laboratory of Prof. Herman Goossens.

After optimization of the conditions of the assay, the use of ferricyanide for the colorimetric determination of the MIC of antibiotics was investigated. MIC tests were performed using gentamicin as model antibiotic and the previous bacterial strains for validating the robustness of the assay. The MIC was defined as the first condition resulting in a complete inhibition of bacterial proliferation, here determined as the condition where ferricyanide was not metabolically-reduced after 20 hours of incubation. This longer incubation time was chosen in agreement with current golden standard protocols and used for comparison. **Figure 6.11** illustrates the values measured in the experiment, concretely the absorbance at 420 nm including ferricyanide and bacterial scattering, absorbance at 600 nm associated to bacterial scattering and ferricyanide kinetics resulting from the subtraction of bacterial scattering to the ferricyanide absorbance. It is clear from the results that ferricyanide absorption was so weak that it was hard to define the MIC cut-off if only considering the magnitude at 420 nm. The reason was the large absorbance increase associated to biomass scattering, responsible for most of the changes in light intensity, which masked ferricyanide reduction in a large extend. The MIC cut-off was clearer at 600 nm, where bacterial scattering was measured without inference of ferricyanide. The correction of ferricyanide kinetic after subtraction of biomass scattering also provided clear MIC cut-off, enabling the determination of the MIC magnitude with the antibiotic under test, although not improving conventional scattering measurements in terms of sensitivity or response time.

To determine the analytical capacity of the method, MIC values determined by the ferricyanide-based test (FeCN) based on BMD as described in **Chapter XX** were compared to golden standard broth microdilution (BMD), obtained by visual observation as recommended by EUCAST, and quality control values as stated by EUCAST (tabulated values corresponding to control strains and used to test alternate detection mechanism to ensure the experimental results are reliable). For data interpretation, it is important to consider that EUCAST states that a MIC value can differ 2-fold from the BMD method to still be reliable. An overview of the results is presented in **Table 6.1**.

**Table 6.1: MIC results of various strains when tested with gentamicin after 20 hours.** The first column specifies the tested bacterial strain. The second column shows the obtained MIC value using the broth microdilution (BMD) method. The third column uses the modified BMD assay, by the addition of 2 mM potassium ferricyanide. The MIC values were based on both the colour of the well and the biomass. The final column shows the values of each quality control (QC) strain as defined by EUCAST. Using this data, the reliability of the performed test can be evaluated.

Bacterial strain	BMD (mg/mL gentamicin)	FeCN (mg/mL gentamicin)	QC EUCAST (mg/mL gentamicin)
<i>E. coli</i> ATCC 25922	2	2	0.5
<i>S. aureus</i> ATCC 29213	0.5	2	0.25 – 0.5
<i>P. aeruginosa</i> ATCC 27853	0.5	2	1

It could be noted from **Table 6.1** that the MIC determined by ferricyanide tended to be higher than that obtained through BMD and/or established in QC EUCAST. In the case of *E. coli*, FeCN-based assay and BMD provided similar results, which fell slightly outside the QC values in both cases. This may suggest some alteration of the strain by mutation or contamination with another more resistant strain. The offset of FeCN was even more pronounced for the other two bacterial strains, with an MIC value up to a factor of 8 higher compared to the QC, while BMD was inside the margins. The results with *Pseudomonas* and *Staphylococcus* may suggest some interaction between the reagent, i.e. ferricyanide, and the antibiotic under test. Although gentamicin was demonstrated not being able to reduce FeCN directly (as shown in the control experiments), the presence of this compound may interfere with the antimicrobial properties of gentamicin, and thus would not be suitable for MIC determination in this case. This clearly compromises the use of the FeCN-based protocol in MIC determination. It could also be noted that the MIC values could be detected within 4 hours (not shown), though this was contributed to the scattering of the biomass and not to the ferricyanide reduction itself. Apart from that, and as illustrated in **Figure 6.11**, the assay required either a high bacterial concentration or long growth times to provide MIC values not improving the results obtained by simply measuring the bacterial scattering.

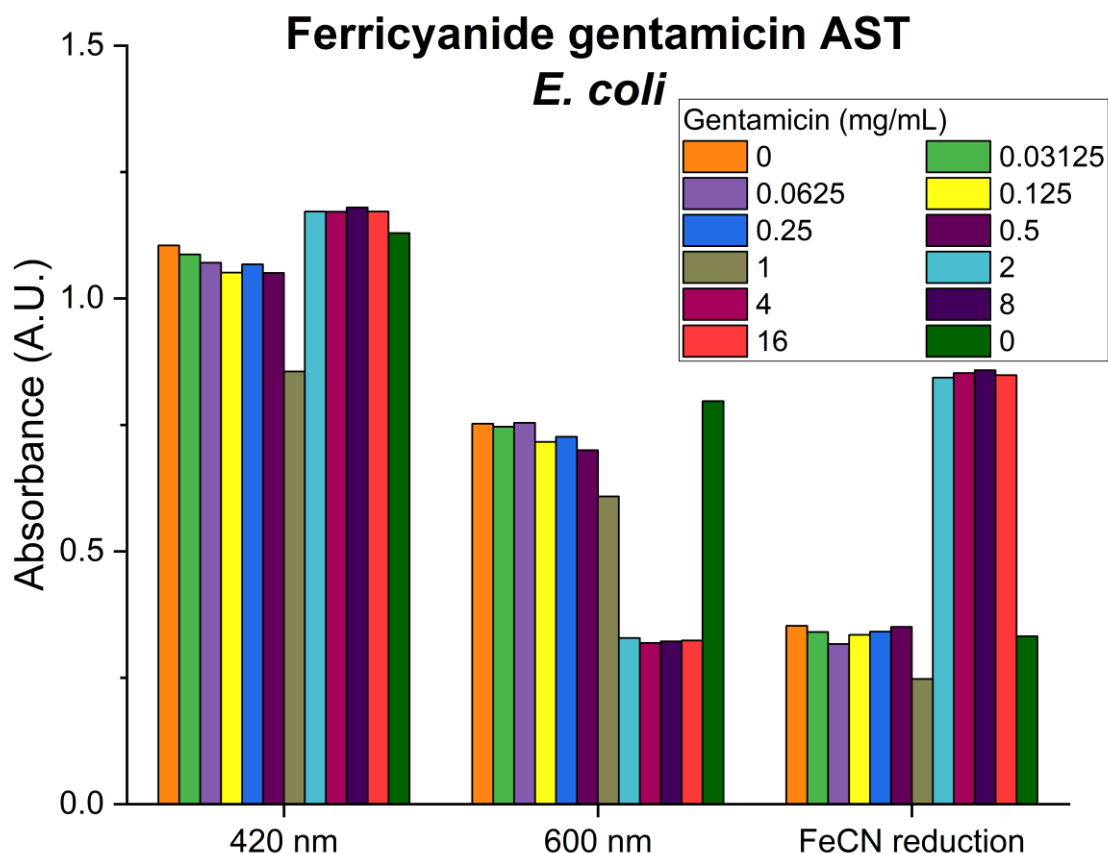


**Figure 6.11: Gentamicin MIC using ferricyanide.** Each of the columns shows the absorbance value at the corresponding wavelength for each gentamicin concentration. The third group of columns is the difference between the first two. Tests were performed using *E. coli* at a starting concentration of  $5 \times 10^5$  CFU/mL, according to EUCAST standards, and data was acquired after 20 hours of growth.

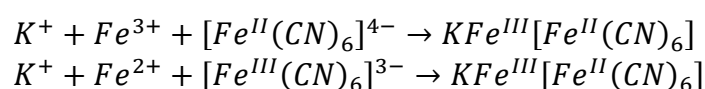
**In conclusion, ferricyanide-based protocol reported on bacterial concentration through a simple colour change, but its implementation to MIC tests was not straightforward by: (i) the need of data treatment (i.e. biomass scattering subtraction), the interaction with some antibiotics, e.g. gentamicin, not improving current golden standard (i.e. BMD) in time-to-result or simplicity. The low extinction coefficient inherently limits its use as fast AST test.**

### 6.3. Prussian blue formation

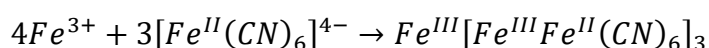
As already discussed in **Chapter 6.1.2**, the ferricyanide can be coupled to additional chemical reactions towards the formation of Prussian blue (PB) molecules as a way to amplify the low optical signal of ferricyanide associated to its small molar extinction coefficient. In general, PB is formed by the reaction between ferrocyanide, resulting from the bacterial metabolic reduction of ferricyanide, with iron (III) ions in the medium, with an absorbance maximum between 680 and 720 nm. PB has an extinction coefficient 30 times higher than ferricyanide, providing more sensitivity. This chapter studies the use of this metabolic generation of PB by bacterial metabolism in antibiotic susceptibility testing in solution as a continuation of **Chapter 6.1**.

#### 6.3.1. Prussian blue reaction mechanism

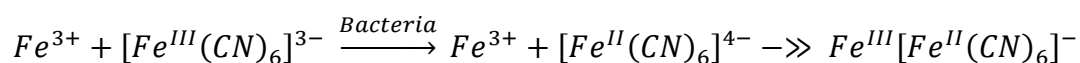
The formation of the PB complex relies on the interaction between a cyanide-complexed iron molecule and free iron ions, both at different reduction states. The most common reactions to describe PB formation are presented below [7]:



The redox state of the iron bound to the cyanide molecule does not impact the final product, resulting in PB. Providing an equimolar amount of both iron molecules results in the “soluble” form of PB, composed of nanoparticles of very small size that remain in suspension. However, if an excess of the iron (III) molecules is provided, the final product becomes “insoluble”, meaning that the particles aggregate producing the sedimentation of the PB [8]:



As already mentioned, the formation of PB can be coupled to bacterial metabolism as shown in **Figure 6.12**. The basic reaction relies on the one shown in **Chapter 6.2.1**, describing the interaction between bacteria and ferricyanide. The reaction is expanded by the introduction of a second iron (III)-based molecule (brownish molecule). Iron ions and ferricyanide cannot react directly since the iron in both cases is in iron (III) oxidative state. However, after metabolic reduction of ferricyanide, the formed ferrocyanide can react with the free iron (III) ions, resulting in the formation of PB molecules. This metabolically-mediated PB formation reaction is illustrated in the reaction below:



It needs mentioning that PB requires an acidic to neutral pH for being stable, optimally in the range of 4 – 7. As was stated in the Materials and Methods **Chapter 5.3**, the pH of the medium was always lowered to 6.6 for this reason.



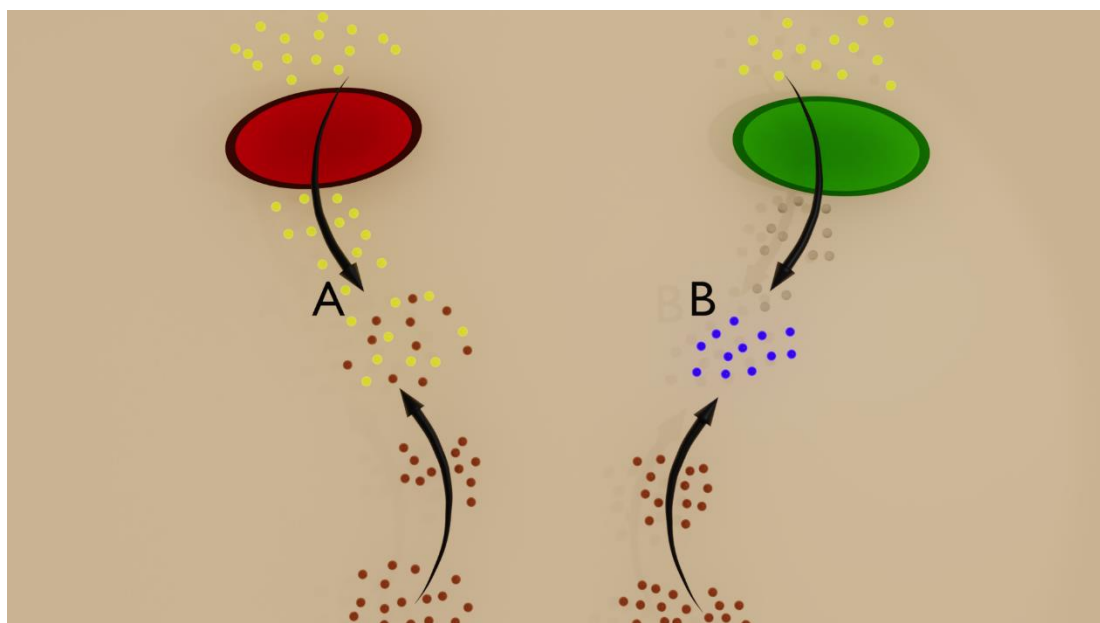


**Figure 6.12: Reaction mechanism of Prussian blue formation by bacterial metabolism.** A) ferricyanide (yellow) does not interact with dead bacteria (red), nor with the added iron (III) molecules (brown). B) Live bacteria (green) reduce the ferricyanide to ferrocyanide (colourless). The ferrocyanide will further react with the added iron (III) molecules resulting in the formation of Prussian blue (blue). (Made in Blender)

### 6.3.2. Prussian blue formation by bacterial metabolism

To verify the analytical potential of the metabolic production of PB molecules in the determination of bacterial concentration and antibiotic susceptibility testing, several bacterial concentrations were incubated with the PB precursor solution, and the PB formation was evaluated spectroscopically through the increase of the 720-750 nm peak, corresponding to the blue colour of the products. The results are summarized in **Figure 6.13**, where the full visible spectrum (from 400 – 800 nm) was acquired 0 minutes and 60 minutes after incubation in *E. coli* suspension, which was again used as model organism.

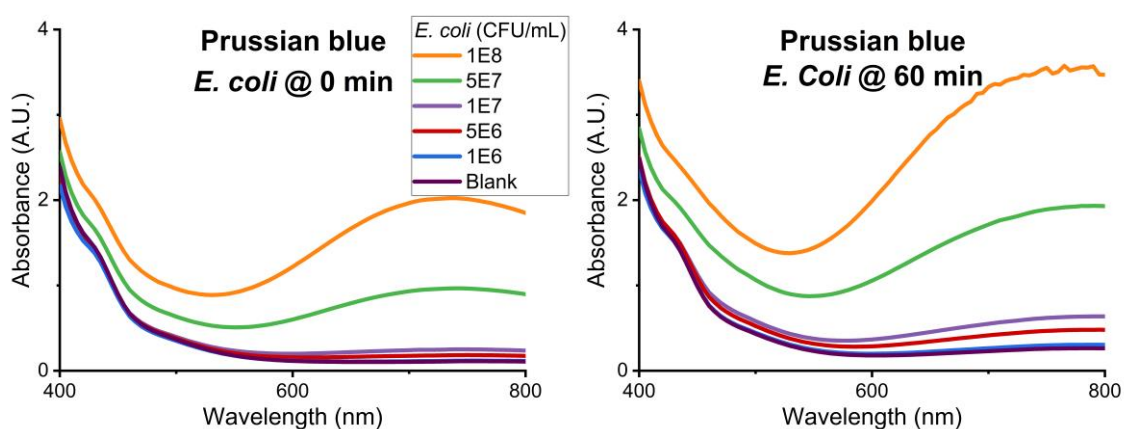


**Figure 6.13: Formation of Prussian blue by bacterial metabolism.** Using various concentrations of *E. coli* together with potassium ferricyanide and iron (III) chloride will result in the formation of Prussian blue. Prussian blue has an absorbance maximum around 720-750 nm, and is broadened due to scattering effects. Measurements were taken after 0 min and 60 min of incubation.

The formation of the characteristic Prussian blue peak was recorded in all bacterial concentrations within one hour of incubation, while the peak intensity followed the expected tendency with more intense absorbance peaks recorded by higher bacterial concentrations since presenting more metabolic activity.

Three main advantages were observed when compared to the ferricyanide-based test:

- The maximum absorbance of the peak correlated directly to the bacterial concentration without the need for bacterial scattering correction.
- The changes were observed within one hour of incubation, in contrast to the 5 hours needed for ferricyanide (for a concentration of  $5 \times 10^7$  CFU/mL).
- PB allowed the detection of a 10-fold lower bacterial concentration than ferricyanide.

However, it should be noted that, with a concentration of  $10^6$  CFU/mL, the resulting signal was barely distinguishable from the blank (control without bacteria). Furthermore, a shift in the absorbance peak was observed in the spectra of the blank, which may be associated to a possible cross-reaction between the medium and the PB precursors.

It is also evident from the results that the PB peak got wider over time, when the PB concentration increased. This may be associated to the particulate nature of PB, with particles that produce scattering particularly visible when in high concentrations. This scattering not only resulted in the broadening of the characteristic peak, but also in an increase of the overall absorbance magnitude recorded. This suggested a size of the aggregated particles above  $1 \mu\text{m}$ , being able to affect the full visible spectrum range. The formation of PB particles was here advantageous since it increased the sensitivity of the test due to the additive nature of absorption. That is, the absorbance magnitude combining PB absorption and particles scattering was higher than that attributed to each process separately. Finally, it should be emphasized that a significant peak was observed within “0 minutes” of culturing by the temporal limitation of the setup used for the assays (96-well plate reader), which required 10 minutes to read the full plate with the 96 experiments running in parallel. Higher bacterial concentrations tended to be placed towards the final corners of the plate, resulting in an additional 10 minutes incubation time before readout. This limitation is due to the size of the performed assay but can be resolved in later tests.

### 6.3.3. Optimization of the Prussian blue protocol for bacterial detection

Confirming the possibility to generate PB through bacterial metabolism, the optimal concentrations and proportions between reagents were investigated.

A first experiment was performed as proof of concept to evaluate the effect of small variations in the reagent concentration. Experiments were performed varying the concentrations of iron (III) chloride (FeCl) from 1 to 2 mM and potassium ferricyanide (FeCN) from 2 to 4 mM. The formation of PB was evaluated in a  $10^8$  CFU/mL suspensions of *E. coli* and *P. aeruginosa* by monitoring the absorbance magnitude at 720 nm for 5 hours (**Figure 6.14**).

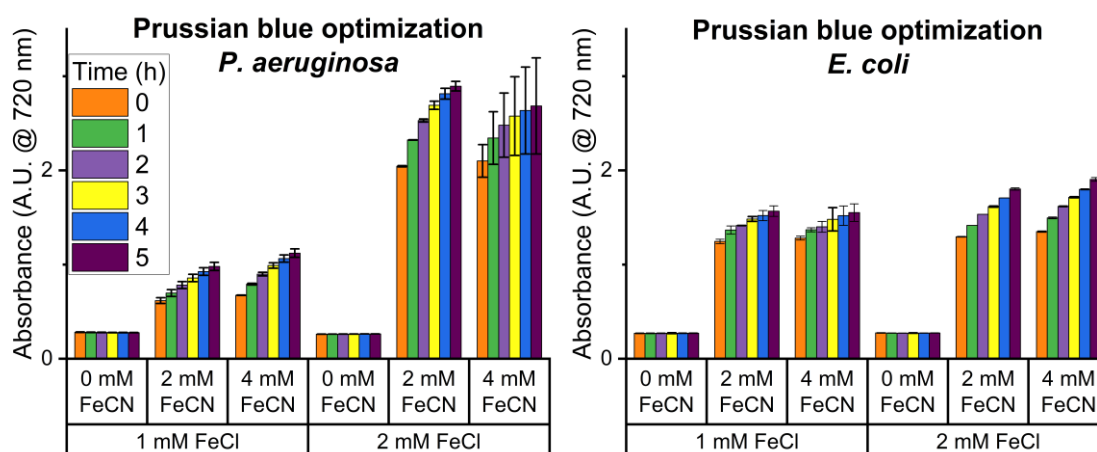


**Figure 6.14: Optimization of the Prussian blue assay.** Various concentrations of potassium ferricyanide (FeCN) (0, 2 and 4 mM) were tested against iron (III) chloride (FeCl) (1 and 2 mM). The formation of Prussian blue was tested using both *E. coli* and *P. aeruginosa* at a concentration of  $10^8$  CFU/mL. Data was acquired every hour for a total of 5 hours at a wavelength of 720 nm. (n=2)

It is clear from the results that PB formation requires both FeCN and FeCl reagents: in absence of FeCN PB formation was not observed at any condition, while all experiments combining FeCN and FeCl resulted in an increase in the absorbance magnitude associated to the presence of PB. The absorbance magnitude resulting from PB formation increased over time, confirming the kinetic nature of the metabolic generation of this compound. No significant differences were observed in the case of *E. coli* when changing the concentration of FeCN or FeCl. In the case of *P. aeruginosa*, a high increase in the absorbance was observed when increasing the FeCl concentration from 1 to 2 mM. Since apart from a higher magnitude, the kinetic change (change of absorbance magnitude over time) was also larger, the difference may be attributed to: (i) metabolic stimulation by FeCl; or (ii) a higher bacterial concentration in the 2 mM FeCl. Since all samples were prepared using the same *P. aeruginosa* stock, the most plausible explanation was that FeCl had a positive effect on the growth or metabolism of the strain, resulting in faster reductions of FeCN and thus increased PB formation. Since the stimulation was not observed in the case of *E. coli*, the most plausible explanation of this change was that bacterial concentration was slightly higher in the 2 mM FeCl preparations, which resulted in a higher PB formation and kinetic change. In conclusion, both reagents were necessary for PB formation, which was plausible in an important range of concentrations.

Since PB formation is very sensitive to the proportion of reagents and may lead to different compounds, i.e. soluble and insoluble form of PB, a second assay was made to investigate the effect of the ratios of both reagents to the metabolic formation of PB. In this case, the concentration of FeCl varied in the range from 0.1 to 10 mM, while the FeCN concentration was kept constant at 1 mM in all cases to generate the various FeCN:FeCl ratios. The precursors were incubated in an *E. coli* suspension, used as model organism, containing  $10^8$  CFU/mL of bacteria in agreement with standard susceptibility

tests. **Figure 6.15** shows the images of the suspension after 4 hours of incubation at 37 °C.

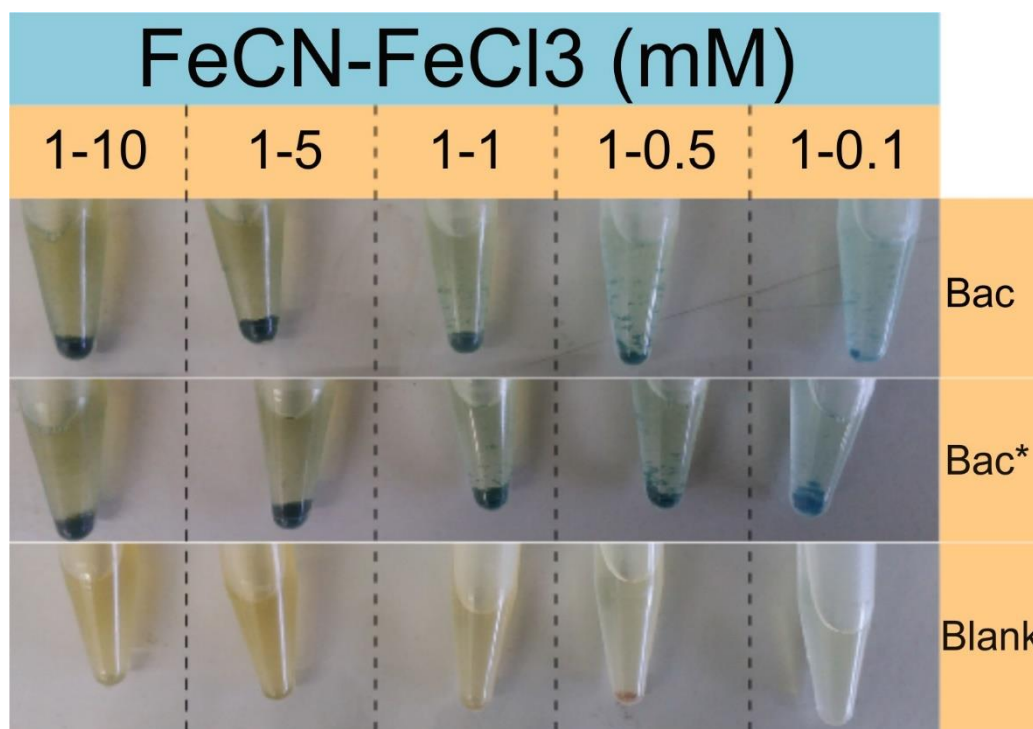


**Figure 6.15: Prussian blue precipitation experiments based on FeCN-FeCl<sub>3</sub> ratios in MH medium.** FeCN was kept at a constant concentration of 1 mM, with a FeCl<sub>3</sub> concentration between 0.1 and 10 mM. The displayed results are taken after 4 hours of growth at 37°C, with rotation at 100 rpm. Bac = 10<sup>8</sup> CFU/mL of *E. coli*, Bac\*= duplicate of Bac, Blank = MH based reference with the reagents.

In general, higher FeCl concentrations led to larger PB production, which was observed as a blue precipitate in the vial resulting from the aggregation and sedimentation of the PB particles (insoluble PB form). A maximum PB production was obtained at a FeCl concentration of 5 mM, which corresponded to a molar ratio of 1:5 FeCN:FeCl. Interestingly, besides from deeper colour intensity, the solubility of the PB also varied with the proportion of the precursor reagents. That is, samples with lower FeCl concentrations were bluer than those with higher concentrations. Also noticeable, there was an important precipitate formation in the blank, which was especially visible in the 0.5 mM sample. Even when the amount of precipitate was much smaller than in the samples, its formation in the blank may have detrimental effects on the final PB assay (i.e. reduction of sensitivity and dynamic range in the analysis of bacteria due to high background noise). This aspect should be taken into consideration and evaluated in next sections.

#### 6.3.4. Metabolic formation of Prussian blue in the determination of MIC

To test the potential of the metabolic formation of PB as metabolic indicator in fast susceptibility testing, *E. coli* suspensions (from 10<sup>6</sup> to 10<sup>8</sup> CFU/mL) were incubated in Kmc solutions in the range between 0.01 and 4 mg/mL of antibiotic. **Figure 6.16** shows the absorbance magnitude at 720 nm after 30 and 60 min of incubation.

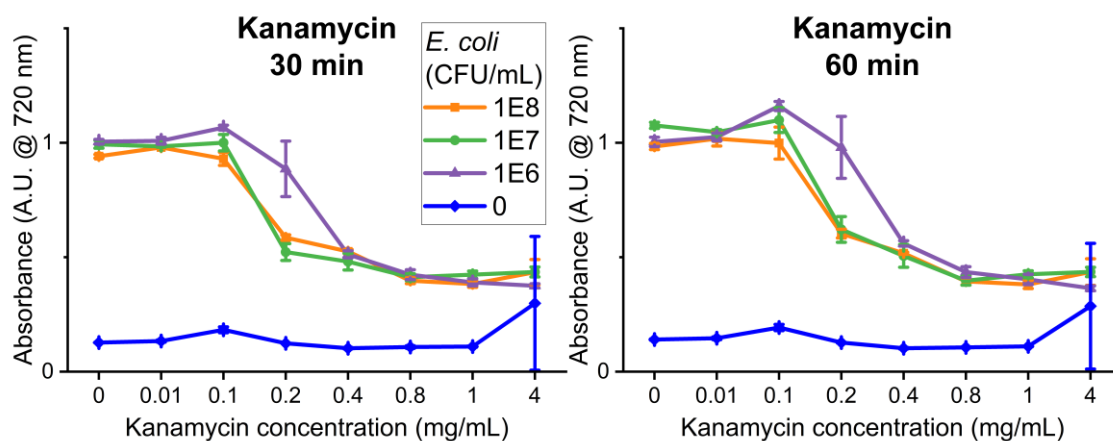


**Figure 6.16: MIC determination of *E. coli* against kanamycin using Prussian blue.** Various bacterial concentrations were used against a gradient of kanamycin antibiotic concentration. For the formation of Prussian blue, a concentration of 4 mM FeCN and 1 mM FeCl were used. Results were measured at 720 nm after 30 and 60 min. (n=3)

In the plots, the reduction of bacterial metabolism when increasing the antibiotic concentration is clearly observed as a decrease in the metabolic formation of PB. Furthermore, the behaviour was independent on the tested bacterial concentrations, and in all cases, the minimum inhibitory concentration (MIC), defined as the lowest concentration in which bacterial growth is inhibited, was found to be in the range between 0.2 and 0.4 mg/mL. The nearly constant blank (with the exception of the 4 mg/mL sample, which was considered to be an outlier resulting from microbial contamination), indicates that the antibiotic did not cross-react with any of the PB precursors. The results confirmed the potential of the PB-based protocol in susceptibility testing.

Next, the PB-based test was validated in standard MIC testing (i.e. standard BMD tests, with  $5 \times 10^5$  CFU/mL of bacteria and MIC determination after 20-24 hours of incubation). The PB-based assay was evaluated against a number of antibiotics and using *E. coli* ATCC 25922 as model organism. The antibiotics were selected for their bactericidal activity and availability of the EUCAST quality control values. Since the PB assay is directly compatible with standard BMD, both were performed on the same 96-well microtiter plate, with the same bacterial preparation and at the same time for comparison. Although each sample was analysed spectroscopically every hour, MIC values were determined after 20 hours of incubation, thus following the standard BMD protocol with the aim of standardization. The overall results are summarized in **Table 6.2**.

**Table 6.2: Summary of various MIC tests performed using Prussian blue generation as indicator.** The bacteria used in the experiments was *E. coli* ATCC 25922. Results are grouped by antibiotic, and ordered chronologically. Multiple tests on the same plate are depicted in their number of repetition n. The final column refers to the data provided by EUCAST, used as quality control in these experiments. BMD=broth microdilution, PB=Prussian blue, QC EUCAST=quality control from European committee on Antimicrobial Susceptibility Testing. PB was formed using the precursors 4 mM FeCN and 1 mM FeCl.

Antibiotic	BMD (mg/mL)	PB (mg/mL)	QC EUCAST (mg/mL)
Ciprofloxacin	2 <sup>-5</sup>	2 <sup>-2</sup> (n=2)	2 <sup>-7</sup>
Fosfomicin	0.5	4 – 8 (n=2)	1
Gentamicin	2	4 (n=2)	0.5
	1	16	
	1	>16 (n=2)	
	1	>16 (n=2)	

As shown in the table, all BMD methods adhere to the QC values (within a factor of 2, as described before), with the exception of ciprofloxacin. The difference was attributed to the solubility and required low concentration of the antibiotic. Not obtaining a fully homogeneous solution, due to an incomplete dissolve, will propagate towards a big deviation after the high number of required dilutions.

Conversely, the MIC value provided by the PB test differed greatly from the BMD and QC, always providing values larger than those obtained by the other two protocols. This difference was associated to some reactivity of FeCl, resulting in the precipitation of insoluble iron-complexes that penalized MIC determinations. Also, as it was described in **Chapter 6.2.3**, ferricyanide might have a negative effect on the antimicrobial properties of the antibiotic. Since FeCN is still a precursor, its influence on the antibiotics could still occur. Finally, PB test presented an additional drawback regarding the time-to-result. Although in **Figure 6.16** the results were obtained in 1 hour, when decreasing bacterial concentration to 10<sup>5</sup> cfu/mL, around 20 hours were necessary to provide reliable results, barely improved the standard methods.

**In summary, even when PB has a higher extinction coefficient, leading to higher sensitivities, the stability of the iron (III) chloride in water was detrimental for the assay. Furthermore, the iron (III) chloride indicated possible reactivity leading to precipitation, preventing optimal MIC determination. For all these reasons, the metabolic formation of PB following the protocol detailed in this section should not be considered ideal for susceptibility testing.**

## 6.4. Cyanotype-based protocol

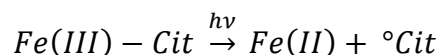
Based on the previous limitation on the use of FeCl in the MIC determination, this reagent was substituted by ferric ammonium citrate as iron donor in the formation of PB. The reason for selecting this iron donor was twofold:

- Strong and stable iron-based complex: The iron is strongly bound to the citrate, preventing its reduction by any of the other reagents present in the medium, including ferrocyanide, antibiotics or bacteria, among others. This has a double effect: reduction of cross-reactivity and decrease in the background noise, something already reported in the previous strategies.
- Photo-catalytic free-iron release: Simple light irradiation will cause the release of free irons to the medium by breaking the iron-citrate bond. It confers this molecule (and the system) with a high control of the reaction through a simple light irradiation process, being able to select the moment when the iron ions are released to the medium and the reaction starts.

This light-mediated formation of PB has been widely used in photography and is known as cyanotype reaction. For this reason, the protocol involving the use of ferric ammonium citrate and light will be named as cyanotype-based assay.

### 6.4.1. Cyanotype-based bacterial detection reaction mechanism

The cyanotype reaction mentioned above relies on the reduction of the iron from a ferric ammonium citrate molecule by UV irradiation, resulting in a free iron (II) ion and a citrate radical. The free iron (II) iron further reacts with the ferricyanide towards the formation of PB as explained in **Chapter 6.3.1**. The basic cyanotype reaction works as follows:



Even though the cyanotype reaction has been extensively used, the full mechanism is not fully understood and controversial in some aspects.

A variation of the previous protocol is here employed in the detection of bacteria for fast susceptibility testing, where conventional UV light is substituted by broadband white light to minimize the bactericidal effects of the energetic UV radiation. In this case, ferric ammonium citrate is used as free iron donor, to interact with the ferrocyanide reduced by bacteria for further PB formation. A schematic overview of the photochemical cyanotype-based reaction is shown in **Figure 6.17**. Ferricyanide is reduced by the metabolism of live bacteria to ferrocyanide, a reduction taking place when live bacteria are present (but not when dead or absent). Iron-cyanide molecules, either ferricyanide or metabolic ferrocyanide, cannot react with ferric ammonium citrate molecules since the iron in this complex is too strongly bound to be accessible, and thus no Prussian blue is formed (D). Upon illumination, ferric ammonium citrate molecules are energized, producing an activated intermediate that results in the release of free-iron ions to the medium, which enables the formation of PB particles (C). The mechanism combining ferricyanide metabolism, ferric ammonium citrate photo-

oxidation and reaction between the two previous reagents is still controversial but the principle's first approach is presented in **Chapter 6.4.4**.

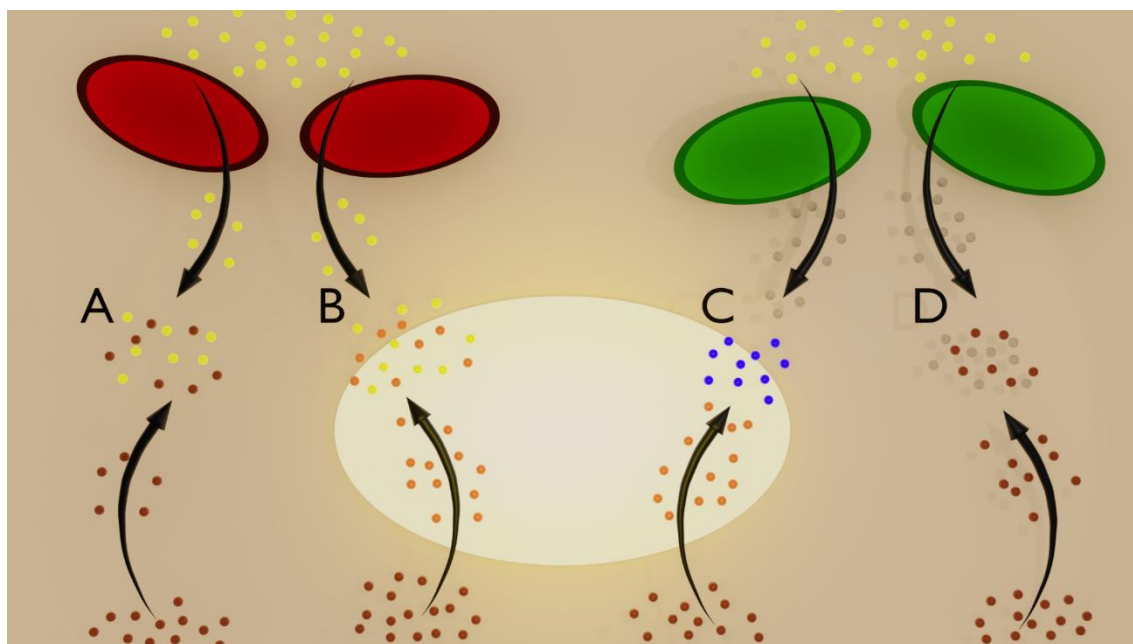


**Figure 6.17: Reaction mechanism of cyanotype based Prussian blue formation by bacterial metabolism.** A) dead bacteria (red) do not interact with ferricyanide (yellow) and neither reacts with ferric ammonium citrate (brown). B) ferric ammonium citrate is “energized” under light (orange), but does not interact with the bacteria nor with ferricyanide. C) Live bacteria (green) reduce ferricyanide to ferrocyanide (transparent), which will interact with the charged ferric ammonium citrate to form Prussian blue (blue). D) ferrocyanide does not react with uncharged ferric ammonium citrate. (Made in Blender)

#### 6.4.2. Cyanotype-based reaction for bacterial detection

The usage of cyanotype reaction for bacterial detection is novel and the concept has to be proven. In order to demonstrate the photochemical nature of the reaction mechanism, two experiments were always run in parallel, one in dark and another under visible light irradiation. Additional controls were used in this case to ensure the reliability and to understand the underlying mechanism, such as the blank (with the reagent precursors, but without bacteria) or a second negative control with bacteria but without the cyanotype precursors. The results of a first assay used as proof-of-concept of the measurement principle are presented in **Figure 6.18**. The experimental conditions were: 1.25 mM ferricyanide, 5 mM ammonium citrate concentration,  $10^6$  CFU/mL of *E. coli* ATCC 25922 and 7 hours of assay, conditions adapted from **Chapter 6.3** using ferricyanide and iron (III) chloride.



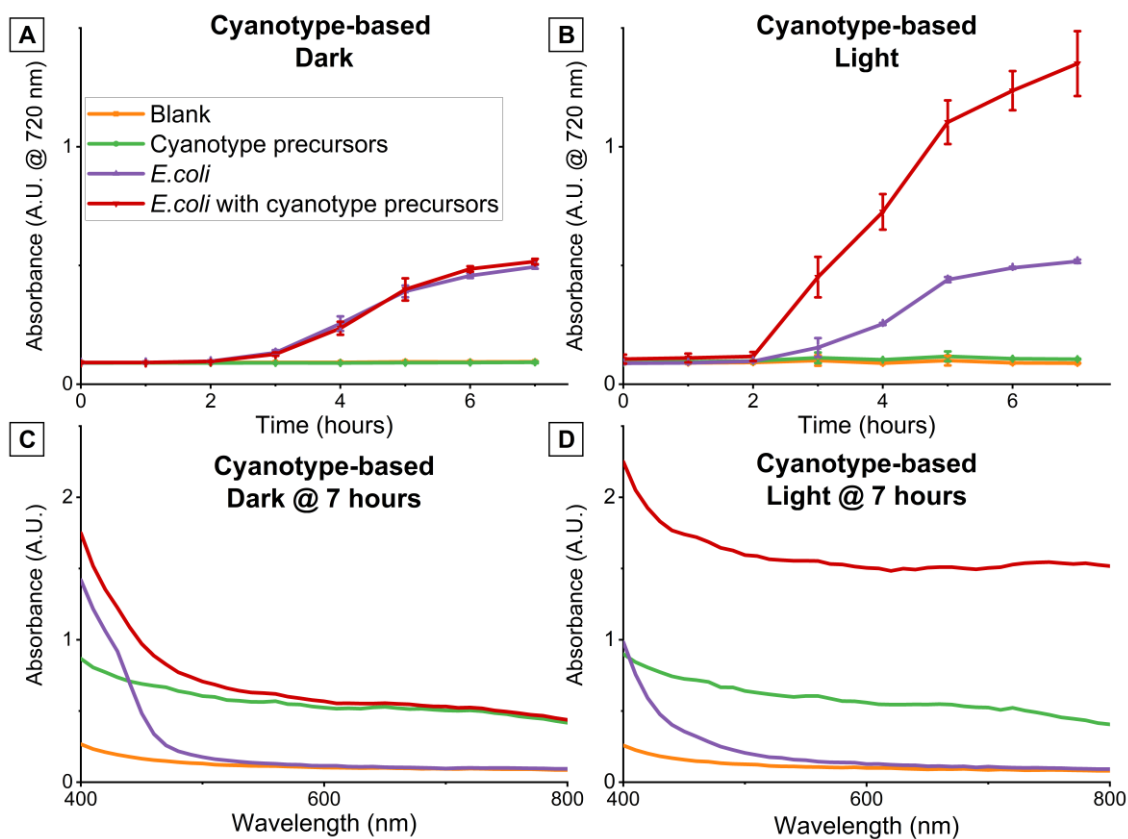


**Figure 6.18: Cyanotype-based reaction proof of concept.** Two experiments performed in parallel, where one plate was continuously kept in dark, whereas the other one was continuously exposed to LED light. Absorbance measurements were performed at 720 nm every hour. A bacterial starting concentration of  $10^6$  CFU/mL of *E. coli* ATCC 25922 was used. The reagents refer to a 1.25 mM ferricyanide and 5 mM ferric ammonium citrate concentration. The bottom 2 plots indicate the absorbance of each condition after 7 hours over the entire wavelength. (n=2)

As it can be observed, in absence of bacteria no changes are recorded for the duration of the experiment. It confirmed the lack of reaction between ferricyanide, iron citrate and the medium, either with or without light irradiation (note that both iron species after light-mediated iron release should have the same oxidative state, according to the proposed mechanism, and should not react to form PB molecules). Thus, this strategy dramatically reduced the background noise of the assay.

Furthermore, in the absence of light, no significant differences are found between samples containing or not the cyanotype precursors. This confirmed the statement that the iron from the iron citrate was not freely available to interact with the reduced ferrocyanide molecules. This result was further emphasised in **Figure 6.18 C**, where the presence or absence of the precursors did not impact the absorbance spectrum. In these spectra, the absorbance bands observed around 400 nm were associated to the cyanotype precursors since both present absorbance peaks in this region. The increase in the absorbance magnitude was associated to bacterial scattering.

Conversely, light irradiation induced the release of free iron ions, which interacted with the iron-cyanide complexes to produce PB. This is clearly shown in the absorbance spectra of the sample after 7 hours, which presents a peak with a maximum around 720

nm, corresponding to PB. **Figure 6.18 D** illustrates the absorbance spectra of the four conditions, taken after 7 hours. As mentioned before, the PB particles contributed highly to the absorbance through both absorbance in the range between 680 and 780 nm and scattering events due to the formation of particles. In this case, the contribution of scattering was much higher than the specific absorption, which was almost impossible to distinguish in the spectra. The light-mediated and metabolically-induced formation of PB resulted in a significant increase in absorbance within 3 hours, which may contribute to the development of a fast bioassay. It should be emphasized that the response resembled a conventional growth curve of the bacteria, but with an amplified signal due to PB formation.

In order to optimize the cyanotype-based photochemical reaction for bacterial detection, a new set of experiments was conducted at several experimental conditions (i.e. ferricyanide and ferric ammonium citrate concentrations and proportions, and bacterial concentrations). Experiments were performed under continuous illumination and at room temperature. Most relevant results are presented in **Figure 6.19**. Using three bacterial concentrations ( $5 \times 10^7$ ,  $5 \times 10^6$  and  $5 \times 10^5$  CFU/mL) and three concentration sets of the precursors (20 – 30, 40 – 60 and 80 – 120 mM ferricyanide – ferric ammonium citrate), a picture of the plate was taken automatically every 10 minutes and analysed by visual inspection. Higher precursor concentrations were tried to compensate for the lack of heating in the sample, and to generate strong visual changes. In general terms, the fastest and most intense PB formation was observed for the higher bacterial and precursor concentrations. From these two parameters, bacterial concentration had a stronger impact on PB formation than the precursor concentration. Thus, at the lowest bacterial concentration, PB formation was only observed at the highest precursor concentration., Increasing 10-fold higher bacterial concentration enabled PB formation at half the precursor concentration after sufficient amount of time. Additionally, the first appearance of PB depended on the initial bacterial concentration in the sample, requiring approximately 6-8 hours of extra incubation time per each 10-fold dilution.

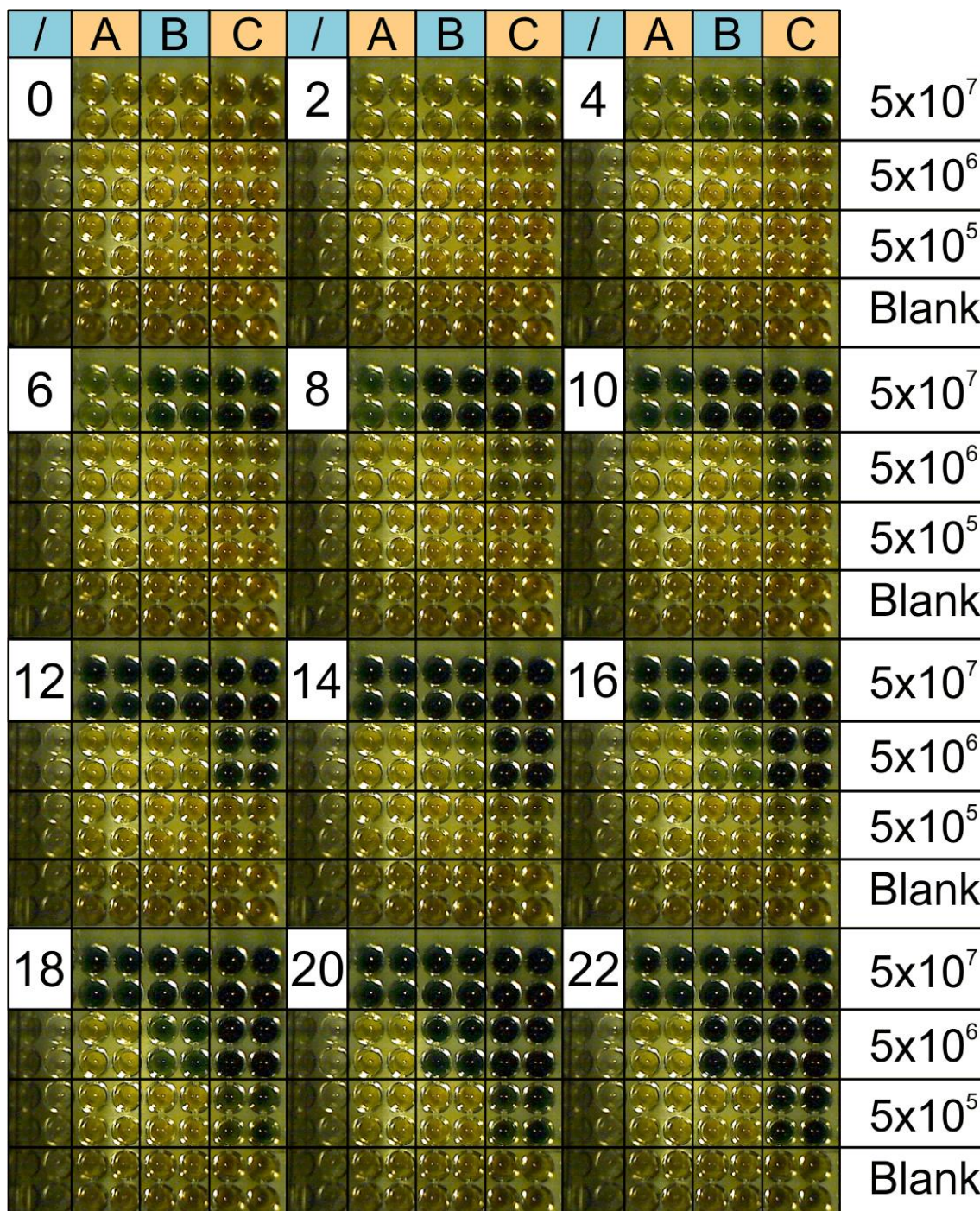


**Figure 6.19: Images of the cyanotyping based protocol for Prussian blue formation by bacterial metabolism.** The time of acquisition is highlighted in each image and is denoted in hours. *E. coli* was used as bacterial organism with each concentration representing the amount of colony forming units per millilitre (CFU/mL). The ferricyanide – ferric ammonium citrate concentrations were 20 – 30, 40 – 60 and 80 – 120 mM for A, B and C respectively.

Therefore, the cyanotype reaction shows great potential for the detection of low bacterial concentrations, within a reasonable reaction time (<5 hours). However, as explained before, the reaction itself is not well understood. The following experiments will optimize the cyanotype variant for bacterial detection, and learn more about the reaction itself.

6.4.3. Optimization of the cyanotype-based protocol for bacterial detection

Even though the underlying reason and mechanisms are still controversial, it was evident from previous assays involving iron-based reagents, like the combination of FeCN and FeCL in **Chapter 6.3.3**, that the ratios of the PB precursors may have an important influence on the assay. In cyanotype, ferric ammonium citrate concentrations ranging from 0 to 40 mM were tested against ferricyanide solutions containing between 0 and 40 mM, both in dark and in light. Data belonging to time 0 and after 5 hours of incubation in  $5 \times 10^5$  CFU/mL of *E. coli* ATCC 25922 are shown in **Figure 6.20** and **Figure 6.21** corresponding to experiments in the dark and light, respectively. The results were measured every hour, for a total of 24 hours, over the entire visible spectrum, with the absorbance plotted at 720 nm. Only four conditions for each experiment are plotted in the figures for clarity. The rest of the results are included in **Supplementary 11.2**.

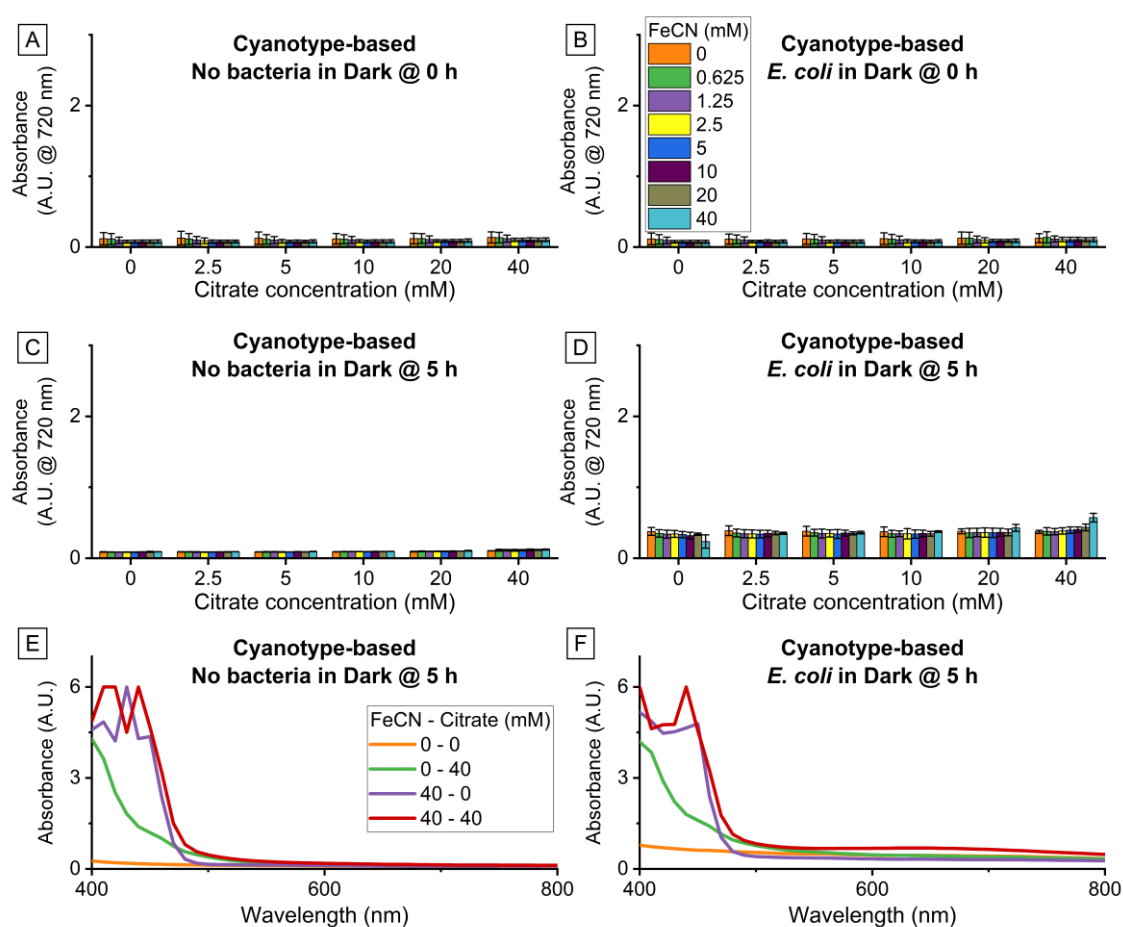


**Figure 6.20: Cyanotyping-based reaction optimization under dark conditions.** A) No bacteria are present, with an incubation time of 0 hours. B)  $5 \times 10^5$  CFU/mL of *E. coli* ATCC 25922 with an incubation time of 0 hours. C) No bacteria are present, with an incubation time of 5 hours. D)  $5 \times 10^5$  CFU/mL of *E. coli* ATCC 25922 with an incubation time of 5 hours. E) Absorbance spectra for 4 conditions, without bacteria, after an incubation time of 5 hours. F) Absorbance spectra for 4 conditions, with  $5 \times 10^5$  CFU/mL of *E. coli* ATCC 25922, after an incubation time of 5 hours. Each group of columns refers to a single ferric ammonium citrate concentration. Each colour corresponds to a specific ferricyanide concentration. Data is plotted at a wavelength of 720 nm for A – D. (n=3)

In the absence of light, the lack of PB formation at any of the conditions was apparent. The constant signal for any of the reagent concentrations in the absence of bacteria indicated that the reagents did not react with either the media or between each other. When bacteria were present, no apparent PB formation was observed either. The only exception was when combining 40 mM citrate with a 40 mM FeCN concentration. The high concentration of both reagents in the precursor solution led to the formation of PB, even if it was very little (see the small band at 720 nm shown in **Figure 6.20 F**).

The absorbance in samples with bacteria was higher than without (**Figure 6.20 E and F**), which was associated to bacterial scattering. Although there were no significant differences between absorbance values at any of the reagent conditions ( $p < 0.05$ ), in the case of the precursor solution containing 40 mM FeCN without citrate, a slight reduction in absorbance was observed. This may be attributed to some toxicity of the ferricyanide when used at high concentrations, as is the case here, which limited bacterial proliferation, reducing the magnitude of bacterial scattering.

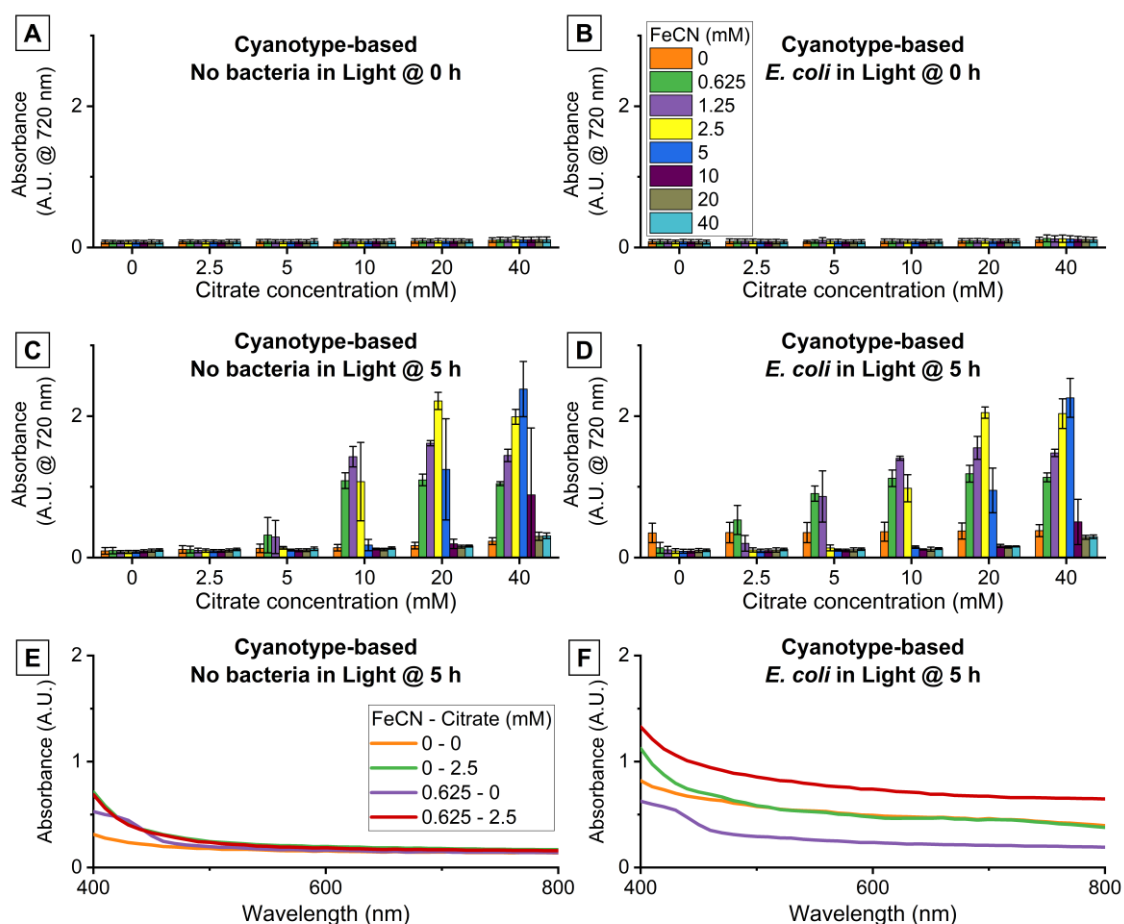


**Figure 6.21: Cyanotype-based reaction optimization under light conditions.** A) No bacteria are present, with an incubation time of 0 hours. B)  $5 \times 10^5$  CFU/mL of *E. coli* ATCC25922 with an incubation time of 0 hours. C) No bacteria are present, with an incubation time of 5 hours. D)  $5 \times 10^5$  CFU/mL of *E. coli* ATCC25922 with an incubation time of 5 hours. E) Absorbance spectra for 4 conditions, without bacteria, after an incubation time of 5 hours. F) Absorbance spectra for 4 conditions, with  $5 \times 10^5$  CFU/mL of *E. coli* ATCC 25922, after an incubation time of 5 hours. Each group of columns refers to a single ferric ammonium citrate concentration. Each colour corresponds to a specific ferricyanide concentration. Data is plotted at a wavelength of 720 nm for A – D. (n=3)

When the sample was continuously illuminated (5 hours of constant irradiation with visible light), the spectra changed dramatically. In the absence of bacteria, PB formation was only observed for precursor solutions with citrate concentrations above 10 mM and when combined with specific FeCN concentrations. Concretely:

- a) 0.625 – 2.5 mM FeCN for 10 mM citrate;
- b) 0.625 – 5 mM FeCN for 20 mM citrate;
- c) 0.625 – 10 mM FeCN for 40 mM citrate.

Furthermore, maximum absorbance occurs at a different concentration for each citrate concentration,

- a) 1.25 mM FeCN for 10 mM citrate;
- b) 2.5 mM FeCN for 20 mM citrate;
- c) 5 mM FeCN for 40 mM citrate.

It was thus evident that a ratio of 8-1 (citrate:FeCN) was optimal for PB formation, which differed from conventional cyanotype processes for photochemical production of PB where a 3 – 1 ratio (approximately 760 mM citrate and 240 mM FeCN) is reported as optimal [9]. Also relevant, a minimum of 10 mM citrate was necessary to produce detectable PB concentrations within 5 hours of experiment.

Three conditions were identified where the presence of bacteria had a significant increment on PB formation when compared to controls without bacteria, namely:

- a) 0.625 – 2.5 mM (FeCN – citrate);
- b) 0.625 – 5 mM (FeCN – citrate);
- c) 1.25 – 5 mM (FeCN – citrate).

All of them presented low cyanotype precursor concentrations and a molar ratio between 4 and 8. From the three, the first one was discarded since the increase was not significantly higher than the biomass itself.

Since the aim of the test was to detect low bacterial concentrations, the signal of the background should be kept as small as possible for sensitive bacterial detection. Hence, the optimal precursor solution was set at 2.5 mM citrate and 0.625 mM FeCN (see **Figure 6.22**; image corresponds to the results after 5 hours of experiment and the red arrow indicates the optimal condition).

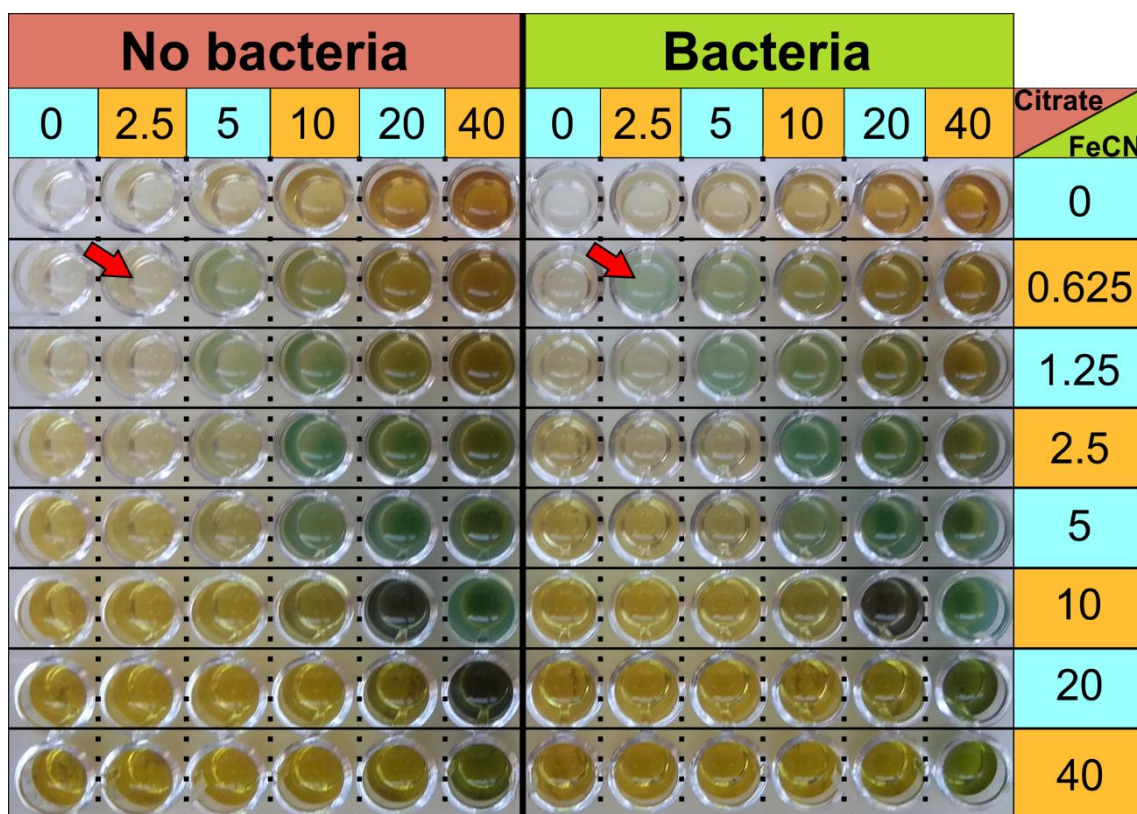


**Figure 6.22: Picture of the cyanotype-based reaction optimization under light conditions.** The picture corresponds to the data from **Figure 6.21 C and D**. Image was taken after 5 hours of growth. FeCN corresponds to potassium ferric cyanide, with the concentration values expressed in mM. Citrate corresponds to ferric ammonium citrate, with the concentration values expressed in mM. A bacterial concentration of  $5 \times 10^5$  CFU/mL of *E. coli* ATCC 25922 was used. The red arrows indicate the optimal condition for the cyanotyping experiment, maximizing the Prussian blue formation due to bacteria, but minimizing the background colour.

Once the composition of the precursor solution was optimized, the cyanotype-based test was studied by considering the response time and the limit of detection of the assay. Regarding this, uraemia (urine infection) involves the presence of more than  $10^5$  CFU/mL [10], while sepsis (blood infection) is considered when the concentration of bacteria in blood reaches 100-1000 CFU/mL [11]. For the experiment, a 10-fold dilution series of *E. coli* was used, and bacteria with and without cyanotype precursors were tested in parallel for comparison, during 24 hours. Results are summarized in **Figure 6.23**, with absorbance values measured at 720 nm.

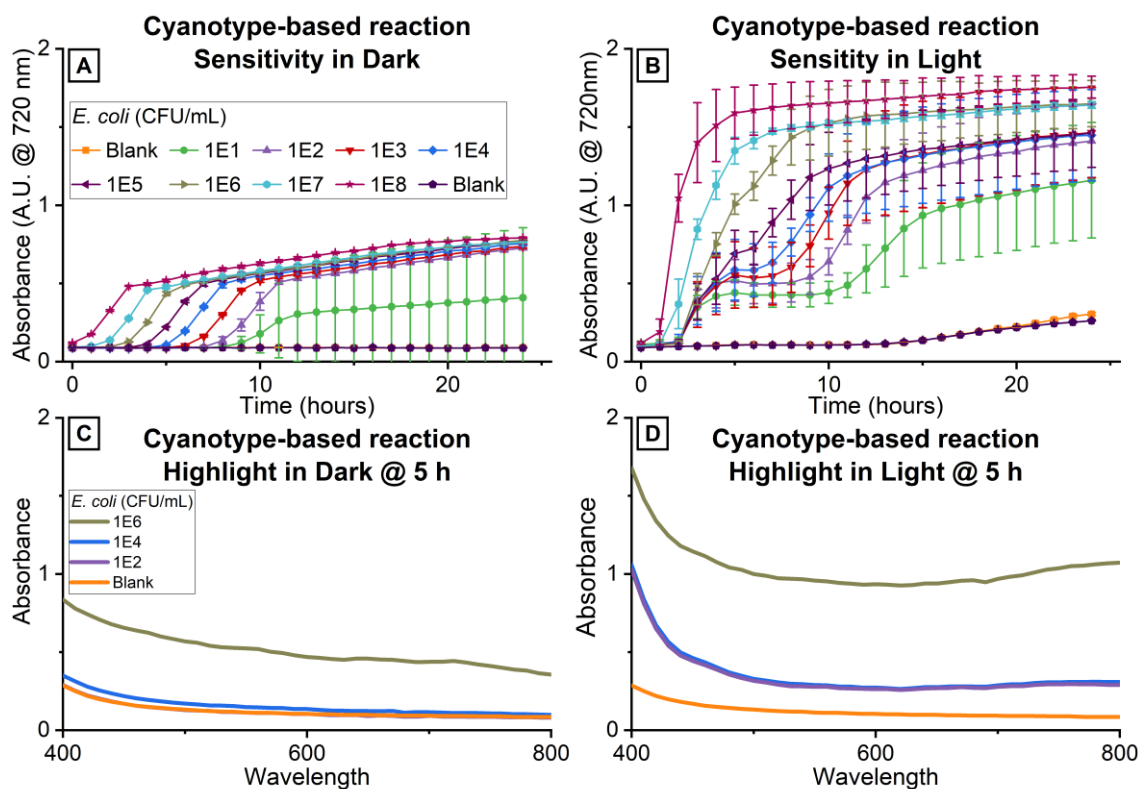


**Figure 6.23: Cyanotype-based protocol sensitivity in dark and light.** A) shows a standard bacterial growth assay, using 10-fold dilution series of *E. coli* ATCC 25922. The measurement was performed using MH medium without illumination. B) shows the formation of Prussian blue under various bacterial concentrations. Again, a 10-fold dilution series of *E. coli* was used. For the cyanotyping, a 2.5 mM iron (III) citrate and a 0.625 mM ferricyanide were used. Samples were illuminated for a total of 5 hours, after which samples were kept inside the dark inside the plate reader. C) absorbance spectra for 4 conditions of graph A after 5 hours of incubation without illumination. D) absorbance spectra for 4 conditions of graph B after 5 hours of incubation with continuous illumination. Results were measured and plotted at 720 nm for A and B. Measurements were taken at every 10 nm between 400 nm and 800 nm for C and D. (n=6)

On the left, bacterial proliferation without cyanotype precursors was monitored through the absorbance magnitude changes resulting from bacterial scattering at each bacterial concentration. In all cases, bacterial proliferation followed a conventional growth curve (see **Chapter 3.1.2**) with a lag phase, exponential phase and stationary phase that depended on the initial concentration in the sample (**Figure 6.23 A**). Thus, samples with lower concentrations required longer incubation times to reach detectable concentrations able to be monitored spectroscopically. In the exponential phase, *E. coli* presented a fast increase in absorbance and concentration of around 10x every hour, which is in agreement with the theoretical duplication time of this microorganism which is 20 minutes (i.e. three duplications per hour, which is  $2^3 = 8 \approx 10$  every hour). The completely flat blank measurements also indicate no contamination of the sample. Particularly remarkable is the case of the sample containing  $1^1$  or 10 CFU/mL (green line in the figure), which is characterized by huge error bars. It should be noted that in this case, since the volume of the samples was only 100  $\mu$ L per well, the sample may contain either 0 or 1 bacterium, turning the assay into a probability test. Since statistically only



half of the wells had bacteria, the standard deviation corresponding to repetitive assays was huge.

Important differences were observed when incorporating PB precursors. In all cases, the final absorbance increased and the magnitude at the end of the experiment was higher than samples without precursors. Even when the solution was clearly blue, the spectral analysis of the samples did not report a band at 720 associated to PB formation but an increase in the full wavelength spectrum, which may be attributed to the scattering of PB particles. Regarding the kinetic variation of the absorbance magnitude, the three samples with highest bacterial concentrations showed growth curves resembling those obtained by the samples without precursor, with inherent signal amplification associated to the photocatalytic PB formation, which doubled the response (and the sensitivity) of the assay.

The other bacterial samples presented a singular behaviour, not previously reported, consisting of a sudden absorbance increase, followed by a stabilization and a second increase. The first increase took place three hours after incubation with continuous light irradiation, and was independent on the bacterial concentration, although only happening in these samples containing bacteria and not in the blanks (**Figure 6.23 B**). The time (lag phase) and magnitude of the second increase was concentration-dependant, and resembled the previous bacterial growth without precursor but amplified by PB formation. It is remarkable that the light was turned off after 5 hours of incubation, which corresponded to the time that the initial increase stopped. However, longer irradiation times did not modify the previous behaviour. The changes reported in the initial stage, even not correlated to bacterial concentration, are very relevant since they provided a way to detect very low bacterial concentrations (yes/no system), which is particularly important to identify early stages of infection. Finally, blanks in this case were not as stable as in the previous experiment without precursors but presented some increment on the absorbance magnitude after 13 – 14 hours of incubation. This increase may be associated to some reactions between precursor reagents and components of the culture media that produce particles and thus scattering. However, it should not have a remarkable effect on the assay since very small in magnitude and delayed beyond the conventional assay time (4-5 hours).

#### 6.4.4. Cyanotype-based mechanism for the detection of very low bacterial concentrations characterization

Previous experiments evidenced a new photochemical reaction based on the cyanotype process which enabled the detection of very low bacterial concentrations and was not reported before. To understand the mechanism of such reaction, a set of spectro-electrochemical experiments were performed aiming to identify the reagents and intermediate compounds involved in the reaction.

Spectro-electrochemistry combines two tests that run in parallel, namely absorbance spectroscopy and cyclic voltammetry. Due to the importance of understanding each and any interaction between the various reagents of the photochemical reaction, experiments were performed simultaneously in light and dark and using controls for

every combination of reagent, which used at the optimal concentration determined previously. The tests were run for a total of 5 hours, and measurements were taken every hour.

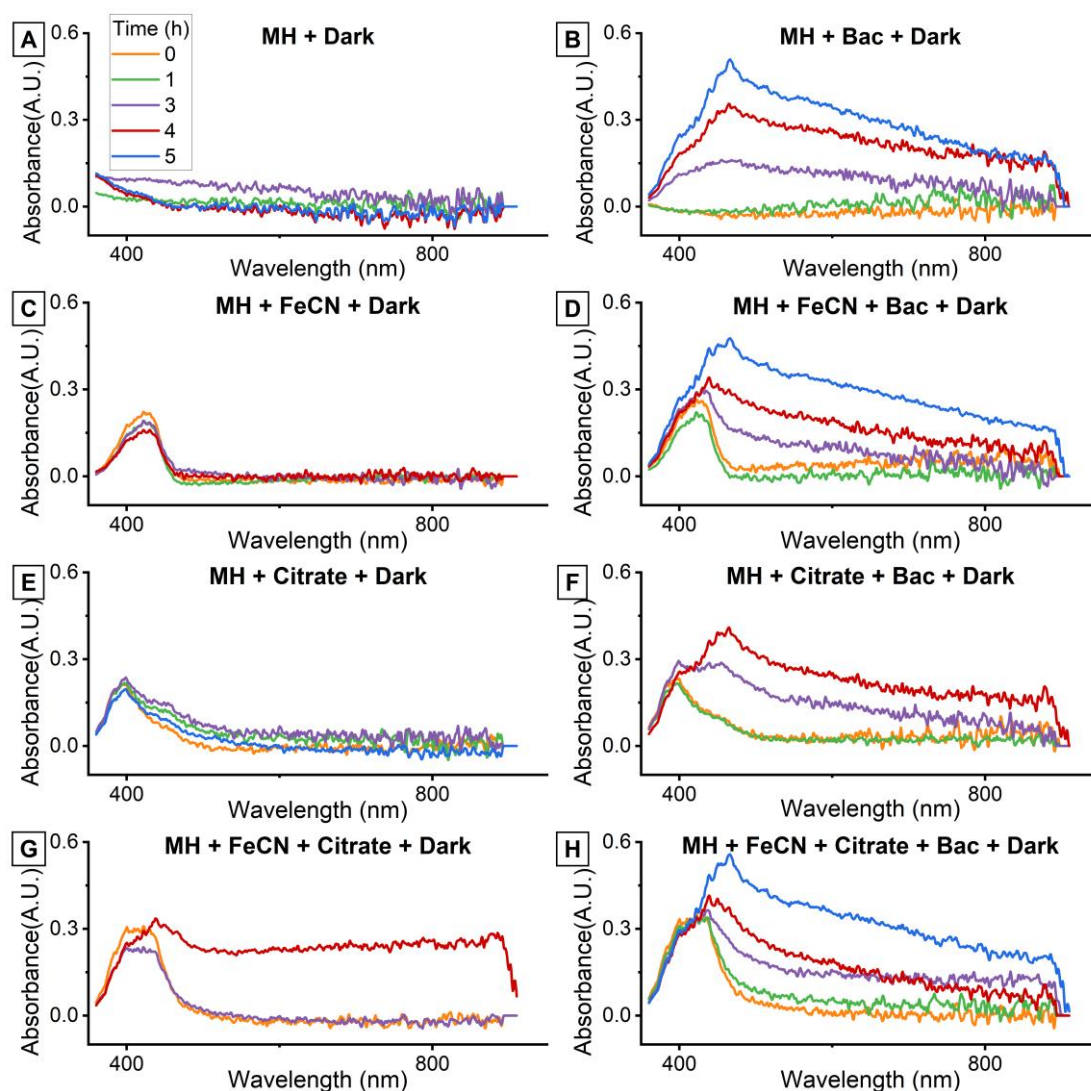


**Figure 6.24: Evaluation of performance and reaction between the various reagents of the cyanotype-based protocol performed in dark.** Measurements were taken every hour, for a total of 5 hours, at every nm between 350 nm and 900 nm. For the cyanotyping, a 2.5 mM iron (III) citrate and a 0.625 mM ferricyanide were used. A bacterial concentration of  $5 \times 10^5$  CFU/mL of *E. coli* ATCC 25922 was used. Lines missing in the plots were omitted due to instrumental errors.

The first set of experiments was performed without illumination to evaluate cross-reactivity between reagents, as summarized in **Figure 6.24**. The four graphs on the left show the lack of reactivity between MH culture medium, ferricyanide and iron citrate since these plots did not present changes in the absorbance spectra over time. Only minor changes were observed in **graph G** after 4 hours of incubation, which were attributed to some contamination. The four graphs on the right replicated the experiments in the left but including bacteria to study their influence in the reaction. The same spectral variation was observed by the four plots, which was due to bacterial

scattering. The impact of biomass scattering on absorbance spectra was very important (i.e. broadband change in the full wavelength range under study) and prevented the observation of additional changes associated to other reactions between reagents. However, due to the similarity between plot B, only containing bacteria proliferating in culture medium, and the other three plots, it may be concluded that there was no Prussian blue formation in any of the experimental conditions previously studied, demonstrating that the light was key for the activation of the photochemical reaction.

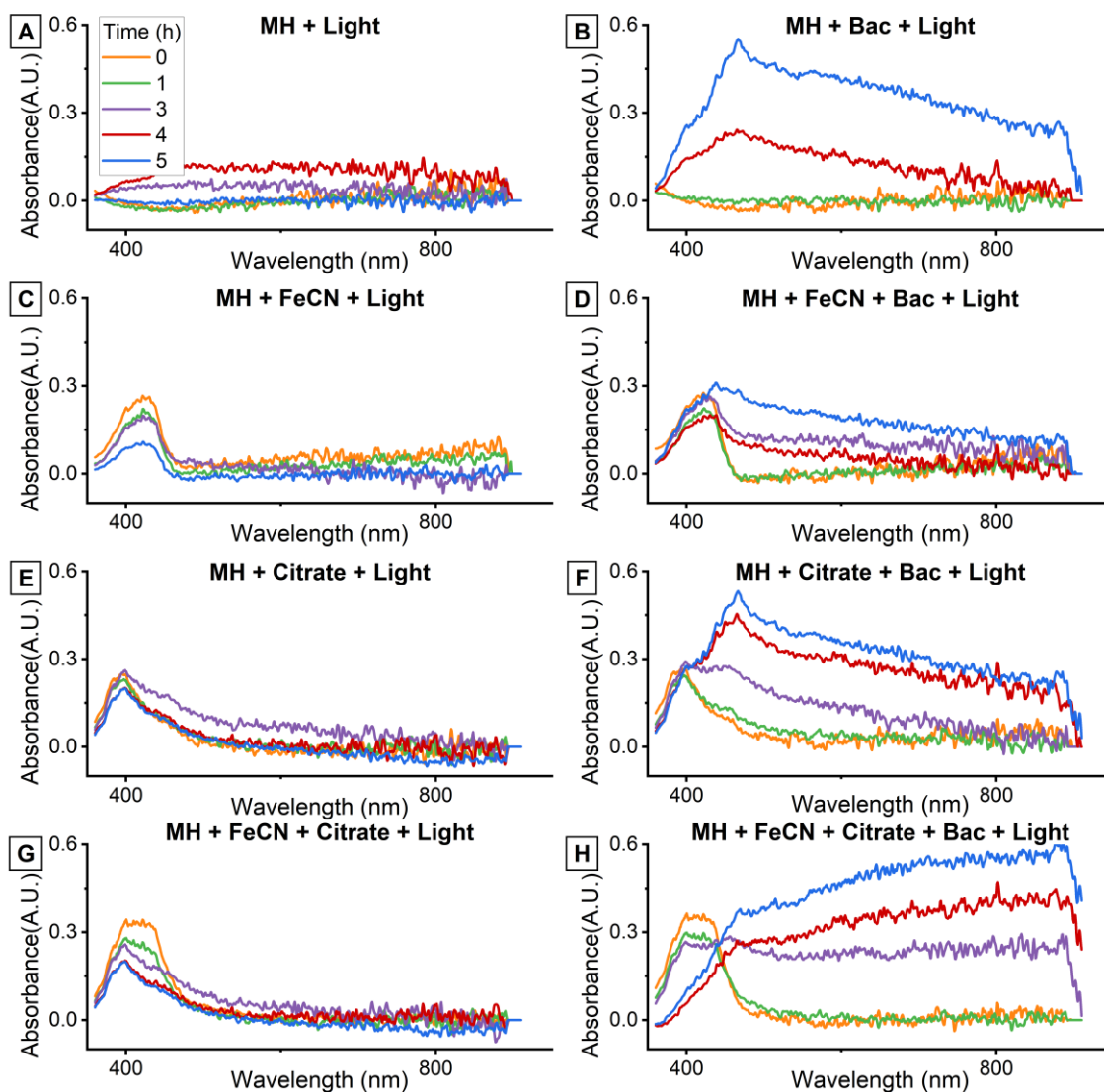


**Figure 6.25: Evaluation of performance and reaction between the various reagents of the cyanotype-based protocol performed under continuous illumination.** Measurements were taken every hour, for a total of 5 hours, at every nm between 350 nm and 900 nm. For the cyanotyping, a 2.5 mM iron (III) citrate and a 0.625 mM ferricyanide were used. A bacterial concentration of  $5 \times 10^5$  CFU/mL of *E. coli* ATCC 25922 was used. Lines missing in the plots were omitted due to instrumental errors.

The same experiment was performed simultaneously, but with continuous visible light illumination, with the results summarized in **Figure 6.25**. Interestingly, no Prussian Blue formation was observed in the four plots in the left, where all reagents were combined

and continuously irradiated in absence of bacteria. Thus, although the mechanisms was photocatalytic, the presence of light was not enough to activate the photochemical reaction and Prussian Blue formation. The most remarkable observation in the plots in the left (without bacteria) was that the absorbance peak attributed to ferricyanide (420 nm) slightly decreased over time, probably due to photochemical degradation (**graph C and G**). When bacteria are present (plots in the right), the spectral response depended on the composition of the medium. Thus, the same increase associated to a conventional bacterial proliferation obtained in the experiments performed in the dark is replicated during irradiation by **graphs B**, only containing bacteria and MH culture medium, **and F**, incorporating iron citrate. This indicated that light, bacteria and iron citrate was not enough to activate the photocatalytic formation of PB. Similarly, the **graph D**, resulting from the reaction of ferricyanide and bacteria in light conditions, presented a bacterial proliferation even lower than in the dark. This confirmed the previous hypothesis suggesting that light may induce some photo-degradation of ferricyanide, probably inducing the release of cyanide ions that killed bacteria and reduce their proliferation. This was in agreement with previous publication by Ojeda et. al. [13] that reported on the liberation of cyanide ions from the ferricyanide molecule under UV-VIS illumination. Finally, the combination of iron citrate, ferricyanide and bacteria under continuous irradiation catalysed Prussian blue formation, as shown in **graph H**. Similar results were obtained by electrochemistry when analysing the cyclic voltammograms (see **Figure 6.26** and **Figure 6.27**): major differences were observed in the voltammograms of **graph H**, where all reagents are present under constant light illumination and the peaks shift due to the formation of Prussian blue.

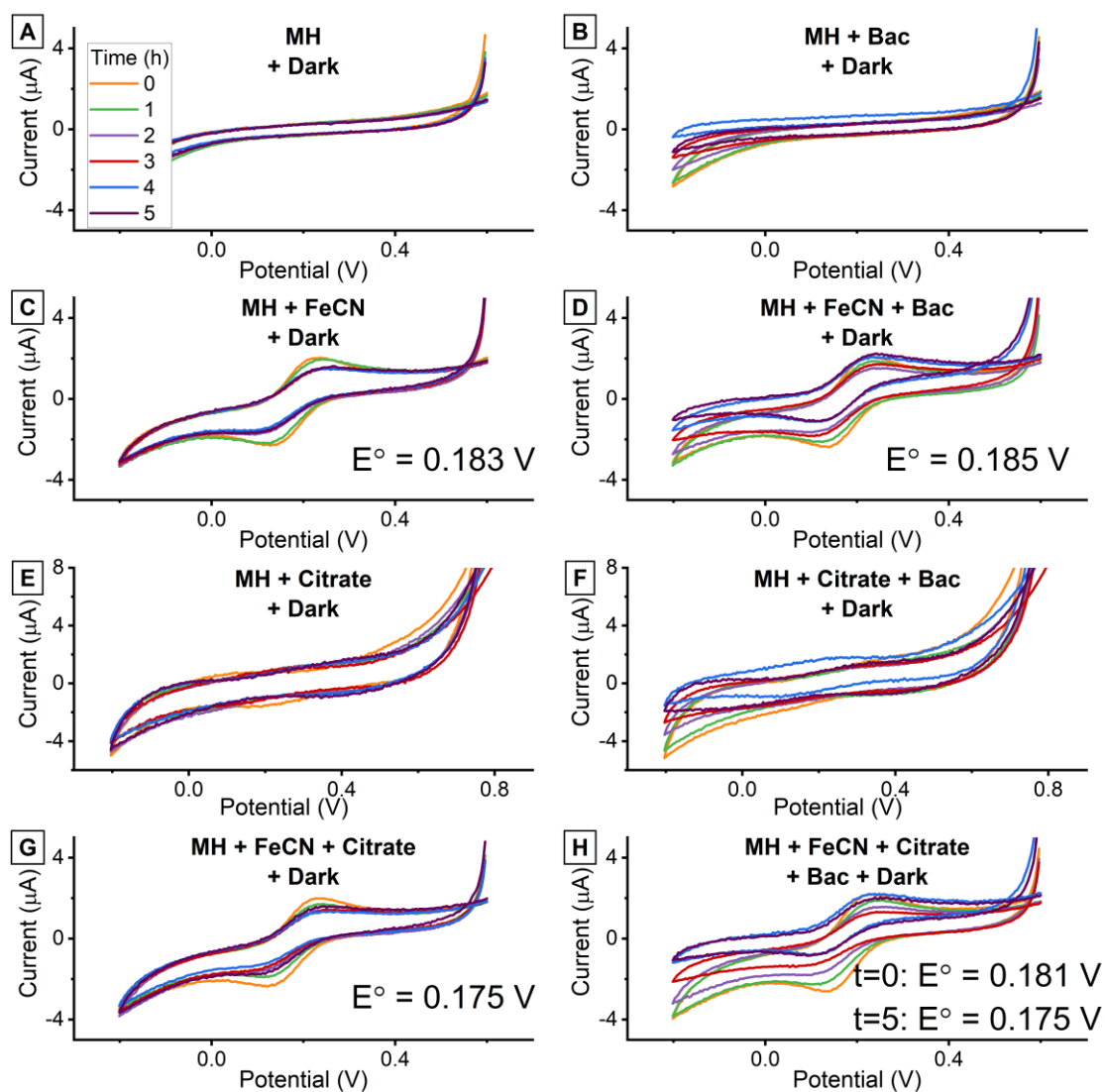


**Figure 6.26: Cyclic voltammograms of the various reagents of the cyanotype-based protocol performed in dark.** Measurements were taken every hour, for a total of 5 hours. A total of 3 cycles were performed, though a single one is shown. In all cases a potential window of -0.2 V to 0.6 V was used, with the exception of E and F, with a from -0.2 V to 0.8 V. The scan rates were 0.2 mV/s and 0.05 mV/s respectively. Potential peaks are indicated in the figure itself. For the cyanotyping, a 2.5 mM iron (III) citrate and a 0.625 mM ferricyanide were used. A bacterial concentration of  $5 \times 10^5$  CFU/mL of *E. coli* ATCC 25922 was used.

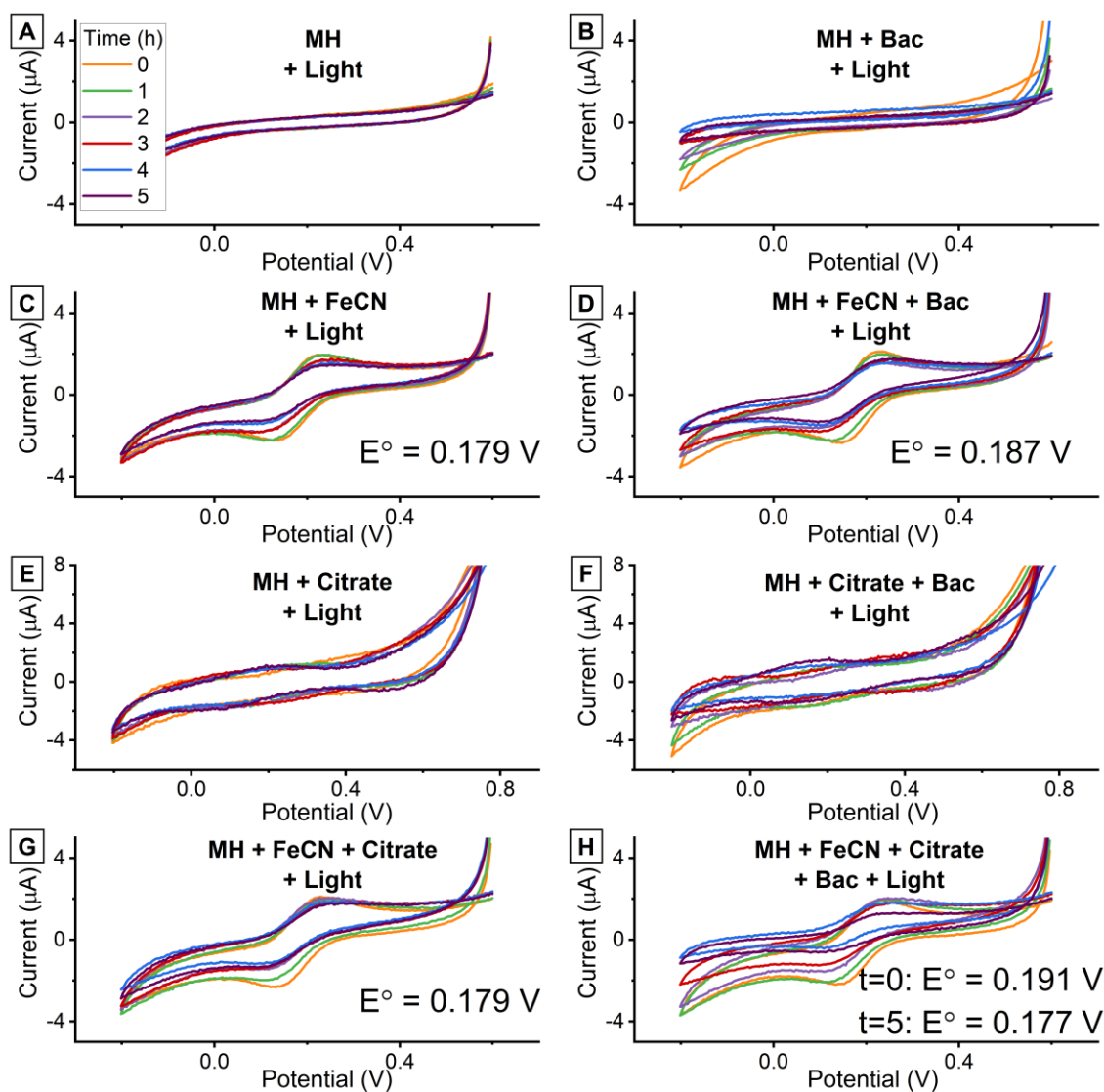


**Figure 6.27: Cyclic voltammograms of the various reagents of the cyanotype-based protocol performed under continuous illumination.** Measurements were taken every hour, for a total of 5 hours. A total of 3 cycles were performed, though a single one is shown. In all cases a potential window of -0.2 V to 0.6 V was used, with the exception of E and F, with a from -0.2 V to 0.8 V. The scan rates were 0.2 mV/s and 0.05 mV/s respectively. Potential peaks are indicated in the figure itself. For the cyanotyping, a 2.5 mM iron (III) citrate and a 0.625 mM ferricyanide were used. A bacterial concentration of  $5 \times 10^5$  CFU/mL of *E. coli* ATCC 25922 was used.

Hence, it is clear from the result that the photochemical reaction based on the cyanotype process here employed required the both the photocatalytic and metabolically-mediated activation of an intermediate compound for the formation of Prussian Blue molecules.

The presence of free iron ions was of key relevance to elucidate the mechanisms of the cyanotype-based photochemical reaction here described, but not possible to attain through previous techniques directly. For this reason, an additional experiment was performed to evaluate the oxidative state of the iron species produced in the photochemical reaction from the ferric ammonium citrate used as free iron source. The experiment performed is summarized in **Figure 6.28**. In the experiment, iron nitrate

( $\text{Fe}(\text{NO}_3)_3$ ) was used as source of free iron (III) ions in the positive controls. The reaction mechanism considered the formation of a complex between the free iron(III) ions and acetylsalicylic acid (AA) (1 mg/mL), which presented an intense purple colour and a clear absorbance band at 565 nm (Figure 6.28 A).

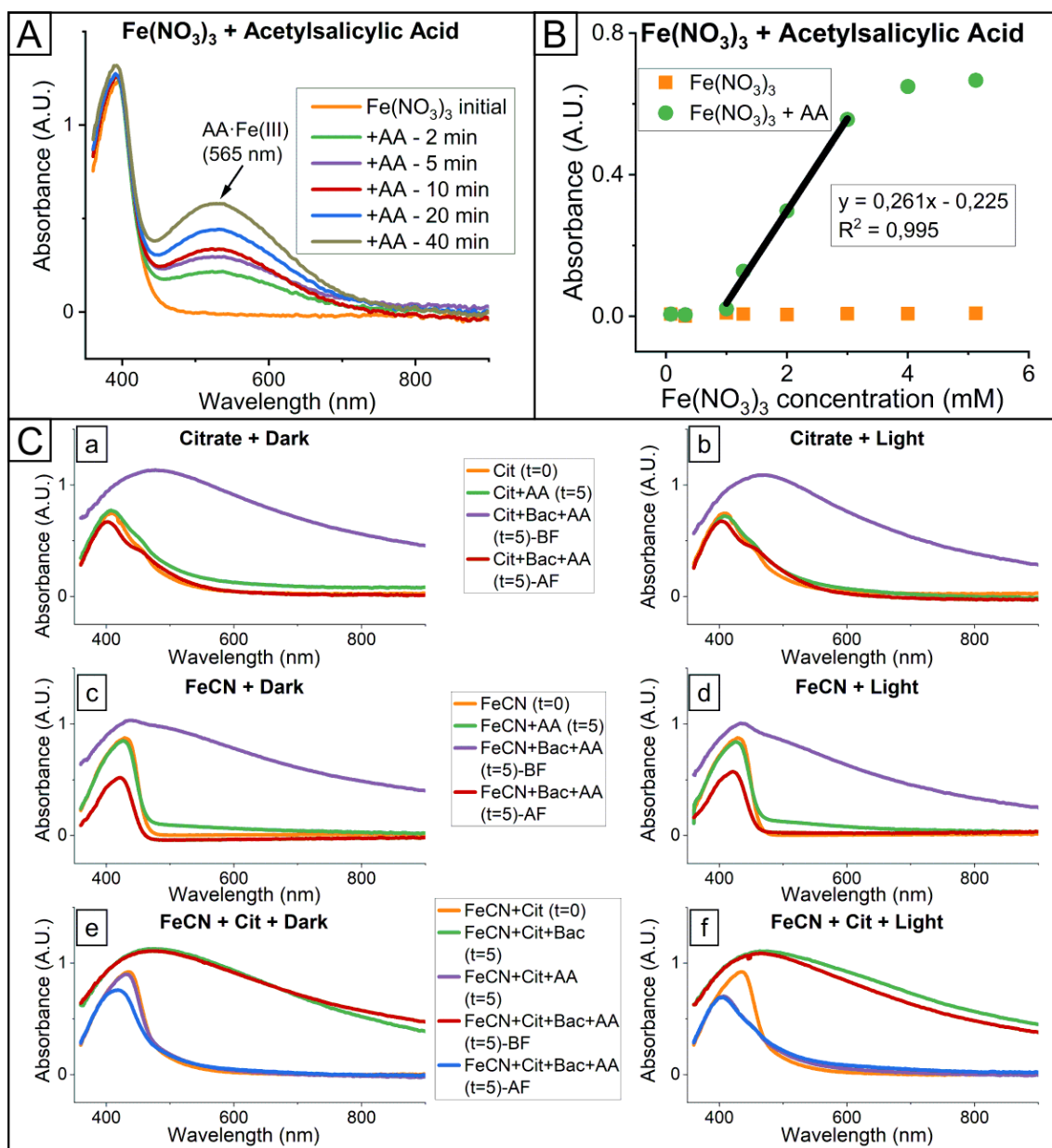


**Figure 6.28: Acetylsalicylic acid experiments for the detection of free iron (III).** A) acetylsalicylic acid (AA) test using iron nitrate as reference. Measurements were performed after the indicated reaction time with AA and taken every nm from 350 – 900 nm. B) Calibration curve of the spectral response of free iron from iron nitrate after reacting with AS for 40 min, measured at 565 nm. C) Detection of free iron from the reagents of the cyanotype-based reaction, measured after 5 hours of incubation in dark or after continuous illumination. Measurements taken every nm from 350 – 900 nm. A bacterial concentration of  $5 \times 10^5$  CFU/mL of *E. coli* ATCC 25922 was used. A concentration of 1mg/mL AA was used. FeCN = Ferricyanide, Cit = ferric ammonium citrate, Bac = Bacteria, AA = acetylsalicylic acid, BF = measurement before filtration of the sample, AF = measurement after filtration of the sample (filter = 200 nm pore size).

**Figure 6.28 A** highlights the increase in absorbance over time of the reaction. Based on the experiment, 40 minutes of reaction was taken as optimal for the reaction. The magnitude of the absorbance band was proportional to the free iron (III) concentration in a range between 1 and 3 mM iron (III). The calibration curve is shown in **Figure 6.28 B**, and results in a LOD of 0.269 mM. Considering the final concentrations of Ferricyanide and Citrate in the cyanotype photochemical reaction (0.625 and 2.5 mM, respectively) the sensitivity of the method should be enough to detect the presence of free iron (III) ions.

Based on the latter, the AA was added to the cyanotype reaction to check for the presence of free iron (III) ions during the reaction. To account for the influence of bacteria on the AA reaction, the samples were also measured before (BF) and after filtering (AF) of the bacteria from the sample. The results of the AA test with various reagents with and with bacteria and with and without light are summarized in **Figure 6.28 C**. None of the reactions studied presented a peak at 565 nm indicative of the presence of free iron (III) ions in the medium at concentrations above 0.3 mM. The drop in absorbance around 420 nm using ferricyanide and bacteria after 5 hours was due to bacteria being able to reduce ferricyanide as explained in **Chapter 6.2.2**. Additionally, if no filtration was performed, the spectra were dominated by the bacterial scattering.

Due to impossibility to measure free iron (III) ions, two hypotheses were suggested: free iron (III) were released and rapidly reacted with iron-cyanide complexed to form Prussian Blue or the iron specie released in the medium was not iron (III) but iron (II). To test these hypotheses, another experiment was performed with controls containing either ferricyanide (able to react with iron (II) ions to form PB) or ferrocyanide, which could react directly with iron (III) ions to form PB. Each of the combinations of ferricyanide, ferrocyanide, citrate and bacteria were tried in the experiment summarized below, using illumination for 5 hours, and following the reaction for 24 hours.



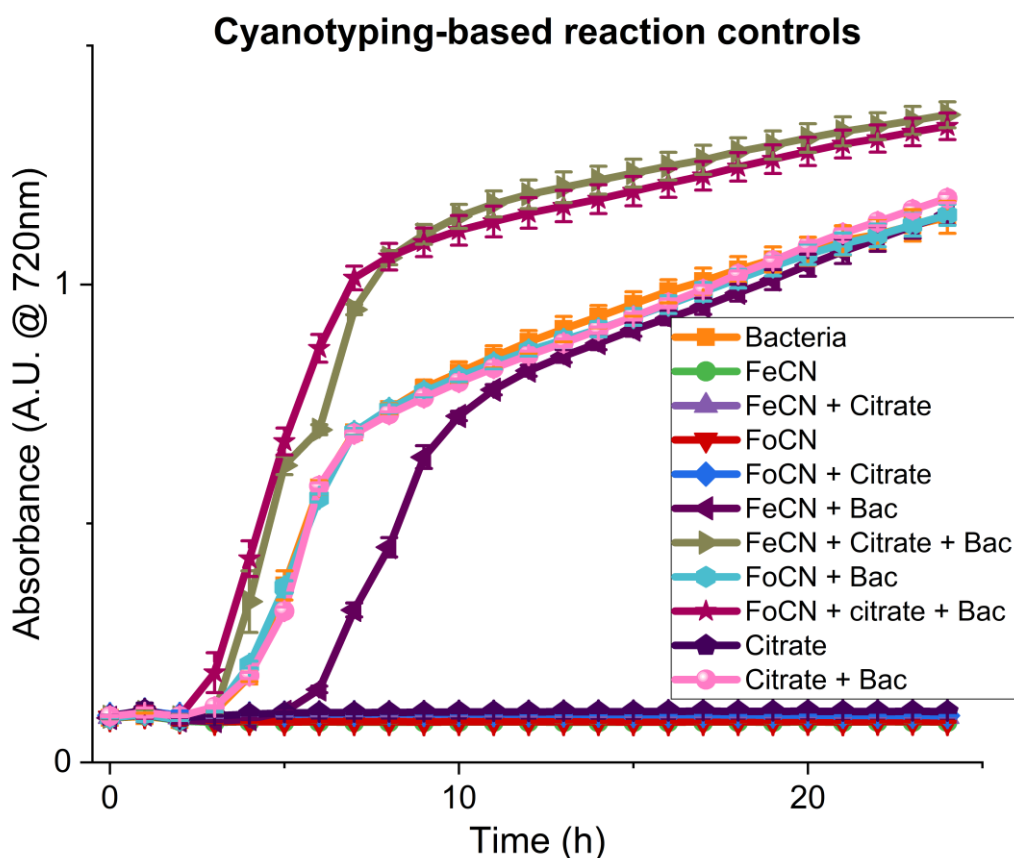


**Figure 6.29: Cyanotype-based reaction and controls.** Absorbance measurements of the various reagents and combination of reagents of the cyanotype-based reaction. Ferrocyanide was included as control for ferricyanide. Measurements were taken every hour for a total of 24 hours. All samples were illuminated for a total of 5 hours, after which samples were kept inside the dark inside the plate reader. Results were measured and plotted at 720 nm. A bacterial concentration of  $5 \times 10^5$  CFU/mL of *E. coli* ATCC 25922 was used. FeCN = ferricyanide, FoCN = ferrocyanide, citrate = ferric ammonium citrate, bac = bacteria. (n=6)

The experimental results are summarized in **Figure 6.29**. As shown, in absence of bacteria there was not change in the absorbance magnitude at 720 nm, confirming that PB was not formed even when combining both cyanotype precursors, i.e. ferricyanide/ferrocyanide and citrate. The absence of reaction when combining ferrocyanide and iron citrate after irradiation was quite surprising since they could react directly without requiring the metabolic reduction of the reagent. This result confirmed that visible light was not enough to release free ions from iron citrate, which remained complexed and inaccessible for ferrocyanide, avoiding Prussian blue formation.

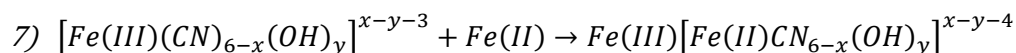
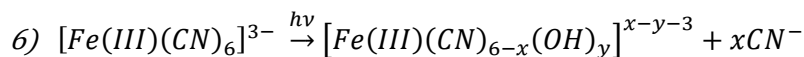
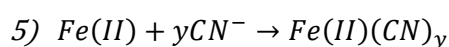
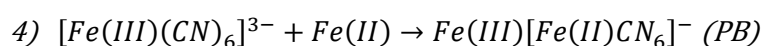
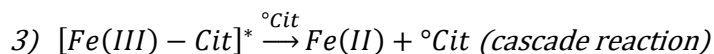
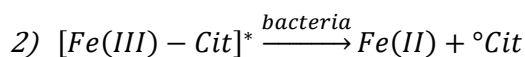
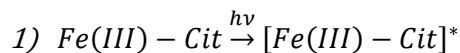
Bacteria alone, without any of the cyanotype precursors, proliferate in a normal growth curve. This curve did not vary in the presence of only one of the precursors, either citrate or ferro/ferricyanide apart from the small toxicity reported in the case of ferricyanide and associated to photochemical release of cyanide ions.. When ferricyanide or ferrocyanide were added to the mixture of bacteria and citrate, Prussian blue was formed in both cases, without a significant difference between both ( $p < 0.05$ ).

The experiment confirmed that apart from photocatalytic, the process was also metabolically-catalysed by bacteria. On the other hand, both iron (II) and iron (III)

species were released from the iron citrate complex being thus able to react with either ferro- or ferricyanide to produce PB.

Based on all aforementioned experiments two reaction mechanisms are proposed below, one for the case of ferricyanide and one for ferrocyanide.

*Starting from ferricyanide*



With the reaction taking place in an aqueous environment and  $[Fe(III) - Cit]^*$  = excited state by light  ${}^{\circ}Cit$  = citrate radical.

First, visible light irradiation excited iron citrate molecules to an activated state but, due to the low energy of this radiation, it was not enough to release free ions to the medium (as it happened in the case of UV light in the cyanotype reaction). Bacterial metabolism, and concretely those proteins involved in the electron transport chain, was able to interact with the excited state of the iron citrate complex, to reduce the complexed iron (III) ions to iron (II), and to release free iron (II) ions and citrate radicals. The released iron (II) ions reacted with the ferricyanide molecules to form the characteristic Prussian blue particles. Very important, citrate radicals initiated a cascade reaction when interacting with other iron citrate molecules thus releasing more and more free iron ions to the medium. Thanks to the photocatalytic cascade reaction, much faster than the bacterial metabolism, all samples containing low or very low bacterial concentrations (below  $10^5$  CFU/mL) presented an identical reaction time of 3-4 hours for initial formation of PB. Additionally, the reduction from free iron (III) to free iron (II) was near instant, rendering it impossible to detect by the AA test.

As side reactions, Ojeda et. al. described photocatalytic loss of cyanide ions from ferricyanide molecules by continuous light irradiation, something also accounting in this case. Free cyanide ions could either: (i) react with bacteria and kill them, reducing bacterial proliferation; (ii) react with iron (II) ions to produce iron-cyanide complexes; or (iii) react with free iron (II) and hydrated ferricyanide, giving rise to more Prussian blue, with the release of water.

The reaction with the radicals kept propagating as long as illumination occurred. If illumination was stopped, the iron citrate molecules were not longer excited, preventing the cascade reaction from continuing.

Starting from ferrocyanide

1.  $Fe(III) - Cit \xrightarrow{h\nu} [Fe(III) - Cit]^*$
2.  $[Fe(II)(CN)_6]^{4-} + [Fe(III) - Cit]^* \xrightarrow{Bacteria} Fe(III)[Fe(II)CN_6]^- + {}^\circ Cit$
3.  $[Fe(II)(CN)_6]^{4-} + [Fe(III) - Cit]^* \xrightarrow{{}^\circ Cit} Fe(III)[Fe(II)CN_6]^- + {}^\circ Cit$  (cascade reaction)

With the reaction taking place in an aqueous environment and  $[Fe(III) - Cit]^*$  = excited state by light  ${}^\circ Cit$  = citrate radical.

When starting from ferrocyanide, the reaction was slightly less complex, involving the direct reaction between the excited iron-citrate form with ferrocyanide molecules (without photocatalytic reduction of iron molecules) and without cyanide ions release, since it was not possible to see any negative effect on bacterial proliferation in this case. Thus, the light itself excited the iron citrate as before, but instead of forming an intermediary iron (II) ion, they catalysed the reaction between ferrocyanide and the excited iron (III) citrate in the direct formation of Prussian blue. Citrate radicals were still released, and further propagated the reaction as long as illumination occurs.

#### 6.4.5. Cyanotype-based protocol for susceptibility testing

The cyanotype-based photocatalytic reaction was employed for fast antibiotic susceptibility testing. Two bacterial strains of clinical interest, i.e. *E. coli* and *S. aureus*, and three common antibiotics, i.e. gentamicin, fosfomycin and ciprofloxacin, were used in the validation of the protocol for MIC determination and detection of resistant bacteria. All samples were spectroscopically analysed over time, although MIC was determined after 20-24 hours of incubation and by visual inspection for the sake of comparison with the standard BMD test. The results are summarized in **Table 6.3**, where each experiment tested the standard broth microdilution and cyanotype reaction simultaneously. The last column shows the expected MIC values of the tested strains as provided by EUCAST.

**Table 6.3: Summary of various MIC tests performed using cyanotyping based bacterial sensing.** The bacteria used in the experiments were *E. coli* ATCC 25922 and *S. aureus* ATCC 27853. Multiple tests are depicted in their number of repetition n. The final column refers to the data provided by EUCAST, used as quality control in these experiments. BMD=broth microdilution, QC EUCAST=quality control from European committee on Antimicrobial Susceptibility Testing. Cyanotyping was formed using the precursors 0.625 mM FeCN and 2.5 mM ferric ammonium citrate.

Strain	Antibiotic	BMD (mg/mL)	Cyanotyping (mg/mL)	QC EUCAST (mg/mL)
<b>E. coli ATCC 25922</b>	Gentamicin	1 – 4 (n=7)	>16 (n=7)	0.5
	Fosfomycin	1 – 2 (n=8)	4 – 8 (n=2), 32 (n=6)	1
	Ciprofloxacin	2 <sup>-5</sup> (n=5)	2 <sup>-5</sup> (n=5)	2 <sup>-7</sup>
<b>S. aureus ATCC 27853</b>	Gentamicin	2 (n=3)	16 (n=4)	0.25 – 0.5
	Fosfomycin	1 – 2 (n=2)	8 – 16 (n=2)	1 – 2
	Ciprofloxacin	2 <sup>-2</sup> – 2 <sup>-3</sup> (n=5)	2 <sup>0</sup> – 2 <sup>-1</sup> (n=6)	2 <sup>-2</sup>

MIC values related to gentamicin differed widely from the quality control (QC) tables provided by EUCAST in both strains. A plausible reason may be the photo-inactivation of the antibiotic resulting from the continuous illumination during the assay or interaction with some of the components of the precursor solution. This point is still under consideration in the group since there are no clear evidences of photo-inactivation or any interaction between any precursor and the antibiotic.

For the other two antibiotics, fosfomicin and ciprofloxacin, the BMD results were closer to those tabulated. The main discrepancy was with ciprofloxacin for *E. coli*, which should be associated to the low solubility of the antibiotic in water that may hamper sample preparation. Something remarkable was that all MIC values provided by the cyanotype experiments were higher than those reported by the QC tables, or the BMD assays. A first factor responsible of these differences was the high sensitivity of the cyanotype-based test, capable to detect the presence of 10 CFU/mL in 4 hours. This implied that, even when the antibiotic killed over 99.9 % of the bacteria from the  $5 \times 10^5$  CFU/mL used in standard BMD tests, a signal corresponding to PB formation by the remaining 0.1% ( $\approx 5 \times 10^5$  CFU/mL) bacteria was detected as a clear blue colour formation. A second factor may be attributed to the antibacterial mechanism of the antibiotic, i.e. bactericidal or bacteriostatic. Hence, ciprofloxacin, which targets bacterial DNA directly preventing growth and cell division, presented the MIC values closest to the reported ones. Fosfomicin, on the other hand, inhibits cell wall biogenesis, meaning that it only affects bacteria that are actively dividing and needs to be actively taken up by a bacterial transporter. This should cause a slower cell death compared to ciprofloxacin and thus, bigger differences between the standard and the cyanotype-based method. Finally, gentamicin targets the bacterial ribosome, causing the ribosome to incorporate wrong amino acids within synthesised proteins. These proteins lose function and aggregate, eventually leading to cell death. However, as long as the cell was alive, metabolism still occurred, making gentamicin the slowest bactericidal antibiotic of the three and the one presenting the largest differences between methods.

#### 6.4.6. Cyanotype-based bacterial detection in real samples

The major goal of the bioassay chapter was to develop a test for rapid antibiotic testing from purified cultures. However, as mentioned in **Chapter 2.2.2**, culture purification inherently delays the collection of the antibiogram by 20 – 24 hours, depending on the type of infection. Testing directly from real samples overcomes this issue, at the cost of more complex matrices and, since identification often occurs after purification, without any information of the tested strains.

This final chapter was intended as a first step towards testing in real samples, using uninfected human serum (obtained from Sigma Aldrich) and pig's blood (donated by Department of Basic Science at Universitat Internacional de Catalunya). The experiments performed in serum (**Figure 6.30**) and blood (**Figure 6.31**) were conducted under the experimental conditions optimized before (2.5 mM citrate – 0.625 mM FeCN) as a proof-of-concept. To maximize the results of the tests, some preliminary sensitivity tests were performed in each matrix. Serum and blood were spiked with bacterial

samples and diluted half with the precursor solution (in MH). Since the pH of the solution was crucial for the assay (PB dissolves at basic pH), three separate experiments were performed where the pH of the MH was adjusted to 6.6, 6.1 and 5.5 respectively.

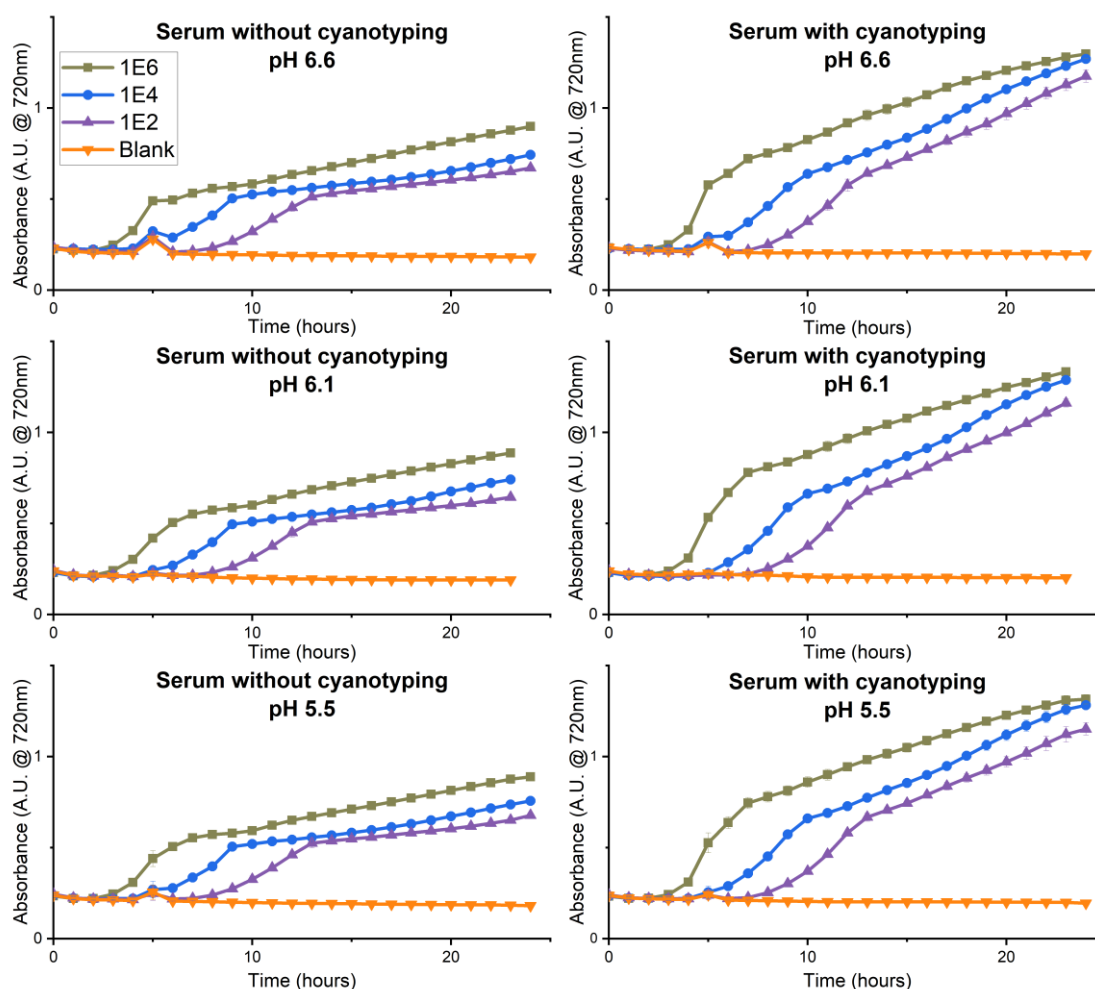


**Figure 6.30: Sensitivity of the cyanotyping assay performed in spiked human serum.** *E. coli* ATCC 25922 was used as model organism. The measurement was performed using a 1:1 serum - MH dilution, under continuous illumination for up to 5 hours. For the cyanotyping, a 2.5 mM iron (III) citrate and a 0.625 mM ferricyanide were used. Results were measured and plotted at 720 nm. (n=6)

Even though three very distinct samples of MH were prepared, the resulting pH after mixing with the serum was  $7.0 \pm 0.1$  due to their buffering effect resulting in no significant differences between experiments. Results from the experiment are plotted in **Figure 6.30**. As before, both experiments (i.e. with and without PB precursors) showed a conventional bacterial proliferation curve with the lag, exponential and stationary phases clearly visible. The main difference between samples was again the absorbance magnitude, this being higher in the samples containing precursor reagents due to the signal amplification associated to PB formation. The absence of the sudden jump after 3 – 4 hours of incubation in the samples containing PB precursors may be associated to some matrices effects. As already commented, PB formation is very sensitive to the reagents proportion and the optimal one may vary in this case due to

some interaction with components of the serum. Additionally, the higher pH value could also limit PB formation.

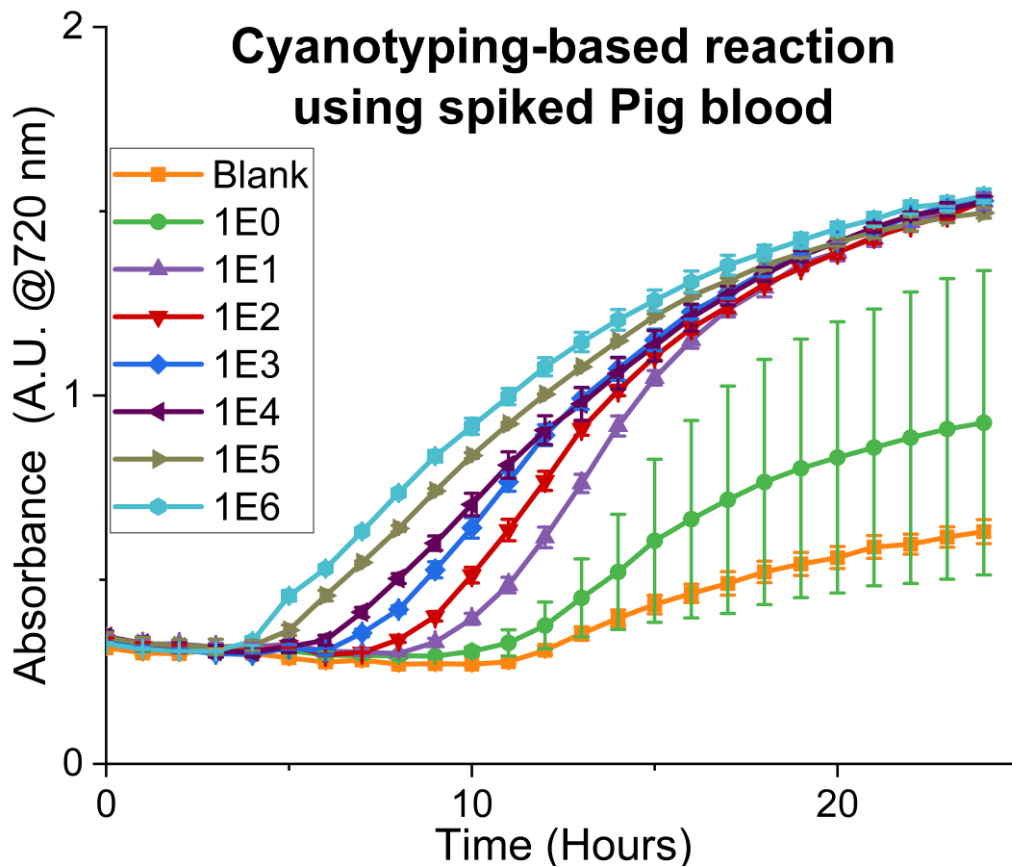


**Figure 6.31: Sensitivity of the cyanotyping assay performed in spiked pig's blood.** *E. coli* ATCC 25922 was used as model organism. The measurement was performed using a 1:1 blood - MH dilution, under continuous illumination for up to 5 hours. For the cyanotyping, a 2.5 mM iron (III) citrate and a 0.625 mM ferricyanide were used. Results were measured and plotted at 720 nm. (n=3)

Finally, a cyanotype based test was also performed in complete blood samples (**Figure 6.31**). As with serum, all bacterial concentrations followed a conventional proliferation curve with the amplification associated to PB formation. It confirmed that the assay could be performed in complete blood without interference of any of the blood components, opening the possibility for direct bacterial detection in blood samples. One of the aspects to be improved was reagents proportion since, as also observed in the case of serum, the initial sudden increase that reported on the presence of low bacterial concentration, was not obtained in this case. Two more aspects should be remarked from these results. First, as commented in other situations with low bacterial concentrations, the  $10^1$  CFU/mL sample converted the measurements into a probability assay, resulting in a growth curve with big error bars. Second, the blank line was not completely stable but presented some increase that may be due to some late reaction (after 11h of reaction) between precursor components to produce PB. Therefore, the results did not indicate cross-reaction between precursor reagents and matrix components allowing bacterial detection in complex matrices such as serum and blood directly and without any pre-treatment.

#### 6.4.7. Cyanotype conclusions

In conclusion, the usage of ferric ammonium citrate as iron (III) donor for the formation of Prussian blue gave rise to an **unprecedented light sensitive, cyanotype-based** test for bacterial detection. The stability of the reagent **minimized background** and enabled precise initiation of the reaction. Furthermore, the inherent cascade reaction enabled detection down to **a single bacterial cell** within **4 hours**. Though this sensitivity currently limited its use in ASTs, the protocol opened a new window of possibilities for fast and cheap bioelectrochromic bacterial detection, including sepsis testing.

## 6.5. Final remarks

The aim on the development of a bioassay was to accelerate the detection of antibiotic resistance upon suspecting a bacterial infection. Taking the production of the bioelectrochromic hydrogel as starting point, a number of bioassays were developed with the objective of increasing the sensitivity and the speed of the reaction. A brief summary of each generation is highlighted below, with a summarized comparison in **Table 6.4**.

- Bioelectrochromic **hydrogels** were developed as a new substrate for creating a biocompatible environment for bacterial growth under soft conditions. This assay was further expanded to enable fast antibiotic susceptibility testing, though required intense hands-on work, limiting its direct use for high-throughput.
- In the continuation of the usage of bioelectrochromic molecules, **ferricyanide** was used as direct indicator for bacterial metabolism and thus viability after antibiotic exposure. Direct compatibility with BMD, the addition of the reagent enabled visible indication of resistance. However, long incubation times (>10 h) and extra data processing was required for the acquisition of accurate MIC values, due to the low extinction coefficient.
- The ferricyanide assay was improved by the addition of a second iron provider, iron (III) chloride, which resulted in to the formation of **Prussian blue**. Relying on the same principle, Prussian blue, with a higher extinction coefficient than ferricyanide, lead to higher sensitivities and shorter assay times. However, iron (III) chloride was unstable in water, resulting in its precipitation and producing high background levels.
- The substitution of the iron (III) chloride with ferric ammonium citrate gave rise to the light sensitive **cyanotype-based** mechanism. The reaction required both the presence of light and bacteria for the initiation of a photochemical cascade reaction, resulting in the formation of Prussian blue. This double requirement lead to significantly higher stability in various media and minimized background noise. Additionally, the cascade reaction enabled detection of bacterial concentrations down to single cell within 4 hours of incubation.



**Table 6.4: Overview and comparison of the various generations of the bioassays.** The colour codes indicate the quality of the mentioned parameter in the following order: Dark green, yellow, red; corresponding to very good, medium and very bad. a time required to see a positive signal, based on the standard bacterial concentration used for AST testing. \*based on tested media (MH, water, LB, serum and blood), \*\*AST needs to be adapted to the assay for further results.

Parameter	Hydrogel	Ferricyanide	Prussian blue	Cyanotype
Visible change	High	Low	High	High
Complexity	Manual work	Single reagent	Two reagents	Two reagents
Background noise	Medium	Low	High	Low
Medium	Specific hydrogel	Any*	MH	Any*
Stability	Low (dehydration)	Medium (light sensitive, auto hydration)	Low (auto hydration)	High (requires both light and bacteria)
Sensitivity	Medium	Low	Medium	High
Time to result <sup>a</sup> (5x10 <sup>5</sup> CFU/mL)	6 h	10 h	6 h	3-4 h
AST	Yes	Yes	Crosstalk with Abs	Too sensitive**

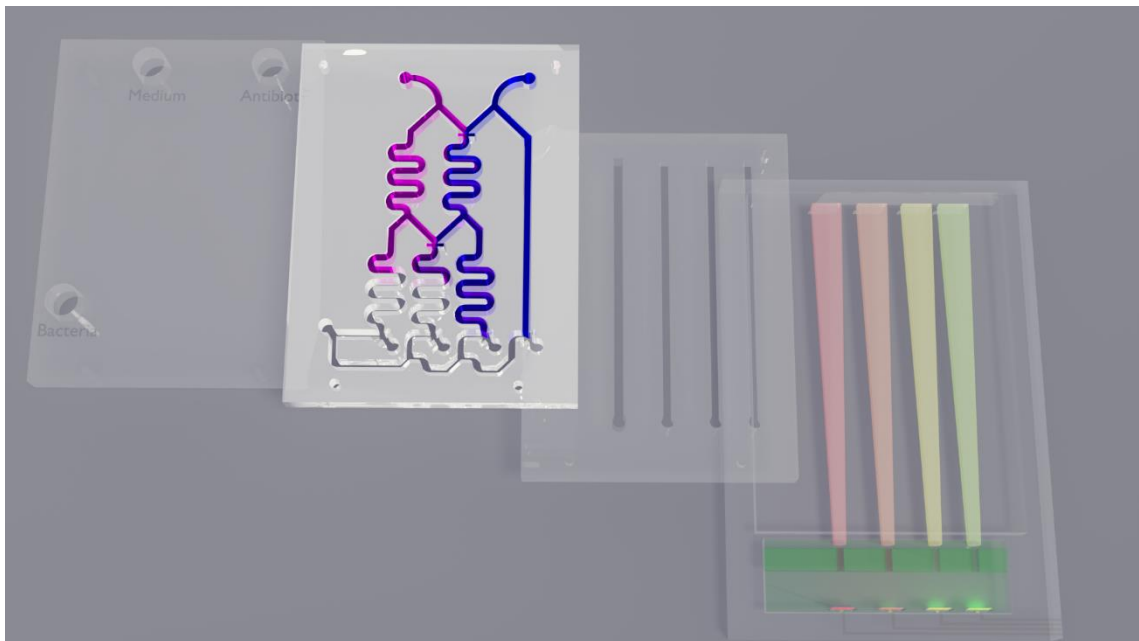
## 6.6. Bibliography

- [1] Z. Jin, A.M. Harvey, S. Mailloux, J.H. Amek, V. Bocharova, M.R. Twiss, E. Katz, Electrochemically stimulated release of lysozyme from an alginate matrix cross-linked with iron cations  $\text{Fe}^{3+}$ , (n.d.). <https://doi.org/10.1039/c2jm32008h>.
- [2] F. Pujol-Vila, N. Vigués, M. Díaz-González, X. Muñoz-Berbel, J. Mas, Fast and sensitive optical toxicity bioassay based on dual wavelength analysis of bacterial ferricyanide reduction kinetics, *Biosens. Bioelectron.* 67 (2015) 272–279. <https://doi.org/10.1016/j.bios.2014.08.030>.
- [3] F. Pujol-Vila, P. Giménez-Gómez, N. Santamaria, B. Antúnez, N. Vigués, M. Díaz-González, C. Jiménez-Jorquera, J. Mas, J. Sacristán, X. Muñoz-Berbel, Portable and miniaturized optofluidic analysis system with ambient light correction for fast in situ determination of environmental pollution, *Sensors Actuators, B Chem.* 222 (2016) 55–62. <https://doi.org/10.1016/j.snb.2015.07.095>.
- [4] F. Pujol-Vila, N. Vigués, A. Guerrero-Navarro, S. Jiménez, D. Gómez, M. Fernández, J. Bori, B. Vallès, M.C. Riva, X. Muñoz-Berbel, J. Mas, Paper-based chromatic toxicity bioassay by analysis of bacterial ferricyanide reduction, *Anal. Chim. Acta.* 910 (2016) 60–67. <https://doi.org/10.1016/j.aca.2016.01.006>.
- [5] U.S. Mehrotra, M.C. Agrawal, S.P. Mushran, by U. S Mehrotra, *Kinetics of the Reduction of Hexacyanoferrate(III) by ascorbic acid*, Cornell University Press, 1968. <https://pubs.acs.org/sharingguidelines> (accessed December 10, 2020).
- [6] F. Pujol-Vila, J. Dietvorst, L. Gall-Mas, M. Díaz-González, N. Vigués, J. Mas, X. Muñoz-Berbel, Bioelectrochromic hydrogel for fast antibiotic-susceptibility testing, *J. Colloid Interface Sci.* 511 (2018) 251–258. <https://doi.org/10.1016/j.jcis.2017.09.004>.
- [7] A.A. Karyakin, Prussian blue and its analogues: Electrochemistry and analytical applications, *Electroanalysis.* 13 (2001) 813–819. [https://doi.org/10.1002/1521-4109\(200106\)13:10<813::AID-ELAN813>3.0.CO;2-Z](https://doi.org/10.1002/1521-4109(200106)13:10<813::AID-ELAN813>3.0.CO;2-Z).
- [8] E. Wiberg, A.F. Holleman, N. Wiberg, M. Eagleson, B.J. Aylett, W. Brewer, *Inorganic Chemistry*, Academic Press, 2001. <https://books.google.es/books?id=vEwj1WZKThEC>.
- [9] M. Ware, *Cyanomicon. History, science and art of cyanotype: photographic printing in Prussian blue*, (2014) 1–298.
- [10] L.E. Nicolle, S. Bradley, R. Colgan, J.C. Rice, A. Schaeffer, T.M. Hooton, Erratum: Infectious diseases society of America guidelines for the diagnosis and treatment of asymptomatic bacteriuria in adults (*Clinical Infections Diseases* (2005) 40 (643–654)), *Clin. Infect. Dis.* 40 (2005) 1556. <https://doi.org/10.1086/430607>.
- [11] O. Opota, A. Croxatto, G. Prod'hom, G. Greub, Blood culture-based diagnosis of bacteraemia: State of the art, *Clin. Microbiol. Infect.* 21 (2015) 313–322. <https://doi.org/10.1016/j.cmi.2015.01.003>.
- [12] N. Seraghni, S. Belattar, Y. Mameri, N. Debbache, T. Sehili, Fe(III)-citrate-complex-induced photooxidation of 3-methylphenol in aqueous solution, *Int. J.*

Photoenergy. 2012 (2012). <https://doi.org/10.1155/2012/630425>.

- [13] J. Ojeda, C.A. Arrell, L. Longetti, M. Chergui, J. Helbing, Charge-transfer and impulsive electronic-to-vibrational energy conversion in ferricyanide: Ultrafast photoelectron and transient infrared studies, *Phys. Chem. Chem. Phys.* 19 (2017) 17052–17062. <https://doi.org/10.1039/c7cp03337k>.

# 7. Fluidics





## 7.1. State of the art

The development of a POC AST device was regarded as the ultimate goal of the thesis. As described in **Chapter 2.2.2.4**, an optimal POC device should adhere to the ASSURED criteria. Using microfluidics for the management and control of the entire system could enable the user-friendly (U), rapid and robust (R) and equipment-free (E) conditions. Microfluidics enable the miniaturization and automation of liquid based tests. The goal is to use capillary based systems, through either narrow channels or paper-like materials, to avoid the usage of pumps and user input. In addition, AST based tests inherently rely on extensive manual work for the preparation of the samples, and mainly the antibiotic dilutions. Microfluidics enable the generation of the required antibiotic concentration gradient on chip by using a gradient generator.

Microfluidic concentration gradient generators (CGG) produce diluted concentrations representing a gradient between input species by manipulating small volumes of reagents through branching microchannels. Even though all CGG essentially create a concentration, a distinction can be made between two major groups: continuous gradient [1–3] and discrete gradient [4,5]. For continuous gradients, continuous flows are used to obtain a gradient at a specific location along a channel due to diffusion where the liquids meet. Inherently, these types of gradient generators require a pumping system to provide a steady flow over time, where the final desired gradient remains in a fixed place depending on the design and flow rate. Discrete gradients merge and separate the fluid flows along the channels, resulting in an absolute concentration at the desired outputs. These designs are often more limited in the flow rates being used to maintain the desired gradient.

All continuous and nearly all reported discrete gradient generators require the use of pumps to control the flow rate and the pressure inside the system to maintain a stable concentration gradient. Additionally, biological experiments, in particular cell and bacterial based methods, often require long incubation times. This can result in large volumes being used, counter-productive to the microfluidic setup and additional complexities related to stabilization and contamination.

Few publications use capillary-driven CGGs, with additional complexities. The work of Hong et al. [6] describes a paper-based chip able to generate a different concentration at each of the five reservoirs by wicking through the paper. However, to obtain the desired concentrations, both liquids have to arrive simultaneously at the merging points, requiring a synchronous deposition at each of the inlets, limiting the robustness and accuracy. Similarly, the work of Gao et al. [7] describes a method using passive pumping by using hydrostatic pressure from the loading reservoirs and capillary pressure to drive the liquid. However, they do not explicitly state the requirement of loading both reservoirs simultaneously, the lack of valves in the system indicates that when loading a single reservoir, the liquid will propagate and disrupt the gradient generation. Finally, Park et al. [8] were able to overcome the issue of simultaneous loading by incorporating a finger-actuated initiation of the flow.

In this thesis, a capillary-driven microfluidic system able to generate a 2-fold dilution sequence has been developed. Additionally, geometrical valves were designed to enable a robust control of the system avoiding simultaneous loading of the various input channels. The progress scheme for the development of the microfluidic systems is illustrated below.

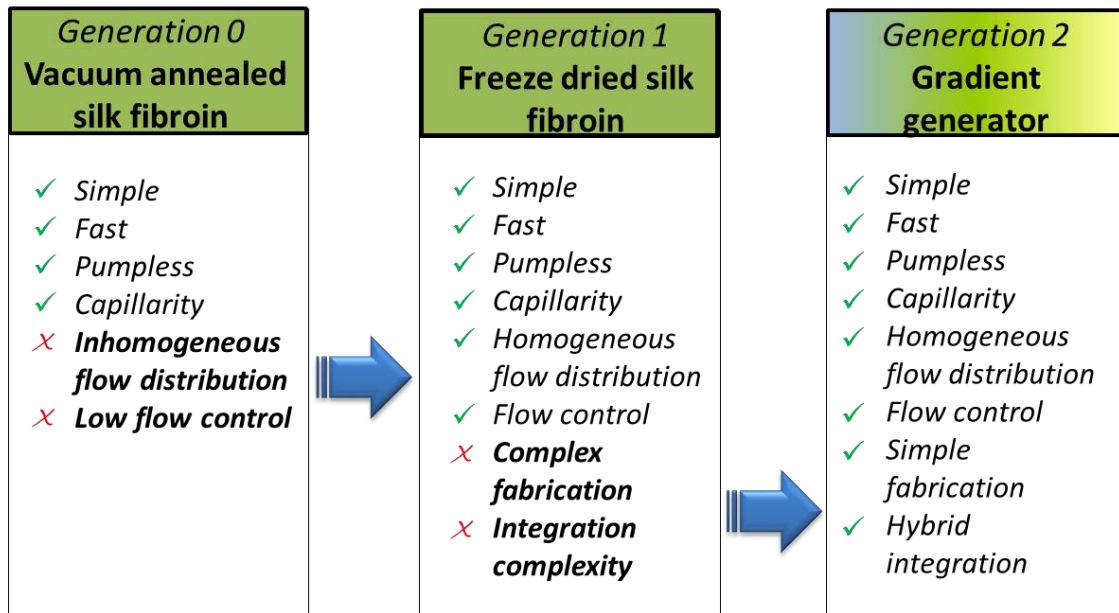


Figure 7.1: Scheme of the continuity of the various generation of the fluidics under development. Each generation depicts a different approach for the development of a fluidic structure that serves as capillary carrier. Under generation 2 a side project was performed, not directly related to the fluidics themselves.

## 7.2. Generation 0: Prior work

### 7.2.1. Gen 0: Vacuum annealed silk fibroin

The usage of silk fibroin films as microfluidic elements was explored in collaboration with Dr. Augusto Márquez during his PhD, which focused on the development of technologies based on biomaterials, i.e. alginate and silk fibroin for biosensing. Generation 0 describes the combination of both prior work and work performed in collaboration that did not appear in his dissertation.

Silk is a natural protein-based biopolymer produced by silkworm and arachnids such as spiders or dust mites [9]. An increase in interest has appeared over the years for the usage of silk fibroin (SF) in the development of electronic and opto-electronic components due to its chemical and thermal stability [10], mechanical robustness [11], biocompatibility [12] and controllable biodegradability [13], excellent optical properties (high transparency and refractive index), production simplicity [14], and high processability with a number of microfabrication technologies including photolithography, electron beam lithography and soft-lithography, among others. Regarding to the latter, the SF precursor is an aqueous solution, which can easily be doped with a variety of elements. Once doped, SF can be crystallized at mild environmental conditions (i.e. room temperature and vacuum), not compromising the structure and/or function of the doping molecules, even if they are bio-macromolecules such as cells, antibiotics and peptides [15]. Even more interestingly, after processing the doped SF film through any of the previous microfabrication technologies, the patterns is obtained using water as developer, which makes the process completely green and eco-friendly.

#### 7.2.1.1. Capillary flow and enzymatic behaviour in silk fibroin films

In his thesis, Dr. Márquez worked on the development of lateral flow platforms using silk fibroin and microfluidic support, thus substituting nanocellulose paper. As proof-of-concept, he developed blood glucose biosensor where the silk fibroin acted as capillary pumping matrix, size-exclusion filter and support for the enzymatic reaction [16]. With this aim, two enzymes, namely glucose oxidase and horseradish peroxidase (HRP), and 2,2'-azino-bis(3-ethylbenzothiazoline-6-sulfonic acid (ABTS) as colorimetric indicator were incorporated in the silk fibroin matrix after crystallization of silk films. By soaking the doped silk with a glucose solution, a gradual colour change occurs due to the enzymatic activity. The reaction with the corresponding colour change is summarized in **Figure 7.2**.



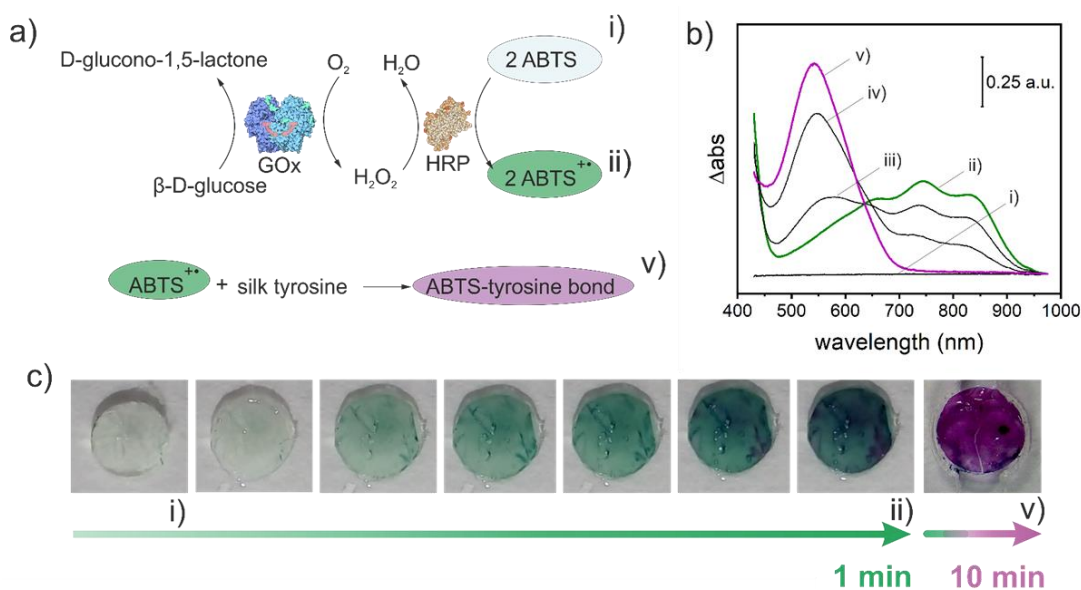


**Figure 7.2: Glucose biosensor using a silk fibroin matrix.** A) highlights the glucose oxidation reaction catalysed by a glucose oxidase (GOx) enzyme, resulting in the formation of hydrogen peroxide. Horseradish peroxidase (HRP), a second enzyme, uses the hydrogen peroxide to catalyse the oxidation of the 2,2'-azino-bis(3-ethylbenzothiazoline-6-sulfonic acid (ABTS). The final product further reacts with the silk tyrosine. B) optical spectra of the glucose reaction in a silk matrix. Each of the letters (i to v) refer to a reaction product. C) images of the glucose reaction when performed using a silk matrix. The enzymes and the ABTS were crystallized together with the silk, and the reaction was initiated by deposition of a glucose solution. With permission, from [16].

### 7.2.2. Gen 0: Freeze dried silk fibroin

It had been reported that altering the parameters of freeze-dried silk fibroin alters its porosity and in turn its capillary properties. In the ongoing collaboration with Dr. Augusto Márquez, the effects of freeze-drying on silk were investigated both in terms of the capillary flow rate as well as its inherent filtering properties.

The porosity of SF is related to the annealing process, due to the alterations in water content, when submitted to vacuum exposure. Various SF solutions containing 1 to 20% w/v SF in water were prepared, freeze dried and annealed, and later imaged by SEM to evaluate the surface porosity (**Figure 7.3 a**). Silk fibroin with high water content (1% - 5% w/v SF) prior to the freeze-drying, showed a higher porosity and higher pore size. A non-freeze-dried film was included as control, which was expected to retain <2% water content. Additionally, differences were found between enzyme-doped and pristine films, where the first obtained an average pore diameter of 6.8 nm and a surface area of 3.2 m<sup>2</sup>g<sup>-1</sup>, compared to 6.3 nm and 1.9 m<sup>2</sup>g<sup>-1</sup> for the pristine respectively. Although the average pore size was barely affected, a higher contribution was observed for the pore size region between 5 and 20 nm for the doped films (**Figure 7.3 c**), suggesting that the enzymes generated defects in the material, increasing locally the surface area and the pore size.

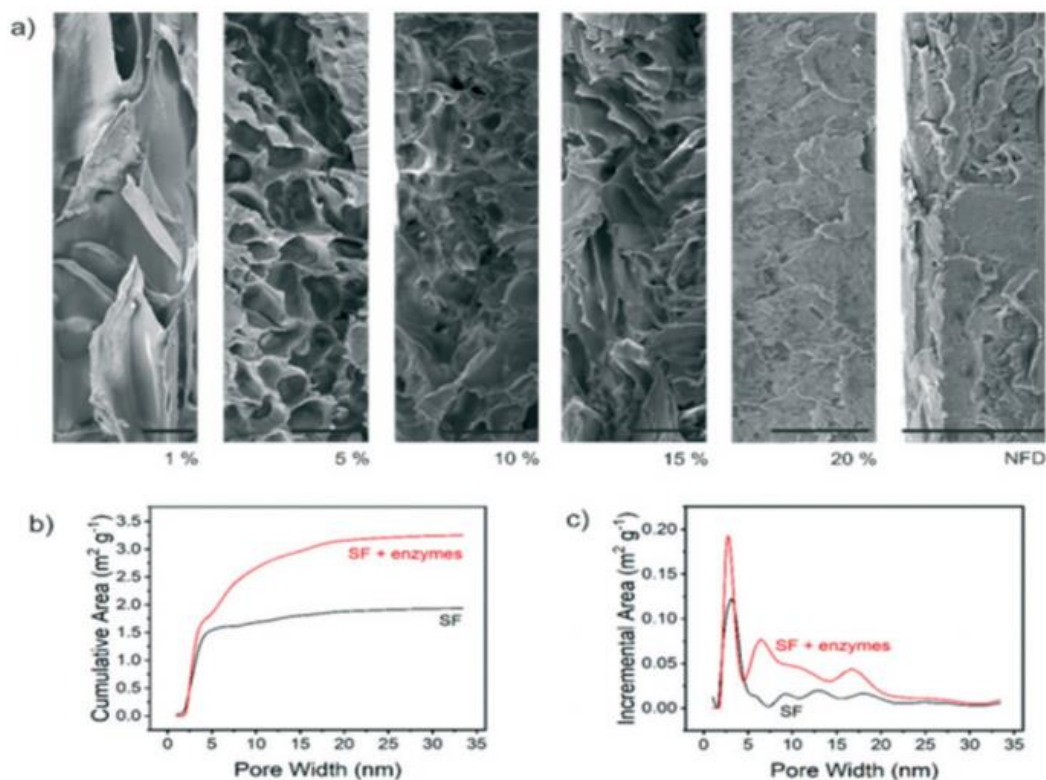


**Figure 7.3: SF microstructure, surface area and porosity.** a) SEM images of freeze-dried cast SF solutions of different concentrations in w/v (1 to 20%) after water annealing and SEM image of a non-freeze-dried film, generated by casting and drying at room temperature (scale bar of 20  $\mu\text{m}$  in every case). b) Surface area measurement (cumulative area) and c) pore size distribution (by incremental area) for the pristine and enzyme-doped SF films. With permissions, from [16].

This porosity, together with its dual hydrophobic ( $\beta$ -sheet domains) and hydrophilic nature ( $\alpha$ -helix regions), endowed the SF films with capillary pumping capacity. Furthermore, as mentioned above, by modifying the silk concentration, the porosity will be altered, resulting in changes in flow rate. A demonstration of the capillary behaviour of the SF can be found in **Figure 7.4**. To investigate the capillary flow rate of the SF thin films, a thin strip was prepared. By using a ruler and coloured solution, methyl red, an approximation of the flow rate could be determined.

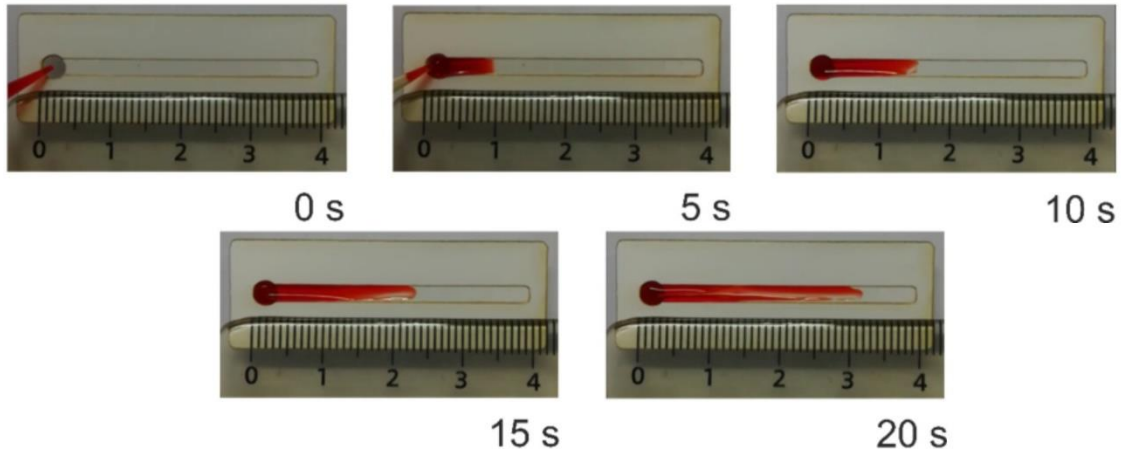


**Figure 7.4: Capillary flow rate using SF thin film.** A red dye is deposited on a SF membrane, after which the flow through the SF thin film is tracked over time and measured using a ruler. With permission, from [16].

The distance from the membrane to the liquid front was measured over time, as indicated by each of the images. Time 0 was chosen from the moment the dispensing of the liquid was initiated, since capillary flow occurred before the full volume was deposited. Furthermore, it can be observed that the liquid maintains a clean front for the first 15 seconds. Since the device was open to air, evaporation caused the liquid front to lose volume, resulting in its spreading and the eventual stop of the flow. Various repetitions enabled a calculation of the actual flow rate, which was approximately 1.5 mm/s. Even though actual flow rates are usually expressed as volume over time, the calculated value here provided a more convenient value. The goal was to develop a lateral flow test, where knowing the flow rate as distance over time, helped determining the optimal length of the channel. It is important to know that the recorded front flow velocity of 1.5 mm/s was in same order of other microfluidic structures, like 1.7 – 2 mm/s for microfluidic synthetic paper [17], 4 mm/s for polymer micropillar arrays [18] or 1.6 mm/s for cellulose-based strips [19].

In conclusion, it should be remarked, that these were preliminary studies on porosity modulation and a more extensive evaluation and optimization will be necessary to achieve precise tuning of the silk film microstructure. The possibility of modifying the porosity of the films may be of great importance in the development of other types of biosensors, where the pore size will impact the filtering properties and the flow rate of the device, e.g. immunosensors.

## 7.3. Generation 1: Secondment in Stockholm

The first secondment was organized as a short training to get accustomed to standard antibiotic testing, as described in **Chapter 6.2.3**. The goal of the second secondment was to use a partner institute, equipped and experienced in fluidics. It was held at the KTH University in Stockholm, under supervision of Prof. Wouter van der Wijngaart. His group is specialized not only in fluidics, but also synthetic paper, namely OSTE (off-stoichiometry thiol-ene polymer), and its patterning and handling, as well as silk technologies. The objective of the secondment was to produce advanced silk-based architectures that contributed to improved liquid management in the lab on a chip architecture developed in the framework of this thesis. For this reason, silk fibroin technologies to pattern silk films and confer them with novel microfluidic capabilities were explored. Two structures were produced and characterized: (i) a honeycomb structure and an origami spring.

### 7.3.1. Gen 1: SF patterning through freeze-drying

Following previous observation that silk films presented intrinsic capillary pumping capacity, the patterning of the layers was studied with the aim to improve the capillary flow and to homogenize it. The pores provide the capillarity of the SF films, and its manipulation would alter the flow behaviour. The original idea of the secondment was to investigate and control exactly these properties through freeze-drying. It was already reported that altering the SF concentration and the freeze-drying conditions (i.e. temperature, duration, etc.) impacted on the characteristics of porosity of the layer, concretely on the size and distribution of the pores [20–22]. Based on that, it was investigated the patterning of silk films using freeze-drying. To pattern the silk, a piece of PDMS with a honeycomb structure was used as master stamp. A 7 % w/v of SF solution was spread on top of the master, and was placed inside the custom made crystallization set-up based on a freeze-drying system. Two dimensions of the hexagonal pattern were available, 100  $\mu\text{m}$  and 25  $\mu\text{m}$  of the hexagonal diameter, and were tried simultaneously. After freeze-drying for two days, the SF film was peeled off using tweezers, and imaged using bright field microscopy and scanning electrode microscopy (SEM), with some results visualized in **Figure 7.5**.

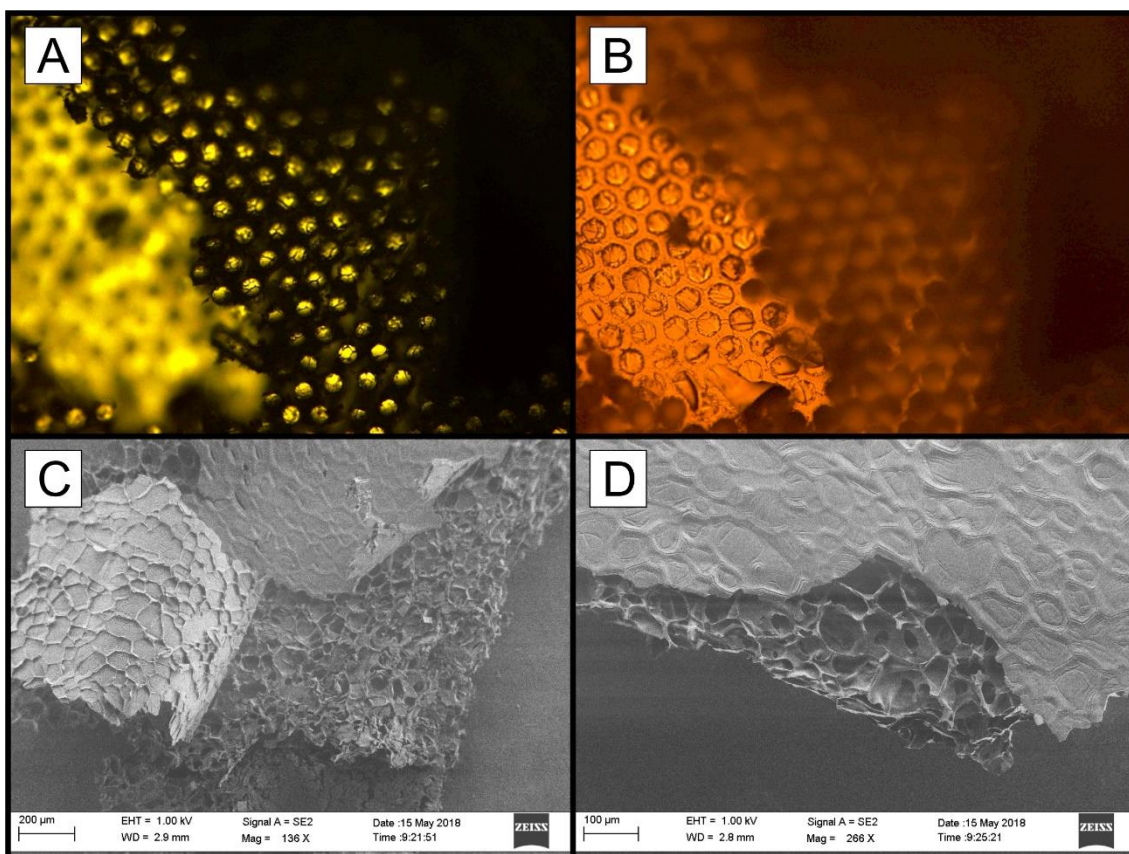


**Figure 7.5: SF thin film with honeycomb pattern.** The top two images (A and B) were taken using bright-field microscopy using a 20x magnification. The bottom 2 images (C and D) were taken using SEM with the following conditions: A) electron high tension (EHT) = 1.00 kV, working distance (WD) = 2.9 mm, magnification (Mag) = 136 x; B) EHT = 1.00 kV, WD = 2.8 mm, Mag = 266 x.

The SF deposited on the 100  $\mu\text{m}$  pattern could be peeled off, though with the risk of tearing the film. However, it was not possible to remove the SF from the 25  $\mu\text{m}$  pattern. The small pattern resulted in a huge overlap in area between both objects, leading higher friction forces than the tensile strength of the silk, causing the silk to tear upon removal. The SF thin films with the 100  $\mu\text{m}$  pattern were further analysed of the transfer of the pattern.

Using bright field microscopy, as shown in **Figure 7.5 A and B**, a repetitive pattern was observed inside the film. The honeycomb pattern was transferred though thin strands of silk pass through the open structures. The clearest image of the pattern is seen in the background of **Figure 7.5 B**, where clear hexagonal structures are discerned. **Figure 7.5 C and D** are SEM images taken to observe more the inside of the SF thin films after freeze-drying. Though some reminiscence of the hexagonal pattern could be observed on the outside of the film, the inside was made up of pore like structures.

Even though the silk acquired the characteristic porous structure, when the film was brought into contact with water, it dissolved. It was believed that the vacuum was not sufficient to produce the crystallization of the silk films, thus they were still soluble and not stable in water. Due to the impossibility to improve the vacuum conditions with the current custom made setup, this strategy was abandoned.

### 7.3.2. Gen 1: Origami silk spring

This second approach was based on the work of Yoshida and Onoe [23], which describes the formation of hydrogel micro-springs through an anisotropic gelation method using bevel-tip capillaries. The authors took benefit from the gelation properties of alginate. It spontaneously formed hydrogels when submerged in solutions containing CaCl<sub>2</sub>. Due to the bevelled tip, alginate at the bottom part of the tip contacted the solution earlier than the top part, resulting in faster gelling. The gelation resulted in a solidification and contraction of the exposed alginate, and thus in an automatic curling, finally resulting in a micro-spring.

Similar to alginate with CaCl<sub>2</sub>, silk is structured in  $\beta$ -sheet domains during its solution-mediated crystallization when in contact with alcoholic solutions, e.g. methanol [24]. Due to overlapping similarities in approach between alginate gelation in CaCl<sub>2</sub> and crystallization of silk in a hygroscopic solution (e.g. methanol), it was hypothesized silk micro-springs could be generated in a similar way.

To test the optimal gelation conditions, various silk concentrations and variations in hygroscopic solutions were studied. The tested conditions are summarized in **Table 7.1**. As described in **Chapter 5.6.2**, a similar setup was prepared as described by Yoshida and Onoe. Using a bevel-tip capillary, the silk solution was pumped into the hygroscopic solution. The flow rates were tried between 20  $\mu$ L/min and 500  $\mu$ L/min (20, 50, 100, 200 and 500  $\mu$ L/min) for every condition. The formation of micro-springs at the different experimental conditions was evaluated by the naked eye.

**Table 7.1: Overview of the various conditions used for the generation of the silk microsprings.** The various conditions refer to the liquids and silk concentrations used. Cond = condition.

	Methanol	Glycerol	Silk concentration (w/v)	Comments
<b>Cond 1</b>	80 %	0 %	6.2 %	Clumps or threads formed
<b>Cond 2</b>	80 %	0 %	7.2 %	Fragile tread (after drying)
<b>Cond 3</b>	80 %	20 %	7.2 %	Flexible threads
<b>Cond 4</b>	100 %	0 %	7.2 %	No treads formed

No micro-springs as the ones reported in the case of alginate were formed using silk, but variations in the conditions impacted the behaviour and formation of the SF. For all conditions, depending on the flow rate, two variations were discerned. At high flow rates, the crystallization resulted in more thread like structures, due to the flow speed being higher than the crystallization process. At low flow rates, the crystallization occurred before silk could fully be ejected from the needle tip. This generally led to clogging of the needle tip, which needed manual cleaning after. Furthermore, due to the higher density of the silk than the solution, all formed products eventually sank to the bottom of the beaker.

For the first condition, both types of results were observed. After ejection, the formed pieces of silk were tried to be collected, but were still too liquid. It was assumed that the

starting silk concentration was too low to generate sufficiently strong structures. By increasing the concentration of the silk in the second condition, the formed threads were solid enough for extraction from the liquid. However, after air drying, they tended to break upon contact due to their fragility. In order to confer silk fragments with a higher mechanical resistance and elasticity, glycerol was introduced in a third condition, which was already reported to interact with silk films and provide them with improved mechanical resistance [25]. Since silk tended to sink fast, it was assumed that the higher density would help to prevent this. The formed thread fragments were significantly stronger than before. After air drying it was also observed they became flexible, able to stretch nearly to 150 % of their starting length before breaking. Nonetheless, no spring formation was observed. The fourth and final condition used a 100% methanol solution, which proved worse than the third generation. For this condition, no real crystallization occurred. Silk floated to the bottom, without the forming of threads, and accumulated there.

After extraction of the formed silk threads, some were taken for further imaging to analyse the formed structure. One such thread is shown in **Figure 7.6** where the image was taken using bright field microscopy. It can be observed that the thread was near perfect straight, due to the weight of silk dragging the formed structure down upon formation. However, the presence of kinks confirmed some partial anisotropic crystallization of the silk. Furthermore, along the length, the silk did not show homogeneous thickness, which was attributed to both the anisotropic crystallization upon ejection and further random dehydration after drying.

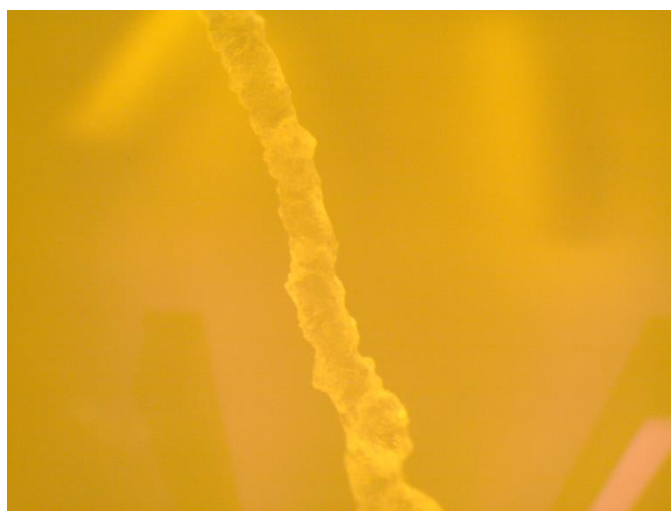


**Figure 7.6: Silk thread highlighted under microscope.** Bright-field microscopy image at a 20x magnification of a strand of silk fibroin generated using 80 % methanol with a SF 7.2 w/v.

In summary, not a single spring formation was observed. Upon ejection from the bevel tip, the flow was too slow and silk aggregated around the bevel tip, or the silk was ejected, usually resulting in the formation of threads. Even if any anisotropic gelation occurred, the weight prevented the formation of the springs. Using an even narrower bevel tip could bypass this issue, by minimizing the weight. However, reducing the tip size may also lead to faster clogging and less absolute distance between the outer edges

for the spring formation. Thus, it was also assumed that using an alternative hygroscopic solution could help alleviate the issue. Both the speed of the gelation and the density of the liquid were critical in the formation of such structures. Due to the complexity of the process, alternative methods for liquid management were studied which did not require the use of silk as microfluidic pumping element.



## 7.4. Generation 2: gradient generator

Taking into consideration the chapters dedicated to the bioassay, it is well understood that the experimental setup requires extensive manual work. The preparation of the antibiotic assay for susceptibility testing requires sequential two-fold dilutions of the antibiotic under test, prior to transferring it to the chip or plate. Microfluidic gradient generators readily exist, but result in either a continuous, not a stepwise dilution, or depend on pumps for accurate dosing and control of the liquids. As stated before, the need of pumps is undesired for Lab on a Chip (LoC) applications for point of care analysis in order to minimize cost, size and weight of the system, which may affect its portability. The idea of the gradient generator described here is to use a capillary driven system, omitting the use of pumps. Additionally, to ensure precise 1-1 mixing occurs a geometrical valve was designed that functions as logic AND-gate, implying that the valve can only be breached when both liquids are present. The basic principle of the geometrical valve is illustrated in **Figure 7.7** below.

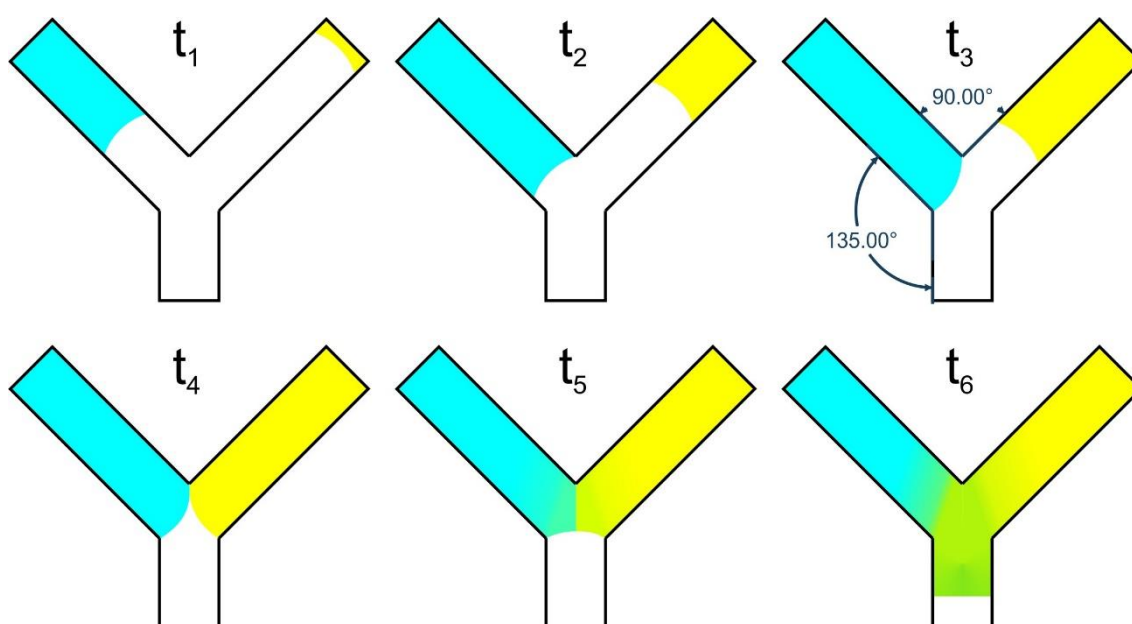


**Figure 7.7: Scheme of the principle of a geometrical valve.** Two identical liquids, highlighted in blue and yellow, enter the valve at a different time  $t$ . Contact at the valve results in the mixing of the two, giving rise to a green colour. Highlighted are the angles between the inlets and the inlet and outlet channel.

Two identical liquids (blue and yellow) are introduced to the system at a different time without additional input pressure. Capillary pull will drag both liquids forward (**Figure 7.7 t<sub>1</sub>-t<sub>2</sub>**). After a specific time (**Figure 7.7 t<sub>3</sub>**), the first liquid reaches the geometrical valve, where the angles between the input channel and the other 2 channels, the second input and the output channel respectively, are both bigger than the contact angle between the liquid and the material. This will prevent the capillary pull and the liquid will come to a stop. The first liquid will remain in position until the second liquid arrives (**Figure 7.7 t<sub>4</sub>**). Contact between both liquids will result in their merging, overcoming the angle limitation (**Figure 7.7 t<sub>5</sub>**) resulting in the bypass of the valve (**Figure 7.7 t<sub>6</sub>**). After merging, both liquids will continue to propagate and mix based on diffusion. Since the presence of both liquids are required and the absence of an external push, both liquids

arrive at near-identical pressures and speeds, resulting in a 1-1 mix after the valve. The work below described the design, simulations and fabrications of the development of the geometrical valve.

#### 7.4.1. Geometrical control valve design and simulations

The development and optimization of the geometrical control valve has been divided into separate generations. Each generation showed improvements on both the simulation part as on the actual function of the valve itself. The major differences between the generations are summarized in **Table 7.2**, with each one further described in the following subchapters.

**Table 7.2: Evolution and comparison of the various generation of the geometrical valve design.** The various generations are compared based on their physical properties and behaviour.

	Gen 1	Gen 2	Gen 3	Gen 4
<b>Channel and valve dimensions</b>	Tiny (um)	Tiny (um)	Large (mm)	Large (mm)
<b>Symmetrical valve</b>	Yes	No/Yes	Yes	No
<b>Liquid comes to a stop</b>	No	Yes	Yes	Yes
<b>Liquids merge and continue</b>	No	Yes	No	Yes
<b>Fast prototyping possible</b>	No	No	Yes	Yes

#### 7.4.2. Gradient generator Generation 1

The first design of the geometrical valve was based on the publication by Melin et al. [26], which described a liquid-triggered liquid microvalve. In order to get familiar with the principle and the COMSOL software, the first generation design was replicated and analysed. The design was drawn in AutoCAD and simulated in COMSOL15. The built-in model wizard was used to quickly generate the required models, using a 2D space dimension and the two-phase flow level set method for laminar flow. The simulation results are shown in **Figure 7.8**. **Table 7.3** highlights all modified parameters, whereas those not listed below were unaltered from their automatic generated value.

**Table 7.3: COMSOL settings of generation 1 level set.** Highlight of the parameters modified from the standards in the COMSOL simulations of generation 1 based on the level set method.

Model	Component	Subcomponent	Value/parameter
<b>Geometry</b>			
Length unit	Scale		μm
<b>Materials</b>			
From library			Air and water
<b>Laminar Flow</b>			
	Inlet	Pressure	P=0
<b>Level set method</b>			
<b>Mesh</b>			
Size	Fluid dynamics		Extra Coarse
<b>Study</b>			
Time Dependent	Range		0:1e-4:1e-2
Time-dependent solver 1	Generalized alpha		BDF order 2
	Steps taken by solver		free
Segregated	Tolerance factor		1
	Anderson acceleration	Dimension	5
		Mixing parameter	0.9
		Iteration delay	1

The length unit was adapted to ensure the correct dimensions were obtained after the import of the AutoCAD file and to match the publication. For the materials, since only the dynamic viscosity and the density of both air and water were relevant, the standardized materials from the library were chosen. Furthermore, to emulate the absence of pumps, the input pressure was set at zero, to avoid any external force to drive the liquid besides the capillary pull. Additionally, to ensure a fast simulation, a coarse mesh was sufficient given the fluid dynamics calibration to enable small enough details around the valve, whilst maintaining a low density in the straight channels. The parameters specified in the study step were chosen to ensure a fast simulation was achieved.

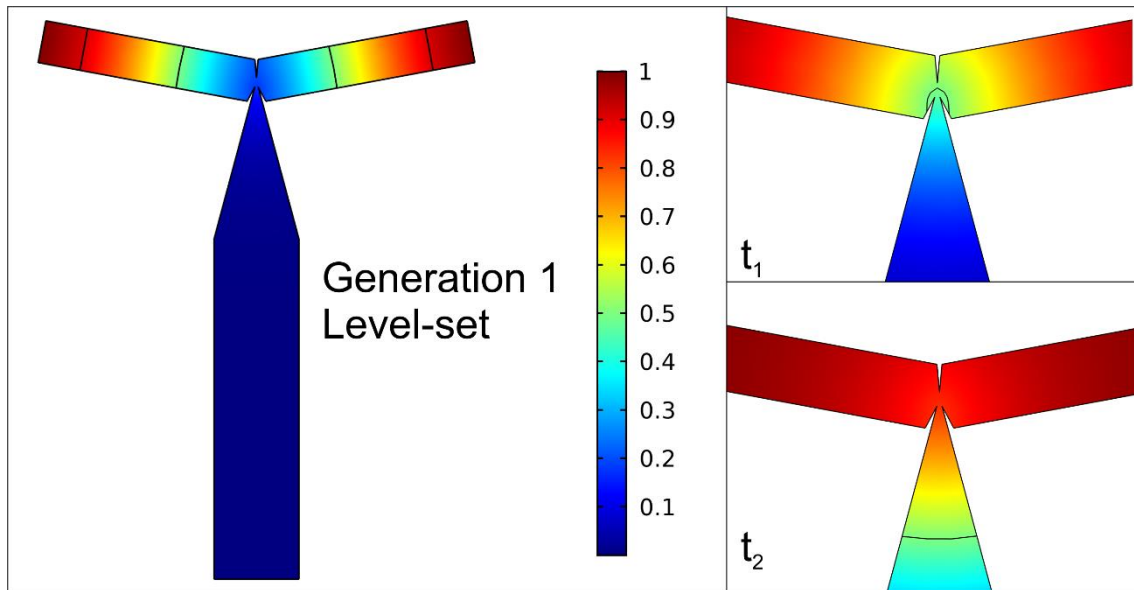


**Figure 7.8: COMSOL simulation of the generation 1 valve using the level set method.** Highlighted in colour is the liquid-air ratio, with red representing 100 % liquid and blue 0 % liquid. Images were taken at different times to highlight the collapse at the valve.

Based on the simulation results, three images were taken from the liquid flow at different time steps. The colour gradient depicts the liquid to air ratio, with 1 signifying 100 % liquid (red), whereas 0 shows 100 % air (blue). A black line was used to highlight the approximate mean position of the interface. It can be noted that both liquids arrive at the valve simultaneously and are able to propagate after. For this first simulation, a level-set approach was used to obtain a quick result. However, this approach provides less accuracy compared to the alternative phase field method. Both differ heavily in the underlying equations used and how they are solved, but a simplified comparison is highlighted in **Table 7.4** below.

**Table 7.4: Differences between level set method and the phase field method,** for the simulation of a multiphase flow using COMSOL multiphysics 5.4.

Level set method	Phase field method
Two phases	Up to three phases
Computationally less expensive (one transport equation)	Computationally more expensive (two additional transport equations)
Mean position of interface is more important than the fine details	Surface shape/exact interface is of primary importance
	Allows fluid-structure interaction and phase separation models

As can be observed, the level set method enables a fast simulation but lacks the required details for the given application. Since the goal is to analyse the function of the geometrical valve and how the liquids behave around it, the phase field method was used in all other simulations. To clarify the differences between both, the first design was simulated again using the new method, with some additional modifications for improving the accuracy of the simulation. The parameters for the simulation are summarized **Table 7.5**, whereas those not listed below were unaltered from their

automatic generated value. Finally, the dimensions employed here were in the micrometer scale, with the opening to the exit channel being 4  $\mu\text{m}$  wide and the channels themselves 50  $\mu\text{m}$  in width.

**Table 7.5: COMSOL settings of generation 1 phase field.** Highlight of the parameters modified from the standards in the COMSOL simulations of generation 1 based on the phase field method.

Model	Component	Subcomponent	Value/parameter	
<b>Geometry</b>				
Length unit	Scale		$\mu\text{m}$	
<b>Materials</b>				
From library			Air and water	
<b>Laminar Flow</b>				
Physical model	Neglect inertial term			
Discretization			P2+P1	
	Inlet	Pressure	P=0	
<b>Phase field method</b>				
	Wetted wall		70 [deg]	
<b>Mesh</b>				
	Size	Fluid dynamics	Fine	
	Corner refinement	Boundaries adjacent to valve	0.05 elemental scaling factor	
<b>Study</b>				
Time Dependent	Range		0:5e-3:5e-2	
	Time-dependent solver 1	BDF	BDF order 2	
		Initial step fraction	1e-2	
		Initial step growth rate	1.5	
		Time step	1e-5	
	Fully Coupled	Damping factor	0.9	
		Maximum Number of iterations	15	
		Tolerance factor	0.5	
		Anderson acceleration	Dimension 5	
			Mixing parameter 0.9	
		Iteration delay 1		

The inertial term in the physical model was set to "neglect", which is characteristic for capillary flow. Additionally, the discretization was changed to P2+P1, which implied second order element for the velocity components, whilst maintaining first order linear elements for the pressure field. Second order velocity components were more accurate for low velocities, and standard for creeping flow. The phase field method also took into account the wetting angle between the liquid and the material, which was set at 70° to match the contact angle between water and PMMA, the material intended to be used

later in the fabrications [25]. Due to the need of a higher precision of the interface in the phase field method, a smaller mesh was used. The general size was reduced to fine, with and additional refinement of the mesh around the valve, to enable high precision tracking of the interface upon merging of the liquids. As before, the study steps were altered to improve the speed and minimize the errors during the simulation. The corresponding results of the simulation are highlighted in **Figure 7.9**.

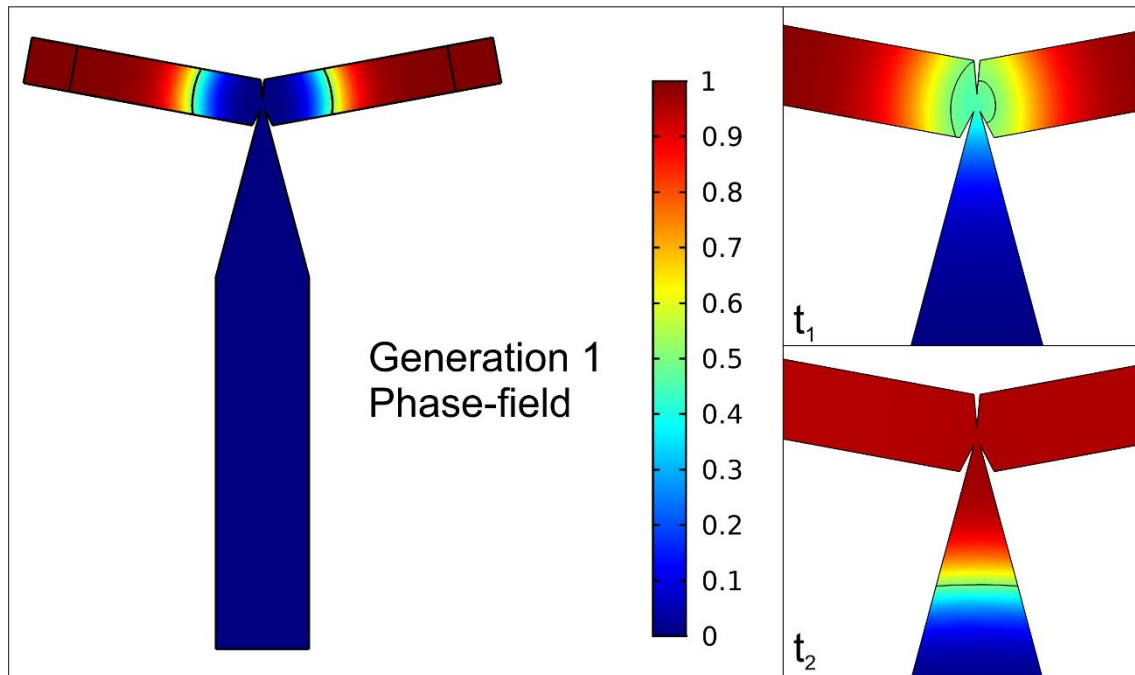


**Figure 7.9: COMSOL simulation of the generation 1 valve using the phase field method.** Highlighted in colour is the liquid-air ratio (red/1 = 100 % liquid, blue/0 100 % air). Images were taken at different times to highlight the collapse at the valve.

Liquid was seen flowing towards the valve, followed by the merging at the valve, and the sequential continuation. Furthermore, the same colour gradient was used, but the gradient around the interface was significantly smaller than in **Figure 7.8** due to the more precise phase field method. Additionally, due to the implementation of the hydrophilic surface with a contact angle of  $70^\circ$ , a meniscus was observed in all cases. The asymmetric arrival at the valve was presumed to be due to some artefact during the calculations.

To replicate time delays between both channels arriving at the valve, an asymmetric design was used. As shown in **Figure 7.10**, the valve did not function as intended and the first liquid to arrive continued past it. Additionally, the breaching liquid continued into both the outlet and the other inlet. It needs saying that the breaching of the valve here, did not impact the system described in the work of Melin et al. [26]. The contact angle was different (due to considering PMMA instead of silicon) and the design was simplified. Nonetheless, the simulation showed that optimizations were necessary for a fully functional valve based on capillary flow.

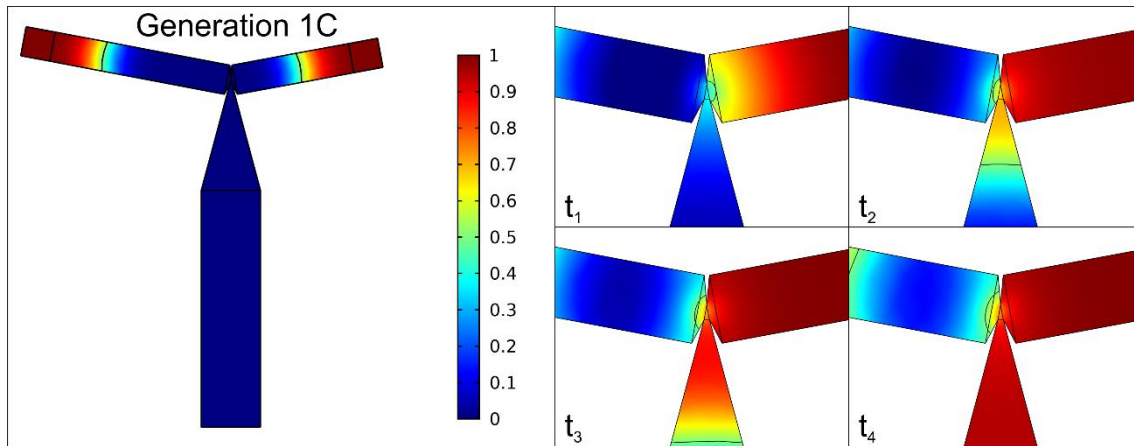


**Figure 7.10: COMSOL simulation of the generation 1 c valve, using asymmetric inlets.** Highlighted in colour is the liquid-air ratio (red/1 = 100 % liquid, blue/0 100 % air). Images were taken at different times to highlight the collapse at the valve.

### 7.4.3. Gradient generator Generation 2

The first geometrical valve relied on a narrowing and immediate broadening of the channel to increase the angle between the channels above the contact angle between the liquid and solid. However, if the dimensions were too small, the generated pressure bypassed the contact angle limitations. Incorporating additional structures next to the valves not only provided larger angles, but also an additional physical margin to compensate for increased pressures. The expanded valves in the second generation were based on the works of Zimmermann et al. [27], which employed an asymmetric flow-disrupting structures. Their work described the design of a microfluidic timer, with one liquid reaching the valve quickly, whereas the other flowed through meandering channels. To avoid the first liquid from continuing two additional openings next to one of the fluidic inlets at the height of the valve were added. Upon arrival of the second liquid, both merged and the valve breached. A specific duration before the valve breach could be controlled by the length of the meandering channel.

The first design of the second generation utilized a similar asymmetrical valve, which was designed in AutoCAD. The opening of the valve support structure between the two inlets was set at 3  $\mu\text{m}$ , the other support structure at 6  $\mu\text{m}$ , and the inlet themselves entered the valve at 5  $\mu\text{m}$ . The outlet had a final width of 20  $\mu\text{m}$ . The parameters for the simulation were identical to those used in **Table 7.5**, and the simulation results are highlighted in **Figure 7.11**.

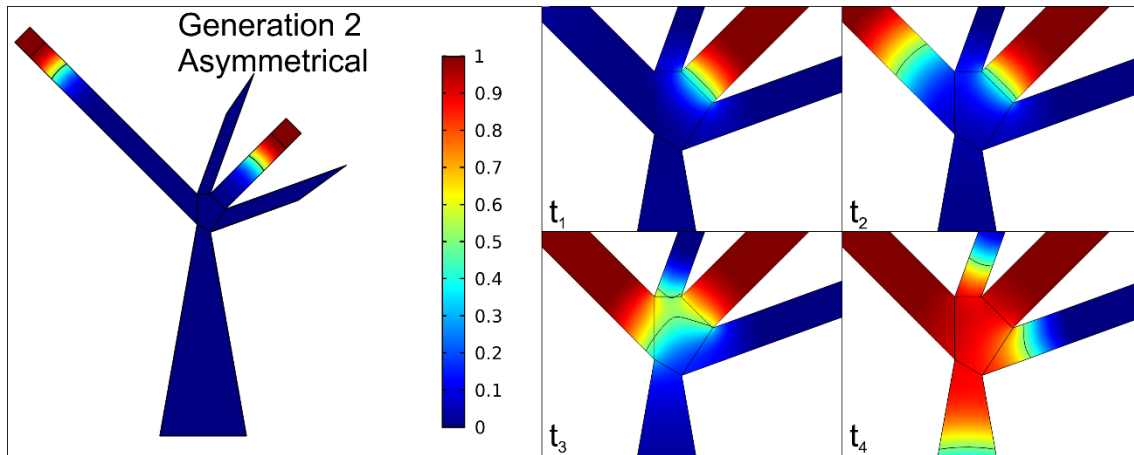


**Figure 7.11: COMSOL simulation of the generation 2 valve using an asymmetric valve and inlet design.** Highlighted in colour is the liquid-air ratio (red/1 = 100 % liquid, blue/0 100 % air). Images were taken at different times to highlight the stopping of the liquid and sequential collapse of the valve.

An asymmetrical inlet design was employed again to emulate a time difference between both liquids. It was observed that the first liquid reached the valve and stopped in place due to the large contact angles. Once the second liquid arrived, both contacted, merged and propagated towards the outlet and, according to the simulations inside the valve side structures. The simulation showed that the additional support structures of the valve improved the retention of the first liquid, but without limiting the fluid from continuing once the second one arrived.

Although the simulation of the asymmetrical valve showed decent performance, due to its intrinsic nature, the valve will only work when the first liquid to reach it came from the correct direction. To increase the functionality of the valve, a symmetrical design was designed, which works independent which inlet was used first. To this end, valve support structures were positioned below each and between both inlet channels. Finally, the dimensions were increased, with the opening of the inlets at the valve sitting and the at  $100\ \mu\text{m}$ , the valve support structures at  $100\ \mu\text{m}$  and  $200\ \mu\text{m}$  for the top and side structures respectively, and the channels themselves were  $300\ \mu\text{m}$  wide. The parameters for the simulation were identical to those used in **Table 7.5**, and the simulation results are highlighted in **Figure 7.12**.



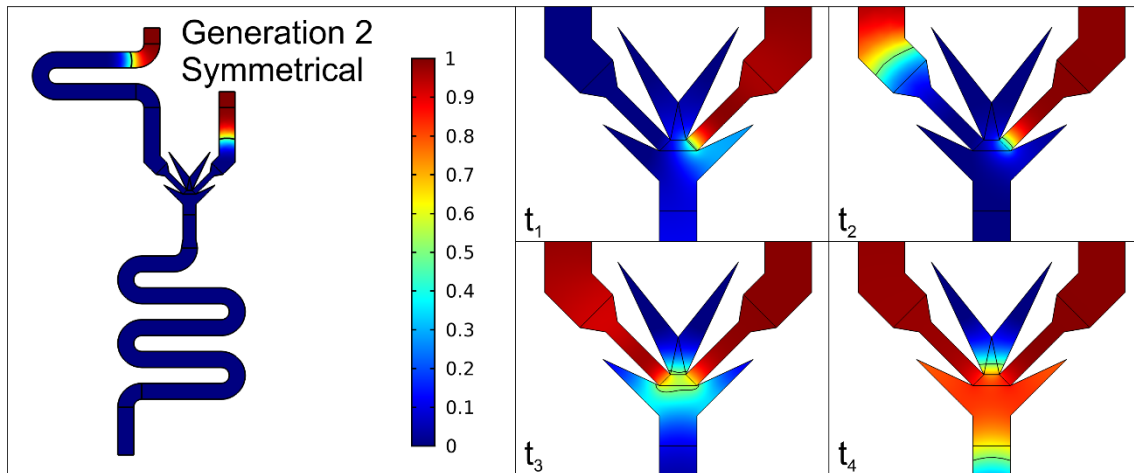


**Figure 7.12: COMSOL simulation of the generation 3 valve, using a symmetric valve and asymmetric inlets.** Highlighted in colour is the liquid-air ratio (red/1 = 100 % liquid, blue/0 100 % air). Images were taken at different times to highlight the collapse at the valve.

As in the previous cases, the liquid stopped at the height of the valve, and continued when the second one arrived. However, both images highlighted a possible drawback with the current simulation parameters. Even though the change from level set to phase field improved the precision of the interface, it was still too large to be reliable. As could be observed, the merging of the liquids occurred at a 'liquid ratio' of 0.5, not at the 1. However, in reality a state of 0.5 liquid does not exist, but represents the uncertainty of the exact interface in the simulation. When the regions of uncertainty overlapped, it created a solution where the liquids began to merge (and later propagate past the valve) even if the actual interfaces might not have interacted.

#### 7.4.4. Gradient generator Generation 3

The purpose of the microfluidic designs and the gradient generator was to develop a system that was low cost and easy to use for the automatization of the bioassay. However, the previous generations, though showing successful simulations, were all designed around dimensions in the micrometer scale. Fabrication at this scale requires high precision, quickly increasing fabrication times and cost, especially when clean rooms are required. To overcome said issue, the designs were scaled up to enable quick manufacturing methods. Furthermore, the larger devices will become less fragile and more bulky, further simplifying testing in the lab.

The third generation, in addition to having larger dimensions, used the custom-made design of the valves of the second generation with minor modifications, leading to four variations in design (see **Figure 7.13**):

- Double: valve support structures were placed between each of the inlets and below each of the inlets respectively, to ensure maximum stopping of the liquid by maximizing contact angles.
- Bottom: the valve support structures were located below each inlet. This ensured a contact between both liquids when they arrived at the valve, but still prevented liquid flow by the increased contact angle towards the outlet. A

potential risk existed where the liquid of one inlet continued up the other inlet (as seen in **7.4.2 Generation 1 c**).

- Top: the only valve support structure was located between the inlets. This avoided the liquids from entering the other inlet, but could risk a single liquid of continuing to the outlet.
- None: Valve support structures were omitted, both as control for the others, and to test the feasibility of the intrinsic angles between both inlets and the outlet as geometrical valve.

Table 7.6: Parameter added to Table 7.5 in the COMSOL simulations of generation 1b.

Model	Component	Subcomponent	Value/parameter
<b>Phase field method</b>			
Interface thickness			pf.hmax/5
	Wetted wall		70 [deg]

Additionally, the dimensions of the channels were increased to 1 mm wide, and the inlets at the valve opening 0.78 mm wide. These increases were made to accommodate the design to the fabrication process, as explained above. Finally, to improve the accuracy of the simulation, a specific parameter was modified, as shown in **Table 7.6**. The interface thickness was reduced, at the cost of an increased complexity and duration of the simulation. The default expression is  $pf.hmax/2$  ( $pf$  = phase field), which means that the thickness was calculated up to half the maximum mesh element size ( $hmax$ ) in the region through which the interface passed. It was increased to  $pf.hmax/5$  making the interface significantly sharper, as can be observed in **Figure 7.13**.

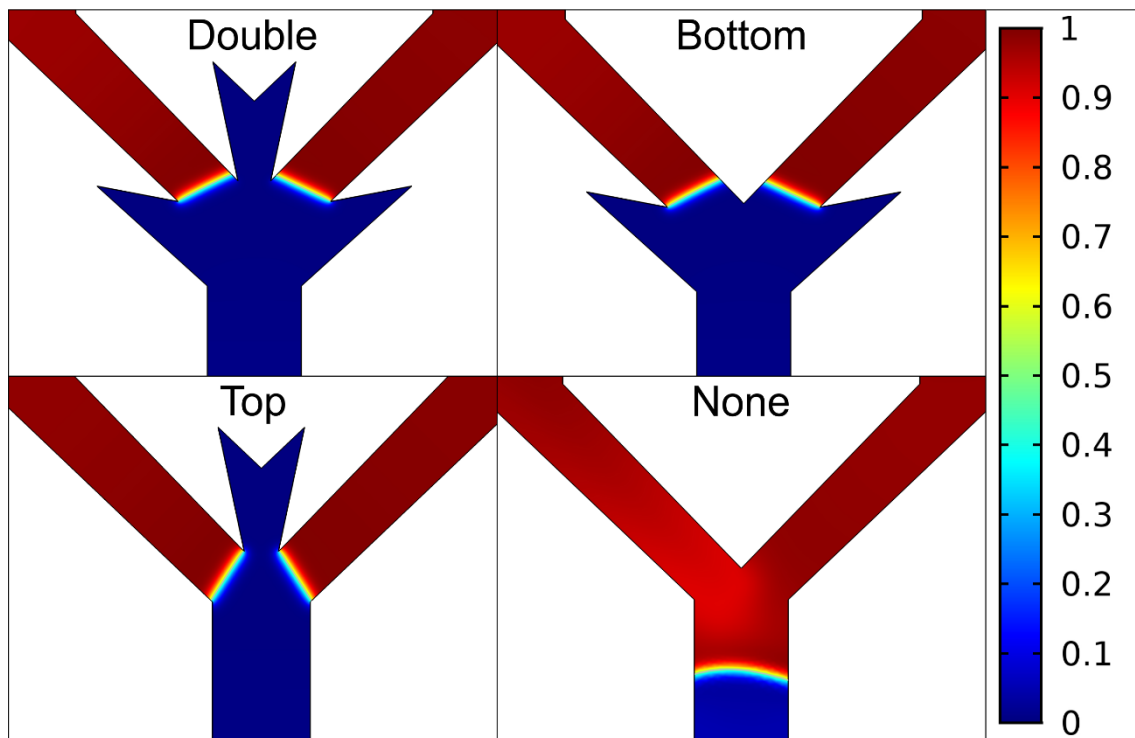
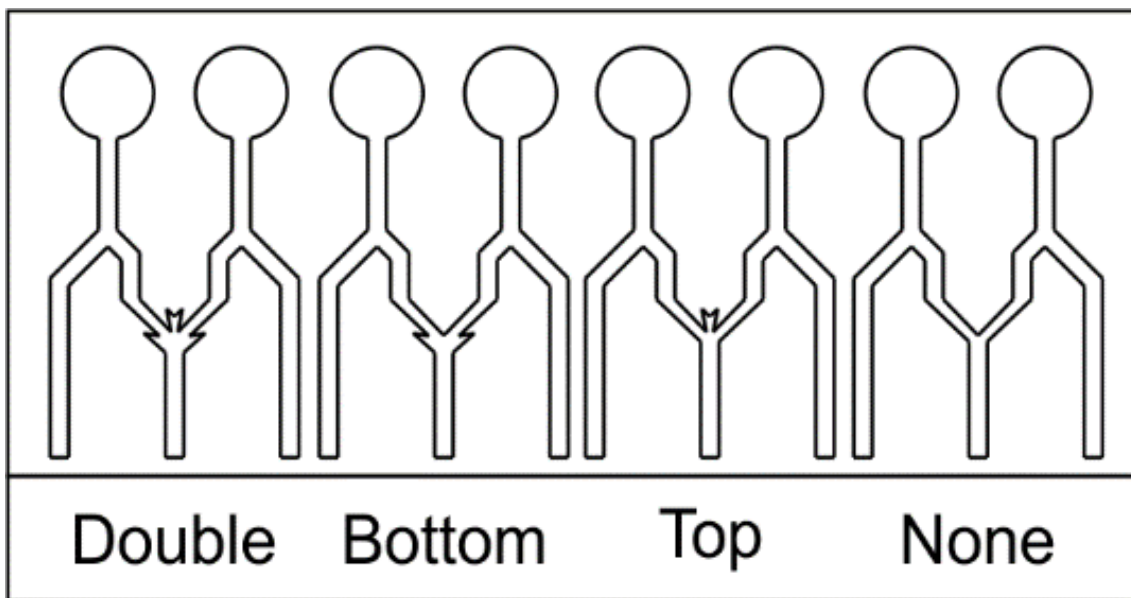


Figure 7.13: COMSOL simulation of the generation 3 valves, with each of the 4 variations. Each image shows the ending of the simulation, indicating the potential breaching of the valve. Highlighted in colour is the liquid-air ratio (red/1 = 100 % liquid, blue/0 100 % air).

With the increased precision of the interface, the liquids were no longer able to pass the valve when any of the support structures were present, since the regions of uncertainty were no longer able to interact. In *Double* this was due to both side structures increasing the angle above the water/PMMA contact angle, preventing the liquids from continuing and merging. In *Bottom*, the valve support structure not only prevented the liquids from automatically continuing, but also from reaching the merging point. Similarly, the valve opening in *Top* prevented the liquids from touching and sequential merging. When no support structures were present, as in *None*, the liquids were freely able to merge and continue. Additionally, though not shown, the liquid still stopped at the valve, due to the angles between the inlets and between inlet and outlet. Based on the simulations, the valve support structures ensure the stopping of the liquid, but likely prevented the continuation too. However, when no support structures were present, the liquids still stopped, but manage to propagate.



**Figure 7.14:** CorelDRAW design of the four fluidic structures, each based on a different variation of the valve of generation 3.

Given the feasible dimensions being used for the 4<sup>th</sup> generation, the fluidic designs were adapted for fabrication. Each of the four valve variations were incorporated into a simple design, as shown in **Figure 7.14**. The four variations were cut by laser ablation from a single PMMA plate, with a thickness of 3 mm. Water was added to each inlet sequentially to test the potential of the valves to stop the liquid, and continue upon arrival of the second one. A summary of the observations of the liquid and valve behaviour is shown in **Table 7.7**.

When the valves were present, the practical results mostly matched those obtained by the simulations. The major difference lied in the possible merging and continuation of the liquids, which was attributed to an additional pressure upon filling of the inlets, whereas the simulation maintained a zero additional pressure calculation. The largest difference was found when no support structures were present, usually leading to breaching of the valve when only one liquid was present. This could be attributed to

potential artefacts during fabrication on top of the aforementioned pressures. Additionally, the dimensions of the valve support structures required adjustments to enable both liquid stop and the sequential liquid mergence.

**Table 7.7: Observations of the performances of the fabricated generation 4 fluidics.**

Valve type	Liquid stop	Liquid merge
<b>Double</b>	Liquid stops every time	Both openings together are too wide for the liquid to continue
<b>Bottom</b>	Liquid stops every time	Liquids can easily touch, but the merging is not always possible to break the rest of the valve
<b>Top</b>	First liquid sometimes continues to the outlet	Liquids cannot touch, making it impossible to break the valve Upon filling, the additional pressure can sometimes cause both liquids to merge and continue
<b>None</b>	First liquid almost always continues to the outlet, sometimes to the other inlet	If the first liquid stops, merging works without issue If the liquid continues, merging not always works due to the increased resistance present for the second liquid

Since the fabrication method would also affect the performance of the valve, two fabrication methods were evaluated for the quick prototyping of the fluidics at this stage: laser cutting and milling. Both methods were compared given their performance, as shown in **Table 7.8**. The laser cutter enabled the fastest fabrication of the fluidic channels, but came at reduced precision during fabrication of the completed design. The biggest drawback was the inherent principle of laser cutting, where a beam of intense power is used to melt through the substrate, which led to uncontrolled melting near the top (and bottom due to reflection at the support grill) of the channels, as shown in **Figure 7.15 Side view**. The same figure also highlights a limitation of potential fluidic designs using any freestanding structures, e.g. channel flowing around a circular structure. The laser cutter cut through the entire material where the final device was later bonded to a new support structure to close the bottom of the channels. However, a freestanding structure would need manual positioning when bonding, leading to losses in precision (**Figure 7.15 Top View**). The laser cutter could also be used at a lower power mode to etch through the substrate, but this could cause more uncontrolled melting and additional artefacts, leading to even lower precision.

**Table 7.8: Comparison between the Laser Cutter and the Milling machine**, related to the fast prototyping of the fluidic designs.

Parameter	Laser Cutter	Milling machine
<b>Machine type</b>	Epilog Mini 24 – 30 W	CNC Roland MDX-40
<b>Speed</b>	Fast limited by substrate thickness and type	Slow limited by milling head and substrate type
<b>Design Dimensions</b>	Down to 600 dpi ( $\approx 42 \mu\text{m}$ )	Milling head dependent (0.5 mm)
<b>Channel roughness</b>	Smooth walls	Potentially rough walls
<b>Wall verticality</b>	Under/overcut due to melting of substrate	Straight cut
<b>Control during fabrication</b>	Low control	High control
<b>Precision</b>	Low (manual starting point)	High (programmable starting point)
<b>Design limitation</b>	Planar and no enclosed structures	3D possible

The milling machine milled away pieces of surface in each cycle, slowly grinding out the desired channels without going fully through the material, thus omitting any latter bond to a bottom support. Furthermore, milling enabled higher precision at the start and during the fabrication by precise programmable control. Additionally, any milling parameter could be adjusted at any point during the process, leading to a high level of control. Though the process was significantly slower, it was a necessary trade-off, since the over/undercut due to melting and the design limitation severely impacted the quality of the fabricated fluidic channels. Nonetheless, milling the channels could lead to potentially rough walls, which could affect the flow behaviour. This was minimized by controlling the velocity and spin rate of the milling. However, increased spin rates may lead to potential melting of the walls due to heat generation by friction. The biggest drawback of the milling machine was the limitation on the dimensions which depended on the size of the milling head, which rarely went below the mm range. Additionally, the smaller the head size, the more prone it was to break, causing delays in the fabrication. Nonetheless, in all subsequent fabrications, the milling machine was used.

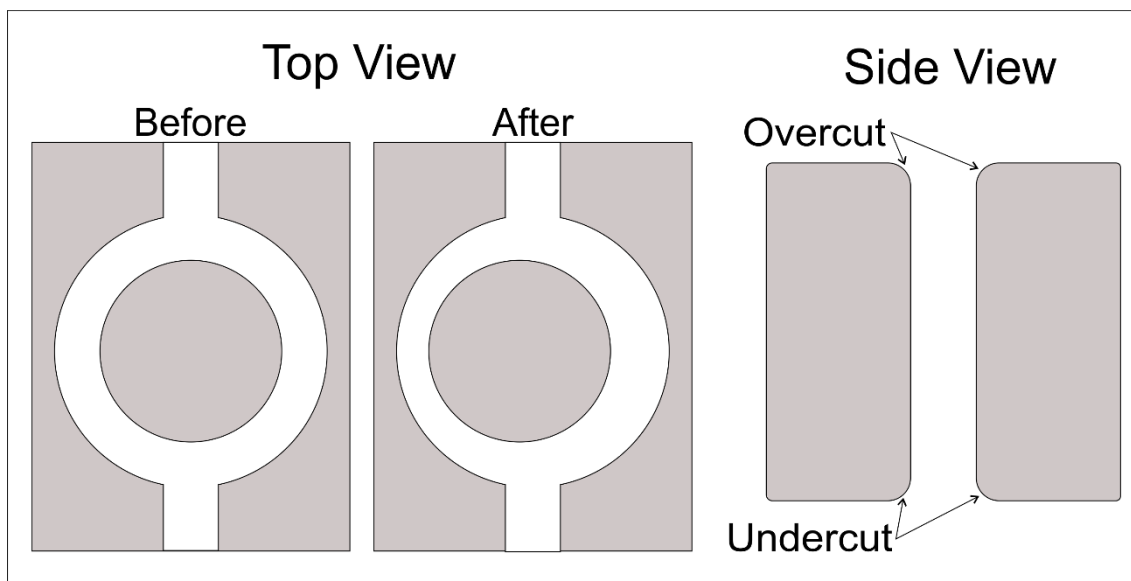


**Figure 7.15:** Depiction of the drawbacks of the laser cutter, for its use as fast prototyping method for the fluidic designs.

Though no bonding required to be made to a bottom support when using the milling, the fabricated channels were still open to the outside from the top. A cover was desired to prevent any outside interactions with the channels, with the exception of the in- and outlets. Various methods were tried for sealing the chip in a reliable way, as summarized in **Table 7.9**. Each of the bonding methods is explained in **Chapter 5.2.2**.

**Table 7.9:** List of methods for bonding the fluidics to a top cover and the impact of the bonding.

Type	Permanent bond	Leakage	Channel obstruction
Methacrylic acid	Y	N	Y
PSA (inlets only)	N	Y	N
PSA (full design)	N	Y	Y
Magnets	N	Y	N
Optical adhesive	Y	N	N

- The **methacrylic acid** provided a permanent covalent bond between the fluidic device and the cover, through an irreversible reaction, and provided maximum coverage between both parts, thus minimizing leakage. However, using high pressure on the cover, the methacrylic acid was squeezed towards and inside the channels, leading to obstructions of the flow and to important changes on the geometry and properties (e.g. contact angle) of the channel/valves architectures.
- **PSA**, or “double-sided tape”, was employed in two ways: adhered to the cover during the fabrication of the inlets/outlets, or adhered to the fluidic design, with all the channels milled through the PSA. A thin layer of flexible PSA maximized the contact between the fluidics and the cover, though if no perfect contact was achieved, liquid spread between. Additionally, when milling through the PSA, loose and rough parts were generated at the height of the channels, possible interfering with the flow.

- **Magnet** holes were created in both the fluidics part and the cover, to create a full reversible bond, whilst avoiding any parts interfering with the channels. However, PMMA was rarely fully homogenously flat, resulting in a non-perfect contact between cover and fluidics. This could be overcome by employing stronger magnets, to enforce the contact, but it would negatively impact the reversibility.
- The **optical adhesive** utilized a similar principle as the methacrylic acid, by binding the fluidics and the cover together, this time using a solvent sensitive to UV irradiation. After spreading the adhesive over the cover, both pieces were placed together and illuminated using UV light (365 nm). The advantage over the methacrylic acid was the higher control of the spreading of the liquid, thus easier prevention of channel obstruction, at the cost of higher chances of leaking.

Using the milling machine two of the valve variations were fabricated, as shown in **Figure 7.16**. The left one utilized the bottom valve, with the one on the right without any valves present. These structures also incorporated the magnets into the design, with the cover currently removed for the imaging. A blue liquid was inserted in the right inlet, stopping at the valve, whilst continuing down the direct channel. After admission of the yellow liquid, the combination of both breached the valve, and started mixing down the meandering channel. Though not visible, the flow was slower than those predicted by the simulations. This was assumed to be due to the capillary pull, with the contact angles inside the system being smaller than assumed. An excess of liquid inside the inlets were required, as additional hydrostatic pressure, to push the liquid forward.

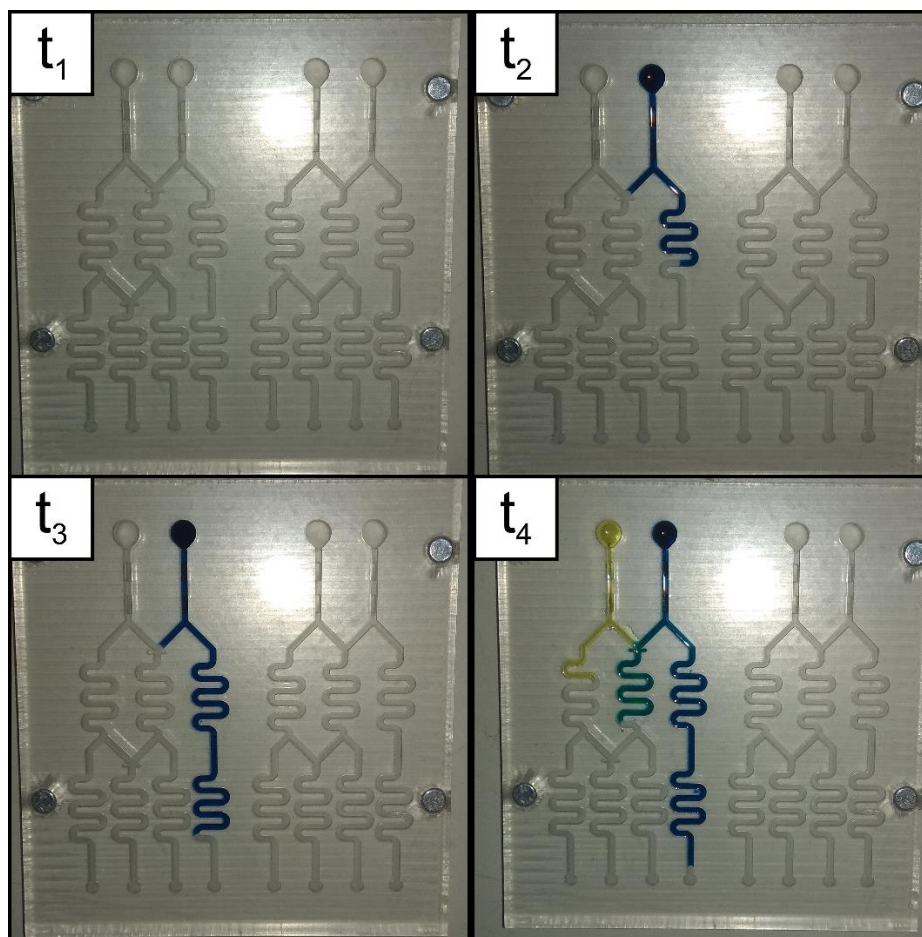


**Figure 7.16: Highlights of the function of the 3rd generation.** The device as shown was composed of two separate fluidic systems, using bottom valves on the left, and omitting the valves on the right. A blue liquid was added in the right inlet. After reaching the valve, a second, yellow liquid was added in the left inlet.

#### 7.4.5. Gradient generator Generation 4

The simulations relied on the theoretical contact angle between water and PMMA to calculate the flow behaviour. However, when observing the flow rates and behaviours in the fabricated designs, important differences with the theory were observed. It was assumed to be caused by the milling, increasing the roughness on the walls and bottom. To improve the simulation, various samples were prepared to calculate the contact angles under different PMMA conditions. The results are summarized in **Table 7.10**. The tested PMMA surface was either left untouched, or milled with either a 0.5 mm or 3 mm milling head. Additionally, two extra conditions were validated. Methacrylic acid, described before as one of the sealing methods, was tested for its interaction with the flow rate upon entering the channels. NaOH was used as to treat the PMMA surface, making it more hydrophilic.



**Table 7.10: Contact angle measurements of PMMA with various treatments.** Each column described the contact angles of PMMA with or without mechanical treatment, whereas each row described the effect of chemical treatment. Measurements were obtained using a KRÜSS Drop Shape Analyzer DSA 100. (n=4)

Chemical treatment	PMMA	PMMA with 0.5 mm milling head	PMMA with 3 mm milling head
Untreated	$30^\circ \pm 3^\circ$	$52^\circ \pm 20^\circ$	$36^\circ \pm 11^\circ$
Methacrylic acid	$79^\circ \pm 1^\circ$	$72^\circ \pm 4^\circ$	$77^\circ \pm 1^\circ$
NaOH	$22^\circ \pm 11^\circ$	$46^\circ \pm 15^\circ$	$33^\circ \pm 18^\circ$

The contact angle measurements were based on the sessile drop method, placing a droplet of distilled water of 5  $\mu$ L on a flat surface, and measuring the resulting contact angle with the surface. This angle was measured automatically, using a KRÜSS Drop Shape Analyzer DSA 100, and averaged over 4 positions as shown in **Figure 7.17**.

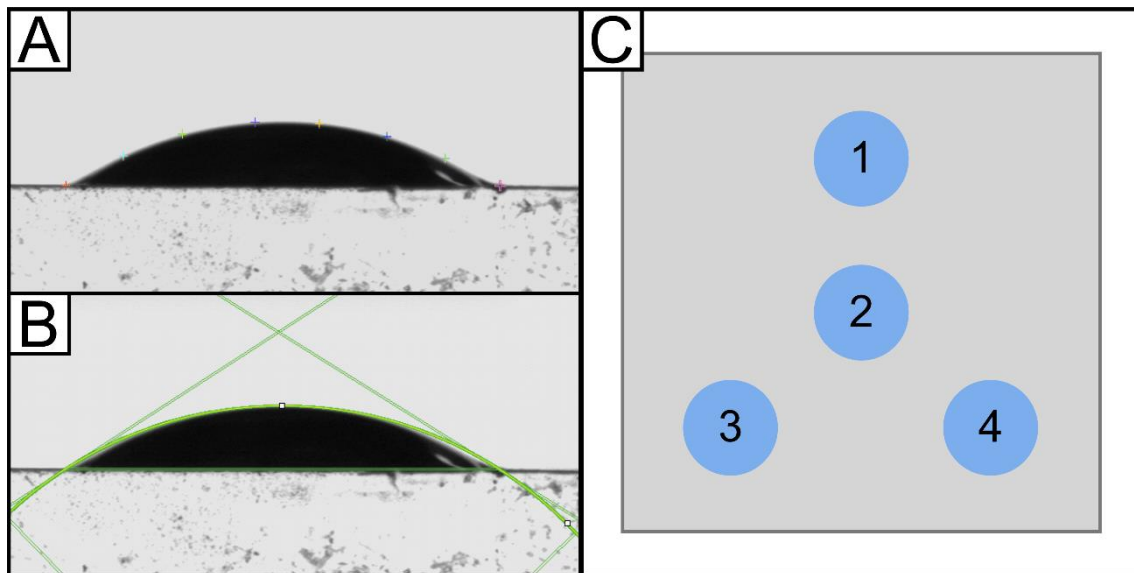


**Figure 7.17: Depiction of the measurement of the contact angle.** A) image of the droplet on top of the PMMA surface, with coloured crosses highlighting the interface between droplet and background. B) depiction of calculation of the contact angle, by connecting the crosses across the interface, and calculating the angle upon connection with the surface. C) highlight of the positions of each of the 4 measurements.

The contact angles of untreated PMMA was near identical to the reported value, though the milling negatively affected the hydrophilicity. In particular, the 0.5 mm mill cause large variations, due to the small scratches on the surface that can cause hydrophilicity by geometry. That is, small inundations will function as barriers, increasing the contact angle between the surface and droplet, resulting in larger contact angles than due to the material. A contact angle of  $50^\circ$  will not only slow down the flow rate compared to the simulations using  $30^\circ$ , but also influence the behaviour around the valves.

Both chemical treatments of the surface further influenced the contact angles in all cases. The methacrylic acid had a detrimental effect on all contact angles increasing its hydrophobicity, further emphasising the downside of the sealing method if it enters the channels. The NaOH treatment however, increased hydrophilicity, though large

variations were observed in the measurements. The effects of the NaOH treatment are further exemplified in **Figure 7.18**.

The various results obtained by the contact angles described some of the discrepancies between simulations and the experiments. In the narrow channels, the biggest contact surface between liquid and material is due to the walls of the channels. The described experiment only measured the impact of the milling head on the bottom of the channels, and not its influence on the walls.

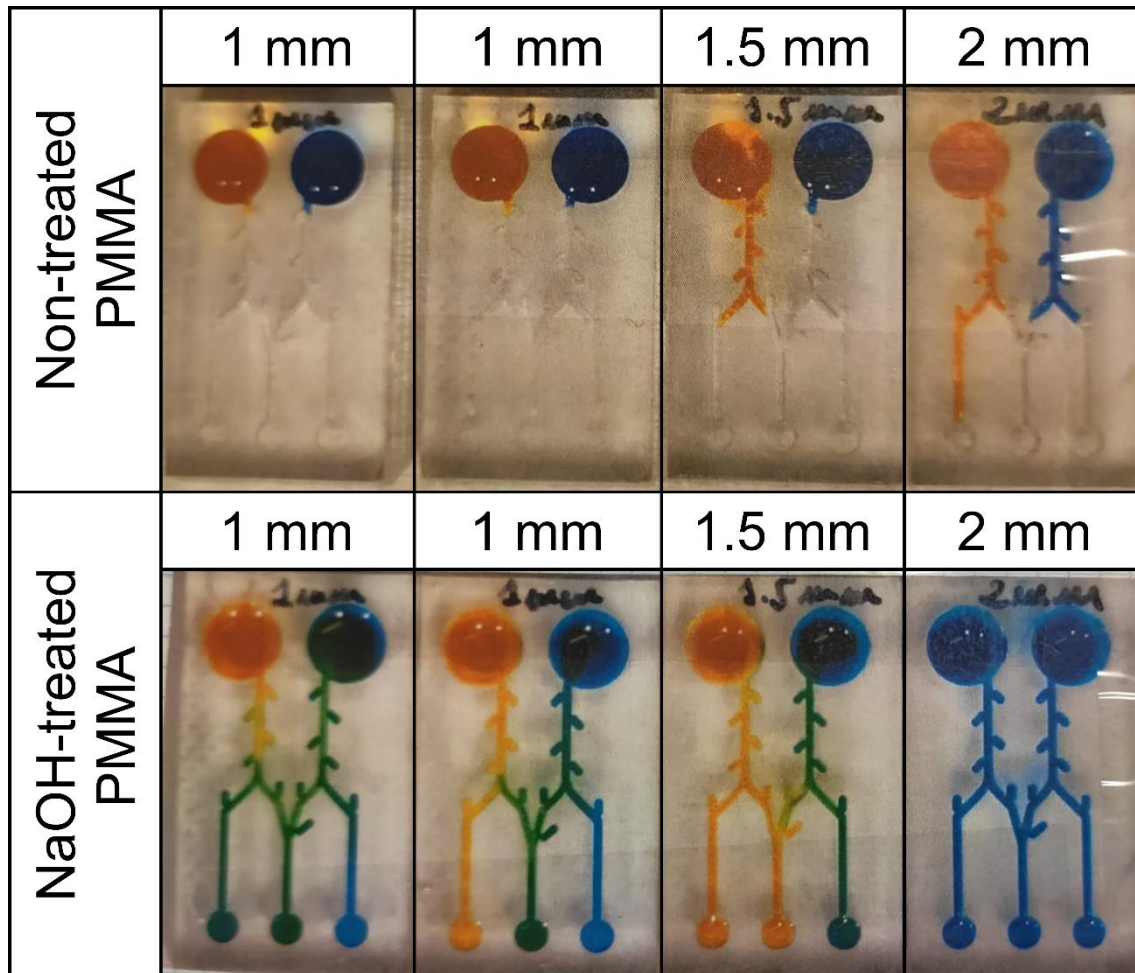


**Figure 7.18: Influence of NaOH treatment and channel depth on flow behaviour.** Various non-treated PMMA devices were fabricated using depths of 1, 1.5 or 2 mm. The bottom row highlights the exact same devices, after 30 min treatment with NaOH at 60 °C. The blue liquid was administered first in every experiment. Both liquids were water with a coloured food dye.

**Figure 7.18** highlights the effect of the NaOH treatment of the flow behaviour inside the system, as well as the impact of the channel depth. When using non-treated PMMA it can be observed that increasing channel depths will have a beneficial effect on the fluid propagation, with no flow occurring at 1 mm depth. Using 1.5 mm and 2 mm, both manage to propagate, but fail to reach the valve. These results further highlight the detrimental effect of the milling on the contact angle, and thus the propagation of the liquid. It needs mentioning that the highlighted systems were equipped with additional

structures below the inlet. A more detailed description of these structures can be found below.

After performing the NaOH treatment, the resulting flow were severely altered, more closely resembling the simulations performed using a 30° contact angle. In all cases does the liquid manage to propagate, and the mixing of the two appears to depend on the depth of the channel. It is important to note that the filling always initiated with the blue liquid, and both inlets were entirely filled to the top. Using a depth of 1 mm, the first case highlights a situation where the blue liquid managed to propagate past the valve, providing a dominant blue-green colour in each inlet. In the second case, the blue liquid stopped at the valve, mixed and passed it upon the arrival of the yellow liquid. Due to the limited dimensions, the mixing propagated back upwards towards each inlet, though each of the outlets highlight the desired dilution sequence: 0 % blue, 50 % blue – 50 % yellow (resulting in green), and 100 % blue. In the case of 1.5 mm, an issue inside the channel impacted the flow of the blue liquid, resulting in a dominant yellow and yellow-green colour. Using 2 mm depth, the blue liquid managed to fill the entire device before the yellow liquid was admitted. The negative effect of the depth was attributed to the filling, since each inlet had the same depth (3 mm) and were filled using the same volume, resulting in larger volumes entering the deeper channels. The NaOH improved the flow rates of the liquids inside the channel, alleviating the drawback of the milling. However, the NaOH treatment is temporary, and the channels rapidly lose their super hydrophilicity upon extended contact with water. Further research was required for a more permanent solution (e.g. modification of the PMMA surface through covalent bonding of hydrophilic molecules).

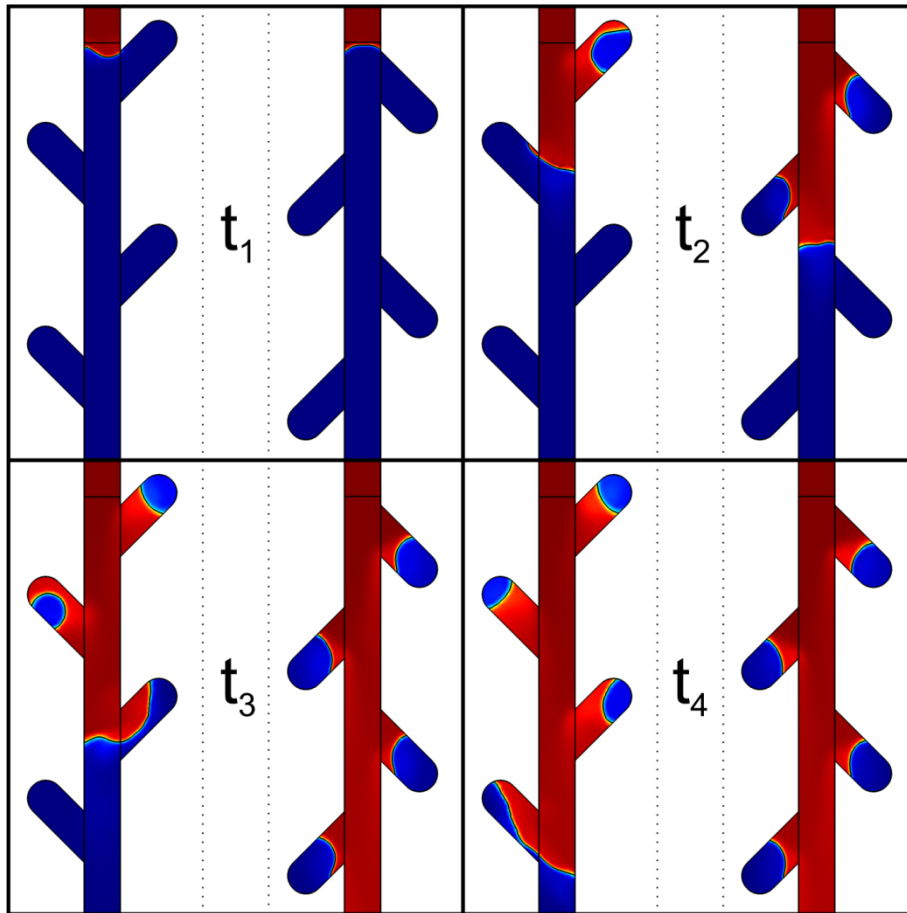


**Figure 7.19: Simulation of flow valves.** Valves on the left are aimed towards the direction of the flow (forward valves), whereas valves on the right are aimed against the flow (backwards valves). Each of the images highlights the passing of a set amount of time.

As could be observed in the highlighted experiment, deeper channel depths led to higher flowrate, possibly bypassing the valve. The added side structure were incorporated to slow down the incoming liquid, which will further result in balancing the pressures between both inlets once they arrive at the valve. The idea was based upon the so-called Tesla valves. These valves are non-mechanical valves, affecting the flow rate depending on the direction of the flow. With a negligible effect when the valve openings are aimed towards the flow, and a severe pressure drop and reduction in flow rate when aimed against the flow direction. The principle was replicated here, though simplified, to reduce the flow of the inlet when large volumes are added.

**Figure 7.19** highlights the simulations of the flow through the inlet channel, equipped side valves, over time. On the left hand side, the valves are aimed towards the flow direction (forward valve) contributing to a minimum loss in flow rate for the tesla valve, with the right hand side aimed against the flow rate (backwards valve). It can be observed that in the same amount of time, the liquid propagated significantly faster in the backwards valve compared to the forward valve, contrasting the behaviour of the tesla valves. This is due to the tesla valves working mainly at the macro scale, used for large flow rates. The largest difference is that the flow here was capillary driven. The backward valves have smaller angles between the valve and the channel when the liquid

arrives, enabling easier propagation and further passing the valve. The forward valves create large angles with the inlet channel, significantly slowing down the flow. Looking back at the results of the non-treated PMMA in **Figure 7.18**, the added valves further limited the flow rate. In the NaOH-treated PMMA, they may have contributed to slow down the flow rate, the direction of the valves were wrong to maximize their function.

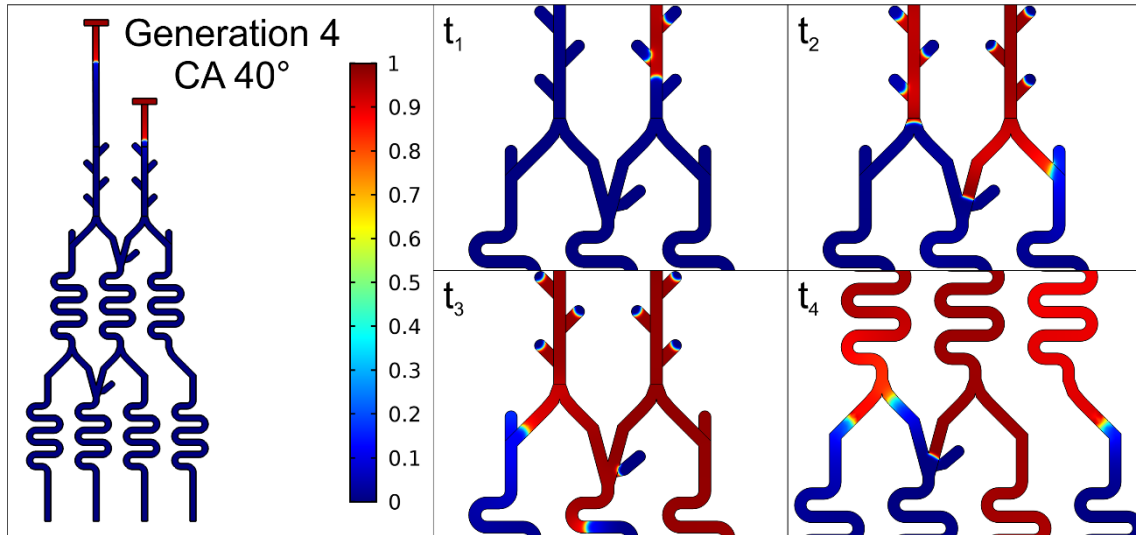


**Figure 7.20: COMSOL simulation of the generation 4 valves, using a symmetric valve and asymmetric inlets.** Highlighted in colour is the liquid-air ratio (red/1 = 100 % liquid, blue/0 100 % air). Images were taken at different times to highlight the collapse at the valve.

Combining the backward valves, the logical AND-valves, and a contact angle of  $40^\circ$  (coinciding with NaOH treated PMMA after a 0.5 mm mill), a final simulation was run, as shown in **Figure 7.20**. The simulation used identical parameters as described for generation 3, with the exception of a smaller interface thickness and a longer time study. A full overview of the parameters is summarized in **Table 7.11**. The simulations indicated a reduction in internal pressure and flow rate due to the backwards valves. Additionally, it is again shown that the AND-valve retains its function, withholding a liquid until the second one arrives.

**Table 7.11: COMSOL settings of generation 4.** Highlight of the parameters modified from the standards in the COMSOL simulations of generation 4.

Model	Component	Subcomponent	Value/parameter	
<b>Geometry</b>				
Length unit	Scale		μm	
<b>Materials</b>				
From library			Air and water	
<b>Laminar Flow</b>				
Physical model	Neglect inertial term			
Discretization			P2+P1	
	Inlet	Pressure	P=50	
<b>Phase field method</b>				
Interface thickness			pf.hmax/10	
	Wetted wall		40 [deg]	
<b>Mesh</b>				
	Size	Fluid dynamics	Fine	
	Corner refinement 1	Boundaries adjacent to valve	0.05 elemental scaling factor	
	Corner refinement 2	Boundaries adjacent to valve	0.05 elemental scaling factor	
	Free triangular	All valves	Scale geometry 6	
	Free triangular	Inlet and inlet channels	Scale geometry 5	
<b>Study</b>				
Time Dependent	Range		0:5e-2:10	
	Time-dependent solver 1	Generalized alpha		
	Fully Coupled	Damping factor	0.9	
		Maximum Number of iterations	15	
		Tolerance factor	0.5	
		Anderson acceleration	Dimension 5	
			Mixing parameter 0.9	
		Iteration delay 1		

In summary, the various designs and simulations function two-fold: the development of a capillary driven logical AND-valve, and an introduction to COMSOL as a simulation tool for bridging the gap between theory and practice. The simulations, improving accuracy and precision with each generation, helped understanding the characteristics of the system prior to fabrication. However, the inclusion of concentration gradients in the simulations were tried, the results were omitted due to lack of accuracy, but would prove useful in future attempts of providing an exact 1-1 dilution. In practice, the

function of the valve proved possible, but accurate control more difficult than anticipated. Further investigations were required into permanent treatments of the channels, to maintain homogeneous, hydrophilic conditions. Finally, with every iteration the simulations and the experiments provided more similar results, proving the possibility of a possible design using a multitude of valves in a single device to create a full on-chip gradient generator.

## 7.5. Conclusions

In conclusion, **SF** possessed interesting properties for the development of microfluidic structures, such as **inherent capillary pull and filtering capacity**, but these could not be exploited in the development of the final system for MIC determination due to, among others, missing repeatability and long-term stability.

On the other hand, a capillary **gradient generator** was designed for the **autonomous** two-fold dilution of the reagents. Various **logical AND-valves** were simulated for their capability to retain a single liquid when arriving at the valve, but enabling breaching when both were present. Providing the inherent time delay of the first liquid, simplifies the sequential homogenisation of both flows. The work described four generations of geometrical valves, optimizing dimensions and simulations with each generation. Though further research is required, the preliminary results, supported by the simulations, of the fourth generation showed great potential for the final system.

## 7.6. Bibliography

- [1] D. Irimia, D.A. Geba, M. Toner, Universal microfluidic gradient generator, *Anal. Chem.* 78 (2006) 3472–3477. <https://doi.org/10.1021/ac0518710>.
- [2] N.L. Jeon, S.K.W. Dertinger, D.T. Chiu, I.S. Choi, A.D. Stroock, G.M. Whitesides, Generation of solution and surface gradients using microfluidic systems, *Langmuir.* 16 (2000) 8311–8316. <https://doi.org/10.1021/la000600b>.
- [3] S.K.W. Dertinger, D.T. Chiu, Noo Li Jeon, G.M. Whitesides, Generation of gradients having complex shapes using microfluidic networks, *Anal. Chem.* 73 (2001) 1240–1246. <https://doi.org/10.1021/ac001132d>.
- [4] H. Sun, C.-W. Chan, Y. Wang, X. Yao, X. Mu, X. Lu, J. Zhou, Z. Cai, K. Ren, Reliable and reusable whole polypropylene plastic microfluidic devices for a rapid, low-cost antimicrobial susceptibility test, *Lab Chip.* (2019) 2915–2924. <https://doi.org/10.1039/c9lc00502a>.
- [5] M. Tang, X. Huang, Q. Chu, X. Ning, Y. Wang, S.K. Kong, X. Zhang, G. Wang, H.P. Ho, A linear concentration gradient generator based on multi-layered centrifugal microfluidics and its application in antimicrobial susceptibility testing, *Lab Chip.* 18 (2018) 1452–1460. <https://doi.org/10.1039/c8lc00042e>.
- [6] B. Hong, P. Xue, Y. Wu, J. Bao, Y.J. Chuah, Y. Kang, A concentration gradient generator on a paper-based microfluidic chip coupled with cell culture microarray for high-throughput drug screening, *Biomed. Microdevices.* 18 (2016) 1–8. <https://doi.org/10.1007/s10544-016-0054-2>.
- [7] Y. Gao, J. Sun, W.H. Lin, D.J. Webb, D. Li, A compact microfluidic gradient generator using passive pumping, *Microfluid. Nanofluidics.* 12 (2012) 887–895. <https://doi.org/10.1007/s10404-011-0908-0>.
- [8] J. Park, H. Roh, J.K. Park, Finger-actuated microfluidic concentration gradient generator compatible with a microplate, *Micromachines.* 10 (2019). <https://doi.org/10.3390/mi10030174>.
- [9] H.J. Jin, D.L. Kaplan, Mechanism of silk processing in insects and spiders, *Nat. Publ. Gr.* 424 (2003) 1057–1061.
- [10] I.C. Um, H.Y. Kweon, Y.H. Park, S. Hudson, Structural characteristics and properties of the regenerated silk fibroin prepared from formic acid, *Int. J. Biol. Macromol.* 29 (2001) 91–97. [https://doi.org/10.1016/S0141-8130\(01\)00159-3](https://doi.org/10.1016/S0141-8130(01)00159-3).
- [11] L.D. Koh, Y. Cheng, C.P. Teng, Y.W. Khin, X.J. Loh, S.Y. Tee, M. Low, E. Ye, H.D. Yu, Y.W. Zhang, M.Y. Han, Structures, mechanical properties and applications of silk fibroin materials, *Prog. Polym. Sci.* 46 (2015) 86–110. <https://doi.org/10.1016/j.progpolymsci.2015.02.001>.
- [12] Y. Yang, X. Chen, F. Ding, P. Zhang, J. Liu, X. Gu, Biocompatibility evaluation of silk fibroin with peripheral nerve tissues and cells in vitro, *Biomaterials.* 28 (2007) 1643–1652. <https://doi.org/10.1016/j.biomaterials.2006.12.004>.
- [13] Y. Cao, B. Wang, Biodegradation of silk biomaterials, *Int. J. Mol. Sci.* 10 (2009)



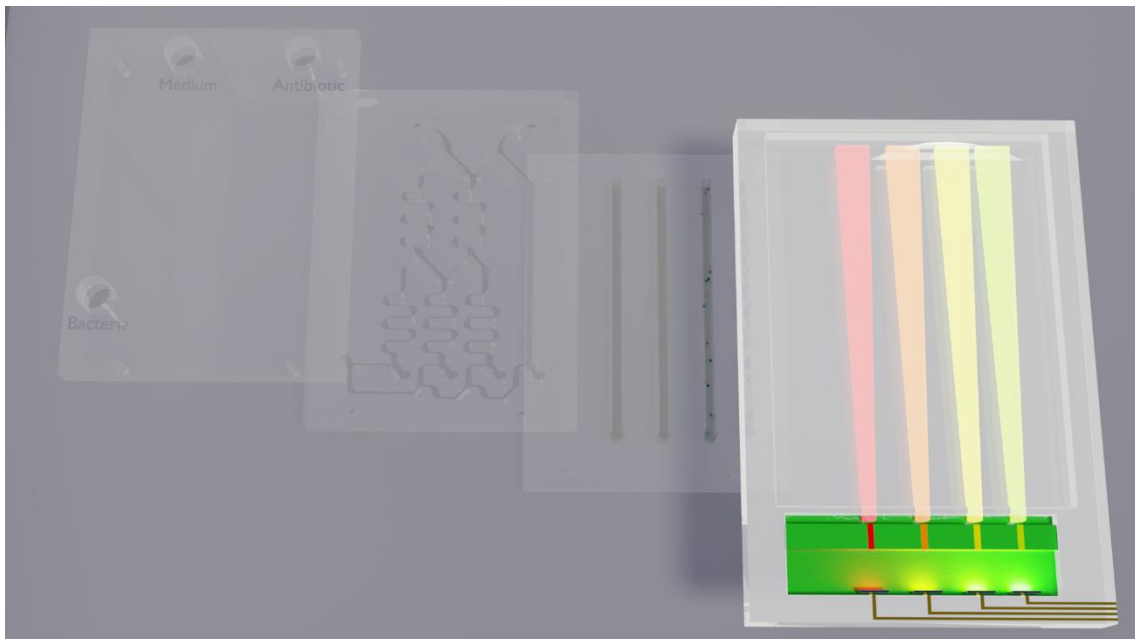
1514–1524. <https://doi.org/10.3390/ijms10041514>.

- [14] D.D.N. Rockwood, R.R.C. Preda, T. Yücel, X. Wang, M.L. Lovett, D.L. Kaplan, Materials fabrication from *Bombyx mori* silk fibroin, *Nat. Protoc.* 6 (2011) 1–43. <https://doi.org/10.1038/nprot.2011.379.Materials>.
- [15] A.B. Li, J.A. Kluge, N.A. Guziewicz, F.G. Omenetto, D.L. Kaplan, Silk-based stabilization of biomacromolecules, *J. Control. Release.* 219 (2015) 416–430. <https://doi.org/10.1016/j.jconrel.2015.09.037>.
- [16] A. Márquez, M. V. Santos, G. Guirado, A. Moreno, S.D. Aznar-Cervantes, J.L. Cenis, S.H. Santagneli, C. Domínguez, F.G. Omenetto, X. Muñoz-Berbel, Nanoporous Silk Films with Capillary Action and Size-Exclusion Capacity for Sensitive Glucose Determination in Whole Blood Augusto, *Lab Chip.* (2014) 1037–1043. <https://doi.org/10.1039/D0LC00702A>.
- [17] J. Hansson, H. Yasuga, T. Haraldsson, W. van der Wijngaart, Synthetic microfluidic paper: high surface area and high porosity polymer micropillar arrays, *Lab Chip.* 16 (2016) 298–304. <https://doi.org/10.1039/C5LC01318F>.
- [18] C. Jönsson, M. Aronsson, G. Rundström, C. Pettersson, I. Mendel-Hartvig, J. Bakker, E. Martinsson, B. Liedberg, B. MacCraith, O. Öhman, J. Melin, Silane-dextran chemistry on lateral flow polymer chips for immunoassays, *Lab Chip.* 8 (2008) 1191–1197. <https://doi.org/10.1039/b800297e>.
- [19] H. Li, D. Han, G.M. Pauletti, A.J. Steckl, Blood coagulation screening using a paper-based microfluidic lateral flow device, *Lab Chip.* 14 (2014) 4035–4041. <https://doi.org/10.1039/c4lc00716f>.
- [20] W. Tao, M. Li, R. Xie, Preparation and structure of porous silk sericin materials, *Macromol. Mater. Eng.* 290 (2005) 188–194. <https://doi.org/10.1002/mame.200400306>.
- [21] R. Nazarov, H.J. Jin, D.L. Kaplan, Porous 3-D scaffolds from regenerated silk fibroin, *Biomacromolecules.* 5 (2004) 718–726. <https://doi.org/10.1021/bm034327e>.
- [22] Q. Lv, Q.L. Feng, Preparation of 3-D regenerated fibroin scaffolds with freeze drying method and freeze drying/foaming technique, *J. Mater. Sci. Mater. Med.* 17 (2006) 1349–1356. <https://doi.org/10.1007/s10856-006-0610-z>.
- [23] K. Yoshida, H. Onoe, Functionalized core-shell hydrogel microspheres by anisotropic gelation with bevel-tip capillary, *Sci. Rep.* 7 (2017) 1–9. <https://doi.org/10.1038/srep45987>.
- [24] S. Zhao, Y. Chen, B.P. Partlow, A.S. Golding, P. Tseng, J. Coburn, M.B. Applegate, J.E. Moreau, F.G. Omenetto, D.L. Kaplan, Bio-functionalized silk hydrogel microfluidic systems, *Biomaterials.* 93 (2016) 60–70. <https://doi.org/10.1016/j.biomaterials.2016.03.041>.
- [25] Y. Ma, X. Cao, X. Feng, Y. Ma, H. Zou, Fabrication of super-hydrophobic film from PMMA with intrinsic water contact angle below 90°, *Polymer (Guildf).* 48 (2007) 7455–7460. <https://doi.org/10.1016/j.polymer.2007.10.038>.

- [26] J. Melin, N. Roxhed, G. Gimenez, P. Griss, W. Van Der Wijngaart, G. Stemme, A liquid-triggered liquid microvalve for on-chip flow control, *Sensors Actuators, B Chem.* 100 (2004) 463–468. <https://doi.org/10.1016/j.snb.2004.03.010>.
- [27] M. Zimmermann, P. Hunziker, E. Delamarche, Valves for autonomous capillary systems, *Microfluid. Nanofluidics.* 5 (2008) 395–402. <https://doi.org/10.1007/s10404-007-025>



# 8. Results Optics





After the development of the first miniaturized analysis systems [1] in 1979 and the introduction of the Lab on a Chip (LoC) concept in the early 90s [2,3], researchers and industry have widely exploited the advantages of such devices in terms of integration, compactness, low-cost, fast response time, small sample volume and reagent consumption. This latter property makes LoC devices ideal candidates in the development of advanced, parallelized multi-sensing platforms, where multiple analytes and/or samples are either simultaneously or sequentially analysed. High-throughput analysis platforms with massive parallelization have already been developed for simultaneous determination of biomarkers [4–7], for drug screening [8], massive hybridization assays for pathogen detection [9] or gene identification [10,11], among others. This has been enabled thanks to the tremendous improvement in microfluidics. Nevertheless, the concomitant development of in-situ transducers for converting a (bio-) chemical event into a readable signal is somehow lacking behind. To date, electrochemical [12], optical (with the so-called photonic LoC, PhLoC [13]), or dual [14] transducers have shown excellent performance, albeit generally in single-chamber measurements. In this context, massive parallelization of such transducers is necessary for key applications such as multiple analyte detection [15], to confer the system with reliability through statistical analysis [16], when requiring multiple control points [17,18] or when the reliability of the assay is subjected to sequential analysis at different wavelengths [19,20]. Although extremely advanced, to date most of these devices rely on complex architectures and fabrication technologies integrating many light sources and readouts in a single photonic LoC, which generally require sub-micrometric precision [21] and thus hampers their massive implantation due to excessive fabrication costs. Alternatively, some multiplexed photonic lab on a chip devices have been developed based on optical routers [22]. In this case, the optical router redirects the light from the light source to each optical detection channel allowing multiple detections with a single light source and photo-detector.

**In this thesis, several strategies to simplify multiplexed analysis have been developed based on optical routers and frequency modulators.** The progress scheme for the development of these opto-electronic components is illustrated below.

## 8.1. Scheme of progress

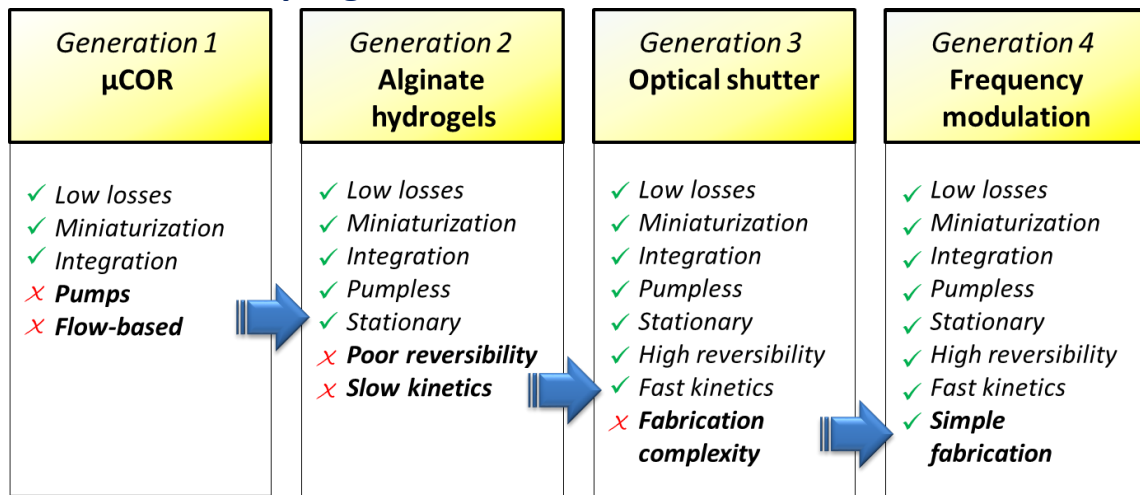


**Figure 8.1: Scheme of the continuity of the various generations of optical routers under development.** Each generation was developed to overcome one or more of the drawbacks of its predecessor. μCOR = microfluidic-controlled optical router.

## 8.2. Gen 1: Microfluidic-controlled optical router for lab on a chip

In this section, we developed a cost effective and simple microfluidic-controlled optical router ( $\mu$ COR) fabricated in polydimethylsiloxane (PDMS) by soft lithography, where micro-optic and micro-opto-fluidic elements are monolithically integrated in a single structure. Airgap mirrors are generated in this case by filling/emptying independent micro-chambers with water using an external pump. The mirrors are used to guide the light to specific regions of the chip, i.e. independent optical detection channels, to perform multiple optical analyses with a single light source and detector. Compared with other microfluidic optical routers developed previously [22], the  $\mu$ COR is advantageous since does not require continuous flow nor high-precision instrumentation. The latter is accomplished by the combination of phase-guides and meandering channels. The switching capacity and performance of such devices are evaluated in here using a  $1 \times 4$  configuration.

This work was initiated by Dr. Andreu Lloberra, together with his master thesis student, Jeroen Goyvaerts. The general idea, the optimization of the components and the designs were executed by them. The performance and characterization of the full system was performed by myself, under supervision of Dr. Xavier Muñoz, and both were responsible for the published manuscript. The full work has been published, with an accepted back cover designed by me, in Lab on a chip [23].

### 8.2.1. Micro-lens systems optimization

To minimize optical losses and optimize the performance of the system, the ray tracing simulation software TracePro was used during micro-lens systems design. Each system was limited to two successive PDMS micro-lenses, separated by and air gap, to minimize the dispersive optical losses at air-PDMS interfaces.

Three different micro-lens systems were designed, namely collimation (input), short-distance ( $< 1$  cm) and long-distance ( $> 1$  cm) focusing (output) systems (**Figure 8.2**). The collimation system was designed to minimize light dispersion from the input optical fiber and turning it into parallel rays. The focusing systems were designed to focus and match the angular acceptance angle of the output optical fibers (0.22 numerical aperture).

The collimation system consisted of a typical plano-convex micro-lens, to correct the dispersion of the light input, followed by a second convex micro-lens with soft spline curves for additional reduction of the dispersion angle. Compared to already published spherical micro-lenses[24] (**Figure 8.2 a – b**), spline micro-lenses were superior for presenting better candela distribution profiles (sleeker profiler, **Figure 8.2 e – f**), higher intensities ( $5 \times 10^5$  vs.  $5 \times 10^4$  counts) and a quarter size reduction ( $650$  vs.  $925 \mu\text{m}^2$ ).



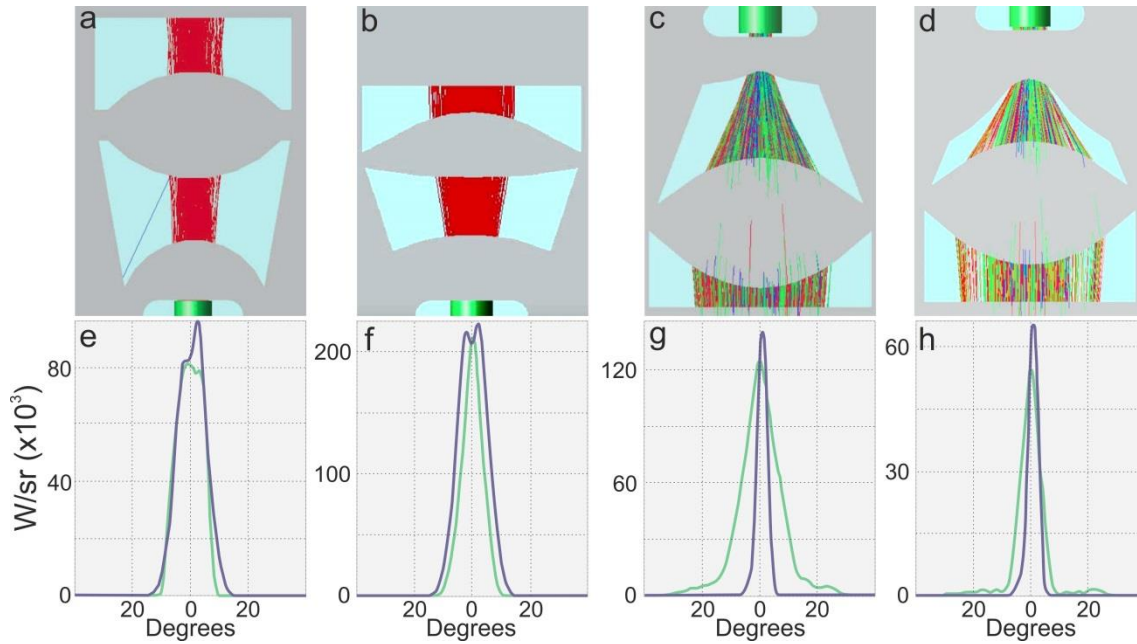


**Figure 8.2: Optimization and analysis of the light focusing lenses.** The top row shows the lenses in PDMS with (a) collimating lens for the fiber input, (b) spline optimized lens for the fiber input, (c) Short distance, (d) and long distance convex lens for the fiber output. The bottom row (e-h) shows the corresponding candela plots.

Maximal incident light collection into the fiber was obtained by using highly convex micro-lenses for first element of the focusing system. The second element was a concave micro-lens located right before the focal point of the first one, which collimating the light into parallel beams. This second micro-lens was small and with extreme high concave spline curvatures to reduce the numerical aperture to match with that of the output fiber. Candela distributions at the fiber input of the short-distance and long-distance focusing systems are illustrated in **Figure 8.2 g – h**.

Spline-optimized systems combining collimation with either short-distance (lens system A) or long-distance focusing micro-lenses (lens system B) were fabricated and evaluated in propagation (lens-to-lens) distances from 0.5 to 13.5 mm. Experimental data and simulations, shown as points and lines in **Figure 8.3**, respectively, were compared with a reference lens system consisting of spherical micro-lenses both as collimation and as focusing micro-lenses. Each experimental point corresponds to an average of 5-7 individual devices.

A good correlation between experimental data and simulations was found in all cases, validating the theoretical model. Experimental results evidenced the superior performance of spline-optimized systems, with an improvement from 3 to 6 dB (depending on the propagation distance) when compared with the previously used micro-lens configuration [24].

Finally, quantitative measurements, similar to those performed by Muller [22], confirmed the reduction of the numerical aperture in spline-optimized systems from  $6.75^\circ$  (in spherical-based systems) to  $4.40^\circ$  (**Figure 8.3 b – c**). Therefore, spline-optimized micro-lens systems were implemented in the final  $\mu$ COR.

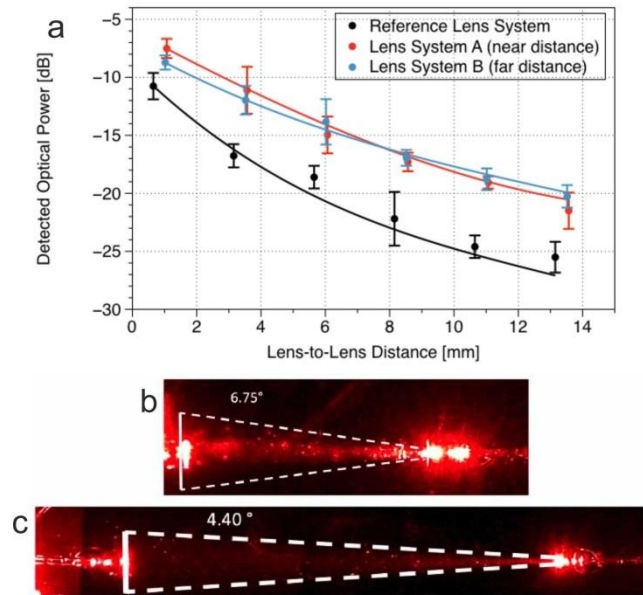


**Figure 8.3: The performance of the spline optimized lens systems** in terms of collected optical power versus propagation distance. A comparison is made between the previously employed lens system in black, versus the short distance (red) and long distance (blue) lenses. Each measurement point consists of 5-7 individual measurements. The TracePro simulations are normalized against a single fiber measurement between the laser and the power meter. For the simulations a 1 mm glass plate and a 1 mm PDMS substrate are used. Figures (b) and (c) show the beam dispersions of the previous lens and the spline-optimized long distance lens respectively.

### 8.2.2. Design and performance of the $\mu$ COR

**Figure 8.4** illustrates the design of the  $\mu$ COR device. It consisted of an advanced architecture integrating all micro-optical and microfluidic elements for in-coupling, guidance and out-coupling of light to four independent optical outputs. Micro-optical elements comprised self-alignment elements for fiber-optics positioning [24], pinholes based on liquid inks to minimize cross-talk between channels, and the previously described optimized micro-lenses. Microfluidic components included a fluidic inlet and outlet, micro-chambers, phase-guides [25] for fluid management inside the micro-chambers and interconnecting meander-like micro-channels connecting the latter while introducing a time-delay between them. All these elements were defined in a single master, intrinsically self-aligning them during the fabrication step. The number of optical channels was fixed to four for appropriate comparison with Muller's work [22], even though thanks to the design flexibility of the  $\mu$ COR, this number could be expanded or reduced freely. However, the amount of possible channels depended on the desired light intensity and application, as more channels led to longer optical paths, in turn resulting in larger optical losses.

Micro-chambers and the corresponding optical channels were numbered from 1 to 4 according to the direction of the liquid flow, with 1 being closest to the fluidic inlet (**Figure 8.4**). They served as the central elements in the  $\mu$ COR and were conceived to operate as fluid-controlled micro-mirrors. The operation principle was based on the modulation of total internal reflection at the micro-chamber wall interface. Considering

Snell's law, total internal reflection was reached at the PDMS-air interface of empty micro-chambers at angles above 45° ( $n_{PDMS} = 1.41$ ;  $n_{air} = 1$ ).

$$\theta_{crit_{PDMS-air}} = \arcsin\left(\frac{n_{air}}{n_{PDMS}}\right) = \arcsin\left(\frac{1}{1.41}\right) = 45.17^\circ$$

$$\theta_{crit_{PDMS-water}} = \arcsin\left(\frac{n_{water}}{n_{PDMS}}\right) = \arcsin\left(\frac{1.33}{1.41}\right) = 70.61^\circ$$

However, it required angles above 71° when filled with water ( $n_{water} = 1.33$ ). Then, micro-chamber walls with an angle between 45° and 71° could reflect and redirect the light when empty, while enabling light transmission when filled with water. In order to reduce the design footprint and the optical losses due to lack of vertical confinement, the angle of the micro-chamber wall was set here at 55°.

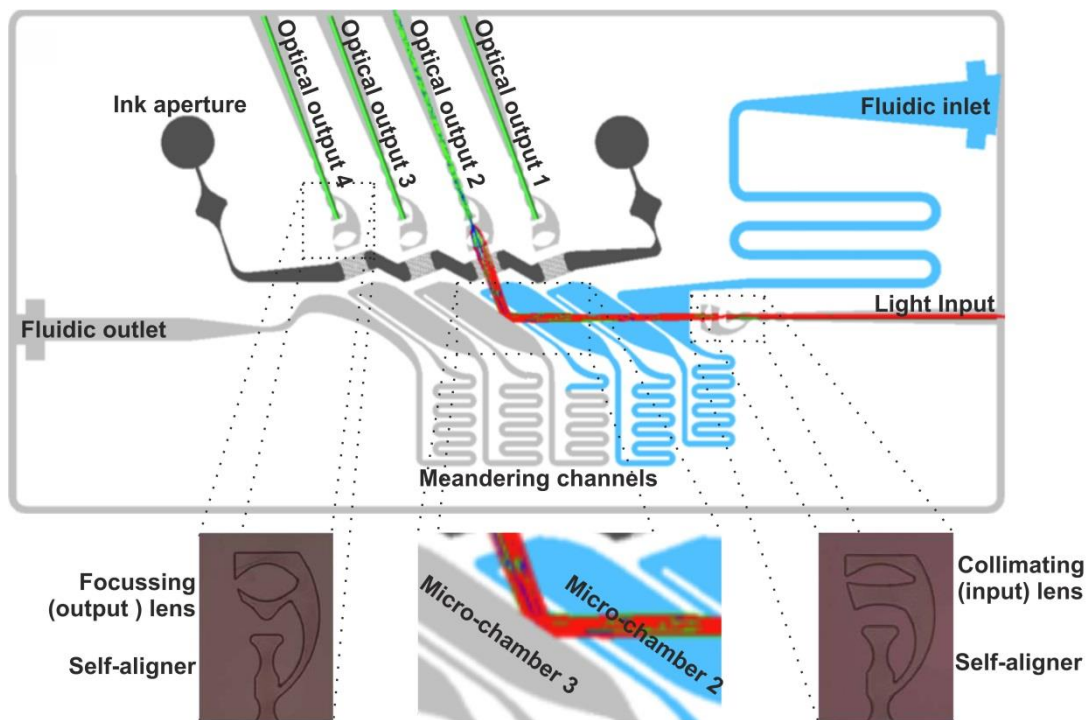


**Figure 8.4: Schematic overview of the optofluidic router and its working principle.** Highlighted in blue is the liquid flow through the device. In red is shown the light beam coming from the light input until reaching optical output 2. The fibers inserted in the optical outputs are highlighted in green. Shown in black is the ink aperture. In the bottom of the image and highlighted on both sides are the optimized lenses for light focusing and centred the TIR working principle conditions.

Two phase-guides were implemented in each micro-chamber structure to optimize the focusing behaviour of the switching liquid, as shown in **Figure 8.5**. Phase-guides are opto-fluidic elements, composed of stripes of material that serve as pinning barriers allowing controlled filling and emptying of microfluidic chambers by altering the surface energy of a channel due to their wettability properties or geometry. Phase-guides enabled a stepwise control of the liquid flow due to a pressure gradient. They guided the liquid to fill the chamber homogeneously along their edge, pushing out air-bubbles as liquid continued to flow. Once filled, the pressure build-up overcame the barrier, allowing the liquid to cross until the next phase-guide was reached. **Figure 8.5 A and B**

highlight the relation between the thickness of the phase-guide and its mechanical rigidity. Narrow phase-guides may bend under the accumulating pressure due to the filling, possibly resulting in the liquid passing the phase-guide prematurely. **Figure 8.5 C to F** highlights how liquid tries to cross a phase-guide during filling, but remains pinned between the phase-guide and the opposite substrate. In this device, the liquid entered at the bottom right corner of the micro-chamber and was pushed towards the top right side, as shown in **Figure 8.6**. Once filled, the liquid crossed the first phase-guide, filling the intermediate space, until reaching the second phase guide. The same principle was repeated until breaching, after which the liquid was guided back down through the interconnecting meander structure and to the next micro-chamber. This configuration enabled a strict microfluidic control of the routing, without requiring highly-precise instrumentation and minimizing the risk of bubble formation or entrapment.

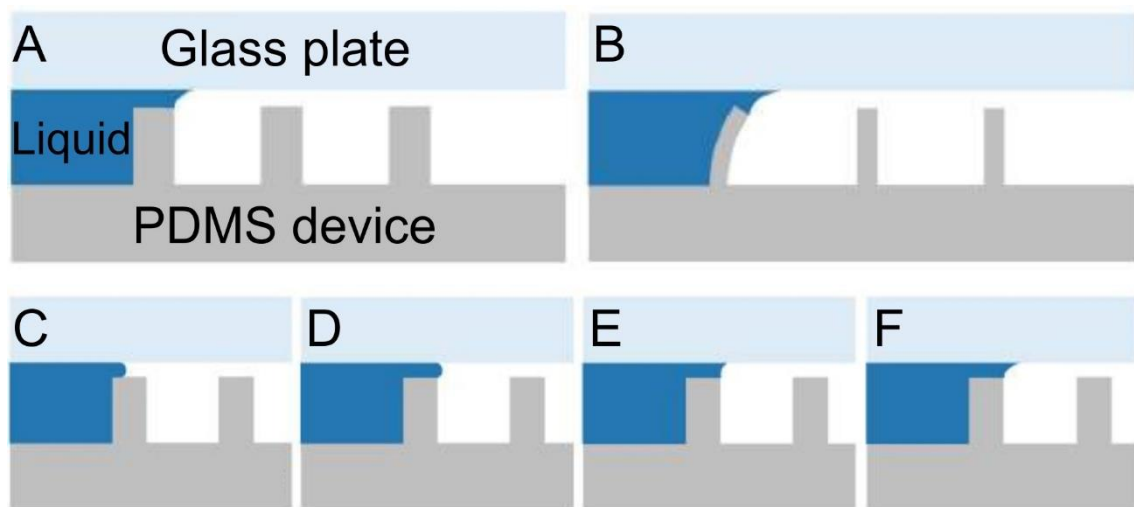


**Figure 8.5: Architecture and working principle of phase-guides.** Figures A and B highlight how the thickness influences the mechanical rigidity. Figure C to F show the working principle of a liquid flowing past a phase-guide and how a liquid is pinned underneath, resulting in a meniscus formation.

In  $\mu$ COR, this working principle was exploited in the development of a 1x4 optical router by sequentially connecting four independent micro-chambers. As demonstrated using simulations, with this design we could obtain a high control of the light flow. For example, light could be redirected to the first optical chamber when only the first micro-chamber was filled, to the second when micro-chambers one and two were filled, or output of the chip when the liquid was present in all micro-chambers. Importantly, since the micro-chambers generating the air-gap were fixed elements,  $\mu$ COR had no movable parts, which provided high mechanical robustness.

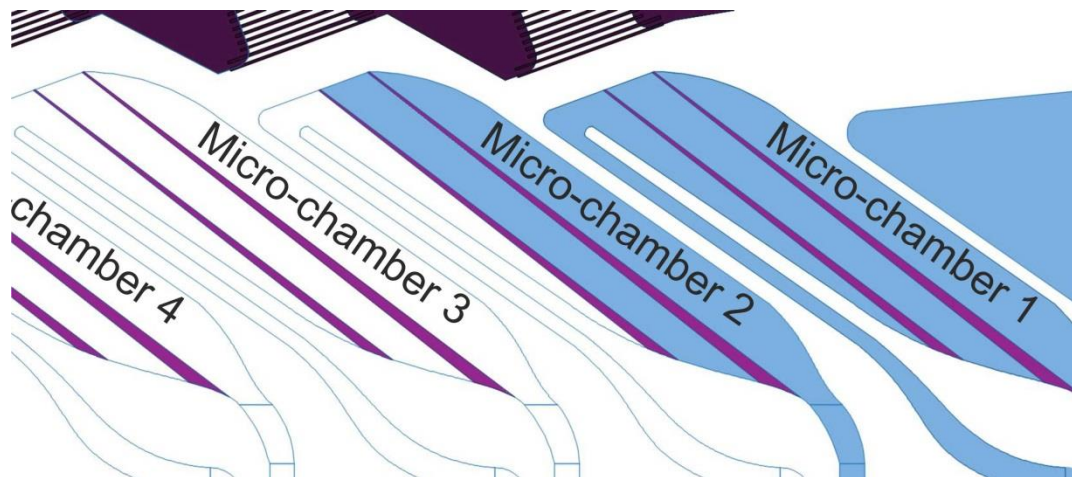


**Figure 8.6: AutoCAD highlight of the positioning of the primer phase-guides and their influence on the flow propagation.** Areas highlighted in blue are the micro-chambers readily filled with water, whereas areas still in white are the micro-chambers still devoid of liquid. The phase-guides, highlighted in light purple, guide the filling of the micro-chambers. Shown in dark purple at the top are the ink apertures.

### 8.2.3. Characterization of PDMS-based $\mu$ COR

To visualize the  $\mu$ COR performance, a 1 mM fluorescein solution (Sigma-Aldrich) was used to fill the system and a blue laser-source (nano-405-100, Linos) was coupled into the input fiber optics. In **Figure 8.7**, it is shown how the input light was redirected to the second light output channel when the first micro-chamber was filled with fluorescein, or through the device when all micro-chambers were filled, enabling a strict control of the light flow and thus validating the working principle of the  $\mu$ COR.

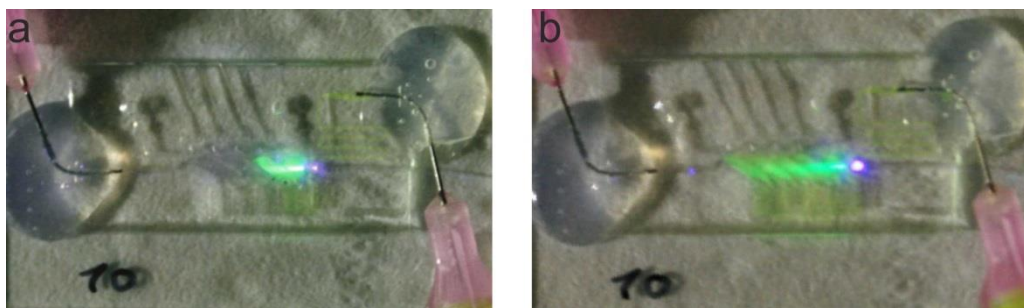


**Figure 8.7: Characterization of the light focusing principle** with different micro-chambers being filled with water. Shown in (a) is the reflection of the light towards optical output 2, due to the filling of micro-chambers 1 and 2. Shown in (b) is light being sent through the device, due to the filling of all micro-chambers.

For the characterization of the  $\mu$ COR performance, three parameters were analysed, namely the switching frequency, lapse-time in the channel, and the cross-talk between channels under continuous flow conditions.

The switching frequency was defined as the time required to switch between two adjacent optical channels, whereas the lapse-time referred to the time during which a specific optical channel provided the maximal light output intensity under a constant flow. This second parameter was of huge importance for potential analytical applications of the presented router since it reported on the time where the light intensity was stable for performing measurements in each channel. Clearly, both

parameters depended on the flow rate and on geometrical features, which affected the flow in the device, e.g. the number of channels, the volume of the micro-chamber, the position, height and width of the phase-guides and the length and calibre of the interconnecting meander. Since all these geometric parameters were identical for each micro-chamber, only the fluidic sequence of the micro-chamber was considered to impact performance. Nevertheless, depending on the application, modifying the parameters described above, the  $\mu$ COR could be designed to have specific switching frequencies and lapse-times.

The behaviour of the measured signal at different flow rates was used to analyse the lapse-times, as shown in **Figure 8.8 a**, where the results of the dynamic range as a function of time at flow rates ranging from 0.025 to 0.250  $\mu\text{L/s}$  are presented. As can be observed, the  $\mu$ COR had a dynamic range close to 15 dB, independently on the flow rate. The shape of the dynamic range was also independent on the flow: in the initial transient phase, the signal had a gradual increase towards its maximum light intensity due to the filling between the final phase-guide and the meandering channel connection. The two short signal drops were attributed to the liquid meniscus propagating between the phase-guides. Because of its shape and refractive index, reflection occurred at the air-meniscus interface, resulting in a temporal decrease of the output signal before stabilization. This exact time was the onset of the lapse-time measurement, which continued until the signal dropped abruptly, corresponding to the filling of the next micro-chamber. As expected, the increase of the flow rate resulted in a shorter transient period, with less pronounced signal drops.

The continuous measurement of this behaviour through subsequent micro-chambers is depicted in **Figure 8.8 b**, where the signal was monitored while applying a constant flow rate of 0.1  $\mu\text{L/s}$ . As intended, two identical micro-chambers provided the exact same behaviour both in the transient phase and in the lapse-time, which confirmed the validity of the proposed  $\mu$ COR. Small variations were attributed to the filling step, where the liquid reflected light at random towards the output. **Figure 8.8 b** allowed us to measure the switching rate, which defined as the time between the onset of the lapse in one micro-chamber and the next. **Figure 8.8 c and d** show the collection of all generated data using the methods shown in **Figure 8.8 a and b**, respectively. In all channels, the switching frequency increased with the flow rate until stabilization around 0.1  $\mu\text{L/s}$ , as depicted in **Figure 8.8 d**. From 0.025 to 0.1  $\mu\text{L/s}$ , it was possible to modulate the switching frequency of the device in a range from  $0.032 \pm 0.003$  to  $0.343 \pm 0.006$  Hz.

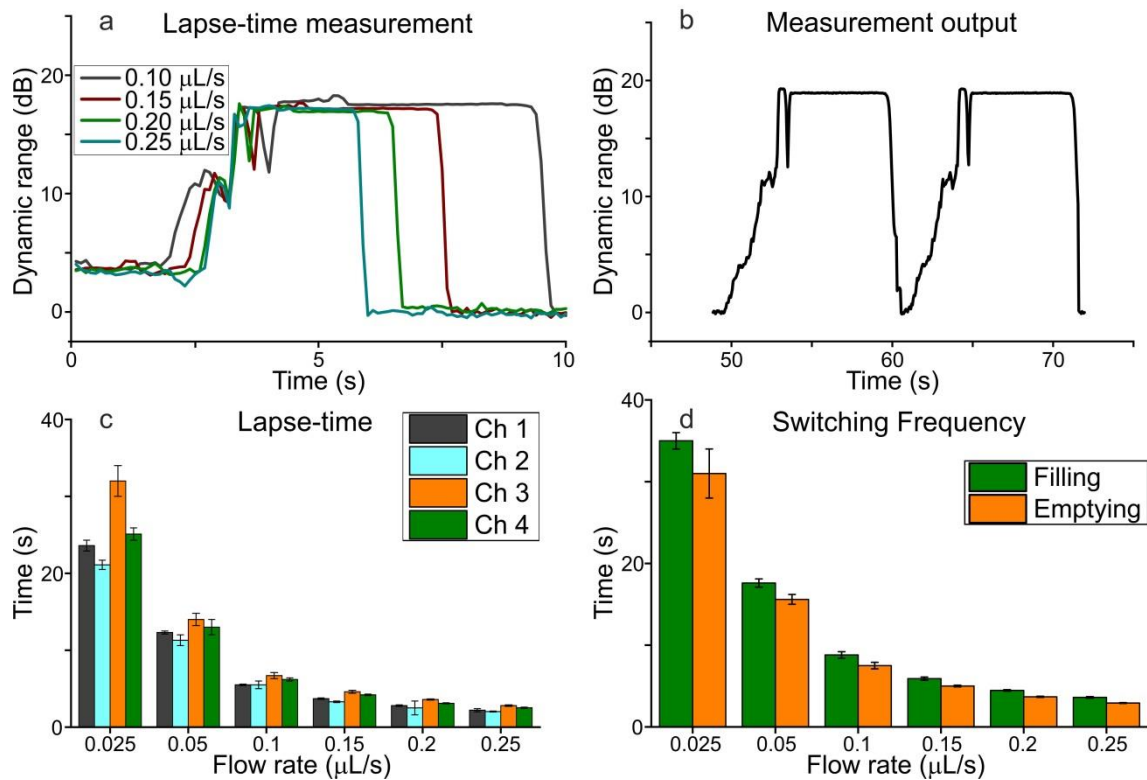


**Figure 8.8: Time dependence of the flow rate in terms of lapse-time and switching.** (a) shows the behaviour of the channel lapse-time at different flow rates, whereas (b) represents the signal generation for two subsequent outputs at a constant flow rate. (c) shows the duration of a stable signal generation, the collection of the data from (a) in function of flow rate during filling. Ch1-Ch4 represent the signal measured at optical output 1 to 4 respectively ( $n=5$ ). (d) shows the combined data of the duration of switching between routers during filling and emptying of the chip in function of the flow rate ( $n=20$ ).

This frequency may be enough for an optical router implemented in a photonic LoC (PhLoC) for biological applications. Additionally, as mentioned above, this frequency could be tuned by modifying both the meandering micro-channels and the micro-chamber volume. No significant differences between channels were found ( $p < 0.05$ ) for any of the flow rates. The data for all 4 channels were therefore grouped together. However, differences were found when either filling or emptying the  $\mu\text{COR}$ . At lower flow rates, emptying the device was significantly faster than filling. This was due to the reduced pressure build-up and beneficial cohesive force of water that were more dominant at lower flow rates. From flow rates of 0.2  $\mu\text{L/s}$  and above, no significant differences were observed. There were no significant differences found between the different channels ( $p < 0.05$ ) and the data shown was the average over all channels at the specified flow rate.

Thanks to its particular design based on phase-guides, the lapse-time in the  $\mu\text{COR}$  was always long when compared with the total time required for changing from channel to channel, as shown in **Figure 8.8 c**. In fact, the lapse-time covered between 56 and 91 % of the total time required for changing between channels, meaning that the optical channel was active most of the time under a continuous flow. The reason of that was attributed to the phase-guides that enabled a fast filling/emptying of the first section of

the micro-chamber and thus the quick generation/elimination of the air-gap mirrors. Contrary to the switching frequency, the lapse-time in the optical channel depended not only on the flow rate, but also on the position of the channel in the device. Regarding flow rates, the lapse-time decreased with an increasing flow rate in the range from 0.025 to 0.1  $\mu\text{L/s}$ , enabling the modulation of the measurement time. Contrary to before, there were some differences between channels, being those closer to the fluidic inlet the ones with shorter lapse-times. The differences were more evident at low flow rates, whereas above 0.1  $\mu\text{L/s}$  the differences between channels were almost not significant. A minimum lapse-time of 2.03 s was reached in Channel 2 at 0.25  $\mu\text{L/s}$ , whereas the maximum, 32 s, was obtained in Channel 3 at 0.025  $\mu\text{L/s}$ .

Cross-talk is a key magnitude in PhLoC applications since it can dramatically alter the validity of the measurements taken. To verify this magnitude, cross-talks between all channels were evaluated at a single flow rate of 0.2  $\mu\text{L/s}$  and illustrated in **Figure 8.9**. To reduce the cross-talk levels, the ink aperture was filled with crystal violet to absorb stray light. A further description of the working principle of the ink aperture can be found in **Supplementary 11.3**.

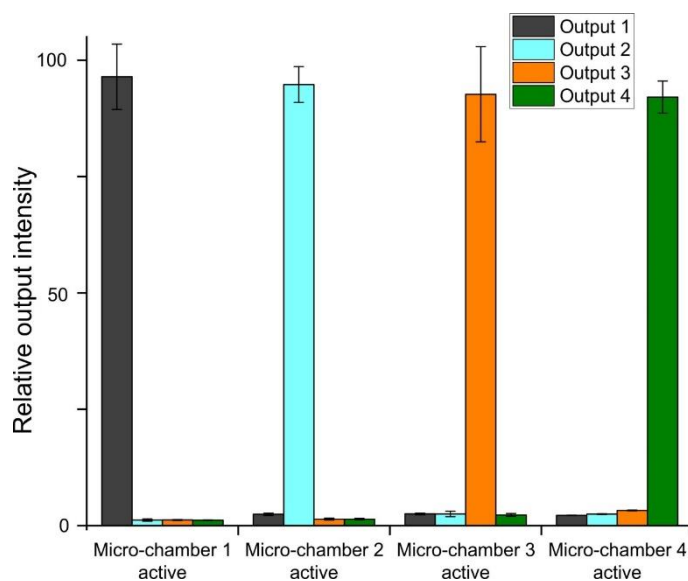


**Figure 8.9: Cross-talk levels between the optical outputs.** Shown are the relative intensity levels for each optical output during the activation of the specified micro-chamber. In each group the total output combined corresponds to 100 % of the measured light leaving the router. Each colour represents individual optical outputs relative signal strength during each of the micro-chambers activations (n=6).

**Figure 8.9** shows the relative power intensity in each optical output during a single micro-chamber activation, which expressed as a light intensity percentage considering the 4 output channels (defined as relative output intensity). Each of the 4 groups in turn corresponded to activating each of the 4 micro-chambers. An average of 94% of the measured light went to the designated output, signifying a total of 6% was lost to either other channels.



The results showed no significant differences between the intensities at the optical outputs when the corresponding micro-chamber was active. Nonetheless, some differences were found when measured at different outputs. For optical output 2, the signal was significantly lower ( $p < 1\%$ ) when chamber 1 was active compared to chambers 3 and 4. At outputs 3 and 4 the signal was significantly higher when the non-corresponding chamber was active, compared to the other first 2. For output 1, there were no such differences. The general trend was higher output intensity when going further in the chip, implying higher cross-talk levels when a longer optical path was required. Additionally, there was a trend towards higher cross-talk levels at an optical output when the liquid passed the corresponding micro-chamber. This increase was probably due to the water-PDMS interface, both having different refractive indices, with TIR conditions being fulfilled at angles above  $71^\circ$ .

In summary, the microfluidic-control of sequential light routing enabled fast routing, with switching frequencies between 0.03 and 0.3 Hz, suitable for most biological assays. Furthermore, thanks to its particular design based on phase-guides, the optical router remained active for optical measurements up to 91% of the total time required for changing between channels with the possibility to modulate the measurement time from 32 to 2 seconds by adjusting the flow rate. However, the need of pumps limited the usability in LoC devices, increasing the size, weight and instrumental complexity of a system thought to operate at the point of care, by the need of external instrumentation (i.e. pumps). Additionally, the fabrication of the device relied on manual steps (e.g. de-casting and bonding), which severely impacts the costs. Furthermore, prolonged usage of the same chip risks its breakdown by the gradual growth of air bubbles. Finally, in a theoretical point of view, the device could expand with more channels, but in practice longer distances would result in a high decrease of system performance due to a substantial increase of the optical losses. Based on these limitations, alternatives based on stationary devices, where no liquid flow is necessary, were studied as light routing elements.

### 8.3. Gen 2: hydrogel waveguide formation by the electrodeposition of an alginate solution

The first generation of optical routers showed a potential approach for fast and accurate multiplexing using a single light input. However, the necessity of pumps makes the device cumbersome to use and less attractive for LoC devices. Additionally, the fabrication relies on clean-room procedures and manual steps, making the fabrication of the device not only complex, but expensive too. The second generation of the optical routers addresses these issues by eliminating the usage of pumps and simplifying the setup to enable easy modifications according to the users' needs.

The idea developed as a continuation of the work of Dr. Augusto Marquez on electro-addressable alginate hydrogels [26] and later exploited by Dr. Nuria Vignes [27] and Dr. Ferran Pujol in the development of bacterial-sensing hydrogels [28]. The light routing principle was based on the capacity to selectively and reversibly electro-deposit alginate hydrogels on a surface with high selectivity and spatial resolution. In an optical point of view, hydrogels present higher refractive index than the alginate solution. Hydrogel electrodeposition generates thus light-guiding structures where the hydrogel acts as the core of the waveguide with the surrounding liquid acting as the cladding. Thus, the hypothesis to produce such optical elements was:

- Alginate hydrogels containing iron (III) ions cross-linked presented **higher refractive indexes** than the alginate solutions with iron (II);
- It was possible to **oxidize and reduce iron ions** on an electrode through a simple redox reaction.

As shown in **Figure 8.10**, using a single input and a specific layout of electrodes, alginate hydrogels could be produced on the electrode surface using a simple electrodeposition step, generating waveguides to focus the light to one of its outputs (1x3, according to the example design). Reducing the alginate would restore the initial situation by dissolving the hydrogel and enabling a new configuration of the waveguides. Even though it has been reported that hydrogels are prone to dehydration, the final router would be fabricated in non-gas permeable materials, e.g. methacrylate, that would minimize liquid evaporation.

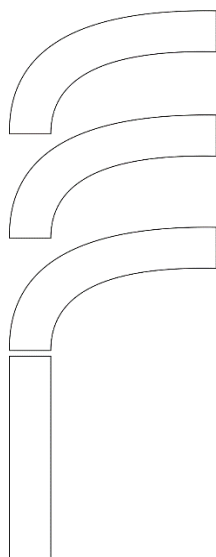


**Figure 8.10: Design of the electrode layout for sequential cycling of the hydrogel formation** to each of the different outputs.

### 8.3.1. Hydrogel optimization

The first set of experiments was performed to evaluate the previous performance principle and concretely, the formation of the alginate hydrogels. Using custom made screen-printed carbon electrodes, the optimal conditions for the hydrogel formation were evaluated, considering iron (II) chloride and alginate concentrations, and potential applied for electro-deposition. An overview of the results is shown in **Table 8.1**. Alginate had a limited solubility in water, with a concentration of 2 % w/v resulting in a solution too viscous for further use in this application. The concentration of the iron (II) chloride impacted on the final state of the formed hydrogel after electrodeposition. Based on the experimental results, a mixture of 1 % w/v of alginate with a 20 mM FeCl<sub>2</sub> was considered optimal for iron-based alginate hydrogels electrodeposition, which was used in all later experiments. A constant 0.8 V vs Ag/AgCl was used for gel formation based on previous works ([29,30]). According to these papers, higher potentials may result in faster electro-deposition times, but relying on less homogenous hydrogels with entrapped air bubbles due to water electrolysis. Air bubbles would act as scattering centres and thus, in a low performance of the optical system.

**Table 8.1: Optimization of the concentrations of the reagents for the alginate hydrogel electrodeposition.** FeCl<sub>2</sub> was diluted in distilled water, and both were mixed in a 1-1 ratio. Electrodeposition was achieved at a constant potential of 0.8 V vs Ag/AgCl for 10 minutes.

Alginate (% w/v)	FeCl <sub>2</sub> (mM)	Observations
2	50	Too much alginate, solution too viscous
1	50	Too much iron, gelation is too strong for further reaction reversion
1	20	Good gel formation, chosen as optimal condition
1	10	Iron content too low to form a solid gel by electrodeposition.

### 8.3.2. Refractive index determination

A critical parameter in the design of optical routers based on alginate hydrogels is the refractive index difference between the alginate solution and the hydrogel, aiming to determine TIR conditions. Two strategies were used to determine the refractive index of alginate hydrogels: ellipsometry and TIR. Ellipsometry analysis was performed with the ellipsometer located in the Clean Room facilities at the IMB-CNM in collaboration with Mr. Alexandre Moreno and Mr. Samuel Dacunha. Gels were deposited on silicon wafer and analysed with the equipment short after deposition to avoid liquid evaporation and the change of optical properties. Although a clear tendency was observed with higher refractive indexed with the gels than with the liquid solutions, it was not possible to obtain reliable values for determining the exact refractive index difference because high variations were recorded in all cases. It was attributed to the fast dehydration of the thin alginate layers deposited on the wafer.

Alternatively, TIR analysis of the hydrogels was used to indirectly determine the refractive index of these samples. In this case, the alginate was deposited on top of a straight piece of electrode, after which the surrounding liquid was removed to have a gel-air interface. The input fiber was aligned with the gel using various angles, which could be precise controlled using a multi-axis stage. Using a camera, the transmission and reflection of the light was observed as the angle changed. By measuring the angle of transmission after passing through the gel compared to the input angle, the refractive index was calculated using Snell's law, as described in **Chapter 3.2.2**. Additionally, upon turning the input angle, a specific angle was found where light was not transmitted anymore, i.e. the critical angle (hydrogel/air). Various examples of the resulting images are presented in **Figure 8.11** below and resulted in an estimated refractive index of  $1.3 \pm 0.2$  (n=14). The precision of the measurements of the exiting angle was too low, resulting in large variations. Additionally, sodium alginate itself has a reported refractive index in the range 1.365 – 1.375 [31], which coincides with the uncertainty range of the alginate gel.

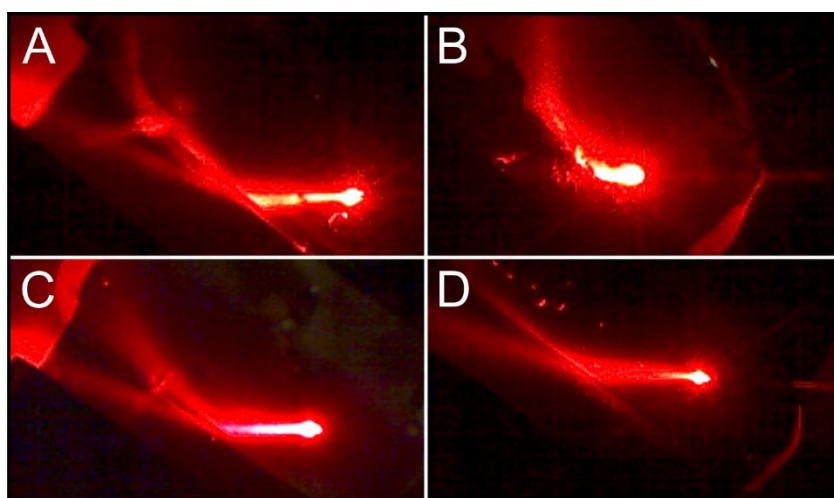


**Figure 8.11: Determination of the refractive index by observing changes in refraction upon passing through the alginate hydrogel.** A red laser was used to visualize the light path upon entering and leaving the alginate hydrogels.

### 8.3.3. Alginate as waveguide: characterization and proof of concept

Using the custom-made setup described in **Chapter 5.5.3.1**, two optical fibers were coupled to the electrochemical systems used for electrodeposition to quantify the amount of light transmitted by alginate in the hydrogel and solution forms. One fiber was positioned at the end of the working electrode and aligned to it, and connected to the light input, i.e. a red laser. A second fiber was aligned with the first one at the opposite end of the electrode but outside of the working electrode's curvature. The second fiber was connected to a detector to register the changes in the transmitted light. A visualization of the positioning of the fibers is included in **Figure 8.12**. The reasoning behind the positioning of the fibers was as follows. The electrode had a fixed curvature, on which the alginate gel will be deposited with the same curvature (i.e. electro-addressing). It is well known that total internal reflection occurs when incident light reaches an interface at an angle greater than the critical angle. Aligning the input fiber with the entrance of the working electrode ensured that the input light would follow the same curvature as the formed hydrogel. Since it was difficult to ensure the reliability of the refractive index values of the gel obtained with the previous techniques, the critical angle could not be determined with precision, which might occur at a smaller angle than the curvature of the electrode. However, with this configuration, light reflection in the gel/solution interface would be detected as an increase in the optical losses. These optical losses would confirm (i) the existence of an interface, (ii) the difference of refractive index between the two phases (i.e. hydrogel and liquid) and thus (iii) the previous light routing concept. This configuration allowed the interrogation of this interface in real time, reporting on hydrogel formation/disaggregation along the experiment.



**Figure 8.12: Image highlighting the positioning of the fibers relative to each other and the electrodes respectively.** The input and output fibers are at the top and bottom respectively, with the red laser light being emitted by the former. From top to bottom are the reference Ag/AgCl, the circular counter and the curved working electrodes respectively. The electrodes were made of carbon.

Various experiments were performed with the previous setup by electrodepositing the alginate hydrogel at a fixed potential. After applying the potential for gel formation, a negative potential was then applied for the reversal of the hydrogel. The electrodes

were cleaned and the liquid replaced after every experiment. A visualization of the intensity of formation and reduction is presented in **Figure 8.13**. Note that due to the setup, a decrease in signal is expected when alginate is formed. For the final application however, the detector should obtain an increase in signal when the alginate hydrogel is formed, using it as waveguide to focus the light to the detector.

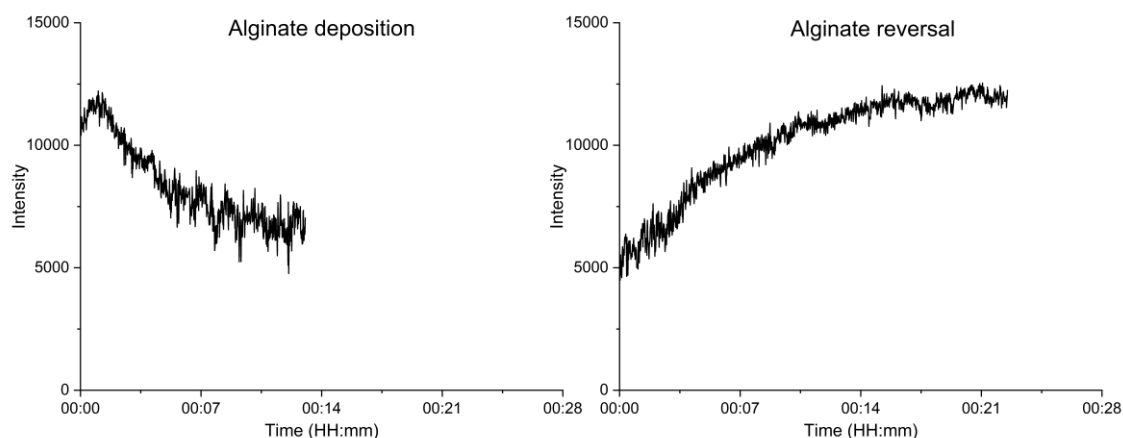


**Figure 8.13: Optical measurements of the formation and reversal of the alginate hydrogels.** Alginate (1 % w/v) was mixed with  $\text{FeCl}_2$  (20 mM) and deposited on the screen-printed carbon electrodes. For the gel formation a potential of 0.8 V was applied for 15 minutes. For the reversal a -0.8 V was applied until the signal stabilized, after approximately 25 minutes.

During electrodeposition, light intensity gradually decreased until stabilization after 10 minutes of deposition. This initial decrease was associated to the formation of a hydrogel/liquid interface on top of the electrode that produced the refraction of the light. This fact confirmed the difference between the refractive index of both liquid/gel phases. The light intensity magnitude registered after 10 minutes of electrodeposition was related to the hydrogel layer thickness. As it was already reported, the thickness of the layer was proportional to the electrodeposition potential and time [26], where longer times and higher potentials produced thicker gels. However, it has thickness limitation. The presence of isolating electrodeposited layers, such as alginate, reduces charge transfer capacity of the system, particularly far from the electrode surface. For this reason, at some extent, the thickness of the hydrogel cannot be longer increased. Although not proved, this may be the cause for the light intensity stabilization after long electrodeposition times.

After stabilization of the amount of collected light, a negative potential was applied, resulting in the reduction of the iron (III) to iron (II), the detachment and disaggregation of the gel and the recovery of the initial intensity magnitude. In many cases, although the gel was mostly disaggregated (which was observed visually), it did not result in a detectable change in light intensity. The reason was on the long electrodeposition times required. Since the deposition was so long, the layer just on top of the electrode became very compact and stable and was very difficult to revert the reaction, remaining in the optical path and reducing the amount of light that finally reached the detector. In the cases that alginate hydrogels fully reverted to the liquid state, the recovery of the initial light intensity required more than 15 minutes with the added disadvantage that after 20

minutes the signal still fluctuated. Therefore, the reversibility of the process was highly limited by the characteristics of the electrodeposition process and the formation of an initial very stable hydrogel layer on top of the electrode, which very difficult to remove.

#### 8.3.4. Conclusions

Alginate hydrogels are good candidates in the production of miniaturized optical routers for point of care devices. This **pumpless** (stationary liquid) approach is **low cost and simple**, since based on electrodeposition, and it has high potential of miniaturization, integration and automation. Gel formation in minutes may be enough considering the kinetics of most of biochemical reactions and particularly those involving bacterial metabolism, as the ones developed in this thesis (which expand some hours). However, it may be improved by increasing the conductivity of the medium, which may accelerate the deposition and reversal steps. Unfortunately, the slow and **incomplete reversibility** of the redox reaction limited their application at this stage, making it very difficult to design a suitable structure for light routing based on this technology. Considering the previous drawbacks, the hydrogel formation-based strategy for light routing, although promising, was abandoned and alternatives based on inorganic materials with higher stability and reversibility were explored.

## 8.4. Gen 3: optical shutter

The third generation kept the usage of electrochemistry as low cost, low energy consumption, miniaturized, integrated and compact approach for developing an optical router but here based on the use of electrochromic switchers (i.e. materials that change of colour as a result of a change in their redox state; see **Chapter 3.1.3** for bio-electrochromic molecules) as electro-active elements. The underlying idea is based on simply blocking the light with a highly absorbing material that prevents light to reach the optical detection channels, with the exception of the selected one. The general principle is illustrated in **Figure 8.14**. A number of optical detection channels are positioned directly between the light source and the detector. At the entrance of each channel an optical element based on this electrochromic switchers, here defined as optical shutter, is positioned in the direction of the optical path. The material has two states: the “on-state”, where the element is completely transparent and the shutter is opened allowing the light to pass through; and the “off-state”, where the shutter is closed since the material is completely opaque and absorbs the light. Each optical shutter can be controlled individually, allowing full control of the detection of each of the channels.

Electrochromic switchers change of colour depending on their redox state, which can be electrochemically controlled with high precision with a simple potentiostat. To be used in the production of optical shutters, the electrochromic switcher should be completely transparent in one redox state (transmittance in the visible range > 85%), whilst being opaque in the other (transmittance in the visible range < 10%). For a fast, reliable and homogeneous actuation, the electrochromic material was deposited on top of the electrode ensuring physical contact, which implied the use of transparent electrode. Therefore, all following experiments were performed using indium tin oxide (ITO) as working electrode.



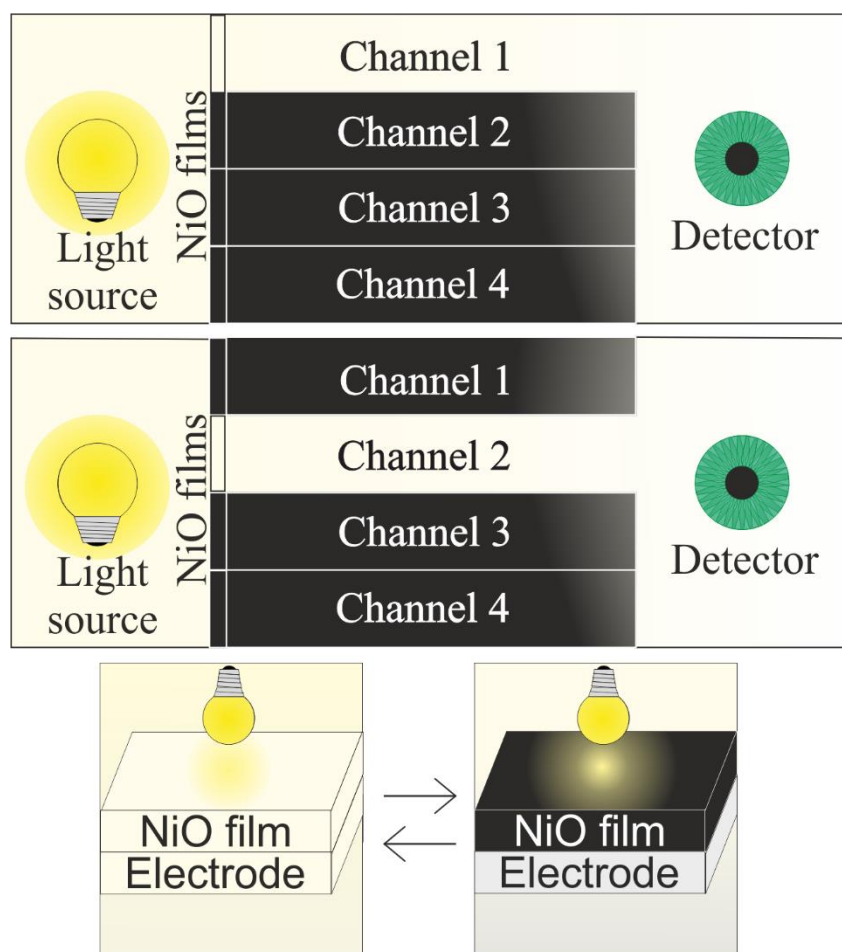


**Figure 8.14: Scheme of the working principle of the optical shutter** to enable multiplexing using a single light source and a single detector. The shutters are based on materials with redox properties, NiO in this figure, where the redox state influences the transparency of the material. In the top figure, the film in the first channel is at a redox state that allows light to go through, whereas the light is blocked in all 3 other channels. In the middle image, the redox states of the films of channel 1 and 2 are reversed, enabling control over which channel receives illumination. The bottom image represents the working principle of a single channel and its effect on transparency.

#### 8.4.1. Optimization

A variety of electrochromic switchers and conditions were studied with the aim to find those optimal for the application as optical shutter. A summary is shown in **Table 8.2**, and discussed below. After each preparation, the formed film was tested using cyclic voltammetry and imaging, for the possibility to change back and forth between transparent and opaque.

**Table 8.2: Summary of the various methods employed in the optimization of the usage and deposition of an electrochromic molecule on an indium tin oxide (ITO) electrode.** The ITO treated refers to a sonication as described below the table. Regarding the pH values: acid = 5, neutral = 7, basic = 13. SDS = sodium dodecyl sulphate, KCl = potassium chloride, EDTA = Ethylenediaminetetraacetic acid, CV = cyclic voltammetry.

Material	ITO treated	Electrolyte	SDS Y/N	Deposition		CV pH	Comments
				pH	Time (s)		
Polypyrrole	No	/	Yes	Neutral	35	Acid	No appreciable colour change
NiCl <sub>2</sub>	Yes	KCl	Yes	Neutral	50	Neutral	No deposition
NiCl <sub>2</sub>	Yes	EDTA	No	Neutral Basic	1800	Neutral	No deposition No appreciable colour change
NiCl <sub>2</sub>	Yes	EDTA, KCl	No	Basic	2200	Basic	Not black enough
NiCl <sub>2</sub>	Yes	EDTA, KCl	no	Basic	2400	Basic	Reversible

For the first set of experiments, 0.05 M polypyrrole was used. Polypyrrole showed great promise as conductive polymer for its use in electrochromic devices. Its deposition on the electrodes only requiring 35 seconds was homogeneous, however, no colour changes were observed during the cyclic voltammetry, probably due to the presence of impurities, its poor stability and/or the influence of experimental factors in the reversibility of the reaction, e.g. pH, ionic composition and concentration of the medium, etc.

The use of NiCl<sub>2</sub> for the formation of Nickel Oxide (NiOx) compounds was studied afterwards. Using 0.5 M NiCl<sub>2</sub>, the selection of a suitable electrolyte was crucial for the homogenous electro-deposition of the compound. At first, either 0.1 M KCl or 0.1 M EDTA were used, but not suitable for electrodeposition. The combination of the later was more appropriated and led to thicker electrodeposited films visible with the bare eye. However, homogenous electrodeposition required the treatment of the ITO electrode surface, involving 30 minutes of sonication inside a bath of isopropanol, acetone and again isopropanol, each for 10 minutes. Additionally, it was noticed that the short deposition time for the pyrrole deposition was insufficient for the NiCl<sub>2</sub>, which required 2400 s to produce sufficiently thick and opaque layer to block the light. Furthermore, it was observed that not only the pH during cyclic voltammetry influenced the electrochromic behaviour, but also that used during deposition of the Ni salts. In both cases, a basic pH of 13 was found optimal.

The nickel in its oxidised NiO state was transparent (transmittance >85 %), but became completely opaque (transmittance <10 %) after reduction and reaction with water to

form nickel oxide hydroxide (NiOOH). The oxidation/reduction reaction could be repeated several times (> 50 times in this case), maintaining similar optical properties (i.e. transparent in one form and opaque in the other). Although still not fully understood by the incorporation of water molecules along the cycles, the reaction mechanism may involve the formation of NiOx compounds of different composition, all of them transparent in the oxidised form and highly opaque in the reduced one. The exact composition of the compound may depend on the pH and the water content of the sample. A possible reaction mechanism is shown in **Figure 8.15**, with the corresponding colour change on the ITO. Due to the optical properties of the electrochromic layer, its high reversibility and fast colour change, this material and conditions were considered optimal and used for further development of the optical shutter.

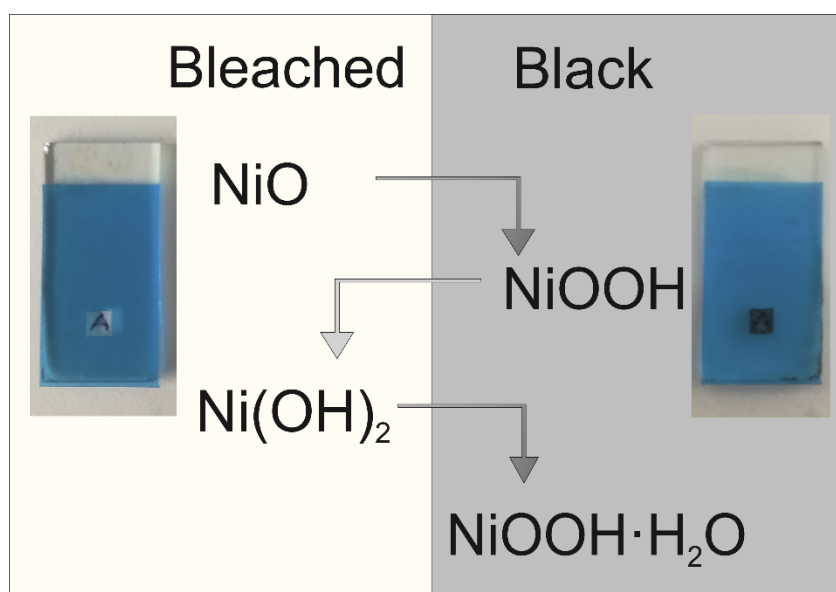
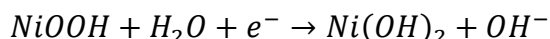


**Figure 8.15: Reaction mechanism of the NiO oxidation reduction process in a water based environment.** The corresponding optical changes are depicted using the photographs on the left and right for the reductive and oxidative state respectively. The ITO electrode corresponds to the entire piece, but only the small square has been treated for the redox reaction.

#### 8.4.2. Characterization

After optimization, the electrodeposited ITO electrodes were analysed using cyclic voltammetry (**Figure 8.16**) and Fourier-transform infrared spectroscopy (FTIR) (**Figure 8.17**) to confirm the deposition of the nickel and its corresponding redox state.

Cyclic voltammetry was used to verify the reversibility of the redox reaction of electro-deposited NiO thin films on ITO electrode. As seen in **Figure 8.16**, two peaks were observed in each cycle, which corresponded to the oxidation and reduction of the nickel oxide compounds. As stated before, ITO was used as working electrode, with Ag/AgCl as reference and platinum as counter electrode, with a scan rate of 50 mV/s. The two peaks were found at 0.47 and 0.69 V for the reductive and oxidative state respectively, giving a standard potential of 0.58 V vs Ag/AgCl. In agreement with the magnitude of the standard redox potential obtained, the most probable NiO<sub>x</sub> species electrodeposited would be:



This reaction also matched the mechanisms stated in **Figure 8.15** since, after deposition, the ITO had a black colour. The peak current values and the areas under the peak in each case are summarized in **Table 8.3**.

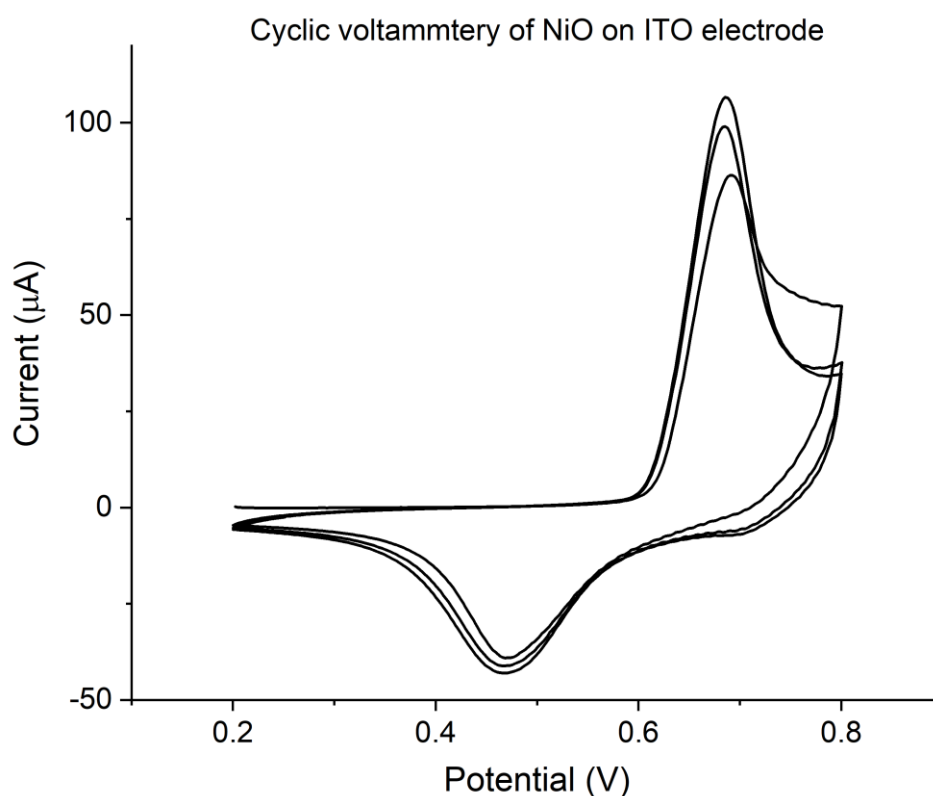


**Figure 8.16: Cyclic voltammery of a NiO film.** Cyclic voltammery was performed at a pH 13 in a KOH solution with 0.1 M KCl. An ITO was used as working electrode, platinum 0.5 mm<sup>2</sup> as counter and Ag/AgCl as reference electrode respectively. A scan rate of 50 mV/s was used for a total of 3 scans.

As can be observed, the peak current for the oxidation is larger in absolute value than the corresponding reduction reaction in each cycle. Furthermore, the corresponding areas under the peaks further follow the same trend. Due to the negligible difference between the molecules in both redox states (single proton difference between NiOOH and Ni(OH)<sub>2</sub>), the difference in values was associated to a higher efficiency of the oxidation process when compared to the reduction one. Thus, the continuous cycling resulted in an increase in the amount of oxidized molecules, which did not revert to the

initial state. In practice, this resulted in the shutter becoming less transparent over time, which was also observed in practice after some cycles.

**Table 8.3: Analysis of the cyclic voltammogram of Figure 8.16.** The peak current and area were calculated for each cycle.

Step	Peak current ( $\mu\text{A}$ )	Area under the peak (nC)
Cycle 1 oxidation	85.9	243
Cycle 1 reduction	-39.1	14.6
Cycle 2 oxidation	98.8	797
Cycle 2 reduction	-41.1	112
Cycle 3 oxidation	107	1130
Cycle 3 reduction	-43.0	176

FTIR was employed here to analyse the deposition of the nickel and its corresponding composition. Oxidized and reduced layers were analysed, which were obtained after constant application of the suitable oxidation or reduction potential for 1 minute. The red FTIR spectrum in **Figure 8.17** corresponds to the oxidized form of the sample, whereas the blue line corresponds to the reduced one. Each of the peaks of both reactions is highlighted in the figure with its corresponding wavenumber. A description of each peak is summarized in **Table 8.4**.

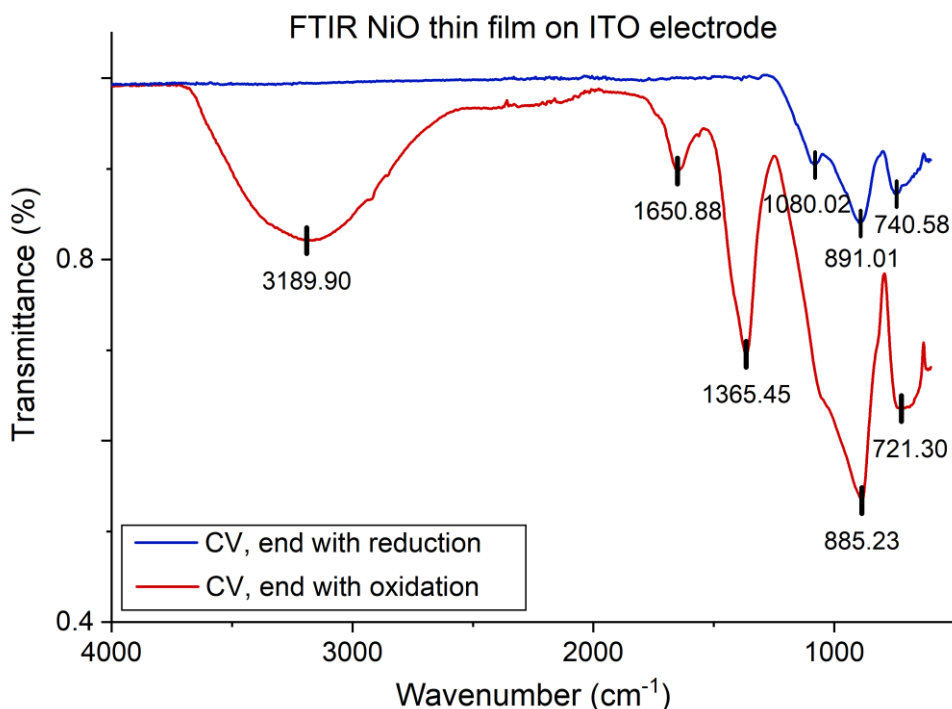


**Figure 8.17: Fourier-transform infrared spectroscopy of NiO redox states.** Spectra were taken after 3 cycles of cyclic voltammetry, with a final reduction (blue) or oxidation (red). Highlighted are the wavenumbers of the observed peaks for each spectrum.

An increased amount of peaks was observed in the oxidized state when compared to the reduced one. The absorption band of  $3189.90\text{ cm}^{-1}$  refers to O-H stretching, due to the weaker O-OH bond in the oxidized state, whereas the absorption band at  $1365.45\text{ cm}^{-1}$  is due to the respective bending. The band present at  $1650.88$  is due to free  $\text{H}_2\text{O}$ , which can be entrapped in the film during oxidation. The absence of these peaks in the

reduced state was due to the direct bond between the OH and the nickel atoms. The remaining peaks, 1080.02, 891.01 – 885.23 and 740.58 – 721.30  $\text{cm}^{-1}$  were lattice effects, presumably due to the nickel matrix itself. Finally, it is important to notice the absence of water and O-H stretches and bends in the reduced stage. As mentioned for the cyclic voltammetry, continuous cycling would result in a built-up of a permanent oxidized state of the film, though no residual of the oxidation was visible here.

**Table 8.4: Description of transmittance peak belonging to the FTIR spectra of Figure 8.17.**

Peak ( $\text{cm}^{-1}$ )	Type
3189.90	O-H stretch (intermolecular bond)
1650.88	O-H bend, free H <sub>2</sub> O
1365.45	O-H bend, alcohol
1080.02	Second order lattice mode
885.23 – 891.01	Combination lattice mode
740.58 – 721.30	Second order lattice mode

### 8.4.3. Performance

After verification of the presence of nickel oxide thin film on the ITO electrode and their pseudo-reversible nature, the rate of change and the optical properties of the optical shutter were analysed. The switching frequencies were monitored after sequential application of reduction/oxidation cycles and imaging with a camera. Representative images of the electrochemical set-up and the oxidation-reduction cycles are shown in **Figure 8.18**. The optical shutter was cycled continuously between both redox states, whilst in a basic solution. A switching rate of 3 seconds was sufficient to completely change between redox states, which was confirmed through an evident colour change of the electrochromic material from transparent to opaque, and vice versa. After multiple oxidation-reduction cycles, the re-oxidation process lost effectiveness, which was evident by a reduction in the transparency of the electrochromic material. However, continuous switching was possible for 50 cycles, when the re-oxidation to the transparent material was too diminished.

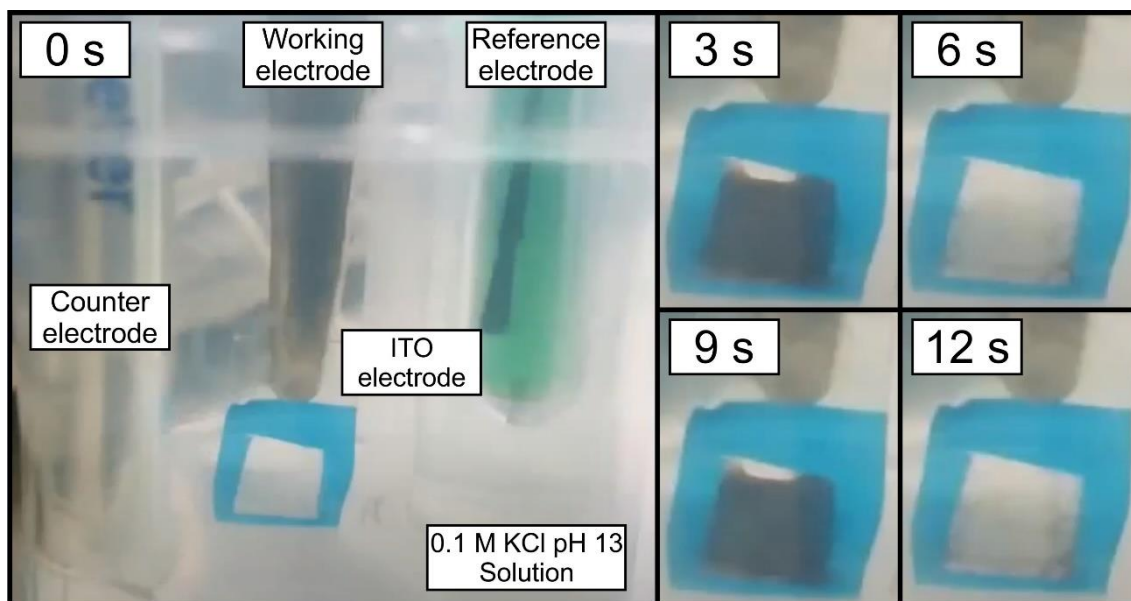


**Figure 8.18: Imaging of the switching rate of the optical shutter at a constant rate between its two redox states.** Each of the components are highlighted in the left figure, with the images on the right corresponding to the electrode's appearance after every 3 seconds of cycling.

#### 8.4.4. Miniaturization and integration

All previous experiments utilized the optical shutter as a stand-alone setup. However, for its practical use as optical router, the developed technology requires miniaturization and later integration into photonic lab-on-a-chip systems. Aiming to miniaturization and integration, the process to produce NiOx layer on ITO electrodes was transferred to mass production-compatible microfabrication technologies. As proof of concept, NiOx was prepared by deposition and thermal oxidation on silicon wafers for simplicity. It is important to remark that ITO is very sensitive to temperature and thermal oxidation may alter its properties. It is known how high temperatures increase the conductivity of the ITO, but also reduce its transparency ([32]). This property should be taken into account when producing the final device, integrating the ITO. In this case, a nickel layer of 200 nm was sputtered on top of the wafer, and was thermal oxidized for 60 min under an oxygen atmosphere. Three temperatures, namely 500 °C, 700 °C and 950 °C, were studied in three independent runs to evaluate the oxidation of the thin film. The different temperatures should not only impact the thicknesses of the NiOx layer, but also its roughness, crystallinity and even optical properties [33]. An image of the resulting film is shown in **Figure 8.19**. At all three temperatures, a film of nickel oxide was formed, but the higher the temperature, the more the thin film was detaching from the surface, due to some dissociation between the oxide layer and the metal. Even at 500 °C, the minimal temperature required for the oxidation of the nickel film, a non-homogeneous deposition was achieved. This, with the detachment at higher temperatures, prevented accurate measurement of the properties of the film, like thickness and conductance. Due to the complications readily encountered on the silicon wafer, further optimization of the microfabrication protocol was necessary before transferring it to an ITO substrate.

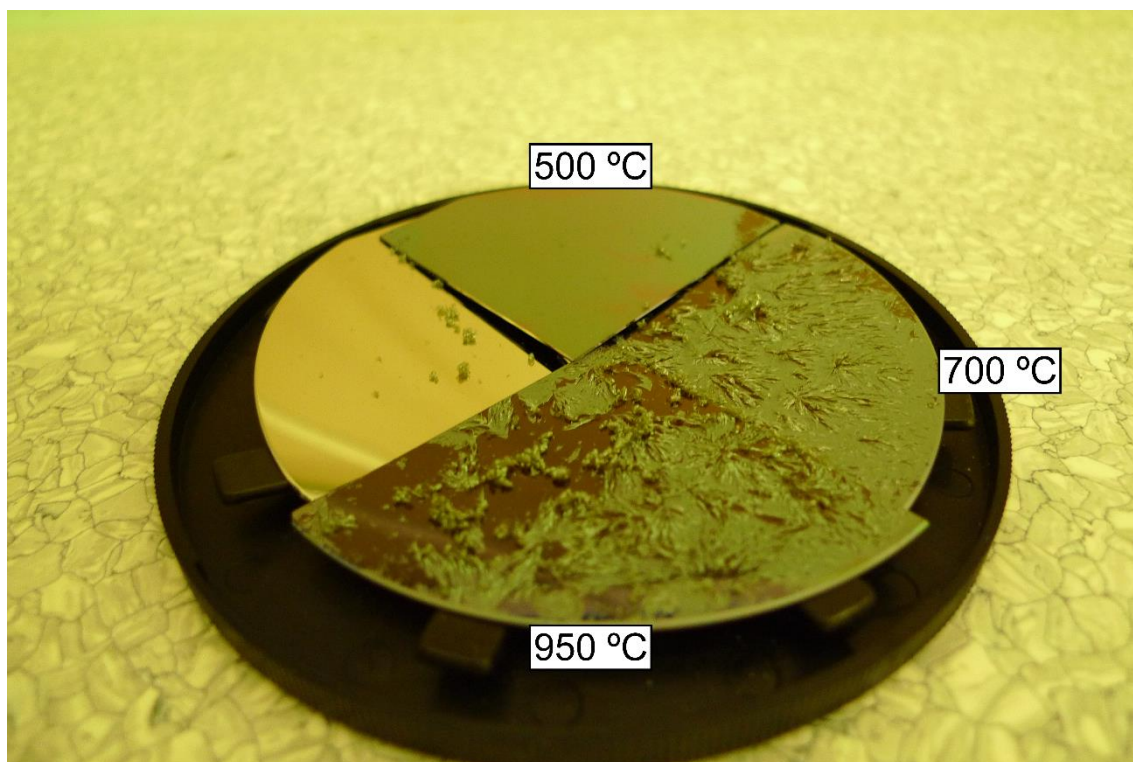


**Figure 8.19:** Image of a silicon wafer with a nickel oxide thin film formed through thermal oxidation. The thermal oxidation was performed for 60 min, in an oxygen environment, at the highlighted temperature.

#### 8.4.5. Conclusions

The nickel oxide based optical shutters provided **fast switching**, within 3 seconds, between both redox states, resulting in rapid changes between opaque and transparent. Additionally, with an over **90 % transmittance** difference of between both states, a large contrast could be generated within seconds. According to cyclic voltammetry the shutter has a limited lifetime, due to a gradual built-up of the oxidized state. Nonetheless, the FTIR showed that, at few cycles, it does not impact the formed layer, and in practice **more than 50 cycles** could be performed before the changes became notable or affecting the performance of the system. Additionally, slower scan rates could improve the reduction step, overcoming the issue. Finally, using thermal oxidation for a more controlled formation of a thin nickel oxide film, increasing its miniaturization and integration potential, had proven complicated due to the detachment of the nickel oxide from the wafer, though it served as a proof of concept that could be optimized. The technology shows great promise, but due to the required amount of optimization, it was decided to try an alternative approach as a backup.

### 8.5. Gen 4: frequency modulation

The last generation of opto-electronic elements for multiplexed analysis of samples using optical transductions was a frequency modulator developed in collaboration with the Integrated Circuits & Systems Group (ICAS) at IMB-CNM, and concretely Dr. Michele Dei, Dr. Francesc Serra-Graells and Mr. Jose Cisneros. Any of the previous routers had the limitation of being based on optical elements that lost information during the



switching process, with the added disadvantages of presenting inherent optical losses by requiring a number of interfaces, mechanisms and materials with more or less capacity to absorb light, as well as potential crosstalk problems between channels. The electronic component presented here overcomes the previous limitations by enabling a continuous read-out of all channels simultaneously, at the cost of using multiple light sources and thus, a smaller degree of integration and miniaturization. This disadvantage may be partially palliated when considering the low-cost, small size and excellent performance of the miniaturized LED sources developed nowadays. Hence, this strategy required the use of a dedicated light source for each of the detection channels, which converged to a single detector for the full system.

In the performance mechanism, each light source is pulsed at a specific but distinct frequency, which will be used as a fingerprint in the detector to identify the wavelength and the origin (i.e. optical channel) of the electrical signal. The detector, therefore, receives simultaneously a multi-frequency signal resulting from the combination of three different wavelengths from 4 different channels ( $3 \times 4 = 12$  individual frequency modulated signals). The electronic circuit is capable to demodulate this complex signal and to isolate each measured signal in real time, thus providing the information of each wavelength at each measurement channel. Additionally, knowing the exact pulsation frequencies further allows filtering of all surrounding noise (e.g. environmental light or sun light), presenting high dynamic ranges.

### 8.5.1. Design and principle

The block schematic shows a multiplexed optical channel readout based on lock-in detection. In short, a lock-in amplifier (also known as a phase-sensitive detector) is a type of amplifier that can extract a signal with a known carrier from an extremely noisy environment. It performs a multiplication of its input with a reference signal and then applies an adjustable low-pass filter to the result. This method is termed demodulation or phase-sensitive detection and isolates the signal at the frequency of interest from all other frequency components. The reference signal is either generated by the lock-in amplifier itself or provided to the lock-in amplifier and the experiment by an external source.

In the conceptual block design, a continuation of a previous design [34,35], each optical channel is characterized by a spectral signature  $H_i(\lambda)$  which contains optical information about the analyte. When stimulated by a white light, the spectral absorption characteristics can be recorded by a conventional spectrophotometer in order to quantify  $|H_i(\lambda)|$  at each  $\lambda$  of interest. This system implies a very selective optical filtering capability. However, the system shown here wants to mimic the same behaviour, without the use of expensive and bulky optical components, e.g. prisms, by sacrificing spectral selectivity. This can be achieved by using a RGB (red, green and blue) LED which will stimulate virtually separate regions of  $H_i(\lambda)$  that can be lumped in three absorption parameters:  $\alpha_R$ ,  $\alpha_G$ ,  $\alpha_B$  accounting respectively for the averaged absorption in the emission region of the red, green and blue LEDs. On the receiver end, the optical connection is finally coupled to a low-cost photodetector which allows for electrical

transduction and further signal processing in the electrical domain which is needed to extract the individual quantities  $\alpha_R$ ,  $\alpha_G$ ,  $\alpha_B$ . The lock-in detection scheme is based on frequency multiplexing, where each wavelength in the LED is assigned to a band around a carrier frequency, and this extended to the different optical channels of measurement (i.e. four optical measurement channels in the current configuration of the system). In the representation of **Figure 8.20**,  $f_{R1}$ ,  $f_{G1}$ ,  $f_{B1}$  are the respective centre modulating carrier frequencies of the red, green and blue LED of RGB1 (LED coupled to the optical channel number 1). The final signal processing in the electrical domain is in charge of channel filtering and baseband demodulation for each channel in order to extract the  $\alpha_R$ ,  $\alpha_G$ ,  $\alpha_B$  values.

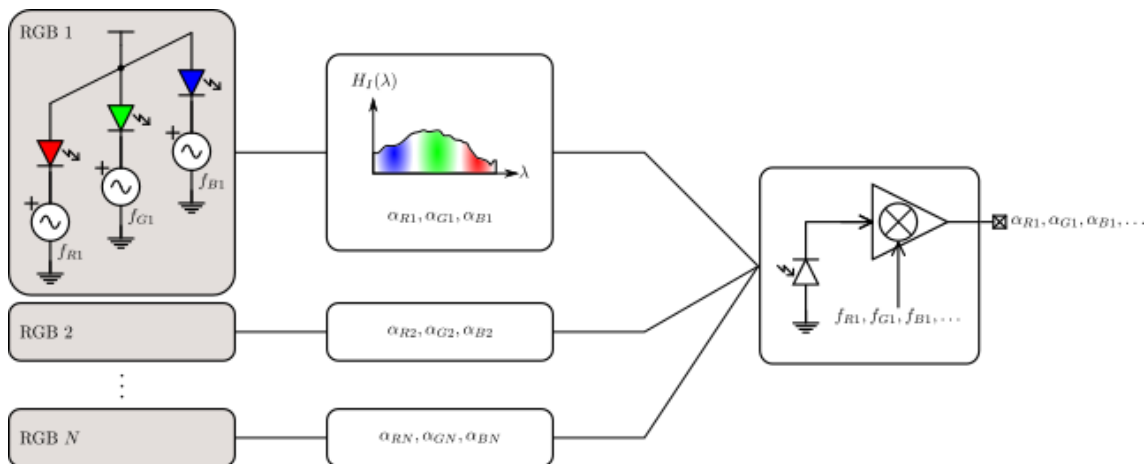


**Figure 8.20: Conceptual block design of the coupling of various RGB LED lights**, each with its respective spectral signature, to a single detector. This detector will extract the spectral response of each individual RBD signal through a lock-in amplifier.

A traditional signal processing scheme consists of a current-to-voltage conversion of the photodiode current, an analog-to-digital converter. The digital data stream is then deconvoluted by a PC or another computational effective unit coupled to the system. The system can be scaled to multiple optical channels, each one stimulated by an RGB emitter for simultaneous multi-analyte detection by choosing additional frequencies for signal modulation. This solution is particularly attractive because it avoids the use of optical elements, such as routers or switchers, simplifying the system performance and increasing its functionality and robustness. Limits on the maximum number of channels are set by bandwidth restrictions and photodiode current saturation. The latter can be traded off with sensitivity by simply coupling less light to the detection point. However, implications on resolution are evident, since each channel will reduce its signal-to-noise performance once the total received optical power is kept constant while increasing the number of channels. On the other hand, bandwidth restrictions are given due to strong environmental interferers, such as utility frequency 50/60 Hz coupled to incandescence bulbs and 10 kHz associated to neon lights. Higher lock-in carrier frequencies ( $> 100$  kHz) can be also employed by using high-performance electronic components, which eventually translate to the need for integrated custom circuits.

A possible solution to both limitations is the use of time-sharing techniques, especially when more channels are required than the maximum number that are being able to be readout simultaneously, by maintaining a sufficient gap between carrier frequencies. Any number of channels after the maximum number will belong to a second set, which is divided into the same carrier frequencies as the first. In this case, the allocation to each set will go in turns, more in line with a traditional router system. The drawback is the loss of continuous detection of all channels. However, for many biological systems, whose rates of changes are not in the millisecond range, this poses no practical restrictions.

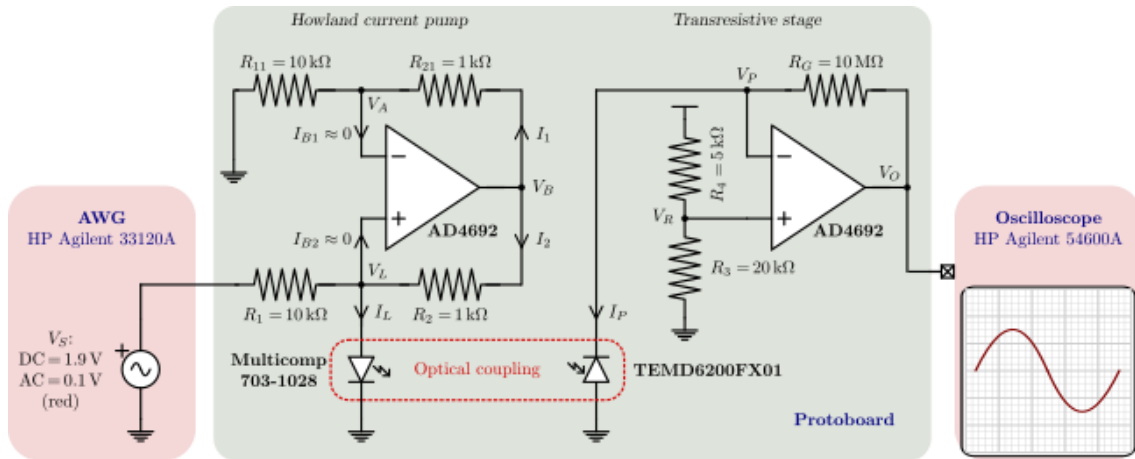


**Figure 8.21: Electronic schematic the RGB spectrophotometer for one RGB channel.** On the left is the signal generator providing an input to the Howland current pump. The resulting optical signal is coupled to a transresistive stage, which will provide a digital output to an oscilloscope.

**Figure 8.21** and **Figure 8.22** show the schematic and the photograph of the RGB spectrophotometer demonstrator for one RGB channel. The current generation for each LED is obtained thanks to a well-known Howland current-pump scheme which is fed by an external signal generator (HP Agilent 33120A). It can be demonstrated that the current  $I_L$  on the LED (Multicomp 703-1028) is determined as follows:

$$I_L(t) = \frac{V_{S,DC}}{R_1} + \frac{V_{S,AC}}{R_1} \sin(2\pi f_S t)$$

where  $V_{S,DC}$  (set at the signal generator) and  $R_1$  are chosen to bias the LED in the desired operating region, and the  $V_{S,AC}$  is chosen for the carrier amplitude at frequency  $f_S$ . On the receiver side, the output voltage of the transresistive stage is given by:

$$V_O(t) = R_G I_P(t)$$

being the  $I_P$  the total photocurrent generated by the photodetector (TEMD6200FX01). The photodetector is reverse biased at the voltage  $V_R$  determined by the supply (5V) ratiometric resistive divider formed by  $R_3$  and  $R_4$ . The value of  $R_G$  determines the gain of the transresistive stage and the sensitivity of the readout signal. Its value is chosen accordingly to the maximum received  $I_P$  value and the maximum available voltage room. The operational amplifiers used in this implementation allows for rail-to-rail operation, which corresponds to the 5V-headroom here. The multiplex frequency is finally read by

a digital oscilloscope (HP Agilent 54600A) configured for fast Fourier transform calculation.

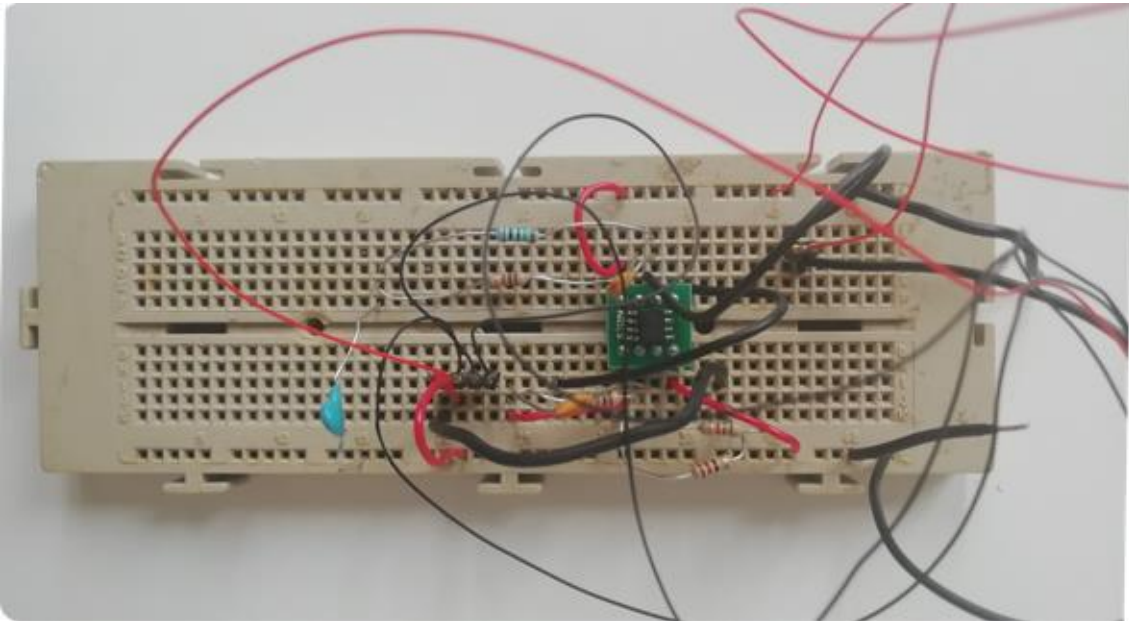


**Figure 8.22: Protoboard setup of the RGB spectrophotometer using a single RBD LED light source.**

The technology has been addressed as a proof-of-concept employing a single light source pulsing at a specific input frequency and integrated in the final structure for validation as the best solution currently accessible for multiplexing.

### 8.5.2. Conclusions

The frequency modulation principle, though still in its infancy, shows great promise for a novel way of overcoming the inherent loss of data of a traditional router during switching. The **continuous and simultaneous** read-out allows the user to analyse all the samples all the time. Additionally, the **multiplexing** is significantly easier than the previous generations, by addition of light sources and providing a pulse frequency not yet used. The maximum amount of multiplexing is only limited on the sensitivity of the system to distinguish close related frequencies. Furthermore, since the system only relies on electronics, the cost of the final device will depend on the aforementioned sensitivity and amount of channels. Finally, the integration of the system is only limited by the collection of the light towards the single detector, making it **highly flexible and adaptable** for any application.

## 8.6. Final Remarks

The development of an optical router for easy and compact multiplexing for lab on a chip underwent four generations of optimization towards the optimal performance related to the previously developed bioassay. A comparison of each generation based on various properties is given in **Table 8.5**. It needs saying that each generation does not inherently perform worse than the latter ones, but that they were discontinued for various reasons mentioned before. Given sufficient time and optimization, each one could serve as novel optical router in a photonic lab on a chip system for specific applications. A brief summary of each technology is highlighted below.

- The **microfluidic-controlled optical routers** of sequential light routing enabled fast routing with long lapse times. However, the fabrication requirement with manual steps and the need for pumps resulted in high costs and low integration nor miniaturization potential.
- Conversion to the electrodeposition of **alginate hydrogels** significantly reduced the cost of the routing system, whilst increasing miniaturization potential. However, the assay was slow, with incomplete reversibility. The system may be ideal for single use platforms but further research is necessary to optimize the conditions for fast routing, by addition of electrolytes and improving the design.
- Continuing the electrochemical approach, the **optical shutter** enabled fast switching between both redox states to generate over 90 % transmittance difference between both. Furthermore, the long lifetimes, simple design and compatibility with mass-production technologies makes it highly compatible with other systems and attractive industrially. Some further work, characterization and miniaturization, is required to maximize its potential as router for lab-on-a chip.
- The **frequency modulation** is the unique system enabling simultaneous analysis of all samples under test to avoid information losses during switching, also minimizing cross-talk between channels due to the inherent filtering system. Since the router system is fully hardware driven, it is extremely compatible with any light-based assay. However, the technology is still lacking a full analysis of its performance in practice.

**Table 8.5: Overview and comparison of the various generations of the optical routers.** The colour codes indicate the quality of the mentioned parameter in the following order: Dark green, light green, yellow, orange, red; corresponding to very good, good, medium, bad and very bad.

Parameter	$\mu$ COR	Alginate hydrogel	Optical shutter	Frequency modulation
Speed	Fast	Very slow	Fast	Continuous
Cost	Very high	Very low	High	Low
Complexity	Highly complex	Very simple	Simple	Simple
Lifetime	Medium	Very short	Long	Very long
Multiplexing capacity	Low	High	Medium	High
Miniaturization potential	Low	High	Medium	Medium
Integration capacity	Low	Medium	High	High
Portability	Very Low	High	High	High
Stability	Medium	Medium	Medium	Very high
Automation potential	Low	High	High	Very High

## 8.7. Bibliography

- [1] S.C. Terry, J.H. Herman, J.B. Angell, A gas chromatographic air analyzer fabricated on a silicon wafer, *IEEE Trans. Electron Devices*. 26 (1979) 1880–1886. <https://doi.org/10.1109/T-ED.1979.19791>.
- [2] A. Manz, H.M. Widmers, N. Graber, Miniaturized total chemical analysis systems: A novel concept for chemical sensing, *Sensors Actuators B Chem*. 1 (1990) 244–248. [https://doi.org/10.1016/0925-4005\(90\)80209-I](https://doi.org/10.1016/0925-4005(90)80209-I).
- [3] Y. Temiz, R.D. Lovchik, G. V. Kaigala, E. Delamarche, Lab-on-a-chip devices: How to close and plug the lab?, *Microelectron. Eng*. 132 (2015) 156–175. <https://doi.org/10.1016/j.mee.2014.10.013>.
- [4] J. Wu, M. Dong, S. Santos, C. Rigatto, Y. Liu, F. Lin, Lab-on-a-chip platforms for detection of cardiovascular disease and cancer biomarkers, *Sensors (Switzerland)*. 17 (2017). <https://doi.org/10.3390/s17122934>.
- [5] J. Park, V. Sunkara, T.H. Kim, H. Hwang, Y.K. Cho, Lab-on-a-disc for fully integrated multiplex immunoassays, *Anal. Chem*. 84 (2012) 2133–2140. <https://doi.org/10.1021/ac203163u>.
- [6] S. Weng, X. Li, M. Niu, B. Ge, H.Z. Yu, Blu-ray technology-based quantitative assays for cardiac markers: From disc activation to multiplex detection, *Anal. Chem*. 88 (2016) 6889–6896. <https://doi.org/10.1021/acs.analchem.6b01604>.
- [7] B.H. Shadfan, A.R. Simmons, G.W. Simmons, A. Ho, J. Wong, K.H. Lu, R.C. Bast, J.T. McDevitt, A multiplexable, microfluidic platform for the rapid quantitation of a biomarker panel for early ovarian cancer detection at the point-of-care, *Cancer Prev. Res*. 8 (2015) 37–48. <https://doi.org/10.1158/1940-6207.CAPR-14-0248>.
- [8] S.M. Ju, H.J. Jang, K.B. Kim, J. Kim, High-Throughput Cytotoxicity Testing System of Acetaminophen Using a Microfluidic Device (MFD) in HepG2 Cells, *J. Toxicol. Environ. Heal. - Part A Curr. Issues*. 78 (2015) 1063–1072. <https://doi.org/10.1080/15287394.2015.1068650>.
- [9] T.Q. Hung, W.H. Chin, Y. Sun, A. Wolff, D.D. Bang, A novel lab-on-chip platform with integrated solid phase PCR and Supercritical Angle Fluorescence (SAF) microlens array for highly sensitive and multiplexed pathogen detection, *Biosens. Bioelectron*. 90 (2017) 217–223. <https://doi.org/10.1016/j.bios.2016.11.028>.
- [10] H. Ben-Yoav, P.H. Dykstra, W.E. Bentley, R. Ghodssi, Microfluidic Arrayed Lab-On-A-Chip for Electrochemical Capacitive Detection of DNA Hybridization Events, in: Humana Press, New York, NY, 2017: pp. 71–88. [https://doi.org/10.1007/978-1-4939-6911-1\\_6](https://doi.org/10.1007/978-1-4939-6911-1_6).
- [11] S.W. Dutse, N.A. Yusof, Microfluidics-based lab-on-chip systems in DNA-based biosensing: An overview, *Sensors*. 11 (2011) 5754–5768. <https://doi.org/10.3390/s110605754>.
- [12] Y. Cui, Q. Wei, H. Park, C.M. Lieber, Nanowire Nanosensors for Highly Sensitive and Selective Chemical Species, 293 (2016) 1289–1292.

- [13] B. Ibarlucea, E. Fernandez-Rosas, J. Vila-Planas, S. Demming, C. Nogues, J.A. Plaza, S. Büttgenbach, A. Llobera, Cell screening using disposable photonic lab on a chip systems, *Anal. Chem.* 82 (2010) 4246–4251. <https://doi.org/10.1021/ac100590z>.
- [14] O. Ordeig, P. Ortiz, X. Muñoz-Berbel, S. Demming, S. Büttgenbach, C. Fernández-Sánchez, A. Llobera, Dual photonic-electrochemical lab on a chip for online simultaneous absorbance and amperometric measurements, *Anal. Chem.* 84 (2012) 3546–3553. <https://doi.org/10.1021/ac203106x>.
- [15] A. Densmore, M. Vachon, D.-X. Xu, S. Janz, R. Ma, Y.-H. Li, G. Lopinski, A. Delâge, J. Lapointe, C.C. Luebbert, Q.Y. Liu, P. Cheben, J.H. Schmid, Silicon photonic wire biosensor array for multiplexed real-time and label-free molecular detection, *Opt. Lett.* 34 (2009) 3598. <https://doi.org/10.1364/OL.34.003598>.
- [16] M. Gutiérrez, A. Llobera, A. Ipatov, J. Vila-Planas, S. Mínguez, S. Demming, S. Büttgenbach, F. Capdevila, C. Domingo, C. Jiménez-Jorquera, Application of an E-tongue to the analysis of monovarietal and blends of white wines, *Sensors*. 11 (2011) 4840–4857. <https://doi.org/10.3390/s110504840>.
- [17] S. Demming, J. Vila-Planas, S. Aliasghar Zadeh, A. Edlich, E. Franco-Lara, R. Radespiel, S. Büttgenbach, A. Llobera, Poly(dimethylsiloxane) photonic microreactors based on segmented waveguides for local absorbance measurement, *Electrophoresis*. 32 (2011) 431–439. <https://doi.org/10.1002/elps.201000482>.
- [18] A. Weltin, K. Slotwinski, J. Kieninger, I. Moser, G. Jobst, M. Wego, R. Ehret, G.A. Urban, Cell culture monitoring for drug screening and cancer research: a transparent, microfluidic, multi-sensor microsystem, *Lab Chip*. 14 (2014) 138–146. <https://doi.org/10.1039/C3LC50759A>.
- [19] C. Dongre, J. van Weerd, N. Bellini, R. Osellame, G. Cerullo, R. van Weeghel, H.J.W.M. Hoekstra, M. Pollnau, Dual-point dual-wavelength fluorescence monitoring of DNA separation in a lab on a chip., *Biomed. Opt. Express*. 1 (2010) 729–735. <https://doi.org/10.1364/BOE.1.000729>.
- [20] H. Jiang, X. Weng, D. Li, Dual-wavelength fluorescent detection of particles on a novel microfluidic chip, *Lab Chip*. 13 (2013) 843. <https://doi.org/10.1039/c2lc41238a>.
- [21] C.F. Carlborg, K.B. Gylfason, A. Kaźmierczak, F. Dortu, M.J. Bañuls Polo, A. Maquieira Catala, G.M. Kresbach, H. Sohlström, T. Moh, L. Vivien, J. Popplewell, G. Ronan, C.A. Barrios, G. Stemme, W. van der Wijngaart, A packaged optical slot-waveguide ring resonator sensor array for multiplex label-free assays in labs-on-chips, *Lab Chip*. 10 (2010) 281–290. <https://doi.org/10.1039/B914183A>.
- [22] P. Müller, D. Kopp, A. Llobera, H. Zappe, Optofluidic router based on tunable liquid–liquid mirrors, *Lab Chip*. 14 (2014) 737–743. <https://doi.org/10.1039/C3LC51148K>.
- [23] J. Dietvorst, J. Goyvaerts, T.N. Ackermann, E. Alvarez, xavier munoz berbel, A. Llobera, Microfluidic-Controlled Optical Router for Lab on a Chip, *Lab Chip*. (2019) 2080–2088. <https://doi.org/10.1039/c9lc00143c>.

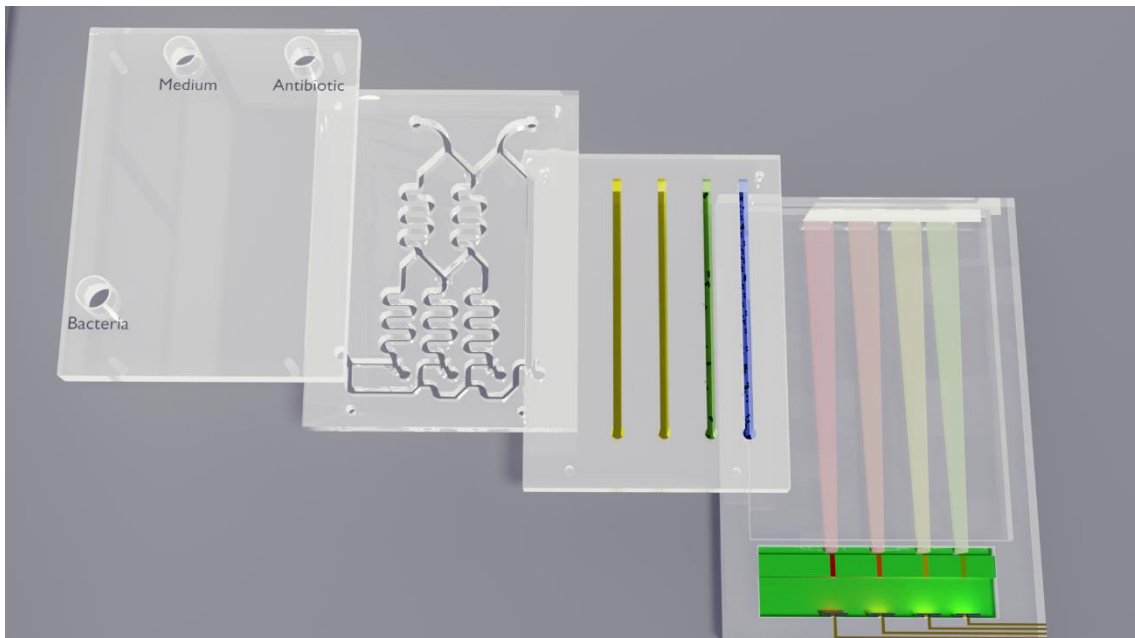


- [24] X. Muñoz-Berbel, R. Rodríguez-Rodríguez, N. Vigués, S. Demming, J. Mas, S. Büttgenbach, E. Verpoorte, P. Ortiz, A. Llobera, Monolithically integrated biophotonic lab-on-a-chip for cell culture and simultaneous pH monitoring, *Lab Chip*, 13 (2013) 4239. <https://doi.org/10.1039/c3lc50746g>.
- [25] P. Vulto, S. Podszun, P. Meyer, C. Hermann, A. Manz, G.A. Urban, Phaseguides: a paradigm shift in microfluidic priming and emptying, *Lab Chip*, 11 (2011) 1596. <https://doi.org/10.1039/c0lc00643b>.
- [26] A. Márquez, C. Jiménez-Jorquera, C. Domínguez, X. Muñoz-Berbel, Electrodepositable alginate membranes for enzymatic sensors: An amperometric glucose biosensor for whole blood analysis, *Biosens. Bioelectron.* 97 (2017) 136–142. <https://doi.org/10.1016/j.bios.2017.05.051>.
- [27] N. Vigués, F. Pujol-Vila, A. Marquez-Maqueda, X. Muñoz-Berbel, J. Mas, Electro-addressable conductive alginate hydrogel for bacterial trapping and general toxicity determination, *Anal. Chim. Acta.* 1036 (2018) 115–120. <https://doi.org/10.1016/j.aca.2018.06.062>.
- [28] F. Pujol-Vila, J. Dietvorst, L. Gall-Mas, M. Díaz-González, N. Vigués, J. Mas, X. Muñoz-Berbel, Bioelectrochromic hydrogel for fast antibiotic-susceptibility testing, *J. Colloid Interface Sci.* 511 (2018) 251–258. <https://doi.org/10.1016/j.jcis.2017.09.004>.
- [29] Z. Jin, G. Güven, V. Bocharova, J. Halánek, I. Tokarev, S. Minko, A. Melman, D. Mandler, E. Katz, Electrochemically controlled drug-mimicking protein release from iron-alginate thin-films associated with an electrode, *ACS Appl. Mater. Interfaces.* 4 (2012) 466–475. <https://doi.org/10.1021/am201578m>.
- [30] Z. Jin, A.M. Harvey, S. Mailloux, J.H. Amek, V. Bocharova, M.R. Twiss, E. Katz, Electrochemically stimulated release of lysozyme from an alginate matrix cross-linked with iron cations  $\text{Fe}^{2+}$ , (n.d.). <https://doi.org/10.1039/c2jm32008h>.
- [31] Ó. Esteban, F. Marva, J.C. Martınez-Anton, Optical constants of a sodium alginate polymer in the UV-vis range, *Opt. Mater. (Amst.)* 31 (2009) 696–699. <https://doi.org/10.1016/j.optmat.2008.08.003>.
- [32] K. Sun, W. Zhou, X. Tang, Z. Huang, F. Luo, D. Zhu, Effects of air annealing on the structure, resistivity, infrared emissivity and transmission of indium tin oxide films, *Surf. Coatings Technol.* 206 (2012) 4095–4098. <https://doi.org/10.1016/j.surfcoat.2012.04.001>.
- [33] F. Hajakbari, Characterization of nanocrystalline nickel oxide thin films prepared at different thermal oxidation temperatures, *J. Nanostructure Chem.* 10 (2020) 97–103. <https://doi.org/10.1007/s40097-020-00332-2>.
- [34] J. Cisneros-Fernandez, M. Dei, L. Teres, F. Serra-Graells, Switch-less frequency-domain multiplexing of GFET sensors and low-power CMOS frontend for 1024-channel  $\mu$ ECOG, in: *Proc. IEEE Int. Conf. Electron. Circuits Syst.*, 2019. <https://doi.org/10.1109/ISCAS.2019.8702544>.
- [35] R. Garcia-Cortadella, N. Schafer, J. Cisneros-Fernandez, L. Re, X. Illa, G. Schwesig,

A. Moya, S. Santiago, G. Guirado, R. Villa, A. Sirota, F. Serra-Graells, J.A. Garrido, A. Guimerà-Brunet, Switchless multiplexing of graphene active sensor arrays for brain mapping, *Nano Lett.* 20 (2020) 3528–3537. <https://doi.org/10.1021/acs.nanolett.0c00467>.



# 9. Final device





The final goal of the thesis was to develop a standalone device capable of fast susceptibility testing of antibiotics in resources limited environments, with minimal instrumental requirements, portability and simplicity. The components of the device, which developed in the previous chapters, are here assembled and tested. The device is designed and manufactured considering a plug-and-play architecture with a low cost disposable part of methacrylate and an optical reader containing the durable elements for the measurement, e.g. LEDs, photodetectors, electronic modules, etc. In this chapter, two main aspects of the final device are presented: (i) the assembly of the layers and (ii) the development of the housing and optical reader.

## 9.1. Disposable part

The disposable part will be fabricated out of cheap materials, using mould injection, hot embossing or an alternative cheap, clean-room free method to quickly and accurately replicate the desired components. It will be composed of four separate pieces working together to provide the bioassay on chip, using minimal manual work. From top to bottom, these pieces are the cover, the gradient generator, the optical detection layer and the bottom support.

- The top layer, the **cover**, sealed the system, preventing user interaction with the optical and fluidic components included inside. In terms of architecture, the cover had three openings, serving as the inlets for the antibiotic, medium and bacterial solution respectively, as denoted on the cover itself. The final device would also feature a non-reversible mechanism to seal the inlets, to prevent liquid loss and contamination, easing the removal of the biohazardous part.
- The **gradient generator** was explained in detail in **Chapter 7.4.5**. The liquids provided through the cover entered the gradient generator to automatically perform the desired dilutions on chip. The exact liquid provided, currently set to 100  $\mu\text{L}$ , to each inlet was crucial in the formation of the gradient. The antibiotic mixed with the medium to form the 2-fold dilution series. Each of these merged with the bacterial inlet, to form a last 2-fold dilution between bacteria and antibiotic, currently generating 4 antibiotic concentrations.
- The **optical detection layer** was composed of a number of straight optofluidic channels, equal to the amount of dilutions provided by the gradient generator. These optofluidic channels served as optical detection system since they contained optical components for the absorbance measurement. Each channel was closed at the end to enable the liquids to come to a standstill. Due to the lack of air permeability of the PMMA, the filling of the channels with the liquid will cause the inherent air to remain entrapped, impeding channel filling. The incorporation of air pockets above the channels enabled the removal of the air from the channel, by pushing it upwards, enabling homogeneous liquid filling. This layer was connected to the gradient generator by holes going through the plastic of the latter transversally, thus creating a 3D microfluidic structure. Inside the optofluidic channels, the actual antibiotic cyanotyping test, as described in **Chapter 6.4.5**, took place, similar to a standard well plate with the main

difference that here optical path was much larger since the light cross the cuvette longitudinally and not transversally as in a plate reader.

- The **bottom support layer** served to give rigidity to the full structure, whilst making it larger to enable easier handling. This layer could be made of a different material, to reduce transparency or increase thermal conductivity (see below), since no patterning was required here.

The four layers were fabricated independently, but permanently bound together before use. This provided consistent alignment of each of the layers, whilst minimizing workload on the user. Furthermore, the permanent sealing prevented leaking of the system. Possible reversible and non-reversible bonding methods were described in **Chapter 7.4.4**, with the optical adhesive being selected, since it did not affect the flow behaviour and the permanent seal provided more sturdiness and prevent the user from disassembling the aligned channels. However, due to the manual labour involved in applying the optical adhesive, further investigation towards optimal bonding, without interfering with the performance of the system would be necessary.

The assembled pieces provided a one-time use, disposable “cartridge”, as shown in the bottom part of **Figure 9.2**. Regarding the performance of the system, the user would prepare the basic solutions off-chip, i.e. the medium (MH for AST testing), the highest desired antibiotic concentration, and the bacteria, mixed with the cyanotyping precursors. The loading of the chip, by simple pipetting of the stock solution into each of the respective inlet, took seconds, after which the filling until the stationary chambers required less than a minute, significantly faster than any manual preparation and loading of the dilution gradient. Finally, the bioassay would be unaltered from the cyanotyping test, providing test results within 4 hours.

## 9.2. Housing

The housing (chip-to-world interface) consisted of more expensive and reusable components, serving as a standalone device able to run one (or more in later versions with expanded designs) bioassay. Just like the disposable part, the housing was composed of various components, such as the casing, the electronic and the optical units.

- The **casing** covered all the components contributing to sturdiness, protection and cover. It combined the holder in which the disposable part was fitted and the surrounding case to protect the electronics. Due to its reusability, it was built in a rigid and stable (chemically and mechanically) material such as opaque polycarbonate, which is non-transparent to prevent any interference from the environmental light to the optical measurement in the system. The **electronic** components encompassed both the wires and power requirements for driving the optical components, as well as the wireless data transmitter to forward the acquired data to a separate device. An Arduino platform was selected as microprocessor for this for being simple, miniaturized, portable and cost-effective alternative. The electronic module also incorporated an internal

storage element to make it function when no connection is available. The final version would include a small LED screen to show rudimentary results, enabling direct monitoring of the test itself.

- The final set of components was the **optical** one. These had a double function, namely detecting the Prussian blue of the cyanotyping assay through optical absorbance measurement, whilst also providing the illumination source for the cyanotyping reaction to take place. To restrain the costs of the chip-to-world interface while ensuring miniaturization and portability, one of the routing strategies as described in **Chapter 8.5**, which was based on pulsing the light at specific frequencies, allowing their identification and simultaneous analysis was employed. An optical funnel was chosen for light collection in a single photo-detector, which is illustrated in **Figure 9.1**. The funnel consisted of a material with a higher refractive index than its surroundings (ORMO-core polymer in this case) that allowed focusing of all incoming light beams towards a specific convergence spot, where the detector was positioned.

All the optical components were integrated inside the casing, to prevent modification and ensure alignment.

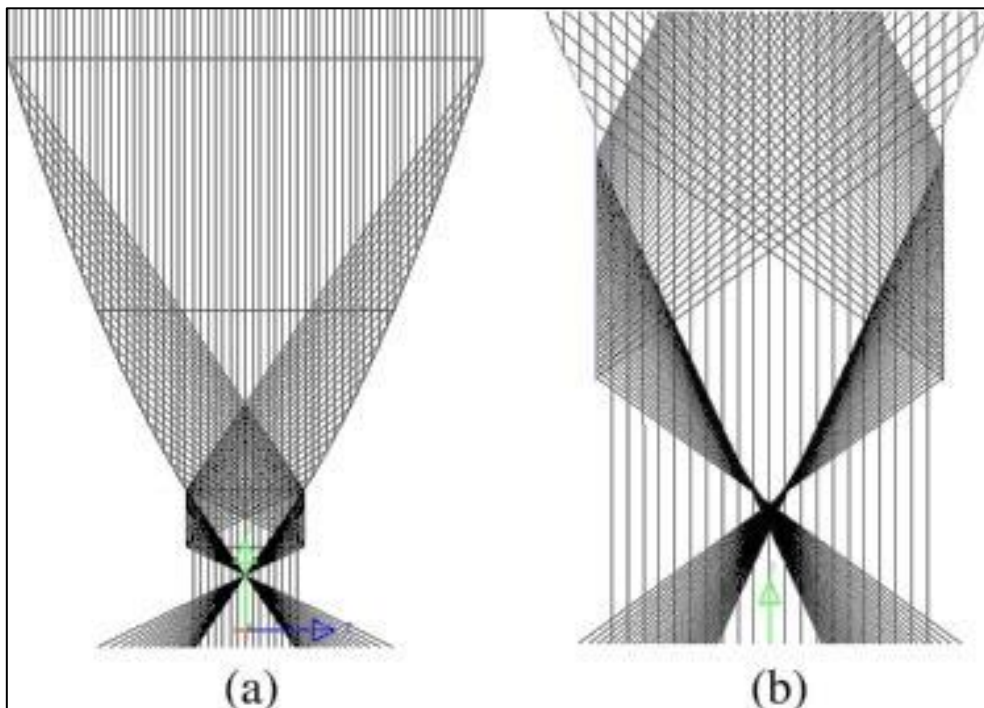


**Figure 9.1: Optical funnel for the collection of parallel light rays to a single output (a).** The curvature of the funnel will influence the exact location of the convergence point, highlighted in (b). Obtained with permission from the work of Zheng et. Al. [1].

**Figure 9.2** shows a first prototype of the final integrated photonic system for MIC determination. As illustrated, the disposable part could be inserted easily in a plug-and-play format on the housing which integrating all the components for the simultaneous measurement of four channels. At this stage, electronic components for the control of the optical measurement were implemented in a protoboard for optimization of the



system's performance. In a future version, all these components will be integrated in a single PCB using Arduino as microprocessor, which will increase the robustness and reliability of the system, while reducing its size.

The functionality of the device was mainly limited by the performance of the bioassay, although the optical components could make a difference in sensitivity of the assay. Given the slow speed of the bioassay compared to the various routing systems, the speed of the chosen optical setup did not influence the performance of the system in the determination of MIC.

Due to its versatility, similar architectures may be used for the determination of other processes involving change in the optical properties due to a (bio-) chemical recognition reaction, e.g. immunoassays. In this case, some modifications may be necessary to adjust the features of the system to the properties of the assay. The speed of detection might be one of the most important aspects to take into consideration, especially when considering the frequency modulation methods (**Chapter 8.5**) used for multiple wavelength analysis in a continuous mode in a cheap and simple electronic format. Regardless the bioassay under evaluation, the amount of optical losses during measurement might differ from those obtained in the standalone experiments. To improve this, various modifications might be necessary, such as altering the material of the stationary bioassay component, making it opaque to minimize cross-talk between channels, or modifications of the channels themselves, to convert them to waveguides, keeping the light inside.

Finally, temperature control was not implemented in this first prototype although crucial in both optical sensing and bacterial proliferation. Two possibilities are considered to guarantee thermal control of the measurement and proliferation:

- Given the small dimensions of the final device, one possibility would be placing the entire device inside an incubator. Even though most microbiological laboratories are equipped with it, it inherently limits the portability of the device.
- The second possibility would place heating pads below the disposable part. As mentioned above, the bottom support layer can be composed of any type of material, so one with optimal heat conductance will provide a homogeneous temperature to the stationary bioassay channels. The biggest drawback of an incorporated heating method is the energy requirement, resulting in either larger batteries (resulting in a larger and heavier device) or the connection to an external power source.

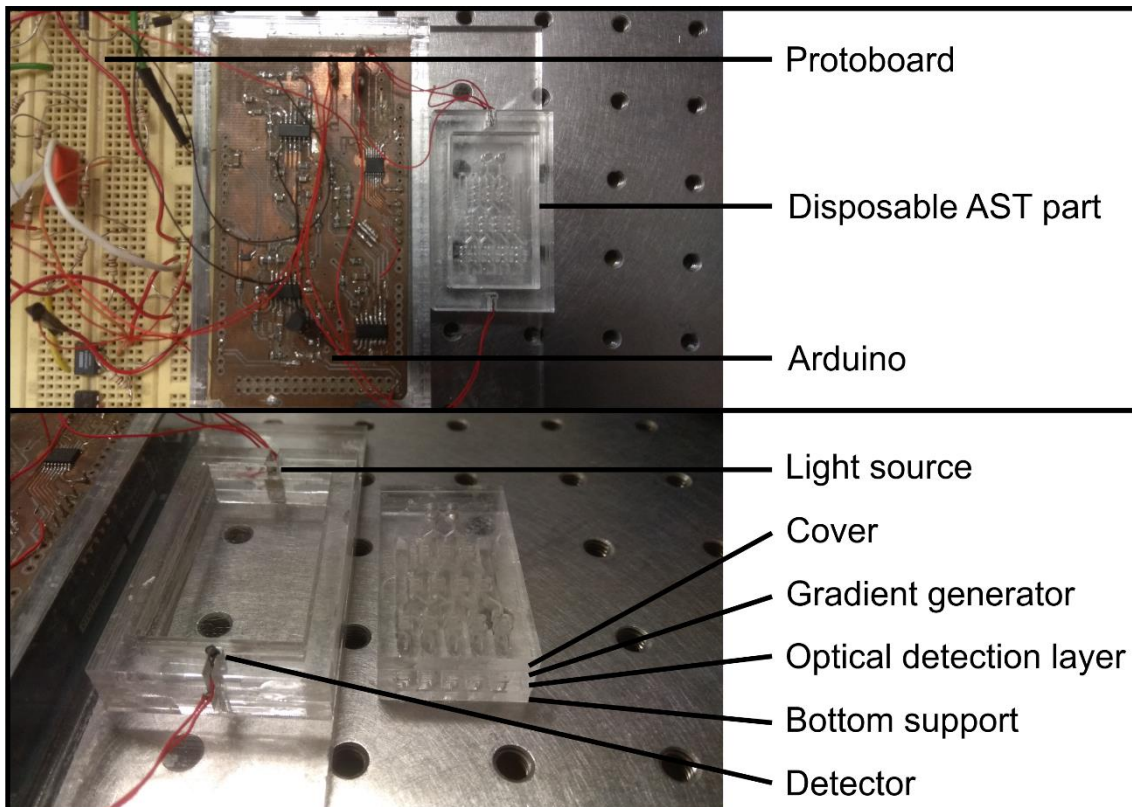


**Figure 9.2: Prototype of the final standalone device for rapid AST testing of antibiotics.** The top figure highlights the major components and electric control of the system. The bottom figure highlights the integration of the various microfluidic layers into a single device.

### 9.3. Bibliography

- [1] H. Zheng, G. Wu, T. Tao, Y. Su, J. Dai, *Energy Convers. Manag.* **2014**, *88*, 785–793.



# 10. Final conclusions

The results in this thesis describe the development of a standalone, capillary driven device, combining the cyanotype-based bioassay and integrated optical routers capable of providing minimum inhibitory concentration results within 5 hours.

According to the stated objectives:

1. The cyanotype-based bioassay enabled antibiotic susceptibility testing from purified bacterial cultures, serum and blood.
  - Relying on two low-cost, commercially available components, potassium ferricyanide and ferric ammonium citrate, a continuous monitoring of the bacterial viability was possible due to the metabolic reduction of the reagents resulting in the formation of Prussian blue.
  - Bacterial metabolism elicited a change in colour by the formation of Prussian blue particles, providing detection by either the naked eye or optical systems based on absorbance and/or scattering.
  - Resistance profiles could be generated using the cyanotype-based assay within 4 hours, currently limited to bactericidal antibiotics.
2. A capillary driven microfluidic chip was developed to perform the sample preparation on chip using logical AND-valves. These valves enabled a controlled 2-fold dilution sequence resulting in the antibiotic gradient for AST testing, without any mechanical pieces or external interaction. The inclusion of a third inlet enabled the full AST preparation and detection on chip.
3. Various optical routers, based on waveguides or electrochromic materials, were developed, capable of sequential detection of each of the optical channels using a single light source and detector. The frequency-modulator sacrificed the reduction in light sources for a continuous monitoring of all samples simultaneously.



# 11. Supplementary

## 11.1. Supplementary: Personal CV

### 11.1.1. List of publications

Pujol-Vila, F. *et al.* Bioelectrochromic hydrogel for fast antibiotic-susceptibility testing. *J. Colloid Interface Sci.* **511**, 251–258 (2018).doi:10.1016/j.jcis.2017.09.004

Dietvorst, J. *et al.* Microfluidic-controlled optical router for lab on a chip. *Lab Chip* **19**, (2019). doi:10.1039/c9lc00143c ; With back cover doi:10.1039/C9LC90067E

Dietvorst, J., *et al.* Current and near-future technologies for antibiotic susceptibility testing and resistant bacteria detection. *TrAC - Trends in Analytical Chemistry* vol. **127** (2020). doi:10.1016/j.trac.2020.115891

Ferrer-Vilanova, A. *et al.* Sonochemical coating of Prussian Blue for the production of smart bacterial-sensing hospital textiles. *Ultrason. Sonochem.* **70**, (2021). doi:10.1016/j.ultsonch.2020.105317

Narayana Iyengar, S., *et al.*, Rapid detection of viable bacteria in whole blood for early sepsis diagnostics and susceptibility testing, under submission since 11 June 2021 in *ACS Sensors*.

Dietvorst, J., *et al.* Cyanotype-based photochemical reaction enabling bacterial detection at single cell level, ready to be submitted as communication in *Angewandte Chemie* at the time of writing (04/07/2021).

Patent application, submitted at the *Swedish Intellectual Property Office PRV* under the title: Selective lysis of mammalian eukaryotic cells and visualization of viable bacterial cells. Current reference number P42106384SE00, no patent number assigned at time of writing (04/07/2021). Patent inventors: Aman RUSSOM, Sharath Tippur NARAYANA IYENGAR, Jiri DIETVORST and Xavier MUÑOZ BERBEL

### 11.1.2. List of planned publications

Paper related to the optical shutter, with Alexandre Moreno as main author. Journal yet to be determined.

Paper related to the gradient generator, with Jiri Dietvorst or Josune Jimenez as main author. Journal yet to be determined.

### 11.1.3. List of conferences

Poster, *Electro-Patternable Hydrogels With Chromatic Biological Response*, **MNE** September 18 – 22, 2017, Braga, Portugal.

Poster, *Microfluidic-controlled optical router for lab on a chip*, **MicroTAS** November 11 – 15, Kaohsiung, Taiwan.

Poster, *Optofluidic PoC for rapid antibiotic susceptibility testing using Prussian Blue*, **DIATECH** 2020 January 27-29, Leuven, Belgium.

#### 11.1.4. List of supervised projects

Bachelor Student, Armand Alsedá Plana, 1<sup>st</sup> of September 2019 – 1<sup>st</sup> of January 2020, towards obtaining the curricular internship under the title: Fast and Sensitive Detection of Bacteria Using Prussian Blue.

Master student, Maryam Pramani, 1<sup>st</sup> of March 2020 – 30<sup>th</sup> of November 2020, towards the completion of the master thesis under the title: Colorimetric Assay based on Photocatalysis of Iron-Complexes for the Early Detection of Bloodstream Infections.

## 11.2. Supplementary: Optimization cyanide-based assay

The following figures provide additional information of the results explained in **Chapter 6.4.3**. Included here are the additional measurements after 1, 2, 3, 4 and 24 hours of incubation of the samples. Cyanotype-based assays performed in light were only illuminated for the first 5 hours, after which they were kept inside the ELISA reader for continuous measurements.

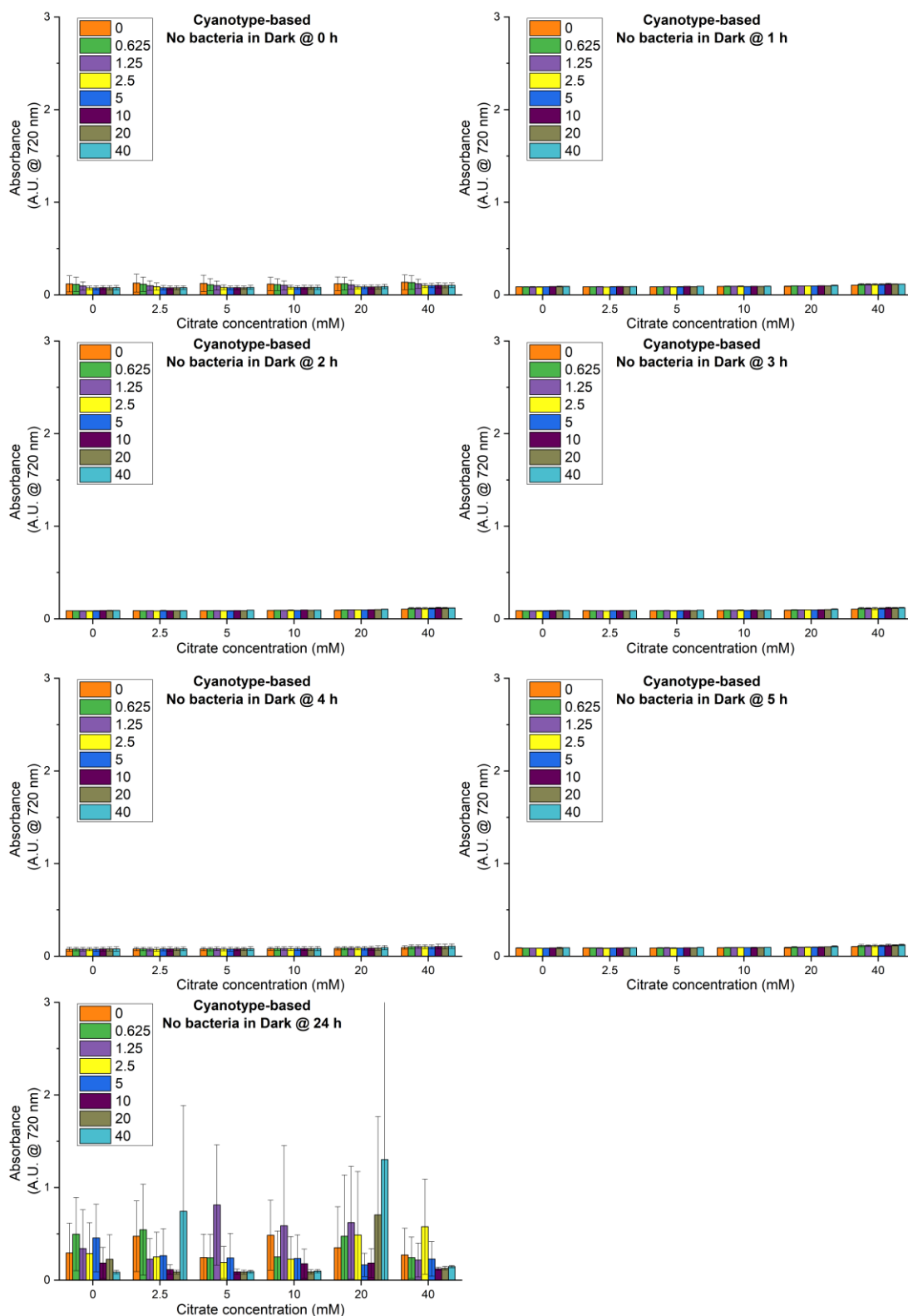


**Figure 11.1: Cyanotyping-based reaction optimization under dark conditions without bacteria.** Each graph shows the incubation of the assay at a different hour: 0-5 and 24 hours of incubation. No bacteria were present at initiation. Each group of columns refers to a single ferric ammonium citrate concentration. Each colour corresponds to a specific ferricyanide concentration. Data is plotted at a wavelength of 720 nm. (n=3)



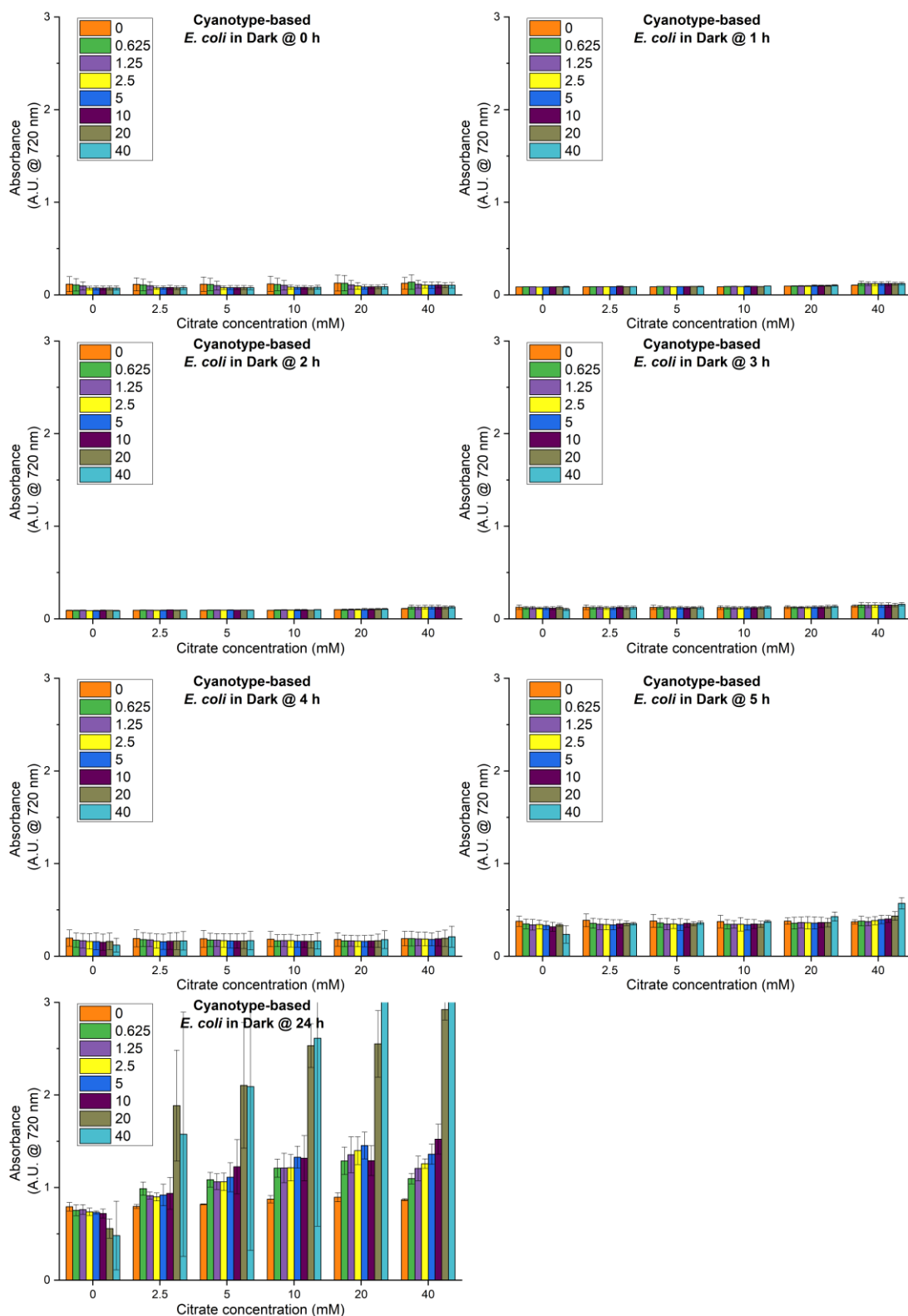


**Figure 11.2: Cyanotyping-based reaction optimization under dark conditions.** Each graph shows the incubation of the assay at a different hour: 0-5 and 24 hours of incubation. A concentration of  $5 \times 10^5$  CFU/mL of *E. coli* ATCC 25922 were present at initiation. Each group of columns refers to a single ferric ammonium citrate concentration. Each colour corresponds to a specific ferricyanide concentration. Data is plotted at a wavelength of 720 nm. (n=3)

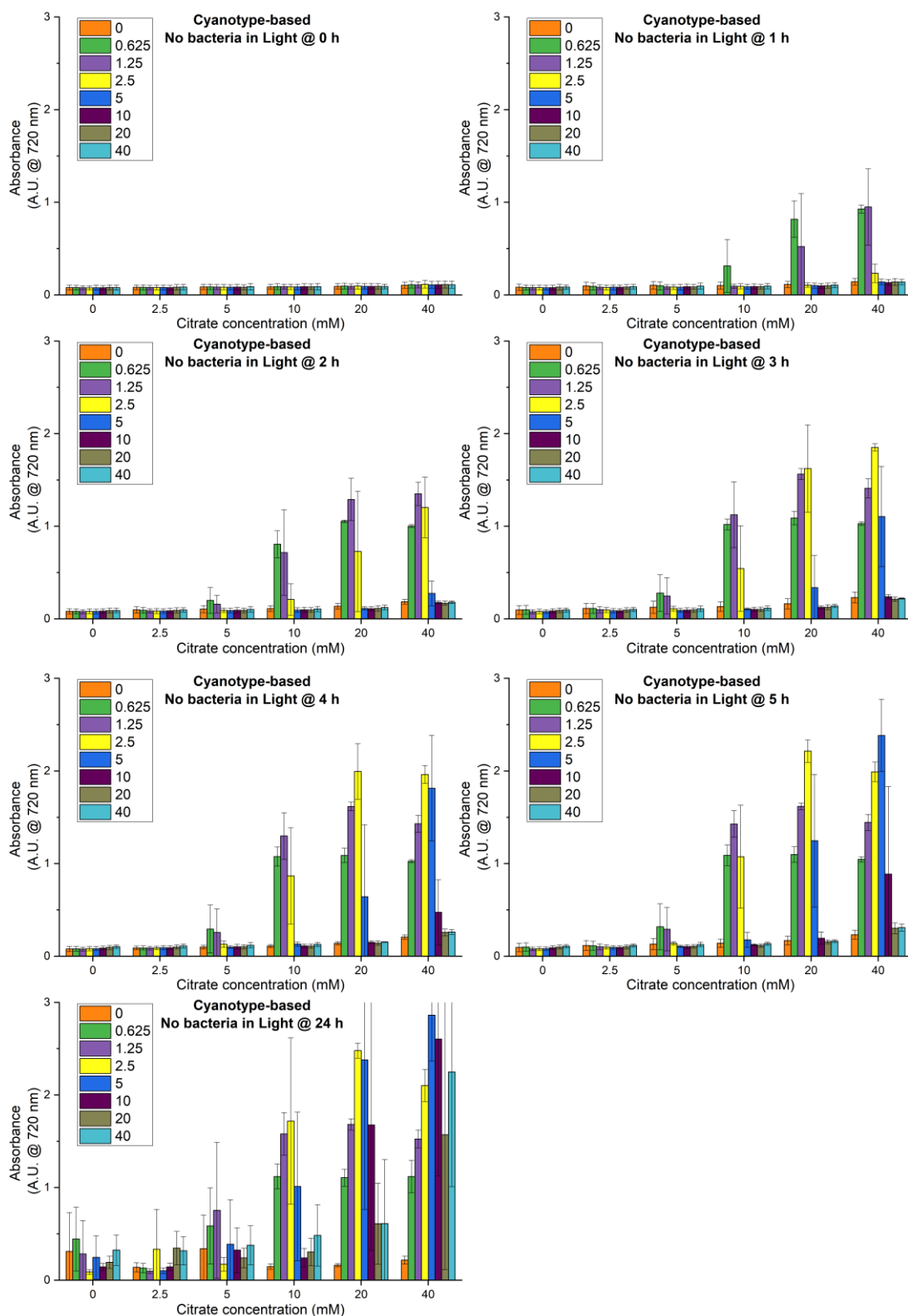


**Figure 11.3: Cyanotyping-based reaction optimization under dark conditions without bacteria.** Each graph shows the incubation of the assay at a different hour: 0-5 and 24 hours of incubation. No bacteria were present at initiation. Samples were illuminated for a total of 5 hours, after which samples were kept inside the dark inside the plate reader. Each group of columns refers to a single ferric ammonium citrate concentration. Each colour corresponds to a specific ferricyanide concentration. Data is plotted at a wavelength of 720 nm. (n=3)

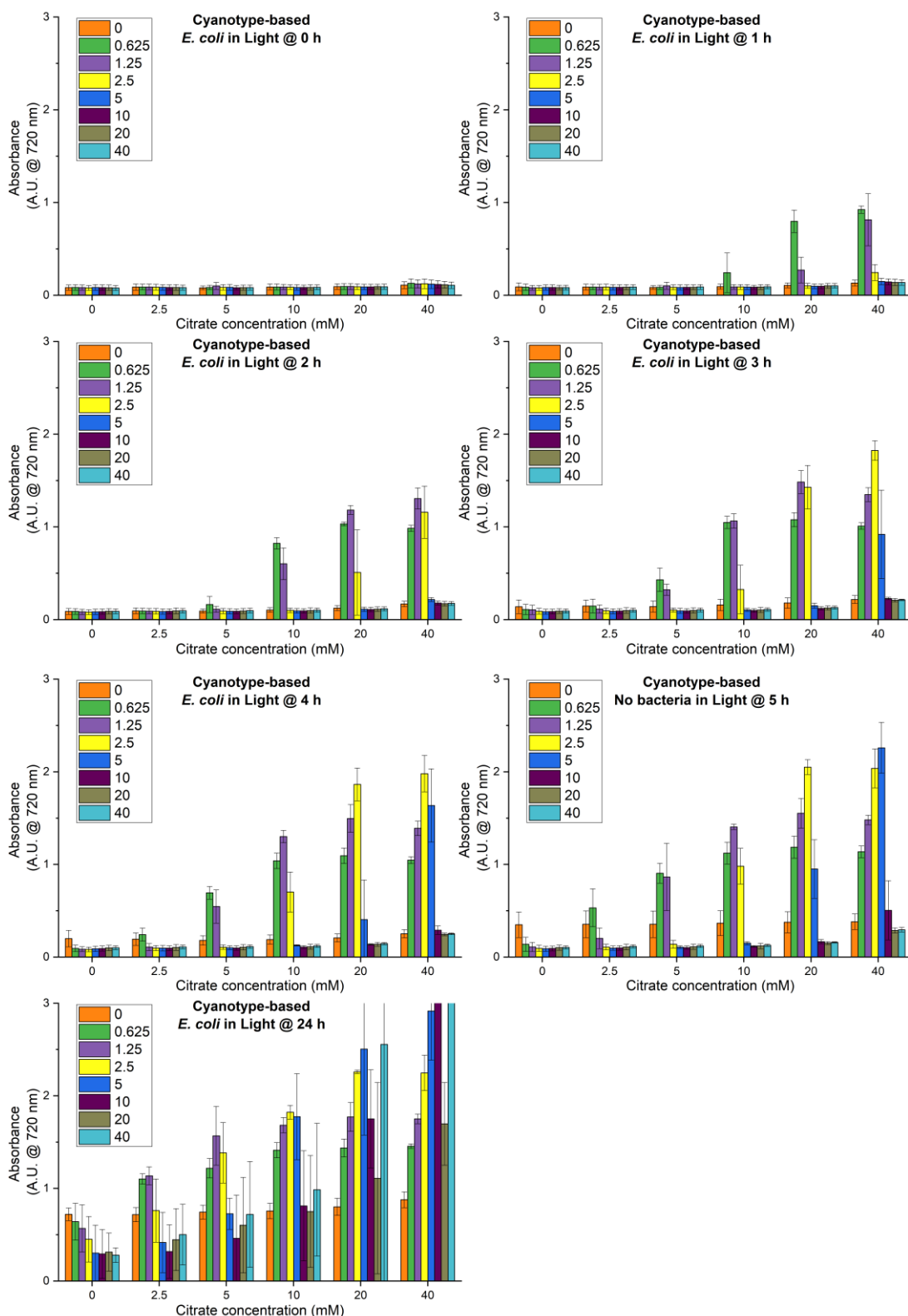


**Figure 11.4: Cyanotype-based reaction optimization under light conditions with bacteria.** Each graph shows the incubation of the assay at a different hour: 0-5 and 24 hours of incubation. A concentration of  $5 \times 10^5$  CFU/mL of *E. coli* ATCC 25922 were present at initiation. Samples were illuminated for a total of 5 hours, after which samples were kept inside the dark inside the plate reader. Each group of columns refers to a single ferric ammonium citrate concentration. Each colour corresponds to a specific ferricyanide concentration. Data is plotted at a wavelength of 720 nm. (n=3)

### 11.3. Supplementary: Ink aperture

The following part provides additional information of the results explained in **Chapter 8.2.3**. An ink aperture has been integrated in the device for reducing cross-talks, noise and the measurement of the backscattering of light. The aperture and its filling liquid serve a dual cause. The liquid is chosen to maximize light absorbance, whereas the design minimizes the absorbance of the focussed light. This is accomplished by using capillary connections at the height of the focussed light beam, the so called pinholes. These capillaries absorb minimal light, whilst serving as a connection between the large reservoirs, simplifying filling. The latter maximize absorption of stray light due to the increased volume and optical path. The filling of the aperture is done by filling one of both inlets with the absorbing liquid. A small vacuum is then applied to the other inlet/outlet, to pull the liquid through. Crystal violet was used as ink due to its absorption maximum at 620 nm, matching the used light source, to ensure maximum absorbance of scattered light. If other light wavelengths are operated, different inks can be used. In case of broadband or a white light source, a black ink is recommended due to absorption in the full visible spectrum.

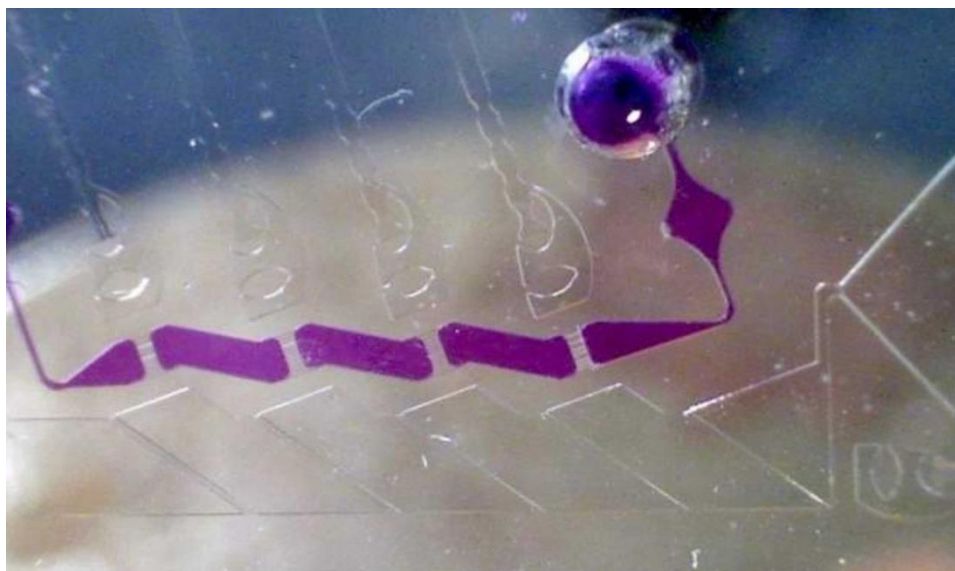


Figure 11.5: Filling of the ink aperture with a crystal violet solution.